Experiments in Turbulent Combustion

Andreas Dreizler

Institute for Reactive Flows and Diagnostics, Mechanical Engineering,

TU Darmstadt, Otto-Berndt-Str. 3

D-64287 Darmstadt, Germany

dreizler@rs.tu-darmstadt.de

Preamble

The aim of this lecture note is to present state-of-the-art experiments in turbulent combustion. The lecture is restricted to generic combustion configurations with a particular focus on gaseous turbulent flames that feature characteristics important to practical applications. The diagnostic methods presented here are well suited to study flow and scalar fields and are all based on interactions between laser light and matter. Some basic knowledge of fundamentals such as quantum mechanics, molecular structure and radiation is presumed.

Following a brief introduction, generic target configurations spanning from simple to complex are exemplified. This selection of generic configurations, of course, is far from complete. Chapter 3 and 4 introduce to most important flow and scalar measurement techniques. At the end of each of these two chapters exemplary applications of the methods are presented. Chapter 5 provides an introduction to combined scalar/flow measurements that can significantly improve our understanding of mutual interaction between chemical reactions and turbulent fluid flows. In chapter 6 recent developments based on high-repetition-rate and volumetric imaging are discussed. These diagnostics complement methods at low repetition rate commonly used to generate an understanding by statistical moments and probability density functions. High repetition rate and volumetric imaging techniques still are an emerging field. Although the most recent developments are included to this chapter, near-future progress in this field will lead to even more interesting insights into combustion phenomena. Due to the important role of numerical simulation in designing future combustion technologies, the final chapter 7 reviews some aspects of how experimental and numerical results compare.

1. Introduction to experimental combustion research

Turbulent combustion is the backbone of primary energy conversion. Although it is desirable that regenerative energy conversion processes such as solar or wind energy gain in their weight, combustion of fossil and increasingly sustainable fuels (e.g. e-fuels) will keep its dominant role in the foreseeable future. This fact and recent public disputes on global change enforce that turbulent combustion processes in their various applications such as electrical power and heat generation, propulsion and mobility must be further improved in terms of efficiency, pollutant emissions, fuel flexibility, and load flexibility.

Different pathways exist to advance combustion technologies. Figure 1.1 highlights the role of experimental methodologies. Experiments may serve either in a **direct** manner to measure key-quantities of a practical combustion process for subsequent design improvements or experimental studies serve in an **indirect** way to support the development of increasingly predictive mathematical/numerical models needed to design improved combustion technologies. Figure 1.1 additionally shows that experimental studies can gain from numerical modelling (e.g. design of appropriate nozzle geometries or assessment of systematic errors) and numerical recipes.

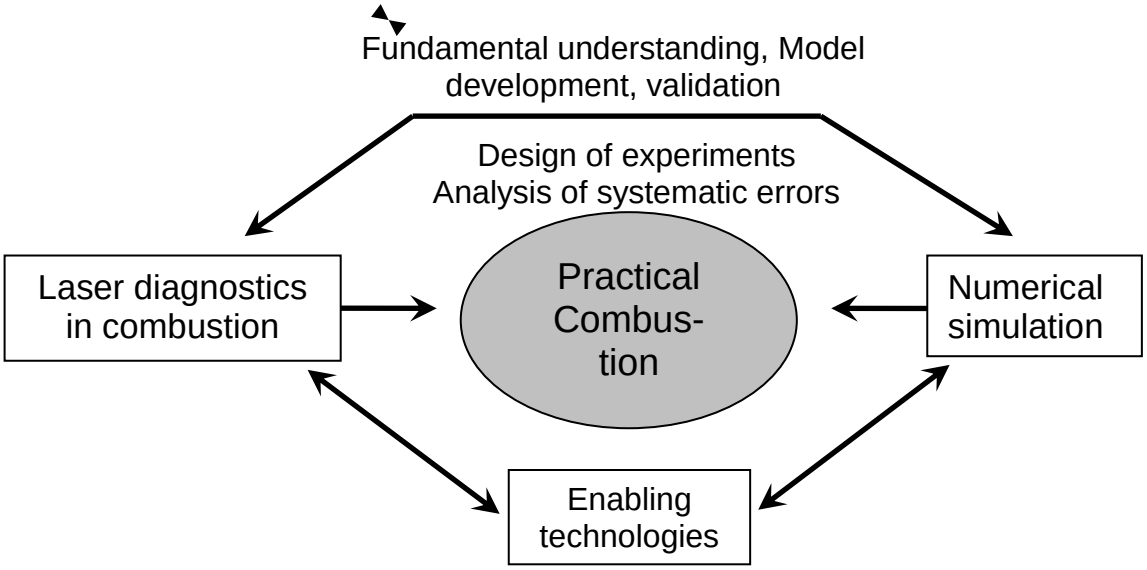

Figure 1.1
Mutual interconnections between experiments, numerical simulations/modelling and numerical recipes to improve current combustion technology.

For an experimental investigation of a combustion process two ingredients are necessary:

1. A test rig where the combustion process of interest can be operated
2. Suitable methods for its experimental characterisation.

Both aspects will be discussed here to some extent but the discussion is restricted only to **generic and gaseous combustion processes** that feature some characteristics of general interest and to in-situ **laser-optical measuring techniques**. Topics such as coal or spray combustion are apparently excluded here.

Optical- and especially laser-based methods are commonly used to study combustion processes in detail. This is attributed to the following features:

1. Optical methods are non- or minimal invasive.
2. Optical techniques can be applied in-situ. The only prerequisite is a suitable optical access.
3. The temporal resolution in comparison to probe-sampling-techniques (gas chromatography, mass spectrometry, etc.) is extremely high. Typical time scales of a practical turbulent combustion process can be resolved.
4. The spatial resolution of optical combustion diagnostics is reasonable. Although it is in general much better than intrusive probe-techniques (thermocouple, hot-wire anemometer, etc.) smallest length scales of highly turbulent combustion processes often cannot be resolved. Therefore the sensitivity of the probe-volume size on the result must be examined for each measurand.

To investigate a turbulent combustion process in detail many different quantities are of interest. These quantities of interest can be divided into flow field quantities, scalar field quantities and inflow/boundary conditions.

Boundary and inlet conditions determine many features of turbulent flames. Therefore they need to be recorded and controlled thoroughly. Dependent on the type of process examined, not only inlet profiles of relevant process parameters (velocities, temperature, chemical composition etc.) at the nozzle exit but profiles inside the nozzle must be known. In case of enclosed combustion, transfer processes (heat, mass, momentum) to the wall should be studied as well. In chapter 2, where examples of optically accessible combustion processes are shown, leadoff approaches are briefly discussed to gain insight into processes inside nozzles. Additionally an experiment is presented to measure the heat transfer from the gas phase to solid walls.

A turbulent flow field is characterised by single- and two point statistics as well as gradients for all three velocity components. Single-point statistics refer to mean and rms-values (rms: root mean square = second statistical moment). Higher moments than the second may be in special cases of some interest but impact of experimental noise and other experimental limitations on precision and accuracy are not well studied. In addition to this pointwise information on mean and rms-values, information derived from two-point statistics such as integral length scales, Kolmogorov length scales, power spectral densities and elements of the rate-of-strain and rate-of-vorticity tensor are necessary to better understand the structure of the turbulence. In chapter 3 and 5 it is discussed how laser Doppler velocimetry (LDV) and particle imaging velocimetry (PIV) can be used to measure these key-quantities of a turbulent flow under chemically reactive conditions.

The scalar field of a combustion process contains the spatial distribution of the temperature, chemical species concentrations and quantities derived from temperatures and/or concentrations. Prominent examples for the latter one are the mixture fraction or scalar dissipation rate in non- and partially-premixed flames or the reaction progress in premixed flames. Linear as well as non-linear spectroscopic methods are widely used to precisely and accurately measure these various key-quantities of the scalar field. However, as quantification in many circumstances is difficult some of these spectroscopic techniques are often used in a qualitative manner only. For example, relative distributions of flame-generated radicals such as hydroxyl (OH) serve to divide unburned from burnt regions. In chapter 4 different spectroscopic methods such as laser-induced fluorescence (LIF), Raman/Rayleigh spectroscopy and coherent anti-Stokes Raman spectroscopy (CARS) are discussed along with exemplary applications.

Turbulent combustion is complex due to the fact that chemical kinetics and turbulent fluid flows mutually interact with each other. More insights into this mutual interplay can therefore be

gained not only from multi-scalar measurements based, for example, on Raman/Rayleigh spectroscopy, but as well from simultaneous flow and scalar field measurements. In chapter 5 combinations of PIV/PLIF and LDV/PLIF show that these simultaneously applied diagnostics allow to switch the point of view from a laboratory to a flame-fixed coordinate system. Averaging and wash-out due to intermittency inherent to turbulent flames is thereby avoided. Furthermore, statistics conditioned on the intermittent flame front becomes feasible.

Laser diagnostics discussed in chapters 3 to 5 are operated in general at rather low repetition rates. In consequence the samples are statistically uncorrelated. To derive reliable statistics and build up probability density functions (PDF) statistically uncorrelated sampling is a prerequisite. However, transient processes may occur in turbulent combustion processes that are not matched appropriately by an unconditioned PDF. For example, cyclic variations in IC engines, ignition, extinction or flash back phenomena may occur. For an improved understanding these transients must be studied additionally from a different viewpoint. For this purpose chapter 6 discusses high-speed diagnostics with repetition rates in the kilo-Hertz (kHz) regime recording statistically correlated information. These rather newly developed diagnostics allow temporally tracking the evolution of flow and scalar field during individual transient events. This cinema-like information complements the traditional way of understanding reactive fluid flows by statistical moments and PDFs. In combination with high-speed imaging scanner concepts are discussed that allow a rapid sweep of a light sheet across a three-dimensional probe volume. Thus, this technology even enables quasi four-dimensional imaging. This approach is complemented by recent developments in tomographic imaging using multiple projections for imaging which is exemplified here for laser-induced fluorescence (OH-LIF).

The role of experimental methods for improvements of combustion technology was shown already in figure 1.1. The increasing importance of numerical simulation in designing future combustion processes is obvious. In a closing chapter 7, the aspect of using experiments for model validation is therefore briefly discussed. It is exemplarily shown that the connection between experiments and numerical simulations is not only unidirectional but numerical simulations can be utilized in quantifying experimental inaccuracies.

2. Generic turbulent flames with optical access

As outlined in section 1, this lecture note is focusing on gaseous turbulent flames. These flames mimic certain aspects in gas turbines, central heating applications and internal combustion engines. However, methods discussed in subsequent chapters are similarly applicable to spray flames [1] or coal combustion [2, 3].

To examine a turbulent flame by optical methods an appropriate optical access is mandatory. Whereas for unconfined, atmospheric conditions an optical access entails no principal difficulty, pressurized conditions increase the effort dramatically. In any case an optical access to the interior of a nozzle is hindered by its rather small dimensions causing interfering reflections.

In the following, three examples of generic turbulent flames and a single-cylinder optically accessible IC engine are presented. The first example is an atmospheric turbulent opposed jet burner that was used to study partially-premixed flames. The second example is an unconfined premixed swirl-burner. The third example highlights a pressurized combustor equipped with a single nozzle closer to practical conditions. Finally, the optically accessible engine is an example of intermittent combustion featuring some geometrical details such as the cylinder head

from a real-world application. This sequence of combustion devices goes from simple to complex. Each of it features certain aspects but none of them the entire complexity of a real-world application. However, by joining these different pieces of information and by parametric variation of inflow/boundary conditions, understanding of turbulent flames in practical applications is improved.

2.1 Turbulent opposed jet flame and in-nozzle measurements

The turbulent opposed flow configuration shown in figure 2.1 is well suited to investigate the transition from stable to extinguishing flames. The burner as well as various optical diagnostics used for characterization of flow and scalar fields is described in more detail in [4]. It consists of two identical vertically-opposed contoured nozzles. A 9:1 contraction ends in a 10 mm long straight section with a diameter of D = 30mm. Perforated plates with a blockage of b = 45% and hexagonally arranged holes with d = 4mm diameter are placed at the end of the contoured nozzle, followed by a 50mm long tube. The perforated plates were selected from a series of plates of different blockage ratios and hole diameters to produce strong fluctuations and almost isotropic turbulence at the nozzle exit. In the nozzle contraction, two annular meshes (5mm wide) were installed to avoid flow separation from the walls. Setting the distance between the nozzles (H = 30mm) equal to the nozzle diameter (H/D = 1.0) allowed to keep the axial dimension of the flow field compact. The half nozzle distance is used as the origin of the axial coordinate z. Consequently, the lower and upper nozzle are located at z = -15mm and z = +15mm respectively. An annular coflow of nitrogen with a diameter of 60mm and a bulk velocity of one third the fuel/air mixture bulk velocity shielded the inner jets from the surrounding air. Optical access is obtained without additional measures. Notice that the surrounding nozzles for the concentric coflow are shortened to maximize the angle of observation.

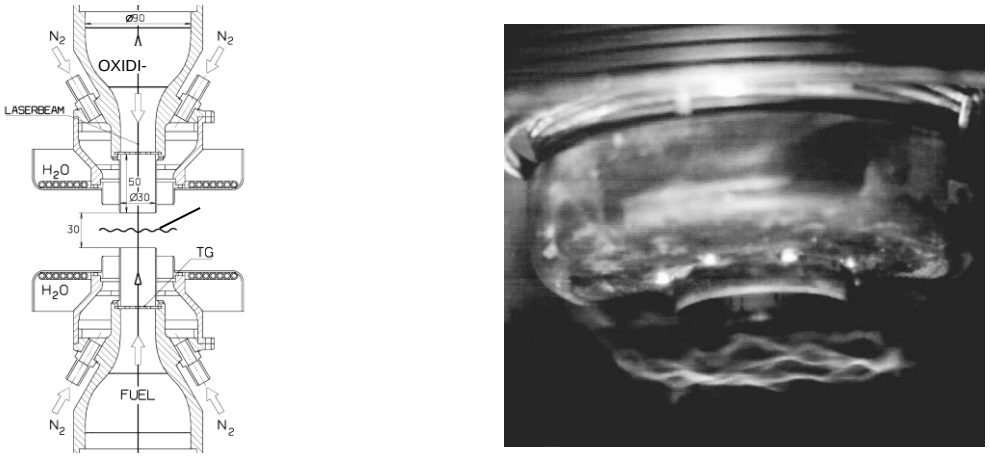

Figure 2.1
Schematic of the turbulent opposed jet burner (left) and snapshot of the luminous flame using a CMOS-camera operated with an exposure time of 2ms.

Table 2.1 summarizes various flow conditions for stable and extinguishing flames.

Table 2.1
Variation of Re-number and equivalence ratio of the fuel-feeding nozzle. This parametric variation allows to study the transition from stable to extinguishing flames.

Re_{air}	a_m(1/s)	Φ = 3.18	Φ = 2.0	Φ = 1.6	Φ = 1.2
3300	115	TOJ1A			
4500	158	TOJ1B	TOJ2B	TOJ3B	TOJ4B
5000	175	TOJ1C	TOJ2C		
6650	235	TOJ1D	TOJ2D		
7200	255		TOJ2E		

A dry and dust-free air stream emanated from the upper nozzle with a bulk velocity W_b and a bulk Reynolds number Re_b based on D and W_b. The air stream impinged on a partially-premixed methane/air stream issuing from the lower nozzle. In order to establish the stagnation plane at the half nozzle distance $H/2$ the momenta of these two opposing jets were set equal. Accordingly, the bulk strain rate is $a_b = (-W_{b,O} + W_{b,F})/H$, $W_{b,O}$ and $W_{b,F}$ are the bulk velocities at oxidizer and fuel sides, respectively. A mean residence time t_{res} in the stagnating flow region was estimated by $t_{res} = a_b^{-1}$. The integral time scale t_0 of the turbulent flow field was computed from auto-correlation functions of hot-wire anemometry data 0.5mm downstream of the oxidizer nozzle exit. Using t_0 and the axial velocity at the centerline, the integral length scale ($l_0 = 4.7\text{mm}$) at the nozzle exit was calculated utilizing Taylor's hypothesis. Thus, the integral length scale was slightly larger than the hole diameter d of the perforated plates.

Based on l_0 and the turbulent kinetic energy $\left(k = 1/2\left(w^2 + 2\times u^2\right)\right)$ a local turbulent Reynolds number, Re_t, was calculated at the centerline (z = 14.5mm). Here, w and u denote axial and radial velocity fluctuations, employing the experimentally verified radial symmetry for u and v. In case of TOJ2D, detailed in table 2.2, the velocity fluctuations in both directions increased from ~0.3ms^{-1} at the nozzle to ~0.42ms^{-1} in the stagnation plane. Since the large-eddy turnover time, $t_{ov} = l_0/(2/3k)^{1/2} = 16.2\,\text{ms}$, was approximately four times the residence time in the mixing layers t_{res}, a 'young-turbulence' emerged. This means, that the residence time was too short to allow the internal dynamics of turbulence to transfer a significant part of the kinetic energy contained in large eddies to the smallest length scales. Consequently, mixing processes at smaller length scales were less intense than in fully developed turbulent flows. The Kolmogorov length scale η_K as smallest flow scale was estimated using the turbulent Reynolds number and the integral length scale as ~0.16 mm. Since the Prandtl number Pr, the ratio of kinematic viscosity ν and thermal diffusivity D_T, in this flow is less than one (~0.65 to ~0.80), the smallest scalar length scale to be resolved is larger than η_K. For $Pr < 1$ the smallest spatial extension of scalar gradients to be resolved and hence the scalar dissipation rate is active on the Obukhov-Corrsin scale ($\eta_C = (D_T^3/\varepsilon)^{1/4}$, ε is the dissipation) [5]. Hot-wire anemometry has been used to estimate the dissipation ε at the oxidizer nozzle exit. From this information the value for η_c at the nozzle exit was determined as 0.18 mm.

Table 2.2
Flow field quantities for flame TOJ2D

Bulk velocity W_b	3.4m/s
Turbulent Re-number Re_t	90
Bulk strain rate $a_b = \left(-W_{b,O} + W_{b,F}\right)/H$	231s $^{-1}$
Residence time in mixing layers $t_{res} = a_b^{-1}$	4.3ms
Large-eddy turnover time $t_{ov} = l_0/(2k)^{1/2}$	16.2ms
Integral time scale T at nozzle exit	1.6ms
Integral length scale l_0 at nozzle exit	4.7mm
Kolmogorov length scale η_K at nozzle exit	0.16mm
Obhukov-Corrsin scale η_c at nozzle exit	0.18mm

Flame extinction is the ultimate consequence of intense turbulence – chemistry interaction. Therefore, extinction limits were experimentally determined with a precision better than 0.7% using calibrated mass-flow controllers. A flame was defined as 'extinguishing' if the flame could not be stabilized at least twice for a time period of 30s in 50 consecutive attempts. The extinction limit of the flow for the current fuel composition was reached at Re_b = 7200, which corresponds to a bulk strain rate of 255s^{-1}.

The design of the perforated plates to enhance turbulence shows significant impact on the flame [6]. In accordance to this experimentally observed sensitivity, large-eddy simulations [4, 7] (LES) critically depended on the initial choice of the flow properties through the perforated plates. Therefore an experimental analysis of the developing turbulence directly downstream of the perforated plates inside the nozzles is desirable. This is achieved by replacing the 50mm straight metal tube that is attached to the contoured nozzles by a quartz tube. Of course the concentric nozzle for the N_2-coflow was dismounted. Using particle imaging velocimetry (PIV) detailed in chapter 3 the flow field emanating from the individual 4mm-dia. holes was investigated. The initial turbulence level as well as the break-up of the individual jets will be quantified in this manner. It is expected that from such measurements the relation between inflow conditions and flame characteristics can be studied.

2.2 Premixed swirl flame

The swirl burner introduced in this section [8, 9] is designed to study premixed flames that feature characteristics already similar to practical designs. Parametric variation of *Re*-number/thermal power is easily feasible by increasing mass flow rates. In addition, by variation of the swirl intensity, the transition from a statistically stable to a precessing flame that finally flashs back is possible [10, 11].

A schematic of the unconfined premixed swirl burner is shown in figure 2.2(a). The burner consisted of a 15mm wide annular slit surrounding a central bluff body with d = 30mm. Upstream of the nozzle, swirl was generated by a moveable block geometry. Theoretical swirl numbers $S_{0,th}$ could be adjusted in the range from 0 to 2.0. Values of $S_{0,th}$ exceeding 0.8 resulted in flash back. 70mm upstream of the moveable block, natural gas was injected into the combustion-air flow at 300K using a perforated ring line. Homogeneous mixing was confirmed

experimentally during the development phase of the burner by seeding the fuel with submicron particles and performing planar Mie scattering in a 40x40mm^2 plane monitoring the flow downstream the nozzle exit.

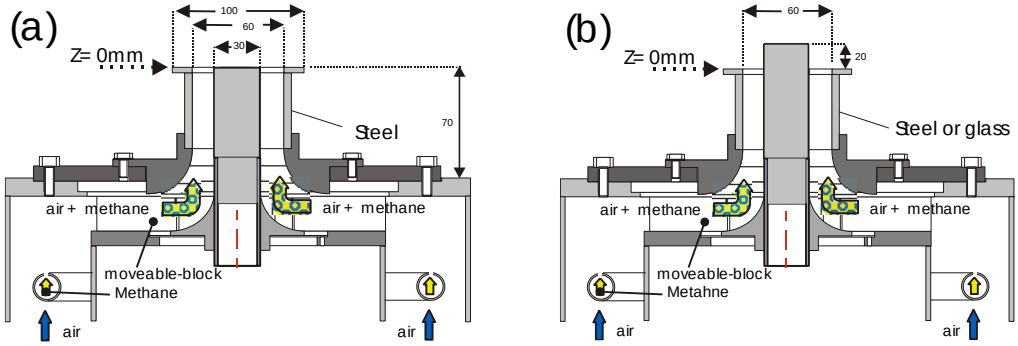

Figure 2.2
Left: Cross-sectional view of the nozzle used for stable flame operation. Right: Adapted nozzle by extended central bluff-body and optical access to the annular slot. This configuration is designed for studying precessing flames and flash back into the nozzle.

To achieve defined boundary conditions, the burner was placed into a coaxial air flow, emanating from an annular orifice with D = 220mm in diameter. The mean velocity of this co-flowing air was set to 0.5m/s. All flow rates were controlled electronically by high precision mass flow meters (Bronckhorst).

The flow field was investigated both for combusting and non-reacting (isothermal) conditions (pure air, same momentum at the nozzle exit as the respective combusting case, compare chapter 3.3.3). Flow conditions are listed in table 2.3. The number within the acronym denotes the thermal power in kW.

Table 2.3
Different flow configurations investigated on the premixed swirl burner. The *Re*-number is calculated for the nozzle exit, bulk velocity and exit area. In the corresponding isothermal cases fuel was substituted by air keeping the momentum at the nozzle exit.

		PSF-30	***PSF-90***	***PSF-150***
$S_{0,th}$	[-]	0.75	0.75	0.75
P	[kW]	30	90	150
ϕ	[-]	0.833	0.833	1.0
Q_{gas}	[m_n^3/h]	3.02	9.06	15.1
Q_{air}	[m_n^3/h]	34.91	104.33	145.45
$Re_{tot.}$	[-]	10000	29900	42300
s_L	[m/s]	0.36	0.36	0.42
l_F	[m]	$0.26 \cdot 10^{-3}$	$0.26 \cdot 10^{-3}$	$0.18 \cdot 10^{-3}$

In order to classify turbulent premixed flames a regime diagram initially proposed by Borghi [12], revised by Peters [13] and others, is commonly used where the oncoming turbulence intensity u' normalised by the laminar burning velocity s_L is plotted versus the turbulent length scale l_0 normalised by the laminar flame thickness l_F. Notice, that for this classification in general equal diffusivities and a Schmidt number of $Sc = 1$ are assumed. Turbulence intensities and turbulent length scales were measured by single and two point LDV, respectively, as discussed in chapter 3. Laminar burning velocities of different equivalence ratios are taken from [13], and the laminar flame thickness is deduced from $l_F = D/s_L$. The molecular diffusion coefficient $D = (\lambda/c_p)_0/\rho_u$ is calculated from the equivalence ratio $\phi = 1/\lambda$, specific heat capacity c_p and density of unburned premixed gases ρ_u taking values from [13] and assuming a mean temperature of 1500K within the internal reaction zone. Resulting values for s_L and l_F are included to table 2.3. Using spatial positions of (x = 10mm, r = 25mm) and (x = 30mm, r = 30mm) as representative positions within highly turbulent shear layers, the respective classification of the investigated flames within the regime diagram is shown in figure 2.3. The configuration PSF-30 is located in the cross-over of corrugated flamelets to thin reaction zones, whereas PSF-90 and PSF-150 are clearly located in the regime of thin reaction zones.

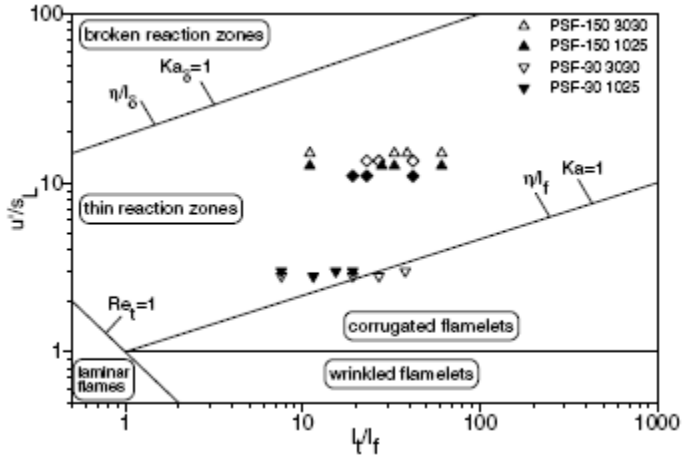

Figure 2.3
Phase diagram to classify turbulent premixed combustion. The flames PSF-30 and -150 are charted by symbols.

Flashback was observed at swirl numbers exceeding a critical value $S_{th,crit}$. It could be associated with the onset of a precessing vortex core (PVC), analogous to the non-reacting case (see section 3.3.3), causing a coherent precession of the flame and eventually reaching back into the annular slot. An experimental review of this hypothesis necessitates slight adaptations of the nozzle.

For this reason the original design of the nozzle shown in figure 2.2(a) was changed by extending the central bluff-body by 20mm (figure 2.2(b)) [10]. By this measure the transitional regime between stable and flashback (termed “meta-stable” and associated with a precession of the flame) was extended and made experimentally accessible for sufficiently long observation times. To allow optical observation of the transient flame during flashback, the outer cylindrical wall of the annular slot was replaced in some of the experiments by a cylindrical glass tube. The inner diameter of 60mm was matched to its stainless-steel counterpart. For easy control of

the swirl number the moveable block was equipped with an electrical stepper motor. By an additional gear reduction the theoretical swirl number could be changed in increments of ΔS_{th} = 0.02. This was sensitive enough to reproduce the various operational modes of the flame as detailed below.

For a global characterization of flame stability, the equivalence ratio and the Reynolds number were varied. The left hand side of figure 2.4 shows the critical theoretical swirl number $S_{th,crit}$ for a fixed Reynolds number of 10000 (based on hydraulic diameter and bulk nozzle exit velocity). At the right hand side $S_{th,crit}$ is presented for fixed equivalence ratios but varying Reynolds numbers. Operation of the flame in regions below the experimental data points corresponds to statistically stable conditions, the regions above the data points correspond to flashback. Due to limitations in the laboratory environment the maximum thermal load of the rig was restricted to 35kW. For $\phi = 1$ this was reached at Re = 10000. Therefore higher Reynolds numbers or richer mixtures were not investigated.

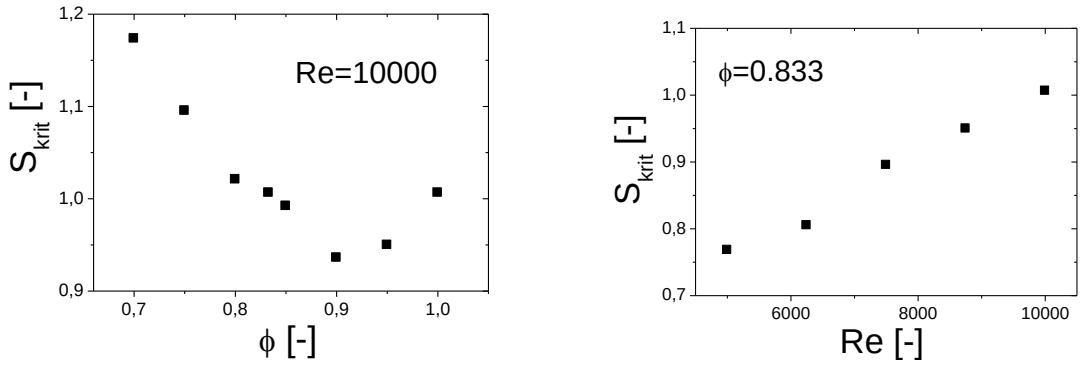

Figure 2.4
Critical theoretical swirl numbers $S_{th,crit}$ where flashback occurs. Left: fixed *Re*, varying equivalence ratio. Right: fixed equivalence ratio, varying *Re*.

In a range from $\phi = 0.7$ to 0.9 $S_{th,crit}$ decreases monotonically. Exceeding $\phi = 0.9$, $S_{th,crit}$ increases again and reaches a value of $S_{th,crit} \approx 1.0$ at $\phi = 1.0$. At $\phi = 0.833$ the critical swirl number was $S_{th,crit} \approx 1.0$. This corresponds to a 25% increase relative to the original nozzle geometry (figure 2.2(a)) and can be attributed to changes in the flow field by the extended bluff-body. Although at a first glance this curve progression appears anti-correlated to the laminar burning velocities s_L, a closer inspection shows that the respective minimum of the curve in figure 2.4 (left) does not coincide with the maximum of s_L for methane/air mixtures ($s_{L,max}$ located at $\phi \approx 1.08$ figure 2.2 in [13]).

For a fixed equivalence ratio $S_{th,crit}$ increases approximately linearly with the Reynolds-number. From this finding one can simply conclude that larger bulk velocities retard the onset of flashback. However, a physically sound reason for this scaling can not be deduced from this stability map.

Figure 2.5 gives a visual impression of the three different operational modes by imaging the spectrally integrated chemiluminescence in the visible and near UV. These images were taken with an intensified high-speed CMOS (complementary metal oxide semiconductor)-camera

system (LaVision). Exposure times for these examples were 100µs. Figure 2.5(a) shows the flame without any swirl acting as an annular jet flame.

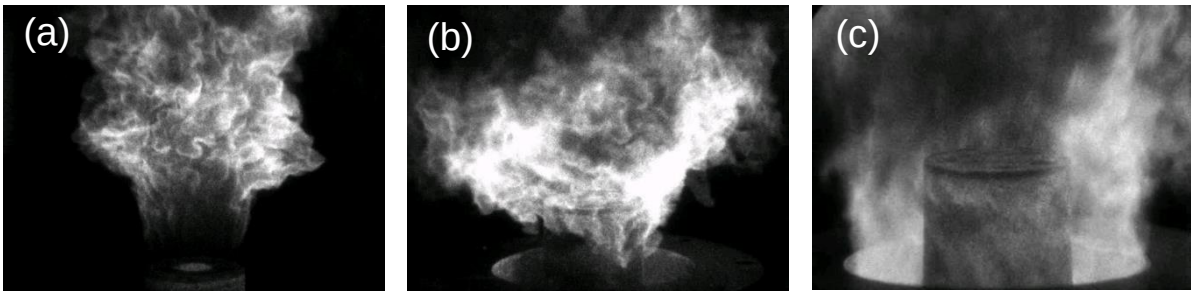

Figure 2.5
Snapshots of turbulent premixed methane/air flames: Re = 10000, ϕ = 0.833. Left: no swirl, no precession of the flame, flame is stabilized at the rim of the bluff-body. Middle: $S_{th} \approx 0.8$, prior to flashback, flame precesses around the cylindrical bluff-body. Right: $S_{th} > S_{th,crit}$, flame after flashback.

It was anchored at the front side of the central bluff-body. No precession of the flame was observable. At the instant of time presented in figure 2.5(a) vortex shedding created the mushroom-like structure of chemiluminescence. Increasing the theoretical swirl number to values in a range between 0.8 and 1.0, the farthest upstream position of the flame left the rim of the bluff-body and moved upstream. As obvious from figure 2.5(b) the flame stabilized freely in the diverging flow field beside the shell of the bluff-body. The stabilization point was highly transient and it precessed around the bluff-body. The average "leading edge" flame position depended sensitively on the swirl number. For $S_{th,crit} \approx 1.0$ only a slight increase of the swirl could cause the flame to reach back into the annular slot. Once the combustion zone was located partly in the annular slot the flow dilatation just upstream the flame was expected to accelerate the flow at neighbouring radial and circumferential locations in the slot. This situation might promote a combustion-induced vortex breakdown. To confirm this expectation high-speed particle imaging velocimetry (PIV) conditioned on the heat release zone is planned for the near future.

When the critical swirl number was met or passed the flame suddenly flashed back into the nozzle and stabilized upstream at the swirler assembly. Figure 2.5(c) shows the chemiluminescence after the flashback. In this mode a combustion instability was observed producing rumbling at rather low frequencies. By high-speed imaging at several kHz a clear oscillation of chemiluminescnce intensity was observed that was associated with heat release oscillation causing the rumbling. Figure 2.6 shows one cycle of time resolved chemiluminescence monitored with the intensified CMOS at a repetition rate of 7kHz. The view was from top but slightly tilted to prevent damaging of the optics due to hot exhaust. That is why the slot appears slightly asymmetric. Based on 14 consecutive cycles, the mean cycle duration was 7.5ms with a standard deviation of 0.6ms (~133±10Hz).

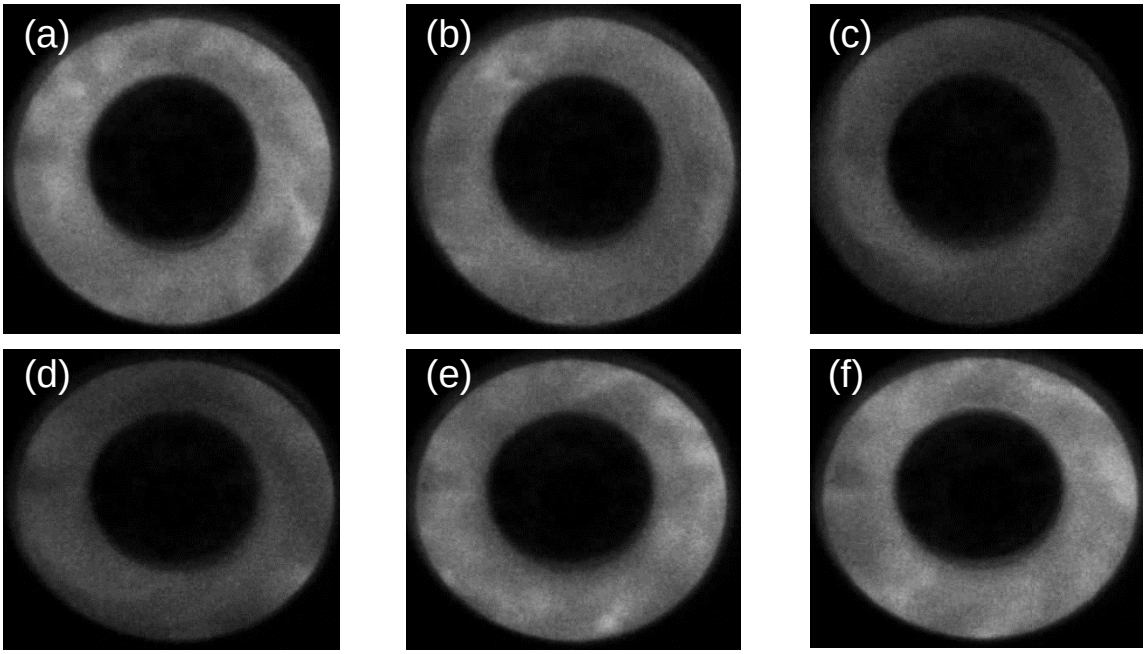

Figure 2.6
Flame luminescence monitored by intensified CMOS-camera at a frame rate of 7kHz. Only 6 exposures of a full cycle are shown. The cycle duration was ~7.5±0.6ms.

2.3 Confined pressurized flame

Confined turbulent flames are considered to study the influence of flame-wall interactions and pressure dependency. These configurations are very close to real-world applications although in most cases only single-nozzles are operated in the combustor.

Two types of generic nozzles are presented here. The first one is based on a scaled version of the nozzle presented in the previous section [14]. Stabilizing a swirling gas flame, the primary intention is to investigate the interaction between the turbulent flame and effusion cooling similar to configurations in modern aero engines [15].

Figure 2.7 shows a cross and longitudinal section view of the single sector combustor (SSC). The flame tube has a rectangular cross-section with a volume of 100x100x180 mm^3. Premixed oxidizer and fuel is supplied through a movable block swirler (scaled version of that shown in Fig. 2.2) to the main stage, realized as an annulus with a surface area of ~ 615 mm^2 in the head plate. Additionally, the central bluff body has a 2 mm central bore which serves as a pilot stage operated with pure fuel. For improved numerical and experimental accessibility, the chemical complexity is reduced by using natural gas from the domestic pipeline compared to liquid fuels. The flame tube is optically accessible from three sides over the entire length. As a bottom segment, a modular cooling geometry can be mounted which is fed by a hot air wind tunnel, ensuring a homogeneous flow pattern upstream of the cooled liner. Cooling air is conditioned independently from the oxidizer mass flow for high versatility and reproducibility. Figure 2.8 shows the effusion cooling geometry used in this study. Pressure and temperature of the effusion cooling air are measured ~ 4mm below the cooling plate in the mid plane. All mass flows entering the flame tube are controlled using thermal mass flow controllers and no additional window cooling air is used on the inside, i.e. the boundary conditions are well-known.

Flame-cooling-air-interaction is investigated using parametric variations of effusion cooling mass flow, geometrical swirl number and staging ratio, defined as the ratio of pilot fuel mass flow to total fuel mass flow. The entire set of relevant boundary conditions is listed in Table 2.4.

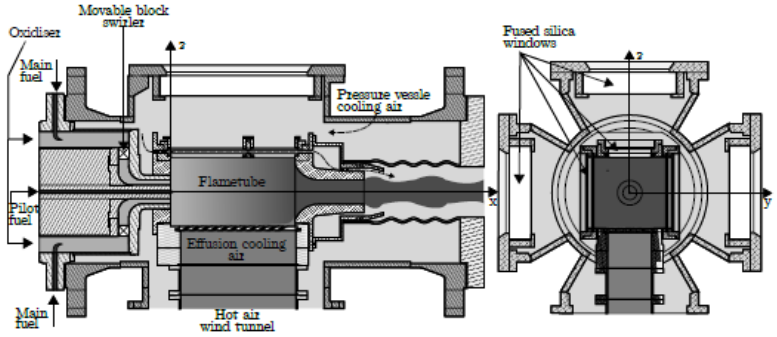

Figure 2.7
Cross-sectional views of the optically accessible single-nozzle combustor.

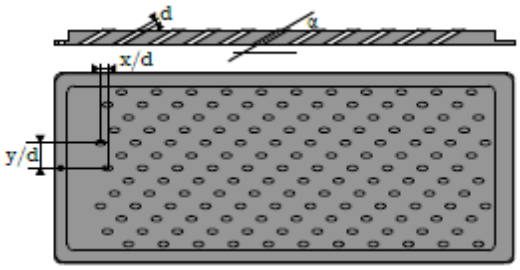

Figure 2.8
Effusion cooling geometry used in this study. Geometrical properties are listed in Table 2.4.

Table 2.4
Geometrical characteristics of the effusion cooling device (left) and boundary conditions (right)

Property	Symbol	Value	Unit	Property	Symbol	Value	Unit
No. of holes	n	145	–	Oxidizer mass flow	$\dot{m}_{ox}$	30	g/s
Angle	α	30	°	Oxidizer temperature	T_{ox}	623	K
Hole diameter	d	2	mm	Eff. cooling mass flow	$\dot{m}_{eff}$	[7.5, 15]	g/s
Intermittency	N	3	–	Eff. cooling temperature	T_{eff}	623	K
Axial distance	x/d	1,38	–	Total fuel mass flow	$\dot{m}_f$	1.128	g/s
Lateral distance	y/d	2,5	–	Pressure	p	0.25	MPa
Porosity	p	4	%	Swirl	S	[0.7,1.0,1.3]	–
Material	-	2.4663	-	Staging ratio	SR	[0,10]	%

The second example of a generic type nozzle presented here is based on a design by TURBOMECA [16, 1]. It consists of a round gaseous fuel jet that is surrounded by a single swirled, heated combustion air flow. The swirl is generated through tangential vanes as can be seen from the schematic as well as the 3D-view of the nozzle in figure 2.9.

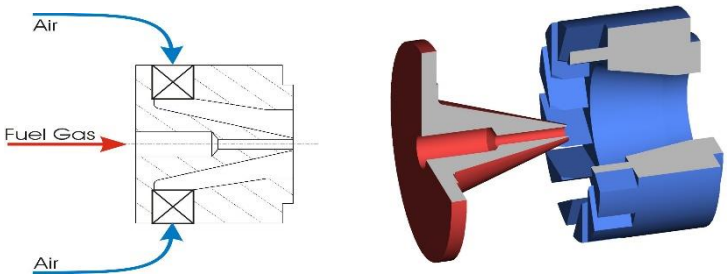

Figure 2.9
Schematic (distorted) and 3D-view of the single swirler nozzle

The operating point was characterized by the combustor pressure p, the preheated inlet temperature T, the air mass flow rate $\dot{m}$ and the equivalence ratio ϕ (see table 2.5). The air flow rate at the given parameter set corresponded to a $\Delta p/p$ = 3% pressure drop across the nozzle, typical for gas turbine applications.

Table 2.5
Operating points for confined pressurized flames, equivalence ratio was constantly 0.8.

Pressure	**2bar**	**4bar**	**6bar**
Combustion air temperature	623K	623K	623K
Fuel temperature	373K	373K	373K
Combustion air mass flow	30g/s	60g/s	90g/s
Re_{Air}	46000	92000	138000
Re_{Fuel}	33000	67000	100000

For the reacting case natural gas was used as fuel. Since the flow field of the reacting as well as the non-reacting case is of fundamental importance, the natural gas was substituted by an appropriate mixture of helium and air in order to get the same density and hence keep up the Reynolds similarity for both cases.

The nozzle was operated in a modular high pressure combustion rig capable of providing gas turbine combustor inlet conditions corresponding to pressures up to p = 10bar and temperatures up to T = 773K with an max. primary air flow of $\dot{m}$ = 150g/s. Air from a compressor (Atlas Copco) was split into combustion air and cooling air by electronically controlled valves with a mass flow ratio of $m_{combustion}/m_{cooling}$ = 1/3. The combustion air was electrically heated, while the cooling air remained unheated. The combustor pressure can be continuously set by an electronically controlled back pressure valve in the exhaust duct. The compressed natural gas was supplied by a piston compressor (Bauer). Its mass flow as well as the mixture composition of the fuel substitute was set and regulated by mass flow controllers. The basic design concept, as shown in figure 2.10, consisted of a double walled, air cooled flame tube encased by a pressure vessel. Thus, no film cooling inside the flame tube was necessary that may disturb the flow field or chemical reactions. Downstream the optical accessible flame tube the cooling air is mixed into the exhaust. Between the combustion chamber and the back pressure valve is a

cooling section of approx. 3m in length. Water injection helps dropping the temperature below 673 K, which is a requirement for the operation of the back pressure valve. Being mainly designed for the application of laser based measurement techniques, the combustor was equipped with large optical access from three sides as shown in figure 2.10. The flame tube cross sectional area was circular with three planar window segments. It's inner diameter was 120 mm with an optical accessible length of 100mm. The height of the inward windows was 60mm.

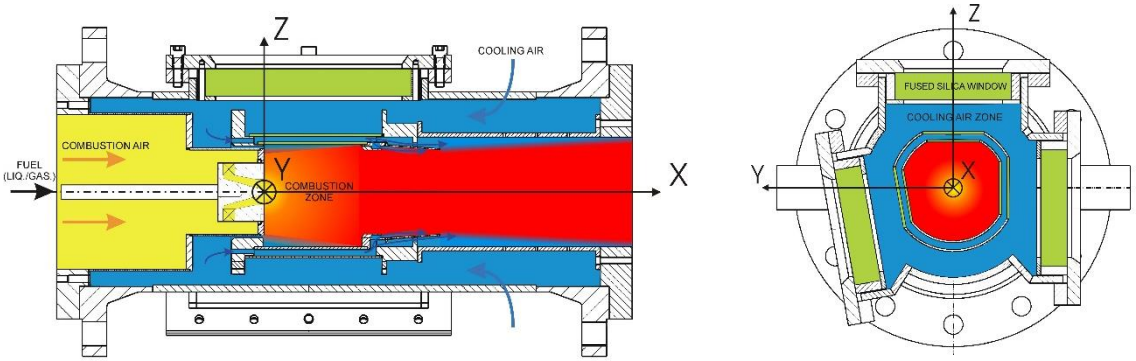

Figure 2.10
Longitudinal (left) and cross section (right) of combustion chamber with coordinate system orientation

The immobile pressure chamber is surrounded by a step motor driven 3D-traversing system (minimum traversing distance $\Delta x = 0.1$ mm). The coordinate system that formed the basis of the conducted experiments and that will be used for the results' presentation can be taken from figure 2.10. Due to the deviation of the cross sectional area from the axis-symmetry velocity measurements were carried out along both radial axes.

Due to space restrictions no experimental studies of enclosed pressurized flames are discussed in this note. The interested reader is referred to [16, 1, 17].

2.4 Optically accessible engine

The single-cylinder direct-injection spark-ignition (DISI) optical engine presented here exemplary (figure 2.11) is equipped with a four-valve pent roof cylinder head. Operating parameters and engine details are shown in Table 2.6.

Table 2.6
Single cylinder engine specifications

Bore	**86 mm**	**Intake pressure**	**50-300 kPa**
Stroke	86 mm	Intake air temperature	295-340 K
Compression ratio	8.5	Intake valve closing	125° bTDC
Displacement volume	499 cm³	Max. valve lift	9.5 mm
Engine speed	≤3,000 rpm	Flow motion	Typically tumble

A quartz-glass cylinder with an optical height of 55 mm (glass thickness: 20 mm) in combination with a Bowditch extended piston with flat quartz-glass piston top enables optical access to the combustion chamber. The flat piston deviates substantially from a real-world geometry and does have a significant impact upon the cylinder flows. However, a flat piston window provides significant advantages in terms of optical imaging. The spark plug can be removed and replaced with a threaded plug for undisturbed flow field investigations. Silicone oil droplets or solid seeding can be seeded into the intake air.

For motored engine conditions the engine is operated by an asynchrony motor. This motor acts as break in case the engine is fired. Dependent on the type of investigations fuel may be a surrogate such as a blend of iso-octane and n-heptane or conventional gasoline. For more information see [18–21, 21–23].

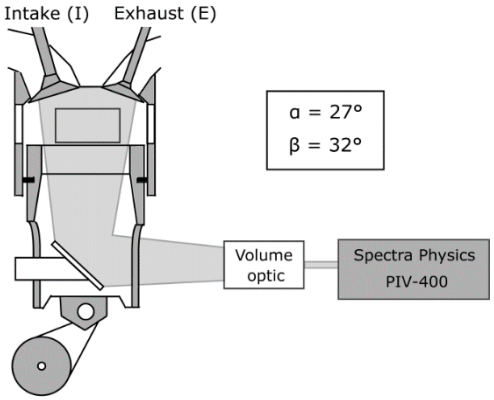

Figure 2.11
Schematic of an optically transparent single cylinder research engine. Optical access is enabled through a quartz cylinder liner and/ or a piston window.

2.5 The role of flame sequences

In terms of a better understanding of turbulent combustion and in terms of providing experimental data for validation of numerical simulations it is crucial to vary parametrically *Re*-number, swirl intensity, pressure, equivalence ratio, and fuel composition. Parametric variations provide insight into mutual dependencies of boundary conditions and the turbulent flame. Of course not all of these variations are feasible using a single test rig. Therefore different generic flames, as exemplified above, need to be investigated using various diagnostic methods. This makes such fundamental experiments studying turbulent combustion so cumbersome and expensive. This fact calls for international cooperation of academia and industry. The International Workshop on Measurement and Computation of Turbulent Flames (TNF) [24] may serve as an excellent example of a fruitful international cooperation. As this Workshop is concentrating on turbulence – chemistry interaction in turbulent flames, a similar Workshop for engine combustion was established [25].

2.6 Heat transfer measurements to walls

Most efforts of the combustion diagnostics community were focused on measurements far from walls. Practical combustion, however, is confined. Therefore the interaction between gas phase

and solid walls needs to be considered as well. This task can be split into two subtasks: (1) diagnostics at surfaces and (2) near-wall gas phase diagnostics. The latter task is impeded by surface-scattered light and the necessity of high spatial resolution due to decreasing length scales closer to surfaces. Surface-scattered light enforces thorough spectral separation from radiation containing designated information. In filtered Rayleigh scattering [26] this task is solved by single-frequency excitation and detection of Doppler-broadened lines through a narrow (atomic or molecular) notch filter cutting away the surfaces-scattered light that is not broadened. Red-shifted fluorescence in LIF-approaches and spontaneous Raman scattering provides sufficiently good discrimination as shown in [27–29]. Even coherent anti-Stokes Raman spectroscopy (CARS) can be applied close to surfaces with wall-normal resolution in the order of 100 µm [30–34]. These near-wall measurements need to be endorsed by (simultaneous) surface measurements of different scalars. In this contribution the focus is only on surface temperature measurements.

Surface temperatures in combustion applications can be measured spectroscopically by phosphorescence [35, 36]. Phosphors are rare-earth or transition metal doped ceramic materials. Many of them show temperature-dependent characteristics. Following a UV-excitation, the phosphorescence decay and the intensity ratio [37] of different emission bands vary with temperature for different phosphor materials. Those materials where these spectroscopic characteristics are exploited for thermometry are termed thermographic phosphors (TGP). Recent reviews summarize important features of thermographic phosphors [36, 38, 35].

Compared to the line intensity method the phosphorescence decay is less disturbed by varying transmission of the optical access to the combustor. The temperature-sensitivity of the phosphor decay time is rather large. Therefore the decay time method is preferred and discussed here. Figure 2.12 shows the experimental setup for TGP-surface temperature measurements. The TGP is coated point- or linewise at the wall using a water-based binder (HPC-Binder, ZYP Coatings Inc.). The layer is approximately 10µm thick. Commonly a q-switched frequency tripled (or quadrupled, depending on the TGP-absorption bands) Nd:YAG-laser pulse (100-200µJ) after passing a 1mm aperture is used for electronic excitation of the TGP. Temporal decay of the phosphorescence is recorded by a photomultiplier tube (PMT). PMT-waveforms are sampled by a digital oscilloscope. Based on single-shot measurements a decay time is fitted using a single-exponential Levenberg-Marquardt algorithm although the decay´s nature is multi-exponential in most cases [39]. Fitting bi- or multi-exponential decays resulted in ambiguous exponential terms and was for this reason discarded. The intensity offset in the individual waveforms is subtracted using temporally averaged intensity distributions prior to the incidence of the laser pulse. Hence, the Levenberg-Marquardt algorithm fitted the initial amplitude I_0 and the phosphorescence decay time τ in $I = I_0 \exp\left(-t/\tau\right)$ as detailed in [40].

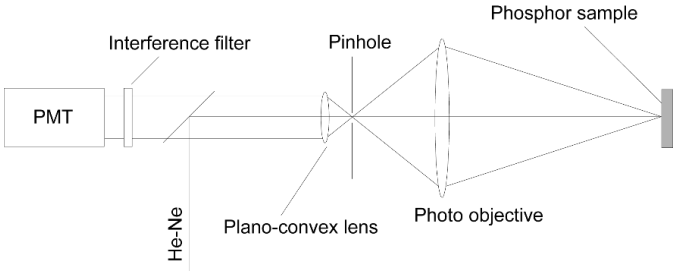

Figure 2.12
Detection unit to measure temporal decay of UV-laser-excited phosphorescence of TGPs coated to solid surfaces.

The method needs to be calibrated against a temperature standard. For this purpose an optically accessible tube furnace is used. A sample coated by TGP is positioned in a region of homogeneous temperature distribution inside the furnace. The actual sample temperature is measured with a conventional thermocouple. In the present case, the phosphor material is Mg_4FGeO_6:Mn. A calibration curve for this phosphor is shown in figure 2.13. The temperature range of this phosphor typically spans from 30 to 900K. The highest sensitivity is obtained for temperatures ranging from 700 to 1000K. This range covers surface temperatures of several practical applications in combustion technology. Using different phosphors, however, the temperature range can be expanded to 1600K. The precision of surface temperature measurement by TGP is remarkable. An average standard deviation of 1.3K is achieved.

A precondition for applications of TGP in combustion applications is the decay time´s independency on surrounding gas composition and pressure. The phosphor material Mg_4FGeO_6:Mn fulfils this requirement, others such as Y_2O_3:Eu do not [40].

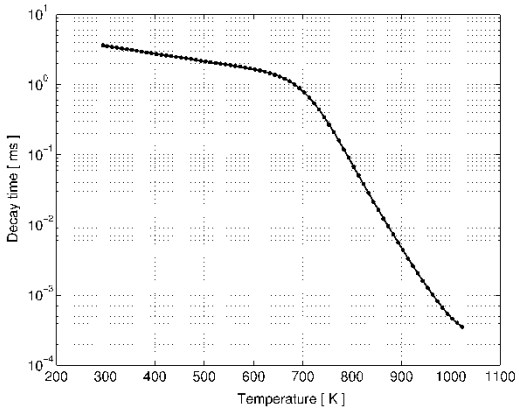

Figure 2.13
Decay time (logarithmic scale) of Mg_4FGeO_6:Mn versus temperature (linear scale, measured by thermocouple) measured in the tube furnace.

To demonstrate the application of TGP figure 2.14 shows the photo of a generic setup. Exhaust gases from a laminar premixed methane/air flame impinge on a copper plate 50 mm in diameter.

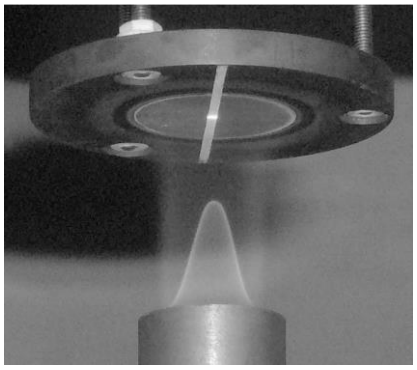

Figure 2.14
Photograph of the flame impinging on a wall coated pointwise with TGP. The bright spot is UV-laser-excited phosphorescence.

Wall temperatures are measured successively at different radial positions. The example shown in figure 2.15 presents the temperature measurements along the vertically orientated symmetry axis. Along with the wall temperature measurement, gas phase temperatures were measured by ro-vibronic N_2-CARS (compare chapter 4) taking advantage of the facility at Delft University [41]. These diagnostics at the surface and within the near wall region demonstrate that a simultaneous application allows the estimation of wall-normal temperature gradients. Additional measurements of the temperature at the other side of the wall enable the estimation of heat transfer in combustors.

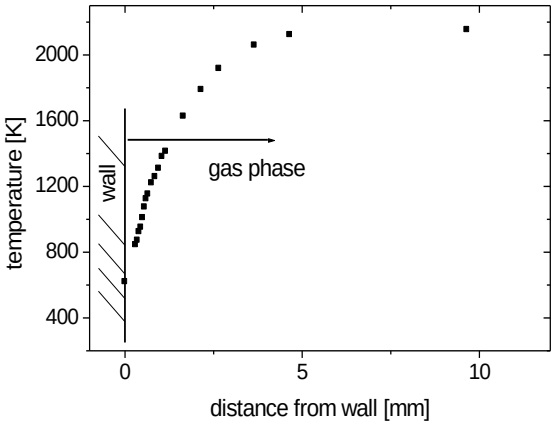

Figure 2.15
Wall temperature and wall-normal gas phase temperature. The wall temperature was measured by TGP, gas phase temperatures were measured by ro-vibronic N_2-CARS.

This experimental technique was applied already to study gas-solid interactions in generic configurations [34] and semi-technical conditions. Inside an optically accessible gas turbine combustion chamber (figure 2.10, [16, 1] with operational conditions detailed in [17]) the wall-normal temperature gradient close to an obstacle mimicking the first stator of a turbine was measured. Figure 2.16 shows the obstacle placed in the post-combustion zone of the pressurized combustor.

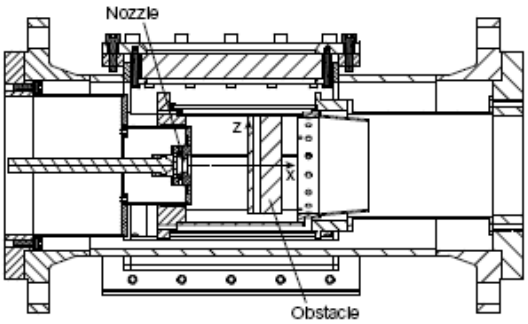

Figure 2.16
Sketch of the pressurized combustor and the obstacle mimicking the stator of a turbine. Wall- and gas temperatures were measured simultaneously by thermographic phosphors and ro-vibrational CARS.

Figure 2.17 shows some results of these illustrative measurements (for more information refer to [42]). Each data point in the gas phase is an average of typically more than 1000 single-shot CARS temperature measurements. The overall trend of decreasing temperature with increasing distance from the nozzle was due to air entrainment that is not detailed here. Obviously the wall temperature matches very well the extrapolation of the gas temperatures.

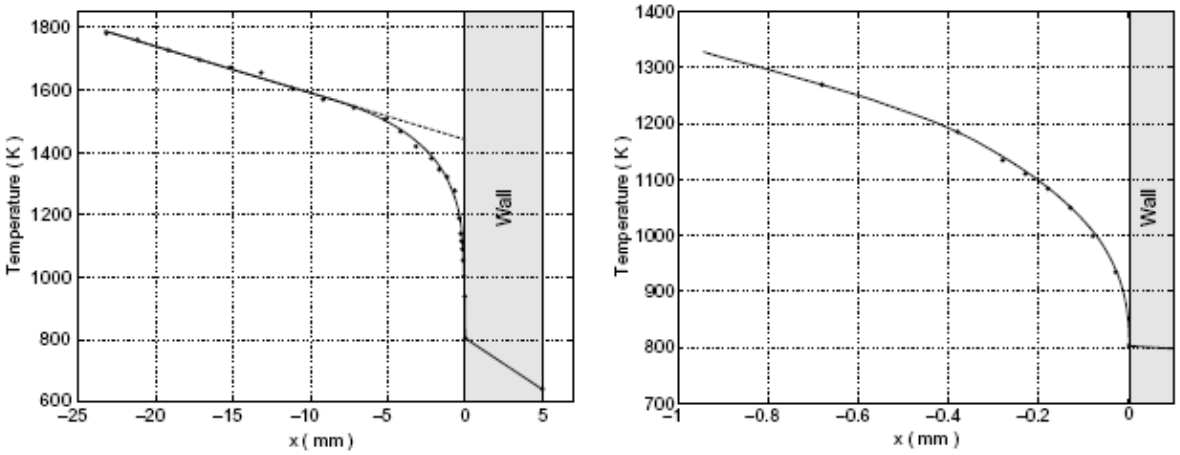

Figure 2.17
Mean wall-normal temperature profiles obtained from simultaneous wall- and gas-temperature measurements. The figure at the right-hand side is a magnification of the overall view presented at the left-hand side.

The obstacle was cooled internally by air. The temperature measurement at x = 5 mm was measured inside this cooling channel using a conventional thermocouple. The temperature distribution from the surface at x = 0 mm (measured by thermographic phosphor thermometry) and x = 5 mm is interpolated (thermal conduction in solids).

Thermographic phosphor thermometry can be extended to two-dimensional wall-temperature measurements [43–46]. These approaches can be supplemented by the use of the decay-time method employing a CMOS-camera operating at high repetition rates. This needs careful calibration of the CMOS-camera because these devices lack from pixel-dependent non-linearity and varying sensitivities [47]. By taking these imperfections into account properly, precisions very similar to point-wise measurements using a PMT can be achieved. Figure 2.18 compares calibration curves for the phosphor material Mg_4FGeO_6:Mn [48].

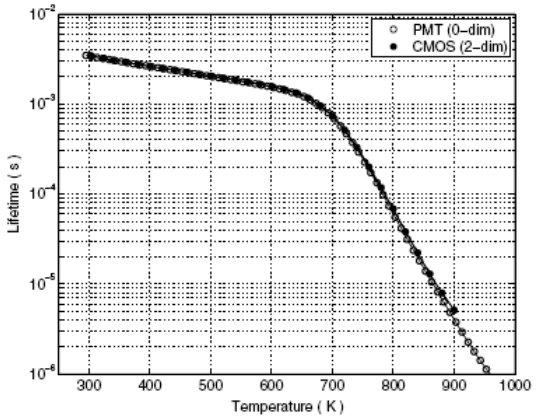

Figure 2.18
Calibarion curves using a PMT and CMOS-camera for the TGP Mg_4FGeO_6:Mn measured in an optically accessible oven.

An example of a two-dimensional phosphor thermometry using CMOS camera is an application of exhaust valve temperature measurements inside an optically accessible engine similar to that shown in figure 2.11 [45]. The phosphor used was $Gd_3Ga_5O_{12}$:Cr [35]. Its temperature lifetime characteristic is shown in figure 2.19. Using this phosphor timescales at in-cylinder surface temperatures typically for engines can be resolved by high-speed CMOS cameras.

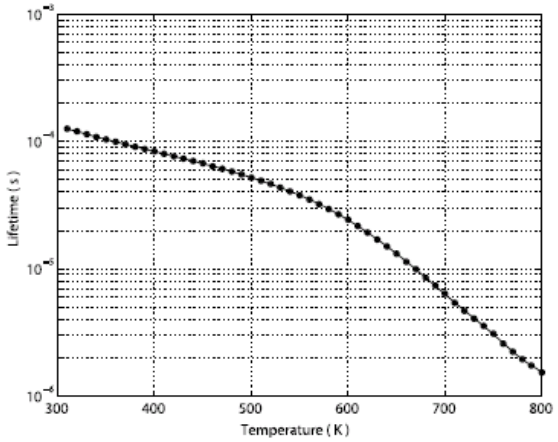

Figure 2.19
Temperature lifetime characteristics of $Gd_3Ga_5O_{12}$:Cr. Each dot corresponds to the average of 12,800 individually evaluated single-pixel and single-shot decays measured by a state of the art CMOS camera. A polynomial fit just guide the eyes.

The bottom view of the pent-roof cylinder head in figure 2.20 shows the exhaust valve that was coated by thermographic phosphor. Laser excitation and detection of luminescence were accomplished through the flat window in the piston.

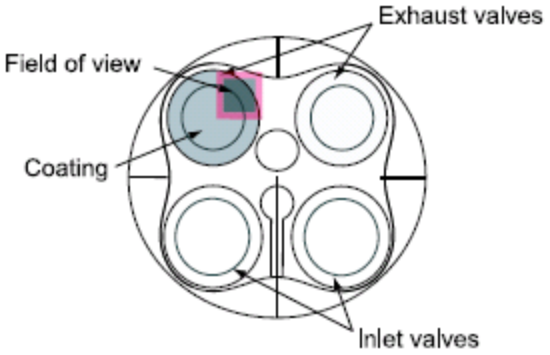

Figure 2.20
Bottom view of the pent-roof cylinder head showing the coated exhaust valve and the field of view (rectangle) of the CMOS camera that was used to measure the temperature-dependent decay pixel-wise. The frame rate of the camera was 360 kHz.

The engine was operated at 2,000 rpm with an indicated mean effective pressure of 2 bar. Following data post-processing figure 2.21 summarizes the phase averaged temperature evolution within the engine cycle. For more details see [45].

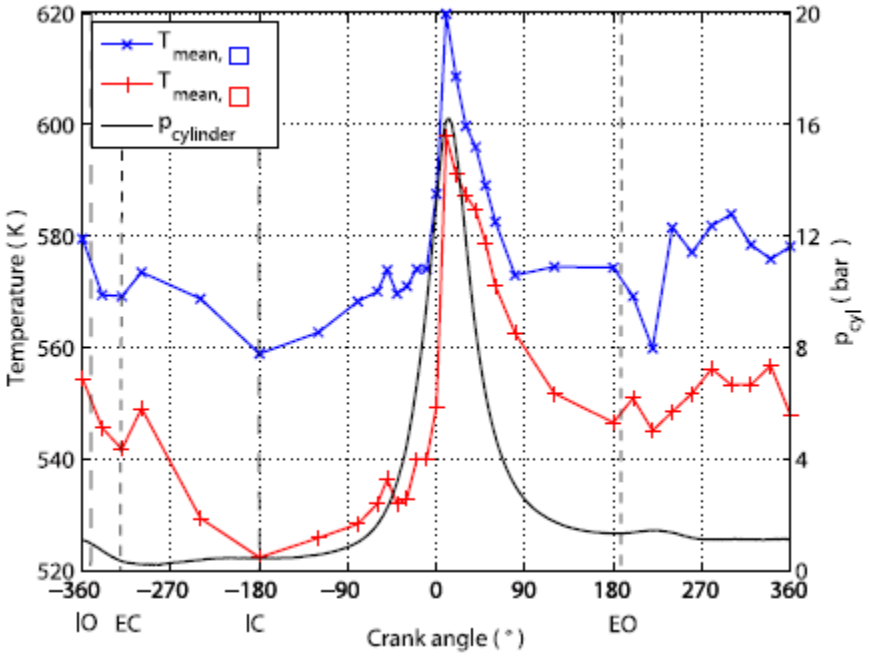

Figure 2.21
Crank angle resolved temperature and pressure evolution for fired engine conditions. Blue and red curves are spatial averages of the outer edge and inner part of the exhaust valve, respectively. The indicated in-cylinder mean pressure is shown as black line. Valve opening (O) and closings (C) are indicated for inlet (I) and exhaust (E) valves.

3. Flow field measurements

3.1 Optical techniques for velocity measurements

Flow field measurements in turbulent combustion benefit from developments in fluid mechanics. The most popular techniques used are laser Doppler (LDV, section 3.1.2) and particle imaging velocimetry (PIV, section 3.1.3). In both cases Mie scattering off chemically inert particles seeded to the flow is monitored. The melting point of the seeding material must be well above the adiabatic flame temperature to access post-flame regions. On the one hand the particle size needs to be sufficiently small to minimize slip relative to the continuous phase. On the other hand the particle response time should allow tracking velocity fluctuations of several kHz with slip of less than 1%. In practice, an upper limit of mean seed particle diameter is at the order of 1-2µm. However, Mie scattering intensity decreases in a non-linear manner with decreasing particle sizes. With common instruments the signal-to-noise might be too low for particles smaller than 0.5µm. More details are presented in the following sub-chapters.

3.1.1 Seeding gaseous flow with particles

Velocities in gaseous flames can be measured by laser Doppler velocimetry (LDV), particle imaging velocimetry (PIV) or particle tracking velocimetry (PTV, briefly discussed in section 5.2). LDV and PIV are discussed subsequently. For a more comprehensive presentation readers are referred to text books and recent reviews [49–51].

All of these measuring techniques rely on Mie scattering off phase interfaces between gas and particles. Accordingly the turbulent flow must be seeded by appropriate particles. Velocity measurements are conducted in hot and cold parts of the combustion process. Therefore the seeding particles must exist at elevated temperatures up to 2500K or higher. Metal oxides with high melting points are for this reason the best choice. Materials proven to work properly are TiO_2, MgO or $ZrSiO_4$. Table 3.1 summarizes important properties of these materials.

Table 3.1
Properties of seed materials commonly used in flow field measurements of turbulent flames.

Material	Short notation	Density [kg/m^3]	Melting point [K]
Magnesium oxide	MgO	3500	2800
Zirconium silicate	$ZrSiO_4$	3900 - 4700	2420
Titanium dioxide	TiO_2	4000	1780

To track the turbulent gas motion correctly, the seed particles must follow the turbulent fluctuations properly. The slip between gas phase and seed particles should therefore be very small. The slip *s* between both phases is expressed by

$$s = \left| \frac{u_f - u_p}{u_f} \right| , \quad (1)$$

with the subscripts *f* and *p* denoting gas (fluid) and particle velocities, respectively. Ideally, the slip should be less than 1%. Using a particle response time

(2) $$\tau_p = \frac{\rho_p d_p^2}{18\mu_f}$$

with μ_f being the kinematic viscosity, the cut-off frequency f_c where the slip exceeds 1% can be expressed by

(3) $$f_c = \frac{\sqrt{\left(2s - s^2\right)}}{2\pi\tau_0\sqrt{\left(1-s^2\right)\left(1+\frac{\rho_f}{2\rho_p}\right)^2 - \left(\frac{3\rho_f}{2\rho_p}\right)^2}} \ .$$

For MgO-seed particles in air figure 3.1 shows the temperature dependency of the cut-off frequency for three different seed particle diameters. The smaller the particle and the higher the temperature the higher is the cut-off frequency and fluctuations can be better tracked. However, as the Mie scattering intensity decreases in a non-linear manner with decreasing particle diameter, particles too small will result in poor signal-to-noise.

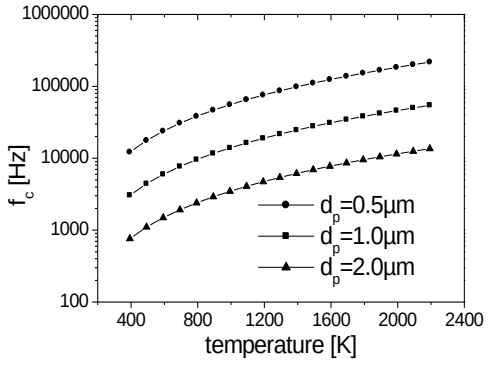

Figure 3.1
Cut-off frequency of MgO-particles at different size as function of temperature.

Particles are seeded into the flow upstream the nozzle. To adjust particle volume fraction, particles are often seeded into a bypass. Different seeders are reported in literature, see for example [52].

It is important to note that all streams must be seeded with approximately the same volume fraction. Otherwise the statistics especially in shear layers between neighboring streams will be biased.

3.1.2 Laser Doppler velocimetry

Laser Doppler velocimetry (LDV) measures instantaneous velocities at **single** probe volumes. In a common LDV-setup two beams from a continuous wave argon ion laser are crossed forming an interference pattern. By such an interference pattern a single velocity component is observed. Figure 3.2 shows constructive interference stripes as black horizontal lines. Obviously the probe volume extension is finite. The spatial resolution is determined by the probe volume

size. Typical values are a probe volume diameter (dx = dy) of 100µm whereas the extension dz is approximately 1mm.

The LDV-probe volume is passed by seeding particles. In an ostensive view Mie scattering occurs at the constructive interference stripes. This results into a temporal sequence of Mie scattering signals, termed Doppler burst. These Doppler bursts are monitored by a photomultiplier tube.

The distance between consecutive constructive interference stripes $d_{fringes}$ is calculated by

$$d_{fringes} = \frac{\lambda_{laser}}{2\sin\varphi} \quad . \tag{4}$$

Herein 2φ denotes the beam crossing angle. A seed particle passing the interference pattern is given by

$$f = \frac{|u_{\perp}|}{d_{fringes}} \quad , \tag{5}$$

with $|u_{\perp}|$ being the velocity component perpendicular to the stripes. As $d_{fringes}$ is known from the experimental arrangement and f is deduced from the Doppler burst, $|u_{\perp}|$ is known.

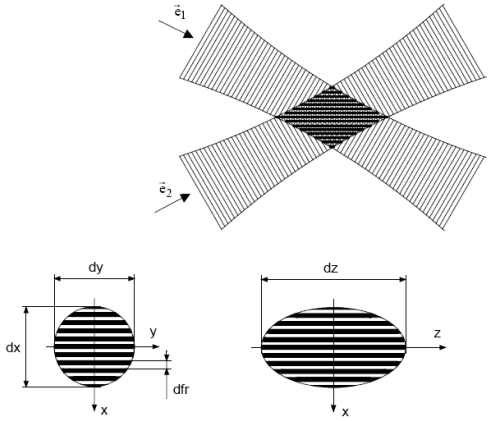

Figure 3.2
Schematic of the LDV-probe volume generated by two crossing argon ion laser beams. By this arrangement one velocity component parallel to the pattern-normal direction is observed.

So far only the absolute value of the considered velocity component is determined. To distinguish particles crossing the pattern from the top or the bottom, the stripes of interference pattern in practice are moving. This is achieved by a so-called Bragg-cell shifting the frequency of one of the laser beams by typically 40MHz. Figure 3.3 highlights the effect of moving interference stripes.

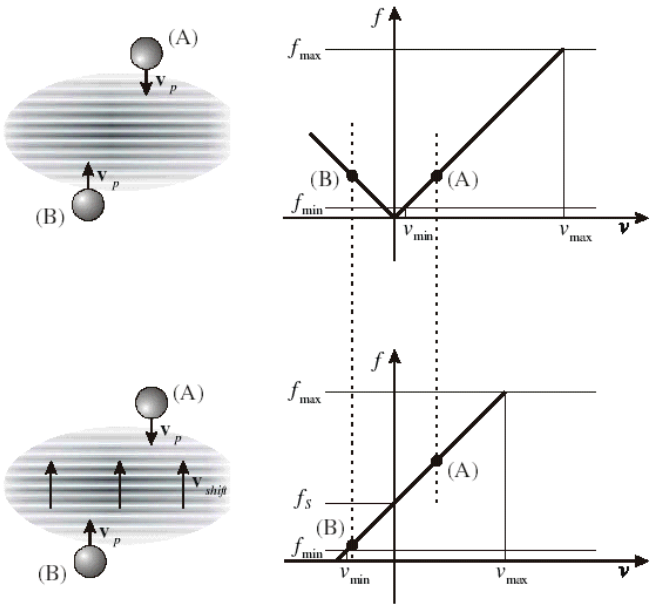

Figure 3.3
The abscissae (v) denotes positive and negative particle velocities, f is the Doppler frequency. Top: Stationary interference pattern: Direction of particle trajectories is not distinguishable. Bottom: Moving interference stripes: Particle (A) creates a Doppler burst with higher f than particle (B) running in the same direction as the moving stripes. Thereby directions of particles with identical absolute velocity values are distinguished.

If more than one velocity component is measured, interference patterns at different orientations are created. To distinguish Doppler bursts from the individual components, different wavelengths (colours of laser radiation) are used. For this reason the argon ion laser is an ideal choice: it emits at multiple laser transitions. The strongest occur at wavelengths of 514.5, 488 and 476.5nm. In front of each photomultiplier tube an interference filter blocks all wavelengths except one.

LDV-setups are commercially available. At present all systems are fibre-coupled. In most cases the Doppler bursts are monitored in backscatter mode due to experimental simplicity. In some cases sending and receiving optics are decoupled. This allows measuring the Doppler bursts in forward scattering mode at a user-defined angle. This increases the Mie scattering signal intensity. Forward scattering can be used additionally to cut down the probe volume length dz to approximately 200µm.

3.1.3 Particle imaging velocimetry

In particle imaging velocimetry (PIV) particles in a fluid flow are illuminated by a sheet of light that is pulsed. The particles scatter light into a lens located at 90° to the sheet, so that its in-focus object plane coincides with the illuminated slice of fluid. Images of the particles are formed on a CCD (charge-coupled device)-array detector (figure 3.4). Images are subsequently transferred to a computer for data post-processing. At least two images are recorded at short temporal delays Δt. The displacement of the particles from one exposure to the next, $\Delta x(r,t)$, can then be used to determine the instantaneous velocity components in the field of view by

(6) $$u(r,t) = \frac{\Delta x(r,t)}{\Delta t} \ .$$

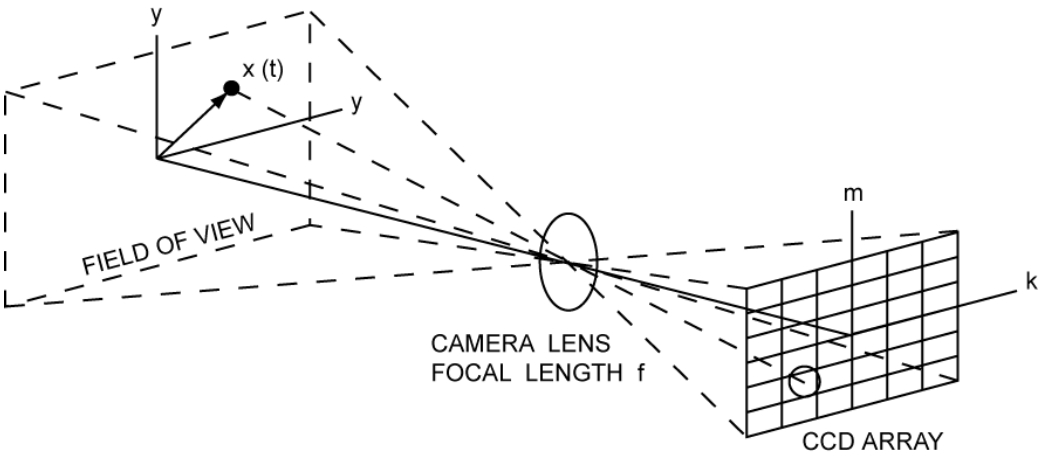

Figure 3.4
Optical system of a planar-image velocimeter.

The analysis of the recorded images is one of the most important steps as it determines accuracy and spatial resolution of the process. The displacement between particle positions in an image pair is derived from the cross-correlation function

(7) $$R_{II'}(x,y) = \sum_{i=-K}^{K} \sum_{j=-L}^{L} I(i,j) I'(i+x, j+y) \ .$$

The variables I and I' are intensity values extracted form the image-pair. The values (i,j) determine the size of the so-called interrogation box (in most cases $i = j$). Its size defines the spatial resolution of the process. The template I is shifted around in the larger template I' without extending over edges of I'. For each choice of shift (x,y) the sum of all pixel intensity products generates one cross-correlation value $R_{II'}(x,y)$. This procedure is applied for various choices of (x,y) with $-K \le x \le K, -L \le y \le L$. This forms a correlation plane of size $(2K+1)\times(2L+1)$.

For shift values where the particle images align best with each other, the cross-correlation value is at maximum. This shift is taken as Δx in equation (6). Thereby the cross-correlation function statistically measures the degree of match between the two samples.

In practice the cross-correlation function is calculated in the frequency domain. The operation is reduced then to a multiplication of the Fourier transformed particle images. For more information the reader is referred to chapter 5.4 in [50].

Efficient noise reduction is critical in PIV since initial errors in recursive correlations propagate down to the smallest scale, resulting in spurious vectors. Similar to [53] for non-reacting flows, correlations for each interrogation area recorded in turbulent flames can be calculated for four additional interrogation areas that are shifted by $(i\times 0.25)$ pixels with respect to the original interrogation area in positive and negative axial and radial directions. An element-wise multiplication of the resulting five correlation tables suppresses noise because it is statistically uncorrelated and correlations that arise at the same location in each of the five interrogation areas are augmented. This reduces the occurrence of spurious vectors and enables relatively high

spatial resolution. As a last step, remaining spurious vectors inconsistent with their local neighborhood are replaced by interpolation. This procedure of correlation-error correction does not decrease the spatial resolution.

3.1.4 3D and volumetric PIV

Imaging of a 3D velocity field can be accomplished using the following imaging techniques: 3D particle tracking velocimetry (PTV) which demands low seeding densities resulting in sparse vector fields [54], 3D light sheet scanning PIV [55, 56] with limitations due to laser repetition and camera recording rates, holographic PIV [57] which is limited to single recordings and includes chemical processing of the photographic holographic plates, and Tomographic PIV (TPIV) [58, 18], limited by spatial dynamic range.

TPIV is a method based on a tomographic reconstruction of the 3D particle distribution and was introduced by [59]. It captures instantaneously the 3D flow field, giving access to the complete stress tensor and vorticity vector. TPIV requires high laser pulse energies to illuminate a measurement volume and allow the imaging systems to operate with a relatively large depth-of-focus (i.e. small lens apertures) for imaging particles within the illuminated volume [59]. TPIV has been applied to unconfined subsonic [59], supersonic air flows [60], and confined water flows [61]. Only recently it has been applied within engines [18]. Limitation in optical access, physical space surrounding the engine, thick curved glass cylinder causing optical aberration effects, and engine vibration have been the leading challenges of the application of TPIV in internal combustion (IC) engines.

As an alternative multi-plane PIV might be considered as a reasonable choice for quasi-3D measurements [56]. This technique allows for flow field measurements in planes separated by large distances that cannot easily bridged by TPIV.

3.1.5 LDV versus PIV

For PIV at least 10 particles are recommended to be contained in each interrogation window. If a certain spatial PIV-resolution is aimed for, the seeding concentration must be adapted accordingly. Below a certain threshold PIV-results will not be reliable. This is different to LDV where arbitrary low seeding densities can be used on the price of extended measurement periods. This difference of seeding concentrations in LDV and PIV can be important if a flame, prone to seeding density variation, is investigated. An example for such a situation is a flame burning very close to its extinction limit (for example turbulent opposed jet flame, see figure 2.1). Slight changes in its thermo-kinetic state caused by alteration of the radiative heat transfer through seeding particles can shift the extinction limits remarkably. Instead of using PIV, particle tracking velocimetry might be an alternative that operates with lower seeding densities as well [62].

Another issue in PIV is the use of image post-processing to evaluate measuring data, which is accompanied by long CPU-times. Statistics are for this reason mostly limited to a few thousand single PIV-shots. In contrast, LDV-time-series measurements comprise up to 10^6 data points at single probe volumes [8]. Furthermore, the common experience is that different PIV-algorithms result into different flow fields. Therefore a PIV-algorithm should be validated against other techniques such as LDV. Ideally, this is done in the flame under investigation.

For fixed spatial resolution the dynamic range of velocities in PIV is determined by the time lag between both exposures. The time lag can be chosen most flexible when two separate

Nd:YAG-lasers are used whose beams are combined to exit from a single port. The minimum time lag is then limited only by the interline transfer time of the CCD-camera (order of 1µs).

The advantage of PIV against LDV is that planar instantaneous velocity distributions are measured. Spatial gradients of the velocity components can be calculated in different directions. This gives access to elements of the rate-of-strain and rate-of-vorticity tensor, information that is in practice not accessible by LDV. PIV can therefore be regarded as a complementary technique to LDV.

By holographic PIV, stereo PIV or tomographic PIV [59] even the third velocity component and a three-dimensional probe volume can be monitored. By using latest solid-state laser and CMOS-camera technology the repetition rate can be boosted to several 10 kHz. PIV is ideally suited to be combined with planar laser-induced fluorescence (PLIF) to give insights into flame-turbulence interactions [63]. Combining LDV with PLIF as demonstrated in [64] is much more laborious. These combinative diagnostics are discussed in some more detail in chapter 5.

3.2 Measurands to be determined

Flow field measurements include at least mean and rms-values of three velocity components. In case of rotationally symmetry two components might be sufficient. In case of LDV high velocities cause higher probability for “fast moving particles”. This can cause a bias in the calculation of the statistical moments. To account for this fact, transit-time t_i (time needed for a particle to cross the LDV-probe volume) is used for correction [65]. Accordingly the equation to calculate mean velocity components from LDV-measurements reads:

$$\bar{u} = \frac{\sum_{i=1}^{N} u_i \cdot t_i}{\sum_{i=1}^{N} t_i} \tag{8}$$

The rms-value is calculated by

$$\sigma_u = \sqrt{\langle u_i'^2 \rangle}\,,\ \langle u_i'^2 \rangle = \frac{\sum_{i=1}^{N} u_i'^2 \cdot t_i}{\sum_{i=1}^{N} t_i}\,. \tag{9}$$

Reynolds-stress components are accessible by two-component measurements. In case of LDV including transit-time weighting these cross-correlations are calculated by

$$\langle u'v' \rangle = \frac{\sum_{i=1}^{N} u_i' \cdot v_i' \cdot t_i}{\sum_{i=1}^{N} t_i}\,. \tag{10}$$

In addition to the statistical moments, one- and two-point measurements at highest sampling rates monitoring the instantaneous axial velocity component can be performed to receive time-series consisting of typically 10^6 samples. In case of two-point measurements one LDV-measurement location is spatially fixed while the location of the second is varied stepwise in ±axial

and ±radial direction. The displacements in axial and radial directions result in longitudinal and in lateral correlations, respectively.

Cross- (evaluation of two-point-LDV) and auto-correlation functions (evaluation of one-point LDV) are deduced from these time-series using the fuzzy slotting technique, local normalization and transit time weighting [8]. This approach is based on the computation of discrete estimated values $R_{11}(k\Delta\tau = \tau_k)$ of the general auto-covariance function $R_{ij}(x,t,\Delta x,\Delta t) = \overline{u_i'(x,t)u_j'(x+\Delta x,t+\Delta t)}$ [66] through summing the time difference products, which are accumulating in N equidistant time slots of width $\Delta\tau$ (notice that R_{ij} denotes non-normalised covariances while ρ_{ij} (eq. 11) represents its normalised values (correlations), k denotes the number of each slot). Averaging over all products contained in a certain time slot and normalizing this mean value with its self-products (compare eq. 11), represents the discrete value of the normalised correlation function ρ_{ij} associated with the regarded time slot τ_k. For the application of the algorithm the arrival time of a seeding particle within the measurement volume is used as a time marker for each single event. Additionally, the transit time of each detected sample is used as a weighting factor w_i for each recorded sample to account for bias [65].

Equation (11) summarizes the procedure of calculating temporal correlations:

$$(11)\qquad \rho_{ij}(\tau_k) = \frac{\sum_{i=1}^{N-1}\sum_{j=i+1}^{N} u_i' u_j' w_i w_j b_k(t_j - t_i)}{\sqrt{\left[\sum_{i=1}^{N-1}\sum_{j=i+1}^{N} u_i'^2 w_i w_j b_k(t_j - t_i)\right]\cdot\left[\sum_{i=1}^{N-1}\sum_{j=i+1}^{N} u_j'^2 w_i w_j b_k(t_j - t_i)\right]}}$$

with

$$(12)\qquad (k-0.5)\Delta\tau < |t_j - t_i| < (k+0.5)\Delta\tau\,,$$

$$(13)\qquad b_k(\Delta t) = \begin{cases} 1 - \left|\dfrac{\Delta t}{\Delta\tau} - k\right| \text{ for } \left|\dfrac{\Delta t}{\Delta\tau} - k\right| < 1 \\ 0 \text{ otherwise} \end{cases}.$$

Notice, that here only the axial velocity component is considered ($u_i = u_j = u_1$). Successive LDV measurements at high repetition rate are conducted at the same location (x, one-point LDV) or at two spatially separated locations (x; $x\pm\Delta x$, two-point LDV). Using the specific weighting function b_k defined in equation (13), smoothing of ρ_{11} is accomplished because a single event contributes to two adjacent slots. Events closer to a slot centre possessed a higher weight for the respective slot than those located at the slot´s edge.

The choice of an optimal slot width $\Delta\tau$ depends on the investigated turbulence structure. Independency of ρ_{11} on $\Delta\tau$ is desirable resulting in $\rho_{11}(t_j - t_i = 0) = 1$. In practice this cannot be achieved due to spatial and temporal averaging by finite measurement volumes and transit times, noise and processor sampling rate limited to typically ~150kHz according to minimum time intervals between two samples of ~7µs. Averaging effects gain on importance if measurement volumes are on the same order as turbulent structures to be resolved. In an illustrative view, subsequent events t_j, t_i with $\Delta\tau > t_j - t_i > (\nu/\varepsilon)^{0.5}$ are counted to the same slot k although they already belong to different turbulent eddies ($(\nu/\varepsilon)^{0.5}$ denotes the Kolmogorov

time scale using viscosity ν and dissipation rate ε). With this in mind, it is obvious that even for a slot width $\Delta\tau$ optimised for the specific turbulent flow field $\rho_{11}\left(t_j - t_i = 0\right) = 1$ can not be achieved in practice. To account for this and to reject noise in addition (for details on noise treatment see [8]) a second normalisation using $\rho_{11}(0)$ is carried out resulting in:

$$\rho_{11}^{(2)}(\tau_k) = \frac{\rho_{11}(\tau_k)}{\rho_{11}(0)} \tag{14}$$

Normalized temporal auto-correlations $\rho_{11}^{(2)}(\tau_k)$ are fitted by polynomials and integrated subsequently. In case of one spatially fixed measurement volume (one-point LDV) this integration represented an estimation of the local turbulent time scales T_{11}. In case of two-point LDV, where the spatial separation between the two measurement locations Δx is varied, the respective values of $\rho_{11}(\Delta x)$ at $\tau_\kappa = 0$ are used for a polynomial fit in spatial dimension resulting in spatial cross-correlations. Integration of this polynomial represents local turbulent length scales L_{11}. As mentioned above, positive and negative displacements in axial and radial directions corresponding to four different spatial correlations $\rho_{11,\pm x}$ and $\rho_{11,\pm r}$ are measured resulting in four different length scales: longitudinal length scales $L_{11,+x}$, $L_{11,-x}$ and transversal length scales $L_{11,+r}$, $L_{11,-r}$.

Using the temporal auto-covariance $R_{11}(x, \tau_k)$ only, the E_{11}-component of the power spectral density (PSD) can be deduced by Fourier Transformation. Figure 3.5 exemplifies a PSD obtained by the procedure outlined above in non-reacting turbulent jets.

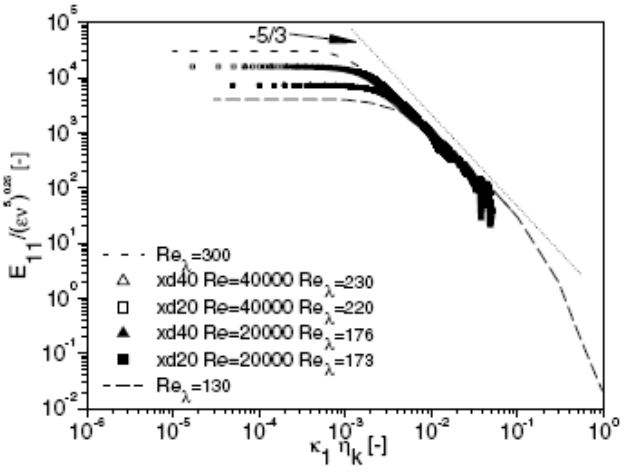

Figure 3.5
Measured (symbols) and calculated (lines) PSD in an isothermal turbulent jet emanating from a round orifice 8mm in diameter. The calculated spectra are based on equation 6.246 in [67].

Additional information on elements of the rate-of-strain or rate-of-vorticity tensor can be raised from two-component PIV measurements as instantaneous velocity gradients are accessible. It must be considered, however, that limited spatial resolution might wash out these gradients. The out-of-plane vorticity component is deduced by

$$\omega = 1/2\left|\partial \mathrm{w}/\partial r - \partial \mathrm{v}/\partial z\right| , \tag{15}$$

with w being the velocity component in *z*-direction, and v in *r*-direction. The 2D-dilatation can be calculated accordingly by

(16) $$\left(\nabla \cdot V\right)_{2D} = \left(\partial \mathrm{w}/\partial \mathrm{z} + \partial \mathrm{v}/\partial r\right).$$

Vorticity and dilatation can be computed accordingly for other directions in case volumetric flow measurements are available.

3.3 Example of flow field measurements: LDV in premixed swirl flames

This section highlights the application of 1- and 2-point LDV in the swirling premixed unconfined flame detailed in section 2.2 [8]. Application of PIV will be presented in section 5 in measurements simultaneously with planar laser-induced fluorescence.

3.3.1 Flow properties at the nozzle exit – combusting conditions

To allow for axial velocity measurements close to the nozzle exit the LDV sending/receiving optics were inclined by 6°. The resulting bias was ~0.5% off the absolute value and could be therefore neglected.

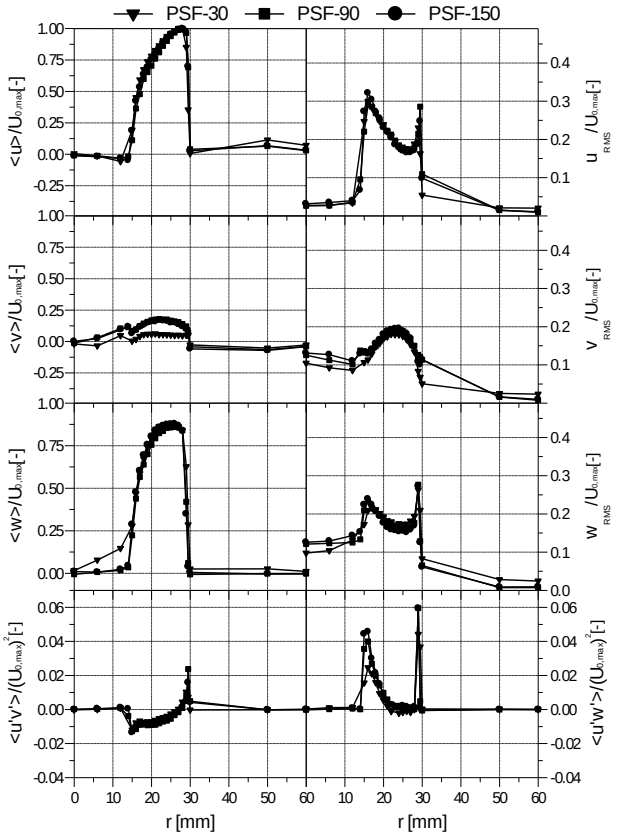

Figure 3.6
Comparison of radial profiles of first and second statistical moments of all velocity components and two Reynolds-stresses at x = 1mm. Data are normalized on the respective maximum nozzle exit velocity. PSF-30: $U_{0,max}$ = 6.48ms^{-1}, PSF-90: $U_{0,max}$ = 20.2ms^{-1}, PSF-150: $U_{0,max}$ = 28.0ms^{-1}.

Figure 3.6 shows first and second moments of all three velocity components as well as two Reynolds-stress components. To facilitate a direct comparison of the three *Re*-number cases (compare table 2.3), data are normalized to the respective maximum axial velocities specified in the figure caption. Axial and tangential velocity components are of the same order of magnitude whereas the radial component catches less than 20% of the maximum axial velocity. Using the most common definition of the swirl number by Gupta et al. [68] and neglecting the pressure term, the actual swirl number at this location was 0.64 – a value reduced by 15% with respect to the theoretical swirl number of 0.75. Two shear layers are observed, located at r = 15 and 30mm corresponding to the bounds of the annular slit. In the shear layers, fluctuations and Reynolds stresses reaches their maximum values.

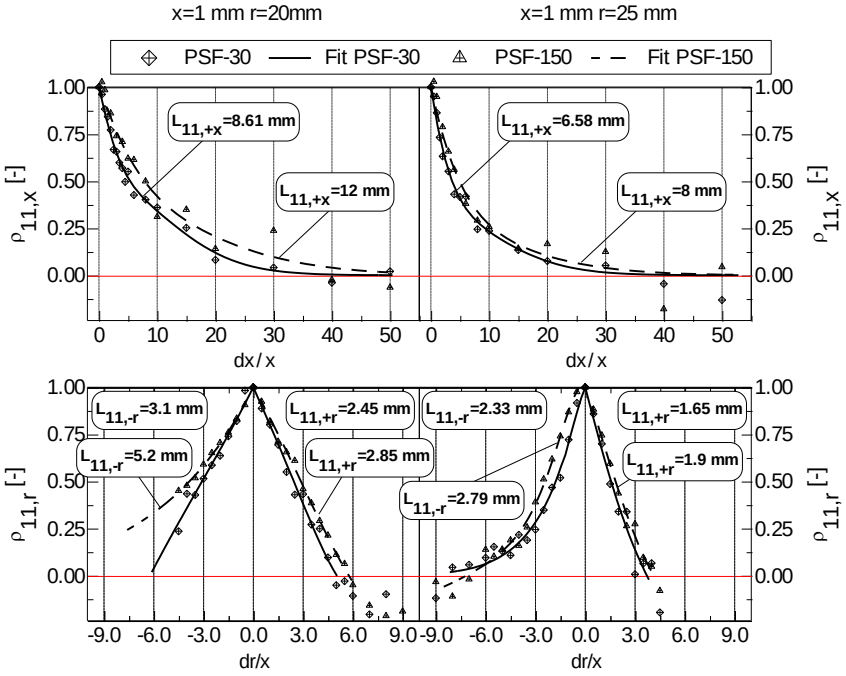

Figure 3.7
Normalised spatial cross-correlations of PSF-30 and -150 measured at two different radii at x = 1mm. Longitudinal ($L_{11,+x}$) and lateral length scales ($L_{11,\pm r}$) deduced from integration of the fitted polynomials are inserted. Notice that axial (dx) and radial shifts (dr) of the moved LDV-system are normalised by the axial height.

Figure 3.7 shows spatial cross-correlations $\rho_{11,+x;\pm r}$ as measured by two-point-LDV at r = 20 and 25mm ($\rho_{11,-x}$ cannot be measured at this axial height). For the sake of clarity PSF-90 is not included to the figure. Straight and dashed lines denote results from the polynomial fit. In general, length scales of the high Re-number case are larger. For both cases, length scales at r = 25mm located closer to the outer shear layer are clearly reduced by ~30%, while the ratios of longitudinal to transversal length scales $L_{11,+x}/L_{11,\pm r}$ of 3.1 and 3.3, respectively, are changing by less than 10% between these two locations.

In figure 3.8 temporal auto-correlations and respective E_{11}-components deduced from the auto-covariance are presented for the same locations. For a direct comparison, the abscissa is normalised by the respective turbulent time scales. The temporal decays are clearly similar. In

accordance to the length scales, time scales T_{11} closer to the outer shear layer are remarkably reduced relative to their values at r = 20mm. For both *Re*-numbers the PSDs show a distinctive inertial subrange. The viscous subrange could not be resolved with the current data rate. Due to the higher fluctuation levels in the axial and tangential velocity component for a given *Re*-number, at r = 20mm the amplitudes are higher but the characteristic frequency where the spectrum fades into the inertial subrange is independent of the position. Therefore enhanced turbulence levels at r = 20mm can be attributed solely to large scale motions. Changing the *Re*-number from ~10000 to ~42000 shifts this characteristic frequency from ~100 to ~300Hz.

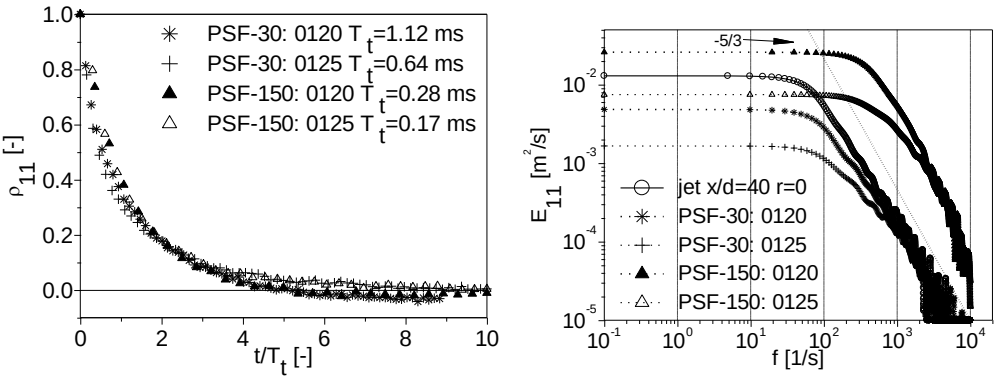

Figure 3.8
Left: Temporal auto-correlations measured at the same locations as in figure 3.7 (denotation: 0120 denotes x = 1mm, r = 20mm). To enable a direct comparison of the different Reynolds-number cases, time is normalised by corresponding integral time scales specified in the insert. Right: PSD deduced from respective auto-covariance. For comparison results obtained from an isothermal jet are included.

3.3.2 Flow properties downstream the nozzle – combusting conditions

Exemplary for PSF-150, figure 3.9 presents a vector plot of the flow field including mean axial and radial velocities. Typical for swirling conditions the flow expands when leaving the nozzle. As a consequence by vortex breakdown [69] an internal recirculation zone (IRZ) is generated due to positive pressure gradients along the symmetry axis of the central bluff body. For the case PSF-150 the IRZ axially extends approximately 120mm. At x = 60mm the width increases to its maximum of ~45mm. The axial velocity component approximately is maintained, but the radial velocity component up to x = 30mm increases on the cost of tangential momentum.

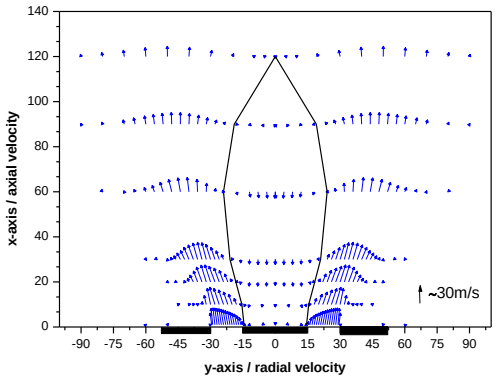

Figure 3.9
Vector plot for the case PSF-150 showing means of axial and radial velocity components in a plane cutting the symmetry axis.

Figure 3.10 presents radial profiles at x = 30 and 90mm of the same quantities as shown in figure 3.6. The cases PSF-90 and -150 show a Reynolds-similarity whereas PSF-30 exhibits a reduced spreading. Fluctuation levels and the Reynolds-stress component $\overline{u'v'}$ peak at radial locations where gradients of mean axial and tangential velocity components are at maximum.

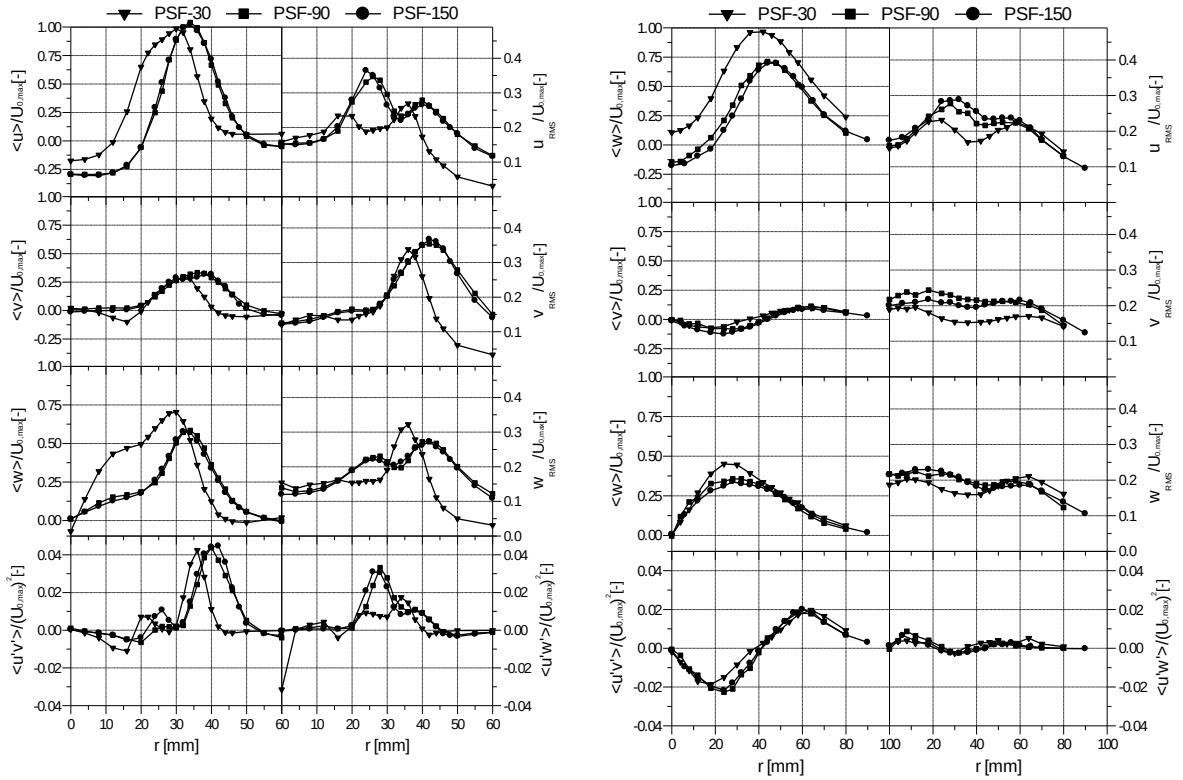

Figure 3.10
Radial profiles of the same quantities as shown in figure 3.6 at an axial height of x = 30mm (left) and 90mm (right).

Figure 3.11 compares spatial cross-correlations for positions at x = 10mm, r = 25mm and x = 90mm, r = 30mm. For clearness, only PSF-30 and -150 are shown. As observed for the nozzle exit flow, for these specific locations the higher *Re*-number case PSF-150 is characterised by significantly increased length scales except of $L_{11,\pm x}$ at x = 90mm. At x = 10mm the asymmetries in $L_{11,\pm x;\pm r}$ can be attributed to the influence of combustion. By traversing the moveable LDV-measurement volume in positive axial or negative radial directions the flame zone is entered which is characterised by reduced density. Here, $L_{11,+x}$ and $L_{11,-r}$ are clearly enlarged.

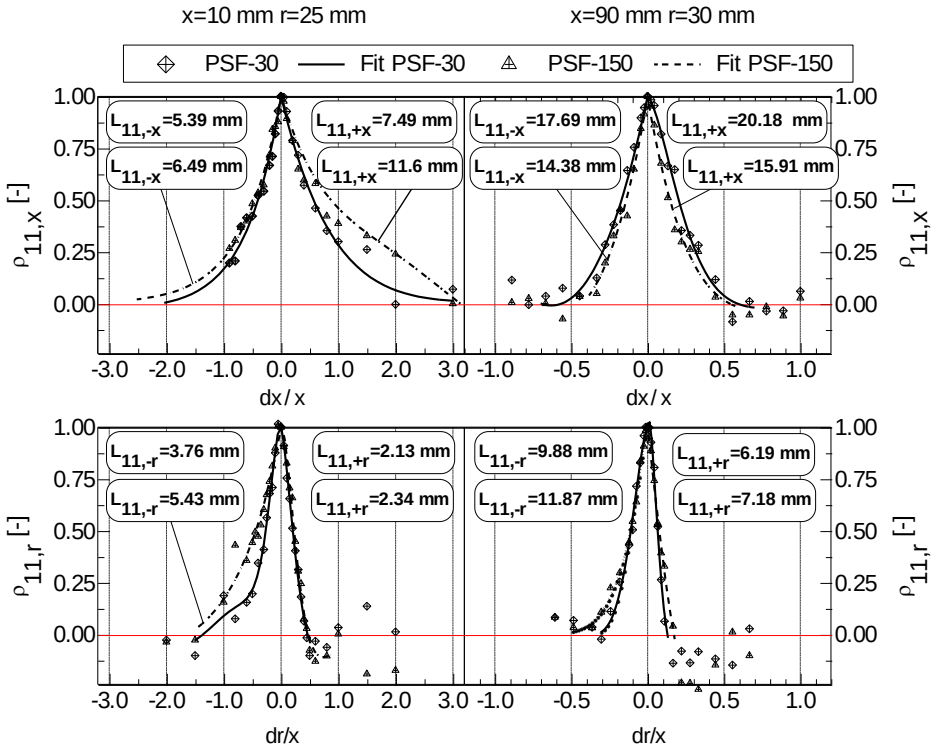

Figure 3.11
Normalised spatial cross-correlations of PSF-30 and -150 measured at two different radii at x = 10 and 90mm. Longitudinal ($L_{11,\pm x}$) and lateral length scales ($L_{11,\pm r}$) deduced from integration of the fitted polynomials are inserted. Notice that axial (*dx*) and radial shifts (*dr*) of the moved LDV-system are normalised by the axial height.

At x = 30mm figure 3.12 in more detail shows the influence of local flow properties on length scales. Taking the case PSF-150 as an example, the radial position r = 20mm is located at the side of the IRZ (compare figure 3.9) whereas r = 30mm is located within the annularly spreading swirling jet. Within the annular jet, length scales are remarkably smaller than at its side. This observation is in accordance to the enhanced turbulence levels as can be seen from figure 3.10. Especially when the IRZ exhibits relative slow negative axial velocities, as is the case for PSF-30, transversal length scales are enlarged significantly. This can be seen from $L_{11,-r}$ at r = 20mm in figure 3.12 where the second LDV-measurement volume is traversed into the IRZ. It is here where $L_{11,-r}$ is approximately twice the value for positive radial displacement $L_{11,+r}$.

The ratio of longitudinal to transversal length scales is dependent on the *Re*-number and the location within the turbulent flow field. As shown in table 3.2 there is a general trend of decreasing $L_{11,x}/L_{11,r}$ ratios in downstream direction (exception is for PSF-30, x = 90mm). Compared to the ratio at the nozzle exit the respective values already at x = 10mm are reduced remarkably. For isotropic conditions a ratio of 2.0 would be expected. The clear deviation from this value shows the strong anisotropic character of this flow. This implies that for numerical simulation of this type of flow simple turbulence models assuming local isotropy are physically incorrect.

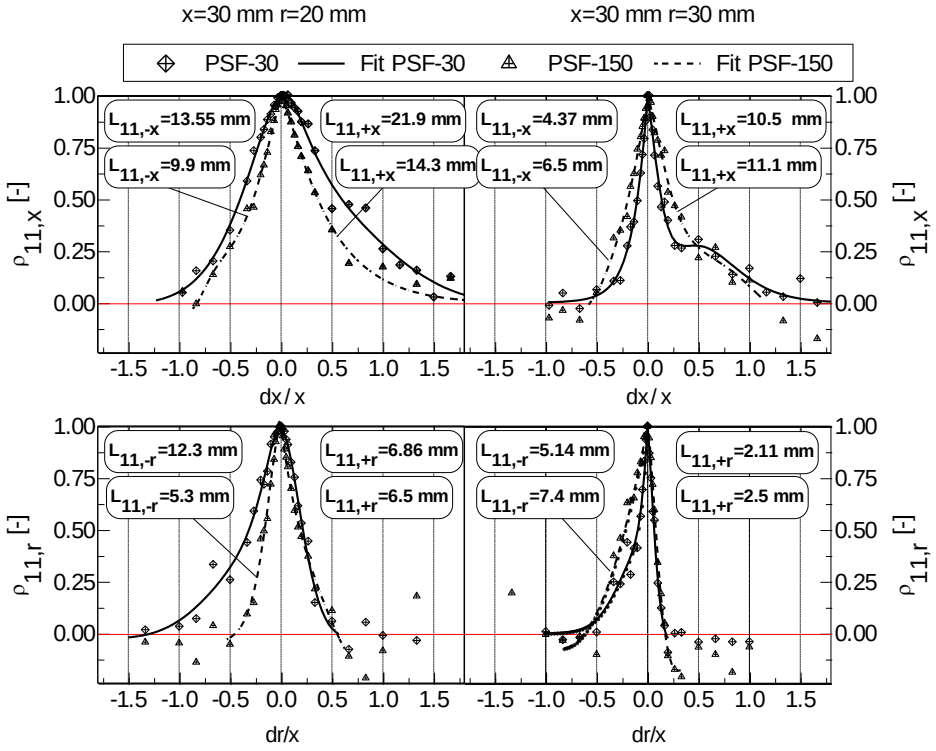

Figure 3.12
Same quantities as in figure 3.11 but at axial location of x = 30mm for two different radii.

Table 3.2
Comparison of longitudinal to lateral length scales $L_{11,x}/L_{11,r}$.

	***x* = 10mm** ***r* = 25mm**	***x* = 30mm** ***r* = 20mm**	***x* = 30mm** ***r* = 30mm**	***x* = 90mm** ***r* = 30mm**
PSF-30	2.85	1.85	2.05	2.36
PSF-150	2.33	2.06	1.77	1.59

Temporal correlations and respective PSDs are presented in figure 3.13. As already discussed for figure 3.10, the case PSF-30 does not show Reynolds-similarity. This indicates that for PSF-30 turbulence is not yet fully developed. Due to increased velocities, the higher *Re*-number case shows a factor 4 – 5 shorter time scales. For both cases, from x = 10 to 90mm the time scales increase by a factor of ~2.5 to 3 indicating a relaminarization due to viscous forces. Comparing both axial positions for different flames, distinct differences between the temporal decay of ρ_{11} is observed within the first few time scales. This appears more clearly by different slopes exceeding 40Hz (PSF-30) and 300Hz (PSF-150), respectively, in the PSDs. At upstream locations

such as x = 10mm, r = 25mm the slope is approximately -5/3 indicating an inertial subrange similar to isothermal jets. Further downstream at x = 90mm dissipation is severely enlarged resulting in a much steeper decay. Therefore turbulence structure further downstream is characterised by higher energy content in low frequent eddies but much reduced energy in the upper frequency range. From this observation one can state that turbulence structure defined by its energy cascade and relative energy distribution in eddies of different frequency is space dependent as expected but very different from locally homogeneous isotropic turbulence.

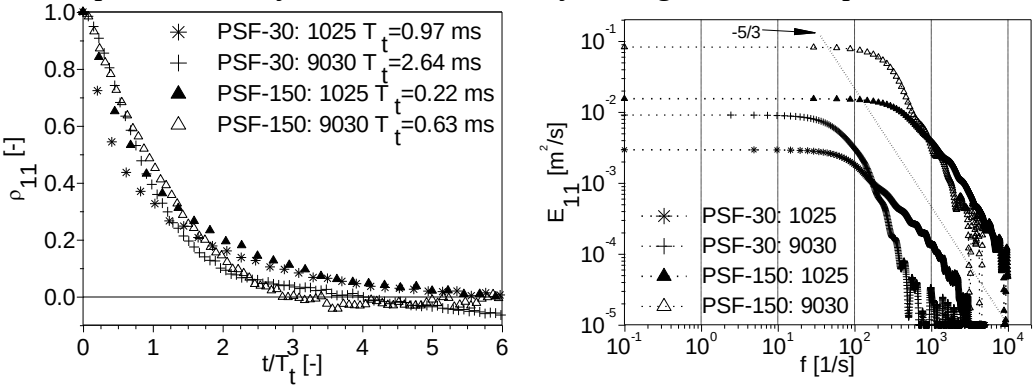

Figure 3.13
Left: Temporal auto-correlations measured at the same locations as in figure 3.11. Time is normalised by corresponding integral time scales specified in the insert. Right: PSD deduced from respective auto-covariance.

3.3.3 Isothermal case

To serve a data base for validation of numerical modelling it proved to be of crucial importance to start with a non-combusting case in order to check whether the chosen turbulence model predicts important features of the flow field correctly. In addition to the flow field in the present case mixing with ambient air is of interest as well and therefore subject of an ongoing project [70]. As for the reacting case, results of the isothermal case are divided into nozzle exit flow measured at x = 1mm and radial profiles at downstream positions spanning from x = 10 to 120mm. Just a selection of data is shown.

Flow properties at the nozzle exit – isothermal conditions
First and second statistical moments at the nozzle exit plane at x = 1mm show very similar profiles as the respective combusting cases and are therefore not shown. Only in the range spanning from r = 0 to 15mm second moments of all three velocity components exhibit a significant increase. This region corresponds to the IRZ which in contrast to the combusting cases shows a coherent precession as revealed in figure 3.14. After an initial decay temporal correlations show strong oscillations. The initial decay is attributed to turbulence, while the oscillations indicate a precession vortex core (PVC) around the symmetry axis. On the one hand, dependent on the measurement location, correlation amplitudes of the oscillations vary from 0 to 0.5. Therefore, the coherent structure at some locations contributes significantly to overall fluctuation levels. For example, at x = 1mm, r = 20mm approximately 28% of the fluctuations are due to the PVC. Amplitudes correlate well with the level of axial velocity fluctuations (not shown). Characteristic frequencies on the other hand are independent on the location but strongly dependent on the *Re*-number. As obvious from the corresponding PSDs characteristic frequencies

peak at 38 and 195Hz for PSF-30 and -150, respectively. Using the Strouhal-number $St = L \cdot f / U$ as dimensionless parameter, similarity of the different cases can be evaluated. With *f* as the lowest frequency peak in the PSD, *L* the hydraulic diameter of the nozzle and *U* the mean axial exit velocity, independent of the *Re*-number a value of $St \approx 0.25$ is observed. Therefore the precession frequency linearly scales with the flow rate indicating that from this view the asymptotic limit already is reached by the present configurations.

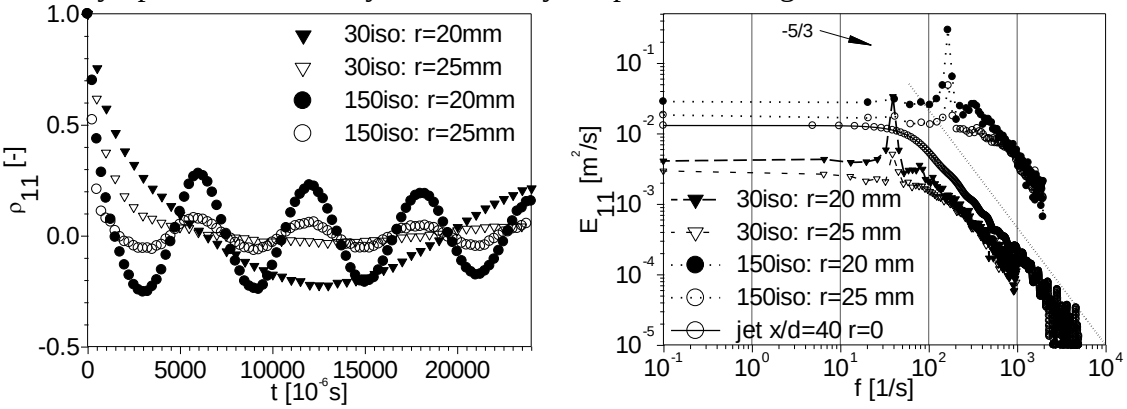

Figure 3.14
Left: Temporal auto-correlations for isothermal conditions. The amplitude of the coherent motion is strongly dependent on the measurement location. Right: Corresponding PSD. Characteristic frequencies are independent on measurement location.

Flow properties downstream the nozzle – isothermal conditions

In figure 3.15 at *x* = 30mm radial profiles of statistical moments and Reynolds-stresses are compared to the combusting case PSF-150. Spreading of the flow is reduced in the isothermal case as can be seen from mean axial velocity profiles. Inner and outer shear layers characterised by high fluctuation levels are consequently shifted to smaller radii as well. The redistribution from tangential into radial momentum is retarded. For radial positions up to ~35mm particularly second moments are enlarged. This observation can be explained similar to the nozzle exit flow by precession of the IRZ.

The region between the inner shear layers is characterised by positive gradients of the circulation $\Omega = \frac{\partial}{\partial r} \rho(\overline{w} \cdot r)^2$. According to the Rayleigh-criterion this indicates stable flow conditions and can be viewed as a solid body rotation. In the vicinity of the outer shear layer Ω is negative. This corresponds to unstable flow conditions because for increasing radii the tangential momentum decreases. This instable region may bear up coherent structures. However, this type of analysis is limited to isothermal flows as long as no simultaneous velocity-density measurements are performed.

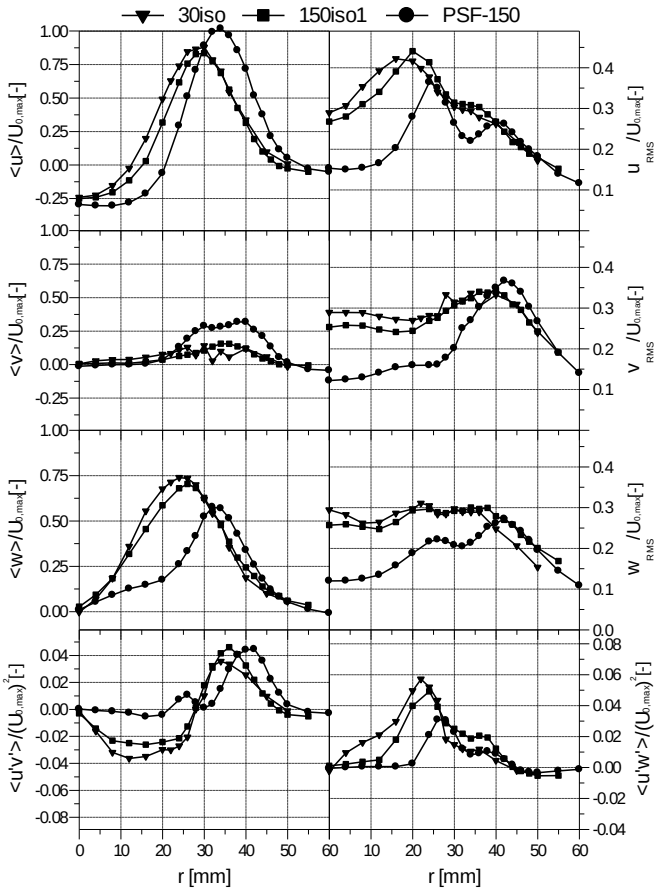

Figure 3.15
Isothermal conditions: Comparison of radial profiles of first and second statistical moments of all velocity components and two Reynolds-stresses at x = 30mm. Data are normalized on the respective maximum nozzle exit velocity. PSF-30: $U_{0,max}$ = 6.48ms^{-1}, PSF-150: $U_{0,max}$ = 28.0ms^{-1}.

To highlight the character of the PVC more clearly figure 3.16 shows temporal correlations measured by using both 1D-LDV-systems simultaneously. Stars denote the temporal auto-correlation at a spatially fixed position (x = 30mm, r = 20mm) where the amplitudes of the oscillation and the axial velocity fluctuations are at their peak values. Triangles represent temporal correlations at different radial locations measured by the second LDV-system, ranging from r = 20mm to -20mm. At identical measurement locations auto-correlations of both channels coincide (figure 3.16(a)) as expected. A negative radial shift of the second LDV-measurement location results in a decreasing amplitude of the oscillation as obvious from figures 3.16(b) to (d). Due to rotational symmetry of the setup, at r = -20mm the oscillations amplitude is fully recovered (figure 3.16(e)). For cross-correlations (open circles) two observations can be made: Firstly, a phase shift appears increasing with displacement of the LDV-measurement locations. At r = -20mm a phase shift of π is reached indicating an almost perfect axial symmetry of the PVC. Secondly, the cross-correlations amplitudes decrease until Δr = 20mm is reached, but increase again for increasing spatial separation of the two LDV-measurement locations and fully recover for Δr = 40mm. The amplitude variation can be

easily explained by the space dependent auto-correlation amplitude of the moved LDV-measurement location. More difficult is a sound interpretation of the phase shift. On average the phase shift implies a bended geometry of the PVC because for increasing radii parts of the PVC lag behind. This hypothesis is sustained by negative circulation observed in the outer shear layer. However, because a phase shift allows not to deduce a direction unambiguously, the PVC at larger radii could - from observations presented in figure 3.16 - hurry ahead as well. A visualization of transient eddies by particle imaging velocimetry promises here a clarification.

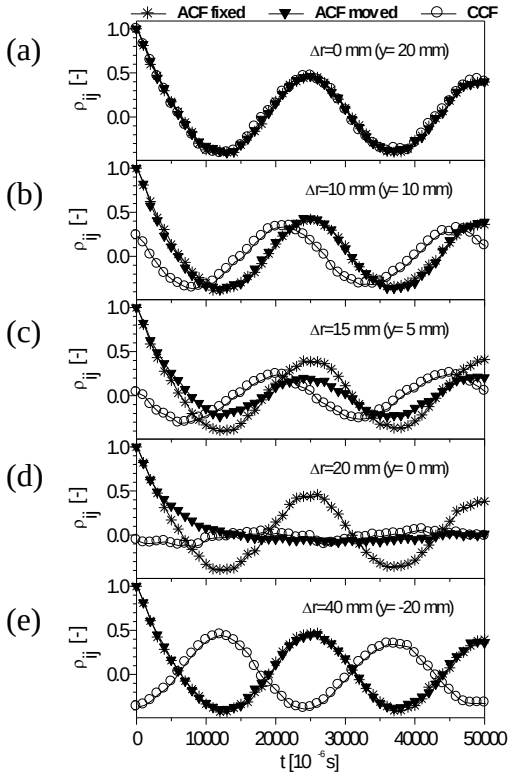

Figure 3.16
Temporal auto-correlations measured by two independent LDV-systems at an axial height of x = 30mm. The first measurement volume was fixed to radial positions (denoted here by y) of 20mm (a), the second was shifted radially to 10mm (b); 5mm (c); 0mm (d); -20mm (e). Temporal dependency of the cross-correlation (open circles) shows variation of amplitude and phase shifts in the oscillations dependent on the spatial separation of the measurement loci.

Due to the almost perfect symmetry obvious from figure 3.16(e) and slow decay of auto-correlation amplitudes at large time intervals, it appears that velocities within the PVC sustain for hundreds of milliseconds. This is worth mentioning as overall fluctuation levels reach up to 40% especially in the shear layers where amplitudes of the coherent motion are at maximum.

To investigate the influence of tangential momentum on the PVC the theoretical swirl number was varied. Figure 3.17 shows temporal auto-covariances for $S_{0,th}$ = 0.75; 1.4; 2.0 at x = 10mm and r = 25mm. For $S_{0,th}$ = 0 no oscillations appeared as expected. With increasing swirl, amplitudes and characteristic frequencies both increase. As obvious from the corresponding PSDs higher swirl cases are characterised by more distinct overtones.

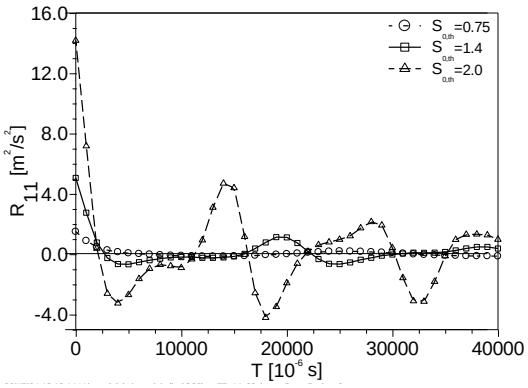

Figure 3.17
Temporal auto-covariance for varying theoretical swirl numbers at x = 10mm, r = 25mm.

Summarizing, the most distinct differences between isothermal and combusting cases are dynamical properties such as the PVC. It is speculated that the PVC in the combusting case was not observed because of a reduced effective swirl number. A reduction of the swirl number is simply achieved by decreased density in the burnt gases. From this perspective as well, combined simultaneous velocity/density measurements similar to [71] are required in future.

In section 6 the application of high-speed diagnostics is discussed to closer investigate flash back using the adapted nozzle geometry shown in figure 2.2(b).

3.4 Tomographic PIV in a motored IC engine

The ability to measure flow velocity with its corresponding 3-dimensional (3D) properties and flow structures within spark-ignited (SI) engines is of particular interest to better understand the physical processes that underline engine performance. Within SI engines, the flow field is inherently 3D and is responsible for fuel-air mixing as well as the transport and development of the flame front. For spray-guided direct-injection (DI) engines operated in stratified mode the complex 3D flow structures play an important role in defining the ignition event and subsequent combustion [72, 73]. For the simulation of these flows, tools like large eddy simulations (LES) are required which provide information on the dynamics of these processes and the spatial structures of the flow. Therefore information of the three velocity components and their derivatives are required to resolve the full turbulent information of the flow field to improve modeling and validate LES simulations. For the validation of combustion LES the comparison of non-reacting flow characteristics is required first [74].

PIV [50] is a well-established technique to capture the instantaneous planar flow field in internal combustion (IC) engines [75]. Previous PIV measurements in IC engines have characterized turbulence properties [76–78], analyzed spatial flow structures [79], investigated influences of cycle-to-cycle variations [80, 81], as well as characterized flows during injection and ignition [82]. However, all previous works have been limited to planar velocity measurements. Although the third velocity component was resolved in an engine by stereoscopic PIV [83], its spatial derivatives as well as the three dimensional flow structures have not been available. To understand the complex 3D structures of the in-cylinder flow, Voisine et al. [79] performed

two-component (2c)-PIV in the vertical symmetry as well as a horizontal plane to reconstruct the quasi 3D flow from the phase averaged flow images. More recently Bode et al. used two vertical PIV measurement planes to track the temporal evolution of larege scale in-cliner motions [84]. For a more detailed view, Dannemann et al. [85] extended this to 8 planes resolving connections of flow structures between the different planes. Despite the success of ability to describe the ensemble averaged 3D flow field, these findings were unable to fully resolve cohesive 3D flow structures, characterize 3D flow properties, and were not capable to capture the instantaneous cycle resolved velocity data.

These limitations can be overcome by tomographic PIV (TPIV, see chapter 3.1.4). TPIV measurements within an optical SI engine (compare chapter 2.4) operating at 800 RPM are presented in this chapter [18]. The TPIV measurements are used to resolve the 3D flow structures and velocity gradient tensors within a 47x35x4 mm^3 measurement volume within the center of the tumble plane. Measurements were obtained at selected CAD during the intake and compression stroke and are used to interpret differences in 3D flow structures for the ensemble average and instantaneous cycles.

3.4.1 Experimental setup

The imaged volume was centered in the tumble plane (figure 2.9 and 3.18). Four CCD cameras (ImagerIntense, LaVision, 1376x1040 pixels, 12 bit, double frame exposure) with identical lenses (50 mm, Nikon) in Scheimpflug arrangement were setup circularly around the optical access (figure 3.18). The arrangement around the center axis of the cylinder axis ensured a similar distortion for all four cameras. Cameras 3 and 4 were set up in an angle of 16° normal to the illuminated volume. This is the maximum angle due to restrictions of the optical access. The angle of camera 1 and 2 was chosen at 13.5° such that each camera projection provides independent line-of-sight information of the illuminated volume. This is compared to [59] on the lower side of the camera angles but still provides a manageable reconstruction quality. The lenses were operated with *f#* of 16 which results in a depth of field of ~8 mm. A two-level spatial target (Type 7, LaVision) was used to calibrate and match the viewing plane for each camera. The alignment of the cameras achieved a visualized area of 47x35 mm^2 with an average resolution of 30 pixels/mm. The cameras and lasers were restricted to a repetition rate of 5 Hz for which TPIV images were obtained at selected CAD during intake and compression (Tab. 1). For each CAD imaged, 300 phase-locked images were acquired and images of the two-level target were taken before and after acquiring Mie scattering images.

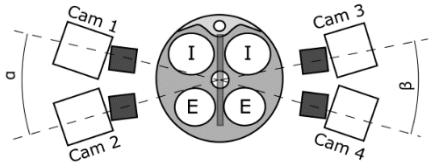

Figure 3.18
Experimental setup TPIV measurements in optical engine

3.4.2 TPIV processing

A commercial software (DaVis 8.2, LaVision) is used for the processing of the TPIV images. A transformation matrix (polynomial approach) based on images of a two-level target was used to match the viewing planes of all four detection systems. A 3x3 pixel sliding minimum is

subtracted from the Mie scatting images to reduce background noise and images were normalized by the local image intensity so that particle intensities were of similar magnitude for all four cameras. A volume self-calibration [86] was performed for each CAD imaged which provided a remaining pixel disparity in the sub-pixel range (< 0.3 pixel) for all cameras. This verified that the repositioning of the glass cylinder after taking images of the two-level target did not negatively affect the triangulation and particle reconstruction and corrects for any influence of engine vibration. The reconstruction of the 3D particle images was performed using an iterative Multiplicative Algebraic Reconstruction Technique (MART) algorithm [87] yielding approximately 200 volumes in the z-direction with an average particle density of ~$2 \cdot 10^{-4}$ particles per volume element to maximize correlation peak quality due to reduced number of ghost particles [59]. The volume cross-correlation was performed with a multi-pass volume cross-correlations algorithm with decreasing volume size and a final step of 48x48x48 pixels^3 and 75% overlap which resulted in a vector spacing of 0.4 mm in all directions. During post-processing, a correlations peak quality check, a 5x5x5 vector neighborhood operation to remove spurious vectors [88], and a 3x3x3 Gaussian smoothing filter was applied to the vector fields.

3.4.3 Assessment of TPIV in an engine

The mass conservation principle is applied to ascertain the uncertainty of the 3D velocity data. Assuming a spatially uniform density, continuity yields: $\rho^{-1}(\partial\rho/\partial t)+\partial u_i/\partial x_i = 0$. During intake, at 270° before top-dead-center (bTDC), the term $\rho^{-1}(\partial\rho/\partial t)$ is neglected because density (ρ) is assumed to be uniform with time. During compression, at 90° bTDC, $\rho^{-1}(\partial\rho/\partial t) = 46 s^{-1}$ deduced from the in-cylinder pressure trace. Continuity is evaluated for cubic control volumes (CV) of equidistant spacing (0.4 mm) throughout the entire measurement volume for 300 images at each CAD. A 0.4x0.4 mm^2 region corresponds to a 2x2 vector spacing for which four velocity vectors are averaged to represent a single velocity vector normal to the surface of the CV (figure 3.19 upper left corner).

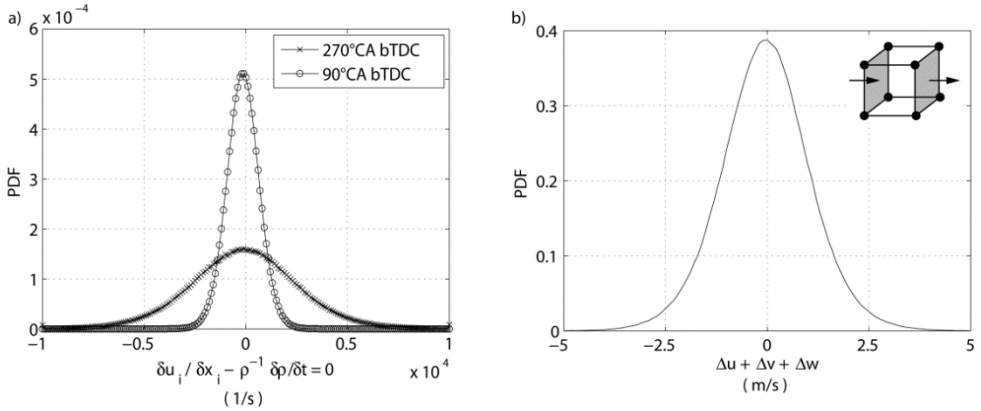

Figure 3.19
Fulfillment of mass conservation principle: PDF of velocity flux for 270° bTDC

In attempt to better quantify the relative deviation from mass conservation, the PDF of the velocity flux ($\Delta U = \Delta u + \Delta v + \Delta w$) for each CV at 270° bTDC is shown in figure 3.19. Assuming constant density and analyzing a cubic CV with equidistant spacing, ΔU can be evaluated to

assess mass conservation [89]. By normalizing ΔU with the averaged velocity vector (u_{norm}) that enters each CV, the deviation of the velocity flux from the true value is calculated by Eq. 17 and found to be σ = 8.2 %

$$\sigma = \sqrt{\frac{1}{N-1}\sum_{CV}\left(\frac{\Delta U(CV)}{u_{norm}(CV)} - \frac{1}{N}\sum_{CV}\frac{\Delta U(CV)}{u_{norm}(CV)}\right)^2} \qquad (17)$$

According to Zhang et al., this deviation is primarily associated with the precision within calculating the velocity gradient tensor due to discretization errors (e.g. inhomogeneous particle distribution within interrogation volume) [89]. For the presented measurements the deviation may also be attributed to the engine environment which includes vibrations and remaining image distortion from the curvature of the thick glass cylinder. A precision within 8.2 % for the velocity gradient tensor is in agreement with other tomographic flow measurements performed within generic configurations [89], and demonstrates the validity of our 3D velocity measurements and capability of TPIV in a motored engine.

3.4.4 Results

Phase averaged three-dimensional velocity field

A first assessment of the 3D velocity field is presented in figure 3.20 and reveals phase averaged flow fields (300 cycle average) during intake (270° bTDC, 180° bTDC) and compression (90° bTDC). The vectors (every 4th vector displayed) represent the local 3D-velocity (u, v, w) at the center plane of the measurement volume (z = 0 mm). Discrete levels of velocity magnitude computed by all three velocity components are displayed by 3D iso-surfaces.

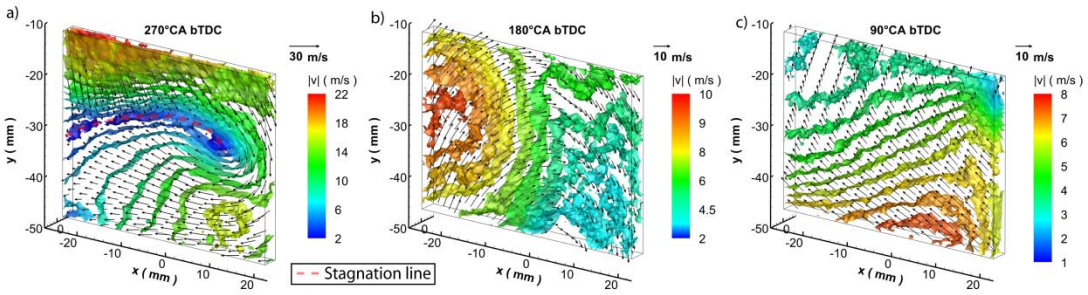

Figure 3.20
Phase averaged flow fields; Iso-surfaces of the 3D-velocity magnitude with vectors (every 4th vector displayed) at the center plane (z = 0 mm)

During intake, at 270° bTDC, the in-cylinder flow in the center plane is characterized by the high velocities generated from the annular flow from the intake valves and the downward motion of the piston. The upper left corner of the image exhibits a downward jet-like flow comprising of high velocities directly beyond the intake valves (valves not shown) and velocity iso-surfaces parallel to the flow direction. For the following discussion, this jet-like flow structure will be referred to as "inlet jet". Beyond the inlet jet to the right, the intake flow is positioned downward and is redirected by the piston top located at y = -52 mm. As a result a clockwise tumble motion is already visible within the symmetry plane and a stagnation front (dashed red line) is formed left of the tumble vortex center where the incoming fluid from the intake valves

impinges on the reversing flow from the piston. The 3D iso-surfaces further complement the illustration of the tumble motion for which the tumble flow direction is perpendicular to the iso-surfaces.

At 180° bTDC the phase-averaged flow field is no longer characterized by large velocities of an inlet jet, but is better characterized by smaller velocities due to the lack of piston movement and near closing of the intake valves. As a result, the instantaneous flow fields (not shown) appear to be more stochastic and do not reveal strong coherent flow structures like the inlet jet. The phase averaged flow field indicates a lower velocity magnitude and the formation of the tumble center is located at the bottom center of the imaged volume.

During compression (Fig. 3.20c) a portion of the tumble motion is visible with the tumble center located near the top right corner. The flow field shows a perpendicular direction to most 3D velocity iso-surfaces and velocity magnitudes remain on a similar level as for 180° bTDC. The phase averaged velocity image does not reveal significant 3D flow structures compared to phase averaged flow fields during intake.

Three-dimensional turbulent kinetic energy

The fluctuations of the 3D flow field can be characterized by the turbulent kinetic energy (TKE) defined as $TKE = \frac{1}{2}\left(u_i' u_i'\right)$ where u_i' is the fluctuating velocity component in the i^{th} direction.

In this work TKE is calculated through the Reynolds decomposition method. Figure 3.21 compares the TKE field calculated from 2D and 3D velocity information during intake (270° bTDC). Measurements are shown in the central plane (z = 0 mm).

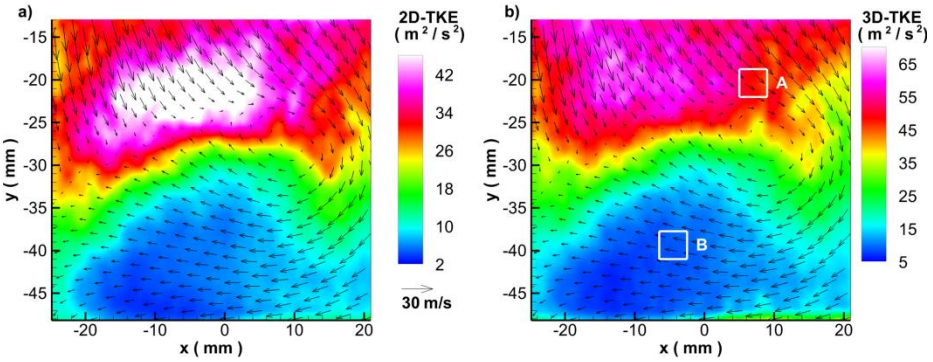

Figure 3.21
TKE at the center plane (z = 0 mm) calculated from a) in-plane velocity components u' and v' (2D-TKE); b) from all three velocities (3D-TKE); Locations of 4x4x4 mm³ areas A and B

The 2D-TKE (Fig. 3.21a) is determined from the two in-plane flow components (u' and v') as would be obtained from (2c)-PIV. The 2D-TKE field shows a region of large velocity fluctuations just above the stagnation line (compare Fig. 3.20a) and is due to large variations of the intake flow directly exiting the intake valves as it interacts with the existing tumble motion. In comparison, the 3D-TKE field shows that high values of TKE are further extended toward the intake valves, revealing a zone of high turbulence that is influenced by the out-of-plane velocity fluctuation. This is within the inlet jet region which is likely to exhibit large velocity fluctuations due to the flow separation from the intake valves.

Another region of higher TKE is found at the bottom right corner of figure 3.21b above the piston surface (2D: 10 m^2/s^2; 3D: 25 m^2/s^2). As described by [79], the flow in this region reaches the physical boundaries of the cylinder and is redirected along the piston surface. Here it is shown that higher levels of TKE are found in the right corner and decay above the piston to the left. In comparison with the 2D-TKE, this analysis reveals that the redirected flow exhibits large z-velocity fluctuations, which decay as the flow is further directed along the piston surface. This analysis demonstrates the need of all three velocity components to better characterize the flow field and reveals misinterpretations that may result when only resolving 2D velocity measurements.

Figure 3.22 a-c shows 3D iso-surfaces of TKE for selected phase averaged CAD. At 270° bTDC, the images clearly show differences in the iso-surface structure between the inlet jet region and regions beyond the inlet jet. As previously shown, the inlet jet is characterized by high values of TKE, but it is also shown that the TKE iso-surfaces are aligned parallel to the flow direction. Beyond the inlet jet, TKE iso-surfaces are aligned perpendicularly to the flow direction and are characterized by lower TKE values.

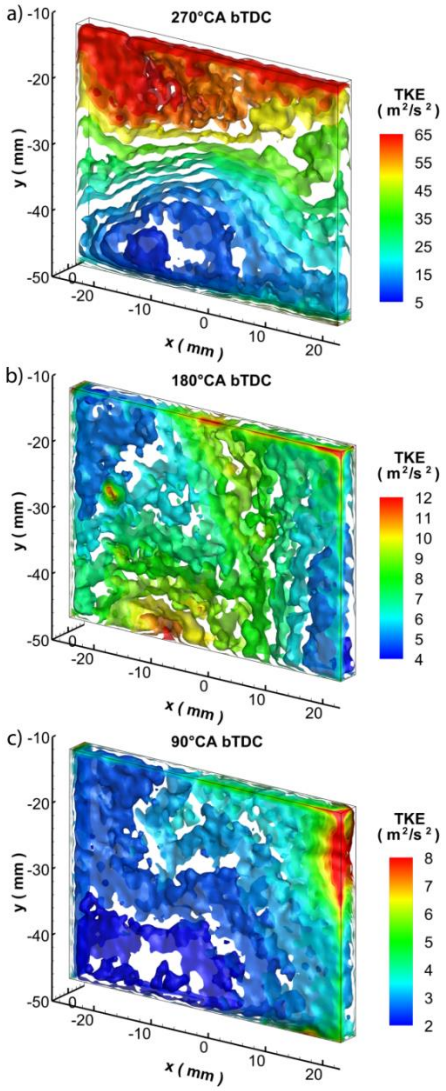

Figure 3.22
3D iso-surfaces of the TKE

At the end of intake stroke (180° bTDC), TKE within the inlet jet region is significantly lower (< 12 m^2/s^2) than at 270° bTDC (> 60 m^2/s^2). Similar to the images of the 3D velocity iso-surfaces, the flow field (fig. 3.20b) does not show a preferred direction towards the 3D TKE iso-surfaces.

During compression (90° bTDC, Fig. 3.22c) TKE decays down to 2-8 m^2/s^2 within the imaging volume and is distributed more homogenously with the exception of the upper right corner. Instantaneous images reveal that the upper right corner is the region where tumble vortex is often located. Although the center of the tumble vortex is characterized by low velocities, TKE levels are relatively high in this region due to variations in the vortex center location as well as the size and shape of the vortex in individual images [80].

Instantaneous 3D velocity images

Figure 3.23a/c shows volumetric velocity field images acquired for two instantaneous cycles (cycle 59 and 167 out of 300 cycles) during intake at 270° bTDC. Although different for each cycle, the flow features such as inlet jet and the tumble vortex locations revealed within the mean flow (Fig. 3.20a) are easily identifiable in the instantaneous cycles. Moreover, the complexity of the turbulent 3D flow field is immediately apparent within the images. To determine vortical structures a threshold based criteria (Q-criteria) is used (Fig. 3.23b/d). It defines vortices as regions with a positive second invariant Q of the local velocity gradient ∇u [90]. Assuming an incompressible flow, Q is defined as $Q = \frac{1}{2}\left(|\Omega|^2 - |S|^2\right) > 0$, with $Q > 0$ indicating a dominance of rate-of-rotation (Ω) over strain (S) within vortex regions.

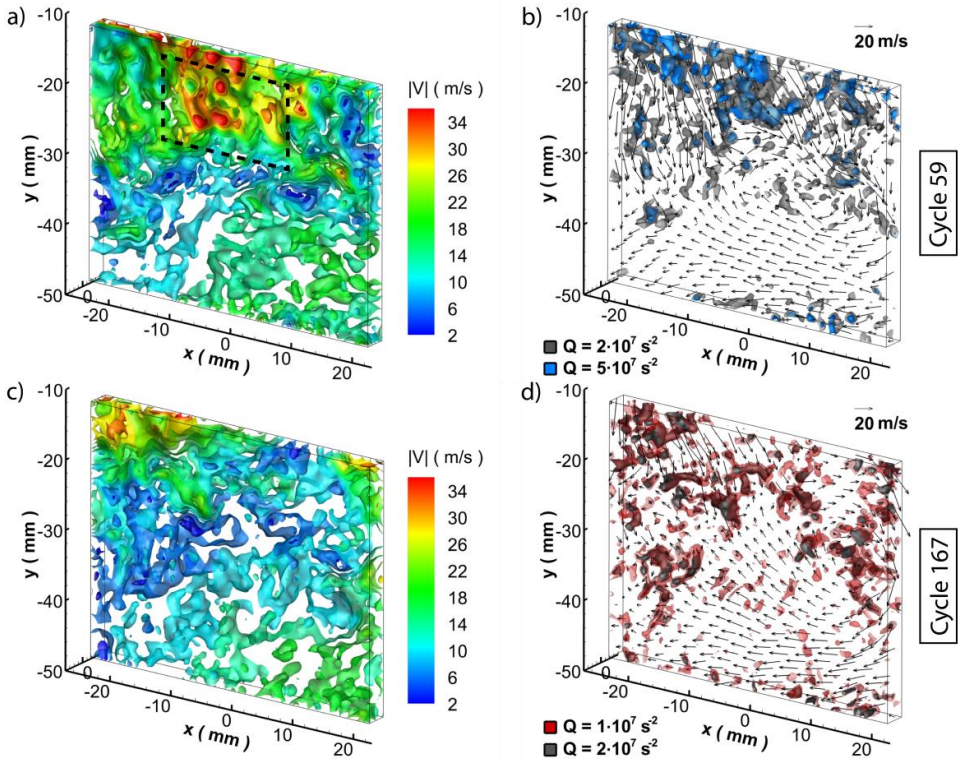

Figure 3.23
Two instantaneous flow field images at 270° bTDC; a) and c) represent iso-surfaces of velocity magnitude; b) and d) corresponding Q-criteria and vector field (z = 0 mm)

Figures 3.23c/d reveal a variety of small scale vortical structures (~2-6 mm in diameter) of different size and orientation in the region of the inlet jet. Although many structures are cut due to the limited thickness of the measurement volume (Δz = ±2 mm) the formation of vortex tubes is visible which are mostly orientated normal to the x-y plane. For cycle 59 (Fig. 3.23a), the intake jet exhibits a region of high velocity with a large vortical structure present (Fig. 3.23b). In comparison, the instantaneous cycle shown in Fig. 3.23c (cycle 167) reveals distinct flow differences. Here the magnitude velocity of the inlet jet is weaker and does not extend as far into the viewing plane. In addition, the Q-criteria (Fig. 3.23d) illustrates fewer vortical structures which are more agglomerated within the left side of the inlet jet. For brevity, instantaneous images at other selected CAD are not shown, but reveal a homogeneous distribution of weaker vortical structures determined by the Q-criteria.

The instantaneous volumetric 3D velocity measurement provides access to the full velocity gradient tensor ∇u. Figure 3.24 shows the probability density function (PDF) of all three vorticity components Ω_x, Ω_y, and Ω_z obtained from volumes (4 mm³ in size) taken at two different regions during intake (regions A and B marked in Fig. 3.21a). The PDFs consist of average data from 300 cycles as well as the two instantaneous cycles shown in Fig. 3.23. In general, the PDFs of the average are centered close to zero, while instantaneous cycles can reveal flows with stronger Ω_y and Ω_z values indicating these cycles have flow structures with predominate rotations in these directions. For volume A, all PDFs show broader distributions of Ω_z indicating a preferred alignment of the vortical structures perpendicular to the x-y plane. These findings are in agreement with the vortical structures revealed from the Q-criteria for the instantaneous flow images in Fig. 3.23. In comparison to volume A, volume B is characterized by lower TKE levels (Fig. 3.22) which is reflected by narrower distributions of vorticity PDF. In general, the 3D velocity gradient information is capable of better characterizing the flow field during the intake which may better quantify fuel-air mixing capabilities for future studies.

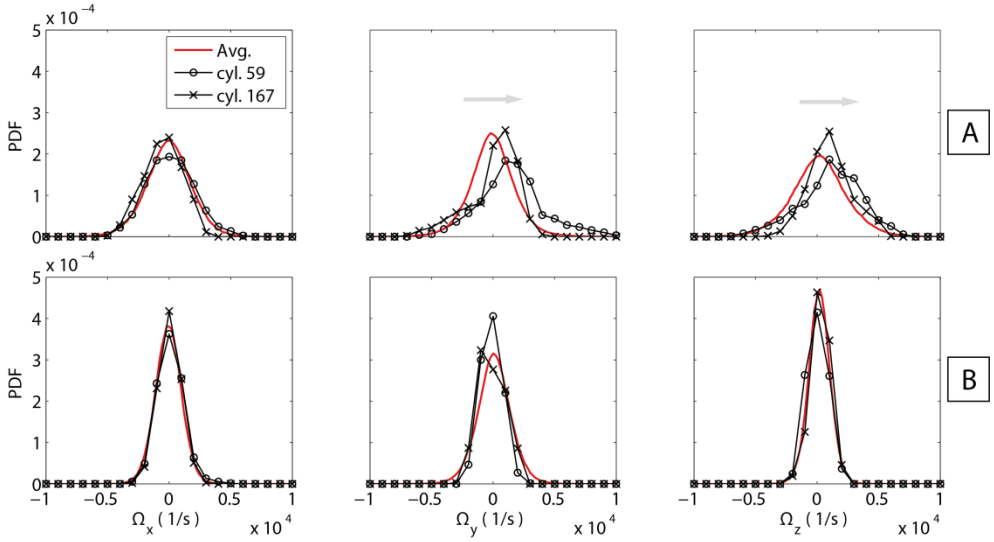

Figure 3.24
PDF of full vorticity vector at 270° bTDC for the two volumes A and B; average and two corresponding single shots (Fig. 3.22)

3.4.5. Conclusions

Tomographic particle image velocimetry was applied within a motored, single cylinder DISI engine to measure the volumetric instantaneous flow field at selected CAD during intake and compression. This first assessment of TPIV demonstrated the capability of the reconstruction of the particle and the volumetric cross-correlation when image distortion caused by the thick curved glass and limited camera angles are present. The uncertainty of the 3D velocity data was addressed using the principle of mass conservation for the inlet flow. Due to this a precision within 8.2 % for the velocity gradient tensor was found which is in the same order of magnitude then volumetric flow measurements conducted in generic configurations, indicating that TPIV measurements are feasible within motored optical IC engines. Based on the volumetric velocity data, the average structure of the flow field was analyzed showing a clear orientation of the velocity inside the imaged volume, which changes during the different phases of the cycle. To further interpret the 3D velocity field the turbulent kinetic energy field was calculated and revealed distinct differences between 3D and 2D TKE fields especially in the region of the inlet jet during intake. The 3D structure of the velocity and TKE illustrated distinct alignment of the flow direction with 3D iso-surfaces of velocity magnitude during intake (270° bTDC) and compression (90° bTDC), while less distinct flow alignment was shown at 180° bTDC. The analysis of instantaneous cycles during intake (Q-criteria) visualized the appearance of strong vortical structures within the inlet jet. Due to cyclic variations these differ clearly in size and orientation. This variability was also assessed by PDFs of all three vorticity components. Comparing instantaneous cycles with the average showing that these structures have a clear orientation by Ω_y and Ω_z.

4. Scalar field measurements

In addition to instantaneous flow field measurements by LDV and/or PIV, spectroscopic methods are exploited to measure instantaneous temperature and/or concentration fields. Although various methods exist this lecture notes focuses only on laser-induced fluorescence (LIF), Raman/Rayleigh scattering and coherent anti-Stokes Raman spectroscopy (CARS). Not all details and possible applications can be presented here. Therefore the interested reader is referred to excellent review articles and text books cited in the corresponding subchapters.

Laser-induced fluorescence with excitation in the UV is frequently used for thermometry and the detection of minor combustion-related molecules such as NO, OH, CH, C_2, HCHO and others. Fluorescing organic molecules have found an interest as tracers that allow quantitatively observing fluid mixing processes as well as fuel concentration mapping. Raman scattering is used to measure major species concentrations such as H_2, O_2, N_2, CO, H_2O, CO_2, and CH_4 precisely. Often it is applied simultaneously with Rayleigh scattering which is used to measure temperatures assuming the validity of the ideal gas law. Rayleigh-based thermometry requires information on the effective cross-section depending on the mole fractions of the main species. Moreover its signal wavelength occurs at the same wavelength as the excitation. Therefore it is prone to spurious light scattered from surfaces. For this reason CARS-thermometry is better suited for studying confined combustion processes.

The scope of this chapter is to introduce into these different techniques and to outline some important issues.

4.1 Laser-induced fluorescence

Laser-induced fluorescence (LIF) is the process of spontaneous emission from an excited electronic state populated upon absorption of a laser photon. Large cross-sections mainly in the visible and ultra-violet spectral range enable species detection down to the sub-ppm range. Many combustion-relevant species like OH, O_2, NO, CH, CN, NH, C_2 can be accessed selectively. Detailed treatments are given in the textbooks of Eckbreth [91], Kohse-Höinghaus and Jeffries [90], and in the review articles of Kohse-Höinghaus [92], Daily [93] and Schulz et al. [94]. LIF can be understood as two subsequent steps. Absorption of (typically) one photon leads to the population of a (typically electronically) excited state in the respective atom or molecule. After a certain lifetime τ this excited species can relax into a lower-lying state by emitting a fluorescence photon. Fluorescence typically competes with alternative processes that lead to a depopulation of the excited state (quenching, photodissociation, ionization). The ratio of fluorescence rate vs. excitation rate is given by the fluorescence quantum yield ϕ.

Equation 17 describes the LIF-intensity I_{LIF} for one species in the regime of weak excitation as

$$(17) \qquad I_{LIF} = c\ I_{laser} N(p,T)\, f_{v,J}(T) B_{ik} \Gamma(p,T) \phi$$

with c being a parameter dependent on the specific experimental setup. The LIF-intensity I_{LIF} is proportional to the number density $N(p,T)$ of the excitable molecules in the probed volume V which is determined by $N(p,T)$ times the temperature-dependent Boltzmann fraction $f_{v,J}$ giving the population of the initial level i. The Einstein-B_{ik}-coefficient describes the absorption probability for transition $i \rightarrow k$. Within the linear regime, the fluorescence intensity depends linearly on the laser intensity I_{laser} and the spectral overlap $\Gamma(p,T)$ of the laser profile and the absorption line. All these factors determine the number density of excited molecules and, therefore, the absorption part of the LIF-process. The fluorescence quantum yield ϕ in equation 18 gives the ratio of the spontaneous emission rate (from level k) versus the total rate of (radiative and non-radiative) relaxation processes:

$$(18) \qquad \phi = \frac{A_{ki}}{\sum_j A_{kj} + Q_k(p,T) + P_k}$$

ϕ therefore depends on the rate of spontaneous emission (given by the Einstein-A_{ki}-coefficient) divided by the sum of the rates of all depopulation processes of the excited state (spontaneous emission from state k to all possible ground state levels: ΣA_{kj}, quenching $Q_k(p,T)$ and predissociation P_k). The detection efficiency of fluorescence photons depends on the observed solid angle $\Omega/4\pi$, the transmission of the optical system ε and the response of the detector η. Effects of polarization are discussed in [95].

When quantifying signal intensities obtained from LIF one usually has to account for numerous temperature-dependent effects. The resulting over-all temperature-dependence in turn is the basis for LIF-thermometry. The spectral overlap factor $\Gamma(p,T)$ can be calculated from spectra simulations which are available for the most important combustion relevant species [96, 97]. This is mainly important in high-pressure applications where collisional broadening causes the individual rotational lines to blend yielding absorption features which are spectrally broader than the laser line. At atmospheric pressure and above the denominator in the fluorescence quantum yield ϕ is dominated by fluorescence quenching ($Q >> A$). For a large number of colliders

quenching rates for, e.g., OH and NO have been determined as a function of temperature and pressure enabling the development of simulation models [98]. Therefore, quenching can be quantified as long as the local gas composition and temperature are known (for example using Raman/Rayleigh spectroscopy simultaneously with LIF). Additional losses from the excited state can occur due to predissociation P_k and photo-ionization.

Besides these processes other collisionally-induced energy-transfer processes must be considered. Vibrational (VET) and rotational (RET) energy transfer populate excited levels within the excited state that can subsequently fluoresce. This especially gains importance if levels with significantly different effective fluorescence lifetimes are involved. Furthermore, fluorescence signal may be shifted to different spectral regions compared to the direct transitions from the laser-populated level. The implications of these effects are discussed in further detail in [91].

With increasing laser intensity a transition from the linear LIF-response (as given in eq. 17) towards a saturation regime (with I_{LIF} independent on I_{laser}) is observed. Saturation occurs through down-ward pumping of population from the excited state. At the same time, the laser-coupled ground state levels can be depleted because of too slow population via RET from neighboring states. The over-all effect can be modeled based on the rate equations of the individual processes. For simple systems with constant laser intensity, the system (that is, its state populations) reaches a steady state after some characteristic time τ_{ss}. If the temporal laser pulse width τ_{laser} is much larger than τ_{ss}, the steady-state solution may be used to describe the overall LIF-process. This yields relatively simple non-transient LIF-models [99]. Transient LIF-models, on the other hand, involve solving the fully time-dependent rate equations [95]. For many practical applications, simple non-transient models yield an adequate description of the LIF-process. This is true in particular for nanosecond-laser excitation and high-pressure environments.

4.1.1 LIF-thermometry: Theory

For LIF-thermometry, different methods have been established that involve generally different experimental and data evaluation procedures: Single-line techniques (where only a single ground state is probed), two-line techniques (where two ground states are probed and the temperature is inferred from the ratio of two LIF-intensities) and multi-line techniques (where three or more ground states are probed and temperature is inferred from a Boltzmann plot or by fitting spectral simulations). Theoretical analysis of line shape, quenching, energy transfer and noise effects for the different techniques have been performed by several authors [95, 100].

Particularly relevant in this context are of course the temperature-dependent terms. The dominant temperature influence in eq. 17 is given by the Boltzmann fraction

$$f_{\mathrm{v},J}(T) = \frac{g_i \exp\left(\frac{hcE_i(\mathrm{v},J)}{kT}\right)}{\sum_i g_i \exp\left(\frac{hcE_i(\mathrm{v},J)}{kT}\right)} = \frac{g_i}{Z(T)} \exp\left(\frac{hcE_i(\mathrm{v},J)}{kT}\right) = \frac{N_i}{N} \tag{19}$$

of the total species population in the laser-excited ground state. The temperature dependence is due to both the exponential factor for the particular transition and the partition function *Z(T)*. The spectral overlap fraction Γ depends on temperature via collisional broadening and shifting

effects. The quenching rate Q depends on temperature due to both the varying collisional frequency and cross-sections. Finally, the number density N of the target LIF-species depends on concentration and temperature via the ideal gas law.

In ***single-line LIF-thermometry***, an overall temperature dependence of the LIF-signal can be calculated from eq. (17) if the spectroscopic data (term energies for Boltzmann fraction, collisional broadening, quenching) are known. The laser intensity I_{laser} is readily measured. It is, however, evident from eq. 17 that the concentration of the target species N must be known. This is the case in non-reactive flows where concentrations are constant (e.g., O_2 in the inlet stroke of internal combustion engines [101] or NO seeded in constant amounts to a flow [102]) or when concentrations can be derived from chemical kinetic simulations (as shown, e.g., for NO in a low-pressure flame [103]). Finally, the calculated relative temperatures need to be calibrated at a known temperature.

Two-line LIF-thermometry is much more frequently used. In this approach, two LIF-measurements are performed from different ground states. The fluorescence ratio R from the two measurements is then given by

$$(20) \qquad R_{12} = \frac{I_{LIF,1}}{I_{LIF,2}} = \frac{c_1 \; I_{laser,1} \; g_1 \exp(-\varepsilon_1 / kT) \; B_1 \; \Gamma_1(p,T) \; A_1 / \left(A_1 + Q_1(p,T)\right)}{c_2 \; I_{laser,2} \; g_2 \exp(-\varepsilon_2 / kT) \; B_2 \; \Gamma_2(p,T) \; A_2 / \left(A_2 + Q_2(p,T)\right)}$$

with ε_i being the term values in Joule. By taking the ratio the species concentration, which is the major unknown factor in most applications, cancels out. This makes the two-line techniques applicable to reacting systems. It should be noted that also the partition function $Z(T)$ cancels out in the ratio.

Commonly, there are more assumptions being made as to the remaining temperature dependent factors: Q is assumed to dominate over A (which is usually the case in atmospheric or high-pressure systems); if Q is the same for the excited states in both measurements (by choosing either a molecule where Q does not depend on rotational quantum number like NO, or by choosing transitions that excite into the same upper state), then Q also cancels out: the ratio R_{12} gets independent of quenching processes. If, finally, the temperature dependence of the overlap coefficients and the influence of laser-energy fluctuations are neglected, then the fluorescence ratio is given by a Boltzmann relation only,

$$(21) \qquad R_{12} \propto \exp\left(-\frac{\Delta\varepsilon_{12}}{kT}\right)$$

depending on the temperature T, the ground state energy difference $\Delta\varepsilon_{12}$, and the Boltzmann constant k. Equation (21) reduces the temperature-dependence of the LIF-ratio to the temperature-dependence of the relative ground state populations, which represents the most relevant temperature influence in the two-line technique. Nevertheless, additional influence of the overlap fraction $\Gamma(p,T)$ and quenching $Q(p,T)$ may become important depending on the specific target species.

The constants c_1 and c_2 in eq. (20) summarize the efficiency of the detection system. If they are the same for both excitation wavelengths, quantitative temperature measurements are in principle possible without calibration if the spectroscopic constants of the two transitions are known. In many cases, however, using known temperature data is necessary to calibrate for the c_1/c_2-ratio.

The precision of any thermometry technique depends on the sensitivity of the involved LIF-signal strength(s) on temperature. In a two-line technique, high sensitivity of the fluorescence ratio R_{12} on temperature is desired, i.e. a large change in R_{12} with temperature. Mathematically, this can be expressed as the second derivative being zero:

$$(22) \qquad \frac{d^2 R_{12}}{dT^2} = 0 \Leftrightarrow T = \frac{\Delta\varepsilon_{12}}{2k}$$

Depending on the temperature range that should be investigated in the two-line technique, this equation gives the condition for ground state energy differences that yield highest temperature sensitivity. For much higher or lower temperatures, the sensitivity may decrease severely. A two-line technique is therefore most sensitive within a certain temperature range only. Table 4.1 compares the sensitivities of different NO two-line thermometry methods used in flames.

Table 4.1
Comparison of the temperature sensitivities of different NO two-line LIF-thermometry methods in flames.

Reference	**Excited NO lines**	**Maximum temperature sensitivity $\Delta\varepsilon_{12}/2k$**
Tamura *et al.* [104]	*A*–*X* (0,0) O_{12}(1.5) and *A*–*X* (0,0) O_{12}(19.5)	498 K
Tsujishita *et al.* [105]	*A*–*X* (0,0) Q_2(17.5) and *A*–*X* (0,0) Q_2(27.5)	566 K
Bessler *et al.* [106]	*A*–*X* (0,0) Q_1 & P_{21}(33.5) and *A*–*X* (0,2) O_{12}(5.5)	1420 K
Bell *et al.* [107]	*A*–*X* (0,0) R_1 & Q_{21}(21.5) and *A*–*X* (0,2) O_{12}(8.5–10.5) bandhead	2300 K

Multi-line LIF-thermometry offers high temperature sensitivity in a wide temperature range by probing a number of ground states with different term energies. In a basic approach we can assume similar to the two-line technique that the main temperature influence of the LIF-signal arises from the ground state population only. Furthermore it is assumed that the temperature influence on the overlap fraction and quenching is equal for all transitions, *c* is equal for all transitions, and $A << Q$ is valid. Then, for any transition *i*, equation (17) can be rewritten as

$$(23) \quad \ln\left(\frac{I_{LIF,i}}{I_{laser,i}}\frac{g_i}{A_i B_i}\right) = -\frac{1}{T}\frac{\varepsilon_i}{k} - \ln\left(\frac{Z(T)}{c \quad N(T)\ \Gamma(p,T)\ Q(p,T)}\right),$$

where the last term is constant for all transitions. The signals $I_{LIF,i}$ and the laser intensity $I_{laser,i}$ are measured, and g_i, A_i and B_i are spectroscopic constants. By plotting the left term of equation (23) versus ε_i for different transitions, the temperature can be derived from the slope of the plot which is $-1/kT$. This is called a *Boltzmann* plot (figure 4.1.)

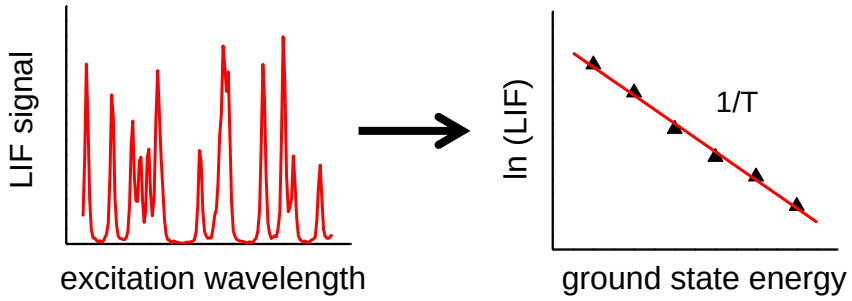

Figure 4.1
Section of a typical LIF-excitation scan (here NO at ~225.3 nm) and the resulting Boltzmann plot. The slope of the Boltzmann plot gives the negative inverse temperature.

In many practical applications there are a number of effects that complicate the simple analysis as given above:

- The assumption that Q is constant for all transitions does not always hold. In OH, for example, Q is known to depend on the rotational quantum number J [108]
- Transitions may overlap, so that the LIF-signal does not arise from a single ground state. This is the case e.g. for NO, especially at elevated pressures. The overlap fractions Γ of many transitions must then be considered simultaneously
- In many practical applications, background signals are present, such that $I_{total} = I_{LIF} + I_{background}$. The simple eqs. (17) – (23) then cannot be applied; instead, corrections for the background contribution are necessary
- The assumption of weak laser excitation that was used for deriving eq. (17) may not hold. LIF-saturation and rotational energy transfer may have significant effects on thermometry techniques [95]
- Especially for larger molecules, the spectroscopy is complex and often only poorly understood

Accurate LIF-thermometry techniques need to include a full description of these effects. This can either be done by multi-temperature calibration measurements (yielding an empirical description of the temperature-dependence of the signals) or by using detailed spectral simulations. For NO-LIF-thermometry a multi-line scanning approach was developed [109] that simultaneously considers the effects of line shape and background contribution based on spectra simulations [97].

In section 5 the application of planar LIF is exemplified in combination with PIV.

4.2 Raman and Rayleigh scattering

If a photon of energy $\hbar\omega_0$, that is non-resonant with any allowed single- or multi-photon transition, interacts with a molecule, with a certain probability elastic or inelastic light scattering occurs. This process is sketched in figure 4.2. The more probable elastic scattering process is termed **Rayleigh** scattering whereas the much weaker inelastic process is called spontaneous **Raman** scattering. After a Rayleigh scattering process the molecule returns into its original quantum state. In contrast, Raman scattering is associated with a net energy exchange between photon and molecule. The energy transfer might have in- or decreased the rotational (denoted by *J*) and/or vibrational quantum state (denoted by *v*) of the molecule. Due to energy conservation scattered Raman photons contain correspondingly de- or increased energy $\hbar(\omega_0 \mp \omega_k)$ with $\hbar\omega_k$ being the energy difference between initial $|i\rangle$ and final $|f\rangle$ quantum states involved to the process ($|i\rangle$ and $|f\rangle$ denote wavefunctions and are solutions of the corresponding Schrödinger equation). In analogy to the postulate of Stokes that fluorescence is shifted towards longer wavelength relative to the exciting wavelength, red-shifted Raman scattered photons $\hbar(\omega_0 - \omega_k)$ are termed **Stokes**-lines and blue-shifted photons $\hbar(\omega_0 + \omega_k)$ **anti-Stokes**-lines.

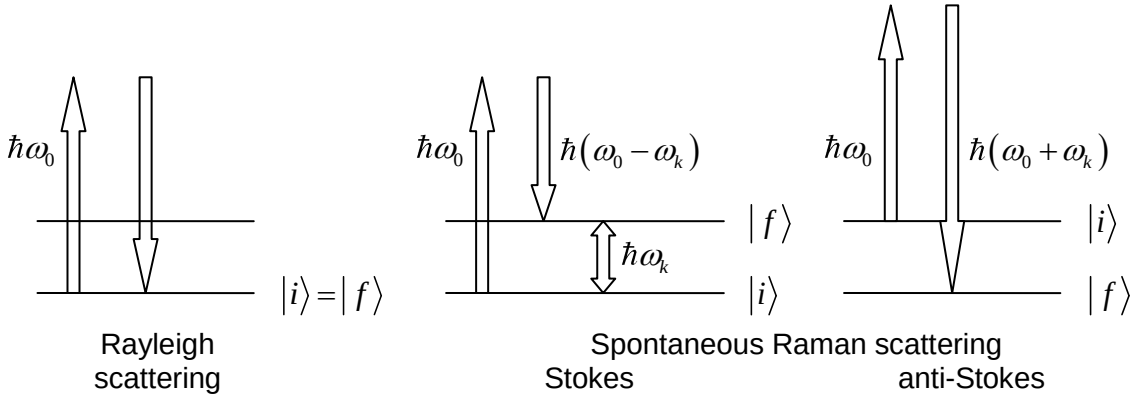

Figure 4.2
Energy level diagram of Rayleigh and spontaneous Raman scattering.

In a semi-classical view where only molecules but not the incident light are treated as quantum objects, Rayleigh and Raman scattering result from a dipole moment induced by the incident electromagnetic field. When a molecule is exposed to an alternating monochromatic electric field the resulting forces push electrons and nuclei back and forth. As a consequence the molecular system behaves analogous to an oscillating dipole. The frequency ω_0 of the alternating electric field and the oscillating dipole frequency are equal and in phase. According to the laws of electrodynamics, the molecule emits light of the frequency ω_0 giving rise to Rayleigh scattering.

The flexibility of this enforced intra-molecular motion depends on the chemical species, temperature and quantum state. It is expressed by the polarizability tensor $\boldsymbol{\alpha}$ which is a tensor of

second rank. The internal degrees of freedom such as rotation or vibration modulate the polarizability. As a consequence, the induced dipole moment oscillates additionally on side bands $\omega = \omega_0 \mp \omega_k$ but with an arbitrary phase difference to the incident radiation. Herein, ω_k denotes a discrete frequency characterizing the internal motion.

For a monochromatic electromagnetic field, as provided by a laser beam, $\mathbf{E} = \mathbf{E}_0 \cos \omega_0 t$, the linear induced dipole moment can be expressed by

(24) $\mathbf{p}^{(1)} = \boldsymbol{\alpha} \cdot \mathbf{E}$.

The aforementioned variation of the polarizability tensor $\boldsymbol{\alpha}$ with internal motions such as discrete molecular vibrations can be expanded into a Taylor series. For the example of a normal vibration *k* with its coordinate Q_k and in the limit of the electrical harmonic approximation that neglects powers higher than the first, the polarizability tensor may be expressed by

(25) $\boldsymbol{\alpha}_k = \boldsymbol{\alpha}_0 + \boldsymbol{\alpha}'_k Q_k$.

The components of the new tensor $\boldsymbol{\alpha}'_k$ consist of the derivatives of the tensor components $\left(\alpha_{ij}\right)_0$ with respect to the normal coordinate Q_k: $\left(\alpha'_{ij}\right)_k = \left(\partial \alpha_{ij} / \partial Q_k\right)_0$. For a harmonic motion the normal coordinate can be expressed by $Q_k(t) = Q_{k_0} \cos \omega_k t$. Herein Q_{k_0} denotes the normal coordinates amplitude. By inserting $Q_k(t)$ into equation (25) the time-dependent polarizability tensor reads:

(26) $\boldsymbol{\alpha}_k = \boldsymbol{\alpha}_0 + \boldsymbol{\alpha}'_k Q_{k_0} \cos \omega_k t$

Equation (24) can be reformulated by using equation (26) and one finally yields

(27) $\mathbf{p}^{(1)} = \boldsymbol{\alpha}_0 \mathbf{E}_0 \cos \omega_0 t + \frac{1}{2} \boldsymbol{\alpha}'_k \mathbf{E}_0 Q_{k_0} \cos\left(\omega_0 - \omega_k\right) t + \frac{1}{2} \boldsymbol{\alpha}'_k \mathbf{E}_0 Q_{k_0} \cos\left(\omega_0 + \omega_k\right) t$.

The first term in equation (27) defines Rayleigh scattering. The condition to observe Rayleigh scattering is that the polarizability tensor $\boldsymbol{\alpha}_0$ is non-zero. In practice this is fulfilled for any molecule. The second and third term in (27) define Stokes and anti-Stokes Raman scattering, respectively. For Raman activity the derivative of the polarizability with respect to the normal coordinate $\boldsymbol{\alpha}'_k$ must be non-zero at the equilibrium position.

To derive an expression for the individual intensities of Rayleigh, Stokes and anti-Stokes Raman scattering, the quantum mechanical transition moments $\Phi(\alpha)$ must be calculated for a specific experimental arrangement. These transition moments replace $\boldsymbol{\alpha}$ in equation (24). In the following Cartesian coordinates are applied and it is assumed that the incident monochromatic electromagnetic radiation is linearly polarized along the z-axis ($E_{0,x} = 0, E_{0,y} = 0, E_{0,z} \neq 0$) and is propagating along the y-axis (figure 4.3).

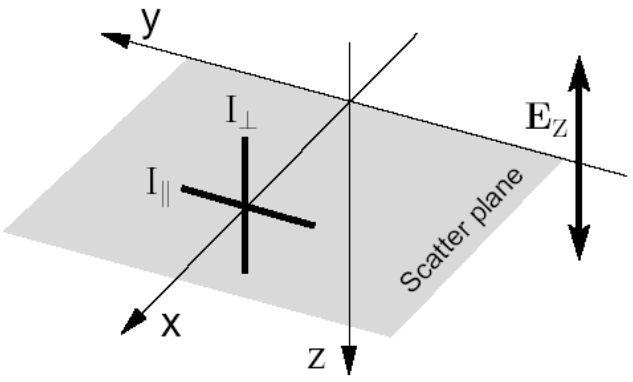

Figure 4.3
Specific geometrical arrangement for Raman and Rayleigh scattering.

Detection takes place along the x-axis perpendicularly to the excitation light propagation ($\theta = \pi/2$). In this specific arrangement the scatter plane is spanned by the x-y-axes. In space-fixed coordinates the polarizability tensor exhibits non-zero off-trace components. Rayleigh and Raman scattered light following the oscillation of an induced dipole moment consists therefore of two polarization components that are aligned perpendicular and parallel to the scatter plane (→*depolarization*). Consequently, two transition moments have to be considered only. For Rayleigh scattering, where strictly no net energy exchange between molecule and radiation takes place, initial and final state are equal, whereas initial and final states are different for Raman scattering. The transition moment relevant for Rayleigh and Raman scattering in the arrangement depicted in figure 4.3 is expressed by

$$\Phi(\alpha) = \langle f | \alpha_{zz} | i \rangle^2 + \langle f | \alpha_{yz} | i \rangle^2 \quad , \tag{28}$$

α_{zz} and α_{yz} are either the tensor elements of the polarizablity $\boldsymbol{\alpha}_0$ (Rayleigh) or rather the derivative of the polarizability with respect to the normal coordinate of the intermolecular motion $\boldsymbol{\alpha}'_k$ (Raman). The two components of the induced dipole moment for the transition $f \leftarrow i$ can be accordingly expressed by

$$\begin{aligned} p^{(1)}_{f\leftarrow i,y} &= \langle f | \alpha_{yz} | i \rangle E_{0,z} \\ p^{(1)}_{f\leftarrow i,z} &= \langle f | \alpha_{zz} | i \rangle E_{0,z} \end{aligned} \tag{29}$$

Following the laws of electrodynamics, the power of radiation emitted by an oscillating dipole with oscillation frequency ω can be expressed with $T_{\perp,\parallel}$ being the polarization-dependent transmissivity of the detection optics by:

$$I\left(\theta, T_{\perp,\parallel}\right)_{f\leftarrow i} = T_{\perp,\parallel} \frac{c}{32\varepsilon_0 \pi^2} \omega^4 \left(p^{(1)}_{f\leftarrow i}\right)^2 \sin^2\theta \quad . \tag{30}$$

The angle θ between exciting radiation and detection direction in the specific arrangement considered here is $\pi/2$. Consequently $\sin^2\theta = 1$. For Rayleigh scattering the oscillation frequency is given by $\omega = \omega_0$. For Stokes and anti-Stokes Raman scattering the frequencies are

correspondingly $\omega = \omega_0 \mp \omega_k$. Exploiting equation (29), the polarization-dependent scattering intensities read

$$
\begin{aligned}
I_{\perp}\left(\theta, T_{\perp}\right)_{f \leftarrow i} &= T_{\perp} \frac{c}{32\varepsilon_0 \pi^2} \omega^4 \left\langle f \left| \alpha_{zz} \right| i \right\rangle^2 \left| E_{0,z} \right|^2 \\
I_{\parallel}\left(\theta, T_{\square}\right)_{f \leftarrow i} &= T_{\parallel} \frac{c}{32\varepsilon_0 \pi^2} \omega^4 \left\langle f \left| \alpha_{yz} \right| i \right\rangle^2 \left| E_{0,z} \right|^2
\end{aligned}
\tag{31}
$$

Assuming that $T_{\perp} = T_{\parallel} = 1$, the total intensity from a single spatially-fixed molecule is given by the sum of both polarization components:

$$
I\left(\theta\right)_{f \leftarrow i} = \frac{c}{32\varepsilon_0 \pi^2} \omega^4 \left(\left\langle f \left| \alpha_{zz} \right| i \right\rangle^2 + \left\langle f \left| \alpha_{yz} \right| i \right\rangle^2 \right) \left| E_{0,z} \right|^2 \tag{32}
$$

Table 4.2
Space-averaged components of the transition moments for Rayleigh and ro-vibronic Raman scattering. The factor K_{v} is given by either $K_{\mathrm{v}} = (\mathrm{v}+1)\frac{h}{4\pi(\omega_0 - \omega_k)}$ for Stokes transitions or by $K_{\mathrm{v}} = \mathrm{v}\frac{h}{4\pi(\omega_0 + \omega_k)}$ for anti-Stokes transitions with v being the vibrational quantum number. The Placzek-Teller coefficients b_{J_f, J_i} are listed in [110].

Process	Branch	Δv	ΔJ	$\overline{\left\langle f \left\| \alpha_{zz} \right\| i \right\rangle^2} + \overline{\left\langle f \left\| \alpha_{yz} \right\| i \right\rangle^2}$
Rayleigh		0	0	$(a)_0^2 + \frac{7}{45} b_{J,J} (\gamma)_0^2$
Rot.-vib.-Raman	O	±1	-2	$K_v \frac{7}{45} b_{J-2,J} (\gamma')_0^2$
Rot.-vib.-Raman	Q	±1	0	$K_v \left((a')_0^2 + \frac{7}{45} b_{J,J} (\gamma')_0^2 \right)$
Rot.-vib.-Raman	S	±1	+2	$K_v \frac{7}{45} b_{J,J+2} (\gamma')_0^2$

For an ensemble consisting of $N_{c,tot}$ molecules of species *C* with $N_{\mathrm{v},J}$ being in a specific initial quantum state $|i\rangle = |\mathrm{v}, J\rangle$, the Boltzmann fraction is relating these two numbers by $f_{\mathrm{v},J}(T) = N_{\mathrm{v},J} / N_{c,tot}$ with T being the temperature. Because molecule movements in a low density gas are random, in an actual measurement space-averaged transition moments (subsequently denoted by overbars) need to be considered. The space-averages of the squares of the transition moments may be expressed in terms of the invariants of the derived polarizability

tensor components associated with the *k*-th normal mode. Commonly, space-invariants are expressed by $(a)_0$ and $(\gamma)_0$ for Rayleigh scattering, and by $(a')_0$ respective $(\gamma')_0$ for Raman scattering. Table 4.2 summarizes space-averaged components of the transition moments for Rayleigh and Raman scattering.

The Rayleigh/Raman scattering intensity then reads:

$$(33) \qquad I(\theta)_{f\leftarrow i} = \frac{c}{32\varepsilon_0\pi^2}\omega^4\left(\overline{\langle f|\alpha_{zz}|i\rangle^2} + \overline{\langle f|\alpha_{yz}|i\rangle^2}\right)\left|E_{0,z}\right|^2 f_{\mathrm{v},J}(T)\,N_{c,tot}$$

This expression can be reformulated by introducing a temperature-dependent differential cross-section

$$(34) \qquad \frac{\partial\sigma}{\partial\Omega}(T) = \frac{c}{32\varepsilon_0\pi^2}\omega^4\left(\overline{\langle f|\alpha_{zz}|i\rangle^2} + \overline{\langle f|\alpha_{yz}|i\rangle^2}\right) f_{\mathrm{v},J}(T)\ .$$

An actually measured Rayleigh or Raman signal is due to the number of photons S collected from a specific probe volume. By using equations (33) and (34) S is given by

$$(35) \qquad S_{c,f\leftarrow i}(\theta) = \frac{I(\theta)}{\hbar\omega} = \frac{1}{\hbar\omega}\frac{\partial\sigma}{\partial\Omega}\left|E_{0,z}\right|^2 N_{c,tot}\Omega\eta\ .$$

Herein, Ω is the solid angle of the collection optics and η is the overall detection efficiency (transmissivity of optics, quantum efficiency of detector). Note, that both factors should be derived from calibration measurements.

For a reliable simulation of Raman signals it is imperative to calculate the transition frequency $\omega = \omega_0 \mp \omega_k$ correctly. In general anharmonic corrections and deviations from the rigid rotator assumption need to be applied. Depending on the molecule under consideration this can already be problematic especially for other than diatomic molecules [111].

The Boltzmann fraction $f_{\mathrm{v},J}(T)$ can be calculated as function of the term values E_i (in wavenumbers) and degeneracy factors g_i by

$$(36) \qquad f_{\mathrm{v},J}(T) = \frac{g_i \exp\left(\frac{hcE_i(\mathrm{v},J)}{kT}\right)}{\sum_i g_i \exp\left(\frac{hcE_i(\mathrm{v},J)}{kT}\right)} = \frac{g_i}{Z(T)}\exp\left(\frac{hcE_i(\mathrm{v},J)}{kT}\right) = \frac{N_i}{N}$$

with $Z(T)$ being the temperature-dependent partition function and N the total number density. This implies the use of correct term values and once again the need for anharmonic and non-rigidity corrections. The space-averaged transition moments so far have been discussed in the framework of the electrical harmonic approximation (compare equation (25)). For high temperatures, such as in chemically-reacting flows, electrical anharmonicities (higher orders in equation (25)) need to be considered as well.

The temperature dependence of the measured Rayleigh and Raman intensities in equation (35) is given through the Boltzmann fraction $f_{\mathrm{v},J}(T)$ and the number density $N_{c,tot}(T,p)$. The latter one can be expressed in terms of the total molar gas number density *n*, the mole fraction x_c of species *C* and the Avogadro number N_A: $N_{c,tot} = x_c n N_A$. By assuming the validity of the ideal

gas law, the total number density $N = nN_A$ is a function of pressure p and temperature T. In the following sections it is discussed how these temperature dependencies can be exploited for thermometry. Notice, that in contrast to thermometry based on fluorescence (section 4.1.1), Rayleigh and Raman scattering processes are not disturbed by inter-molecular collisions.

4.2.1 Thermometry by Rayleigh scattering

Rayleigh-scattered light is in phase with the incident radiation. This can cause interferences by scattering from different molecules. However, this is prevented in gases considered here due to the random motion of the molecules. Furthermore, in Rayleigh scattering all chemical species contained in a finite sized probe volume give rise to a measured signal. Therefore, contributions of each chemical species C as expressed in equation (35) sum up to a total Rayleigh-scattering signal resulting in

$$S_{Ray}(\theta) = \frac{1}{\hbar\omega}\left(\frac{\partial\sigma}{\partial\Omega}\right)_{Ray} \left|E_{0,z}\right|^2 N\Omega\eta \ . \tag{37}$$

Here, an effective Rayleigh cross-section $\left(\partial\sigma/\partial\Omega\right)_{Ray} = \sum_c x_c \left(\partial\sigma/\partial\Omega\right)_{c,Ray}$ is used. In general, $\left(\partial\sigma/\partial\Omega\right)_{c,Ray}$ is approximately independent on temperature. Then, as obvious from equation (37), Rayleigh scattering can be used to assess total number densities N if the gas composition is known. Therefore, for spatially-homogeneous (measured) pressure, temperature can be derived via the ideal gas law.

Rayleigh thermometry is a technique relying in many practical applications on single laser shots [112]. Thereby a high temporal resolution much shorter than typical Kolmogorov time-scales in turbulent (reactive) flows can be accessed. With comparatively low experimental effort Rayleigh scattering can be applied in an imaging setup. A sketch of a typical setup is shown in figure 4.4.

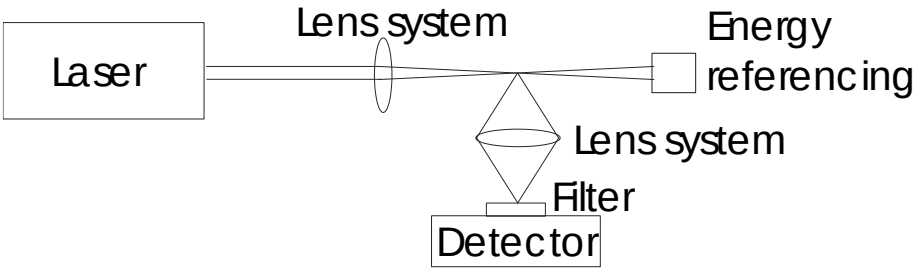

Figure 4.4
Schematic of the experimental set-up for Rayleigh scattering.

Rayleigh thermometry has therefore been widely applied on turbulent systems, e.g. in turbulent flames [113, 114] or internal combustion engines [115]. Inferring number densities from scattering data, however, requires information about local effective Rayleigh cross-sections and therefore the local gas composition which is usually unavailable in inhomogeneously mixed or reactive systems [116]. In combustion, special fuel blends have been proposed that provide

similar total cross-sections for unburned and burned gases [113], enabling Rayleigh thermometry even in turbulent combustion systems. Alternatively, Raman scattering can be applied simultaneously with Rayleigh scattering to measure the gas composition. This is, however, limited to spatially one dimension [117, 118].

Rayleigh thermometry suffers from problems with background scattering (e.g. off walls or windows); in the presence of particles like in sooting flames, this technique is therefore not feasible at all. Here, a filtered Rayleigh scattering technique has been applied [112, 26]. This approach makes use of the fact that gas-phase molecules have a wider Doppler width due to their thermal motion (~0.1 – 0.3cm^{-1}) than surfaces (walls, particles, droplets). If a single longitudinal mode laser is used, the signal of surface-scattered light can be rejected by narrow-band (< 0.05cm^{-1}) filters (usually molecular filters like iodine or atomic vapour filters like mercury contained in quartz cells). Increasing temperature is causing a larger Doppler width of the Rayleigh-scattered light originating from the gas phase. This line broadening causes an increasing signal via bypassing the narrow-band filter. The principle of filtered Rayleigh scattering thermometry is shown in figure 4.5. Exact control of laser wavelength, spectral profile, absorption profile of the molecular or atomic line filter, and knowledge of line broadening is required.

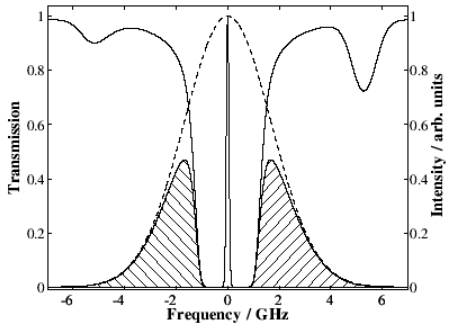

Figure 4.5
Molecular line shape of Rayleigh-scattered light at elevated temperature (dashed line), transmission profile of atomic vapour such as mercury (solid line) and spectral laser emission (peak at 0GHz). The spectral overlap of atomic notch and Doppler-broadened Rayleigh profiles result into the spectral wings transmitted to the detector (hatched area). Reproduction from [112].

4.2.2 Thermometry and multi-scalar measurements by Raman scattering

A sketch of a Raman spectrometer is shown in figure 4.6.

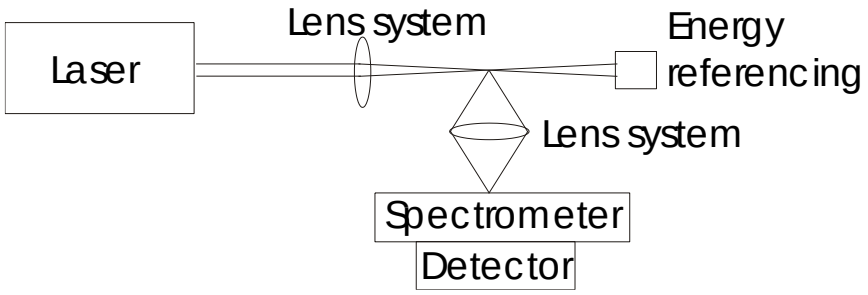

Figure 4.6
Schematic of the experimental setup for Raman scattering.

Each chemical species exhibits a red or blue-shift (Stokes and anti-Stokes lines) according to the energy difference $\hbar\omega_k$ between initial and final states involved to the process. Table 4.3 summarizes averaged relative normalised differential Raman cross-sections for Q-branches ($\left(\partial\sigma/\partial\Omega\right)_Q(T=300\text{K})$) and Raman frequency-shifts of combustion-related molecules.

Table 4.3
Raman shifts and averaged normalised differential Raman cross-sections for the Q-branch of some combustion-related molecules at room temperature. The absolute Raman cross-section of the Q-branch of nitrogen is $(5.05\pm0.1)\times10^{-48}\times\left(\omega_0/2\pi c-2331\text{cm}^{-1}\right)$ cm^6/sr . Data are taken from [119].

Molecule	**Raman shift $\omega_k/2\pi c$ [cm^{-1}]**	$\left(\partial\sigma/\partial\Omega\right)_Q(T=300\text{K})$
CO_2 (ν_2)	1285.0	0.75
CO_2 (ν_1)	1388.0	1.13
O_2	1555.0	1.04
CO	2143.0	0.93
N_2	2331.0	1.0
CH_4 (ν_1)	2914.0	8.55
CH_4 (ν_2)	3017.0	5.7
H_2O	3652.0	3.51
H_2	4155.2	3.86

Averaged differential Raman cross-sections scale non-linearly with temperature. For molecular hydrogen figure 4.7 shows the theoretical temperature dependence of the differential Q-branch cross-sections normalized to its value at 300K. Depending on the theoretical approach [111], the temperature dependency especially at temperatures exceeding 1000K can differ by a few percent dependent on the molecule.

In contrast to pure Rayleigh scattering, signals from different chemical species *C* show species-specific Raman frequency-shifts and have to be hence spectrally dispersed before detection. The advantage of Raman thermometry is that dispersed Raman spectra contain all necessary information to deduce gas temperature. This is in contrast to Rayleigh thermometry or laser-induced fluorescence (LIF) schemes, where additional information on gas composition and collisional energy transfer pathways in case of LIF is required for a thorough analysis. Therefore, despite of the rather low scattering cross-sections that need to be overcome by high excitation laser photon fluxes and low-noise detection components, Raman thermometry can be an important alternative if this additional information is not provided. Notice, that in addition to temperature, the gas composition can be evaluated as well (→ simultaneous Raman/Rayleigh scattering [62, 111, 120–122, 117, 120, 111]). By this, Raman scattering is the only multi-scalar diagnostic based on a single excitation frequency.

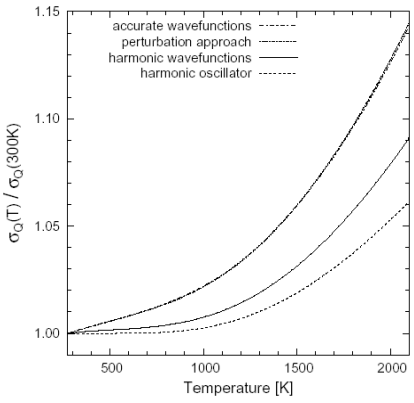

Figure 4.7
Relative differential cross-sections of molecular hydrogen as function of temperature. Dependent on the theoretical description for temperatures exceeding 1000K the differences between the calculated cross-sections differ by a few percent.

Local temperatures can be extracted from Raman spectra in different ways. For the case of high spectral dispersion single rotational or ro-vibronic lines might be resolved. Raman spectra can be simulated and fitted to the measured spectra [111, 123]. However, in addition to equation (35), line widths must be considered as well. Raman lines might be pressure- and Doppler-broadened. In addition, limited spectral resolution of the spectrometer broadens the measured lines as well. Therefore, each allowed transition needs to be convoluted with an effective line shape and a spectrum is received from superposition of all relevant allowed transitions. Figure 4.8 shows schematically ro-vibronic N_2-Raman bands at various temperatures. In this example the effective line width is broad compared to the spetrcal separation of adjacent transitions. This leads to an overlap of ro-vibronic Raman lines resulting in a single Raman band up to approximately 400K and additional hot-bands at higher temperatures than 500K. It is obvious, that Raman bands and spectral intensities are strongly temperature dependent.

A second way to extract temperatures from Raman scattering is to determine number densities of each chemical component present in the probe volume. For this purpose it is assumed that the gas composition is comprised of only Raman-active species at sufficiently high concentrations to allow accurate detection and Stokes-shifts into spectral regions that are actually monitored. Then the number density of all chemical components can be added up to result in the overall number density in the probe volume under consideration. With the validity of the ideal gas law assumed, as in Rayleigh thermometry, the total number density in connection with the (measured) pressure can be used to determine a local temperature.

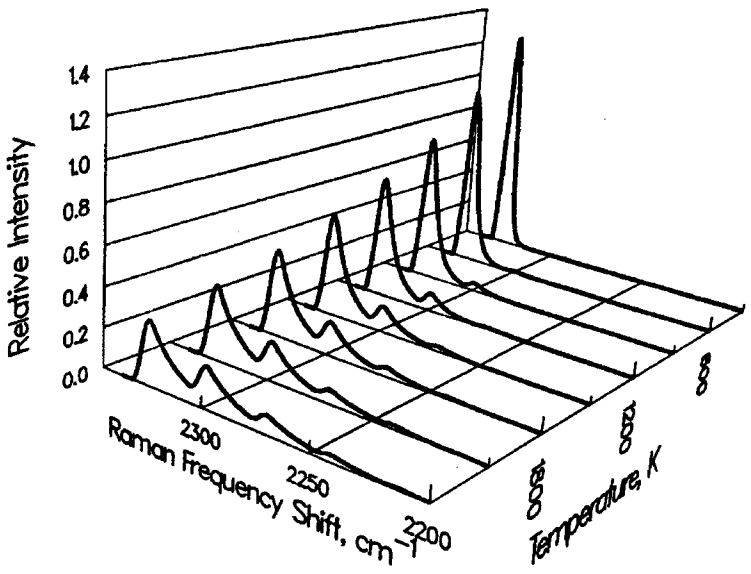

Figure 4.8
Relative Raman scattering intensities of molecular nitrogen for different temperatures [91].

The third way to determine temperatures from Raman scattering is to perform measurements of both Stokes and anti-Stokes shifted Raman lines (or bands). In the limit of the harmonic approximation and identical degeneracy factors for both quantum states, the measured ratio of Stokes and anti-Stokes lines is given by:

$$\frac{S_{Stokes}}{S_{anti-Stokes}} = \left(\frac{\omega_0 - \omega_k}{\omega_0 + \omega_k} \right)^3 \exp\left(\frac{\hbar c \omega_k}{kT} \right) \tag{38}$$

The intensity ratio has to be a value which can be measured with sufficient signal-to-noise ratio. This requires sufficiently high population in the excited state from which anti-Stokes Raman scattering takes place. Near room temperature Raman lines shifted in the range from 0 to 500cm^{-1} are useful, whereas for around 1000K spectral shifts up to 2000cm^{-1} should be used.

4.2.3 Practical considerations

In general Rayleigh scattering can be applied at single points (0D), along lines (1D) or in two-dimensional planes (2D). By combining at least two parallel orientated 2D-planes, quasi-three-dimensional applications are possible as well. As depicted in figure 4.4, for Rayleigh thermometry an exciting light source (most commonly a laser), a detector and some optical components such as a band-pass filter in front of the detector and lens systems are needed. In case of 0D- and 1D-applications the laser might be focussed simply by a long focal length spherical lens, in case of 2D-applications the laser is formed into a light sheet by appropriate spherical and cylindrical lenses.

Raman scattering experiments can be performed also in 0D, 1D or 2D. 2D-applications, however, are only feasible for flows containing just a few main components, as each component needs an individual detector equipped with a suitable band-pass filter. For the general case,

where many components occur in the flow such as hydrocarbon-air flames, Raman scattering can be applied in practice only up to 1D. In this case along the probe volume Raman bands stemming from the various chemical components are spectrally dispersed before detection (cf. figure 4.6).

In the following some practical aspects on hardware components and issues related to calibration are discussed. However, this paragraph is far from complete and for more detailed information the reader is referred to the literature and text books such as [121, 111].

Laser system

Many fluid mechanical problems are characterized by turbulence. Hence, exposure times of single temperature measurements should be sufficiently short to monitor frozen states of the turbulent flow under investigation. The shortest time scales in turbulent flows are charac-terized by Kolmogorov scales [67]. Taking an industrial-type nozzle for combustion applications as an example (compare figure 2.2, ref [8]), Kolmogorov time-scales can be estimated assuming homogeneous isotropic turbulence. Typical Kolmogorov time-scales are at the order of few microseconds. Consequently, single temperature measurements should resolve at least one microsecond. In practice, this requirement presupposes the usage of pulsed lasers in the submicrosecond regime. Due to their high photon fluxes, reliability and ease of operation solid-state, quality-switched lasers are increasingly used for Rayleigh or Raman-thermometry replacing flash-lamp-pumped dye lasers [124] or excimer lasers [125]. Among the class of solid-state lasers, the Nd:YAG-laser currently is the working horse in many laboratories. Typical specifications are pulse widths of 10ns, repetition rates ranging from 10 to 100Hz and pulse energies in the fundamental at 1064nm up to 2.5J. The frequency conversion up to the fourth harmonic at 266nm is easily possible due to the high peak intensities. Generally spoken, highest pulse energies as possible are favoured but in practice optical break down phenomena set a limit. Optical break down occurs by absorption processes most often at remaining dust particles that exist as trace components in many flows. During a break down high light intensities are emitted that can damage photo detectors such as image intensifiers or CCD devices. To lower the probability of optical break down, pulse stretchers are used to lower the intensity but keeping a high pulse energy [121]. Another option might be new developments in laser technology allowing for programmable pulse length. However, more experience must be gained with regard to long-term reliability and specifications such as beam profile properties of such systems before final conclusions can be drawn.

The choice of the excitation wavelength (laser emission wavelength) is depending on the specific application. In general, the Rayleigh and Raman cross-sections increase non-linearly with decreasing excitation wavelength (compare equation (34)). However, laser-induced fluorescence interfering especially with Raman scattering should be avoided furthermost [126]. As electronic resonances of many molecules are located in the ultraviolet region [127, 127], the higher cross-sections in the UV can be exploited only for flows consisting of specific components non-resonant with the excitation wavelength. In combustion-related research, UV-excitation was exploited for the investigation of hydrogen-air flames [128]. For hydrocarbon-air flames, partially oxygenised or polycyclic hydrocarbons might be formed during the oxidation process giving rise to signals interfering with Raman bands [126]. Therefore and on the expense of lessened cross-sections, an excitation laser wavelength in the visible spectral region needs to be used. This loss can be partly compensated by higher laser pulse energies and higher detector quantum efficiencies in the visible spectral region.

Detection

Prior to detection, signal radiation is dispersed in case of Raman scattering using most commonly a Czerny-Turner type spectrometer or filtered by a narrow bandwidth interference filter to reject spurious light in case of Rayleigh scattering.

Due to low Raman cross-sections, signal intensities especially in Raman thermometry are rather low. For this reason a low-noise detector, large solid angle of detection optics and high quantum efficiency are mandatory. For 0D-applications photomultiplier tubes (PMT) have been commonly used. At the exit plane of a suitable spectrometer for each chemical component at least one PMT monitors individual species concentrations. For 1D-Raman applications a two-dimensional array detector is needed (space and wavelength directions). For this reason CCD-detectors are commonly used. The lowest noise level combined with highest quantum efficiency is delivered currently by backside-illuminated CCD-array detectors. If a high temporal resolution is required and some background luminosity is present such as in flames, an additional fast shutter assembly is needed. As exemplified in [129], a fast mechanical shutter with exposure times at the order of 10 µs or shorter [130] can be build from rotating slit wheels.

In case of Rayleigh scattering, the requirements of low-noise and highest quantum efficiency detectors are less stringent in comparison to Raman scattering because of the much higher cross-sections. For 0D applications PMTs are the best solution whereas for 1D- or 2D-applications intensified CCD-array detectors (ICCD) are best suited. The intensifier allows short gating of the detector suppressing very efficiently spurious light. The filter in front of the detector might be either an interference band-pass or a notch (cf. figure 4.5) in case of filtered Rayleigh scattering.

Calibration

Spectroscopic methods are in general not self-calibrated. Several factors such as probe volume size, solid angle of detection, transmission through optical elements or detector quantum efficiency depend very specifically on the individual experimental setup and may in part vary with different wavelengths. For this reason calibration measurements have to be performed. Taking Rayleigh thermometry as an example, a measured temperature can be expressed relative to a calibration condition on the base of equation (37) and the ideal gas law by

$$T = \frac{S_{Ray}}{S_{Ray,ref}} \times \frac{\left(\frac{\partial\sigma}{\partial\Omega}\right)_{Ray,ref}}{\left(\frac{\partial\sigma}{\partial\Omega}\right)_{Ray}} \times \frac{\left|E_{0,z,ref}\right|^2}{\left|E_{0,z}\right|^2} \times \frac{p_{ref}}{p} \times T_{ref} \tag{39}$$

Resolution

The spatial resolution achieved in any optical diagnostic method depends on the laser beam diameter and imaging quality of the optical components imaging the probe volume onto the detector. Beam diameters can be reduced using rather short focal length focussing lenses and operating the laser in its TEM_{00}-mode. Depending on the specific configuration, spot sizes of typically 200µm or less can be easily realized. Using well-designed lenses, imaging of 50 µm spots on the detection side is easily possible as well. In typical experimental arrangements of single-shot Rayleigh thermometry, a probe volume size of ~$(100\mu m)^3$ can be therefore routinely

achieved. This might be not true for Raman thermometry in general, where optical break down often limits the laser spot diameter to values above 200µm.

In contrast to the very high temporal resolution (submicrosecond regime using quality-switched laser pulses) which is often below Kolmogorov time-scales of many practical turbulent flows, the smallest scalar structures of these flows given by Batchelor [5] length scales might not be resolved spatially. The situation is even worse for fluids with Schmidt-numbers much larger than 1. This limited spatial resolution, although much better than typical intrusive probe techniques like thermocouples, can act similar to a low-pass filter and might influence the measurement of local temperatures and, even worse, local temperature gradients in case of 1D- or 2D-applications.

4.3 Coherent anti-Stokes Raman scattering

Coherent Anti-Stokes Raman scattering (CARS) [91] belongs to the class of nonlinear, coherent processes. A typical experimental sketch is presented in figure 4.9.

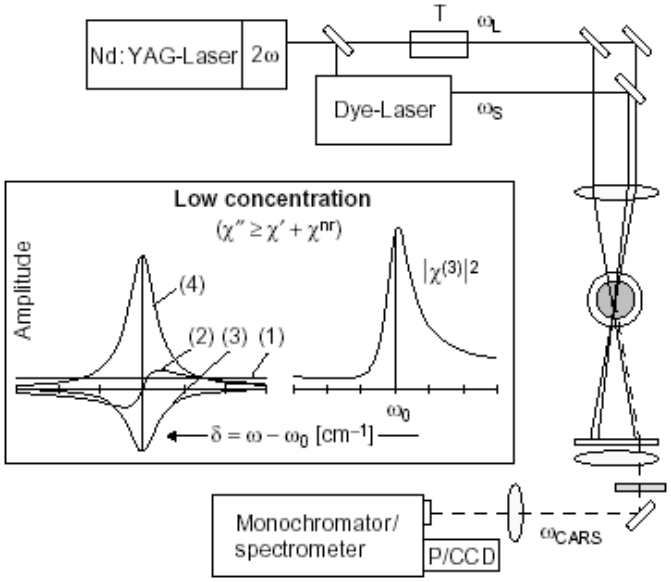

Figure 4.9
Experimental arrangement of a CARS-spectrometer. The dye laser can be either a narrow band laser for scanning CARS or a broadband laser for single-shot CARS-thermometry. In case of scanning CARS a photomultiplier tube is used at the exit plane of the monochromator, in case of the broadband dye laser a CCD-camera is used in connection with a spectrometer. The insets show a typical CARS-lineshape function for an isolated transition at low concentration of the species under consideration. It is composed of the constant non-resonant background (1), the interference contributions with χ_{nr} (2), (3) and the Lorentzian-shaped resonant part (4) of the third order susceptibility $\chi^{(3)}$.

In particular, CARS is advantageous for temperature measurements under difficult combustion conditions. The signals of coherent processes are generally strong and emitted in a laser-like beam, but the signal generation depends nonlinearly on the concentration of the probe molecules and is also intrinsically a nonlinear function of the exciting laser intensities. CARS therefore

imposes stronger demands on the laser source such as stability, beam quality and mode structure, and, since two laser beams are involved, on alignment. For thermometry in air-breathing flames, N_2 is used preferentially as probe molecule because of its large concentration and the complete spectroscopic database. The CARS-technique allows only point measurements; simultaneous thermometry of an extended line or plane (as in LIF or Raman) is not possible. However, due to its high accuracy, CARS is often used to define a temperature standard for the investigation and validation of other thermometry methods.

Among the coherent Raman processes CARS is almost being used exclusively in practical combustion diagnostics. In CARS-experiments one fixed frequency (pump) and one broadband (Stokes) laser beam in the visible with their frequency difference equal to a Raman allowed transition are aligned and focused into the sample to create, in a four wave mixing process, a coherent beam at the anti-Stokes frequency ($2\omega_1 - \omega_2$), well separated spatially and spectrally from all incoming beams. The CARS-radiation then is dispersed in a spectrometer and detected with a CCD-camera (figure 4.9). In the non-saturated regime the CARS-intensity at frequency $\omega_{CARS} = \omega_3 = 2\omega_1 - \omega_2$ for an isolated transition [91] in equation (40)

$$I_{CARS} = I_3 = \frac{\omega_3^2}{n_1^2 n_2 n_3 c^4 \varepsilon_0^2} (l\Delta N_j)^2 I_1^2 I_2 \left|\chi_{CARS}^{(3)}\right|^2, \tag{40}$$

with

$$\chi_{CARS}^{(3)} = K_j \frac{\Gamma_j}{2\Delta\omega_j - i\Gamma_j} + \chi_{nr}; \qquad K_j = \frac{\omega_3^2 (4\pi)^2 n_1 \varepsilon_0 c^4}{n_2 \hbar \omega_2^4 \Gamma_j} \left(\frac{\partial\sigma}{\partial\Omega}\right)_j; \tag{41}$$

is dependent on higher powers of the pump (1) and Stokes (2) laser intensities as well as on the square of the number density difference ΔN_j between lower and upper Raman level of the *j*-th transition. Equation (40) is written for perfect phase matching of the beams, i.e. when $\vec{k}_{sig} = \sum \vec{k}_j$ holds and the corresponding signal intensity is maximized. Γ_j is the total broadening rate of the transition and $\Delta\omega_j = \omega_{\square} - \omega_2 - \omega_j$ the detuning from the Raman transition frequency. The spectral structure of the CARS-signature over thermally populated levels is contained in the expression of the third-order susceptibility $\chi^{(3)}$ (equation (41)), which, therefore, is an accurate measure of the gas temperature. This is exploited for thermometry applications through least squares fitting of computer generated to experimental CARS-spectral shapes, if proper account is taken for the various physical effects contributing to the CARS-spectral signature, such as coherences in the CARS-pump beams [131], saturation and collisional effects [132] or the noise characteristics when broadband Stokes lasers are employed [133].

In their pioneering work Taran et al. [134] recorded the first CARS-spectra of molecular hydrogen in an atmospheric pressure Bunsen flame using a narrowband scanning dye laser as a Stokes beam. Eckbreth et al. [135] introduced single pulse temperature and species measurements by using a broadband Stokes dye laser which covers Raman shifts of the whole investigated spectral branch. Species concentrations can be determined from either the integrated CARS-line intensity or its spectral shape [136] through calibration measurements and spectral modeling, respectively. For low concentrations the (real) nonresonant contribution χ_{nr} in the susceptibility expression (41) is significant and limits the detection sensitivity due to interference with the resonant contribution. To illustrate this behaviour, the real and imaginary susceptibility components determining the CARS-line shape are depicted in the inset of figure 4.9 for an assumed low concentration of the resonant species in a nonresonant buffer gas.

Due to the $\Delta v = 1$, $\Delta J = 0$ selection rules in vibrational Q-branch Raman spectra, individual lines are closely spaced and one needs different laser dyes to cover the whole Stokes wavelengths for detecting different species. Alternatively, Aldén et al. and Seeger et al. excited the pure rotational transitions to enable temperature and species concentration measurements made by the single shot broadband rotational-CARS (RCARS)-technique [137]. The DCM-laser dye covers most of the rotational Stokes shift even for spectra at 1000K or higher and multiple species can be detected within the same spectral range as well. Since both, first pump- and Stokes beam in the respective level scheme originate from the same Stokes laser, additional spectral noise averaging takes place which makes this technique less susceptible to mode noise in the laser sources. Problems in this technique are stray light from the pump beam as well as lower temperature measurement accuracy at high temperatures.

Application of N_2-CARS-thermometry was shortly highlighted in section 2.5 measuring wall-normal temperature distributions.

4.4 Example for scalar field measurement: 1D-Raman/Rayleigh applied to turbulent opposed jet flames

Turbulent, non-premixed flames that are stabilized in stagnation point geometries, have been studied to gain insights into flame stabilization and turbulent mixing. Partially-premixed and non-premixed turbulent opposed jet configurations have been investigated experimentally and theoretically as summarized in [122, 117]. Detailed experimental information on these flames allows a critical assessment of models for turbulent combustion, as for example mixing models.

From a computational point of view, the opposed jet configuration offers significant simplifications since the flow field can be represented reasonably well by a one-dimensional (1D) formulation [138]. Especially for the probability density function (PDF) methods, the 1D-simplification reduces the stochastic errors by running the simulations with large numbers of Monte Carlo (MC) particles, as demonstrated in a previous study of isothermal turbulent opposed flows [139]. However, model development was limited due to the lack of an appropriate experimental data set containing spatially and temporally resolved results on scalars as well as on velocities. To close this gap and to provide data suitable for model validation, temperatures, major species concentrations, scalar dissipation rates [117], spatial OH-distributions [140], axial and radial velocity components between the nozzles [62] and even inside the nozzles [141] have been measured using various diagnostics such as single-shot 1D-Raman/Rayleigh scattering, laser-induced fluorescence, PIV/PTV/OH-PLIF, high-speed PIV and 2D-LDV.

The MC-PDF-model used in [139] has been developed in several areas including the incorporation of a modelled equation for the scalar dissipation rate and an adaptive particle distribution scheme. Mixing models have been investigated in detail in partially-premixed jet-flames [24] but these models were hardly validated in other flames with simple flow fields. The partially-premixed turbulent opposed jet flame is distinctly different from commonly studied jet flames and exhibits a relatively simple flow field. However, a comparison of MC-PDF-simulations with spatially and temporally resolved experimental data, particular on the scalars, have been not conducted so far. This section examines the performance of mixing models in a turbulent opposed jet. Thus, an assessment of the models for a simple flow different from jet flames is provided. Note that for validation purposes the focus here is on temperature, mole fractions of main species and the flow field, whereas in [4] the focus is on scalar dissipation rates.

Model formulation and numerical method

As a good approximation the opposed jet flame is described by the 1D-formulation [138] using the Reynolds stress model by Launder et al. [142] for modelling the turbulent flow field. The scalar dissipation rate is computed directly by its modelled equation [143]. With the mixture fraction variance, the mixing frequency is determined without making any assumption about the time scale ratio between turbulence and mixing. Monte Carlo simulation is conducted for solving the joint scalar PDF with a non-uniform distribution of particles per grid point. This distribution is adapted according to the mean temperature profile so that more particles are placed in the reaction zone [144]. The resulting non-uniform distribution contains a maximum of 1600 particles per grid point near the stagnation plane and 400 particles near the jet nozzle exits. As such, the stochastic errors can be reduced without a significant increase in com-puting time.

The 12-step CH_4-air reduced mechanism with 16 species developed by Sung et al.[145] is used with ISAT [146] to further reduce computing time. Simulations are carried out with several mixing models including modified Curl, IEM, EMST [147], and a 1D-flamelet like mixing model [144]. The 1D-flamelet like mixing model considers the particles to undergo a 1D-diffusion process resembling the transient flamelet model. Monte Carlo particles in each grid are arranged in a 1D-domain according to their respective mixture fraction values. In the 1D-domain, the particles are placed with equal distance and the following diffusion equation is solved for each scalar

$$\frac{\partial \phi_i}{\partial t} = D_M \frac{\partial^2 \phi_i}{\partial x^2}, \quad i = 1, K \tag{42}$$

where D_M is the model diffusion coefficient and K is the total number of scalars. During the simulation, D_M/L^2 is set proportional to the mixing frequency, where L is the size of the 1D-domain. The proportionality is selected to yield the correct level of mixture fraction fluctuations.

4.4.1 Results and discussion

Simulations with the modified Curl and the IEM-mixing models lead to flame extinction even after the bulk strain rate is reduced to one fifth. Similar findings for the extinction behaviour of the modified Curl and the IEM-model are reported by Subramaniam and Pope [147]. Hence, results will be presented only from two mixing models, namely the 1D-flamelet like and the EMST-model. An analysis of simulation results indicates that in the flame zone, the present turbulent opposed jet flame falls into the flamelet regime based on the criterion by Bilger [148]. Mixing models, such as the modified Curl and IEM-models, do not have the localness property and fail to predict burning flames. In contrast, the EMST-model was developed particularly to include the localness leading to results consistent with those from a flamelet like model.

Axial profiles

Figure 4.10 presents a comparison of experimental and numerical results of velocities.

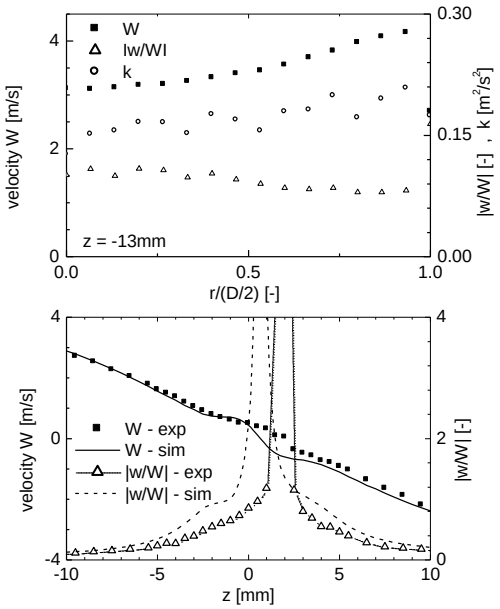

Figure 4.10
Top: Radial profiles of mean axial velocity *W*, normalized *rms* of axial velocity *w/W* and turbulent kinetic energy k measured by 2D-LDV at z = -13mm (fuel jet). Bottom: Comparison of profiles for mean axial velocity and normalized axial velocity fluctuations from experiment and simulation. Position z=0 represents the half distance between the nozzles. Notice, that both mixing models resulted in almost identical axial velocity profiles.

The top of figure 4.10 shows radial profiles of mean and normalized *rms* of axial velocity as well as the turbulent kinetic energy. The velocity exit profile has characteristics in between the plug flow and potential flow conditions. Plug flow characteristics since mean radial velocities (not shown) are close to zero at *z* = -13mm, and potential flow characteristics because the mean axial velocity profile is not constant but has a minimum at the centerline. While a large constant value of approximately 0.1 was found for the normalized fluctuation of the axial velocity around the centerline, a slow increase of turbulent kinetic energy can be observed towards the nozzle edge. The bottom of figure 4.10 shows comparisons of axial profiles for mean and normalized *rms*-values of the axial velocity component. Except in the region around the stagnation point (*W* = 0m/s), numerical results are in reasonable agreement with the measured velocity component. Deviations in the vicinity of the stagnation point are at least in part due to the LDV-measurements featuring a bias, as seeding densities in the fuel and oxidizer flows are not perfectly matched. From a statistical point of view, volume elements from the flow with slightly higher seeding density are over represented, resulting in a bias. Since the skewness of the axial velocity is largest around the stagnation plane, an over-seeding of the fuel stream is likely. However, quantifying this bias as discussed by Korusoy and Whitelaw [149] was not attempted so far. Therefore, for model validation purposes the biased stagnation point should not be overvalued. The normalized fluctuations approaches infinity where the mean velocity tend to zero. As the predicted and measured stagnation points are at slightly different locations, the experimental and numerical results peak at different positions. However, viewing the neighbouring regions, one can see that the measured and predicted values at the tails agree

within a factor of approximately two. Taking into account the uncertainties in both model and measurements, this agreement in the second moments is reasonable.Figure 4.11 shows axial profiles of the mean and variance of mixture fraction. The comparisons focus on a region of $z = \pm 10\text{mm}$ since the whole mixing layer remains within this range. The location of the stoichiometric mixture fraction (f_{stoich} = 0.53) and stagnation plane (f_{stag} = 0.50) are almost identical, the first is found at $z = -0.1\text{mm}$ while the latter is located at $z = +0.1\text{mm}$. Simulations show a good agreement with experimental findings for both the width of the mixing layer and the level of fluctuations. This agreement is independent of the mixing model. The peak value of mixture fraction fluctuation $(f'_{max} = 0.33)$ is well matched by the simulations, although the predicted maxima are slightly shifted towards the oxidizer nozzle.

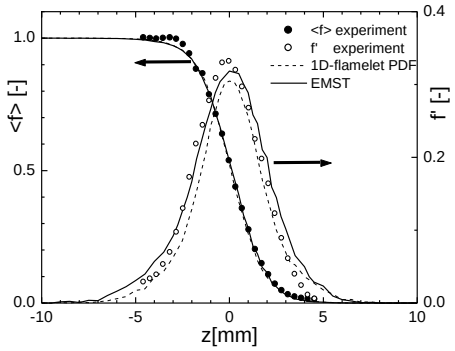

Figure 4.11
Axial profiles of mean and *rms* of mixture fraction.

A comparison of temperature profiles is presented in figure 4.12. The peak value in the mean temperatures is lower more than 600K than the adiabatic flame temperature. This results from flame stretch and the pronounced movement of the turbulent flame, which dithers around the stagnation point. Two-dimensional OH-radical distributions [140] measured by planar laser-induced fluorescence have revealed that the mean reaction zone moves within z = ±1.1mm. Subsequently, the temperature fluctuations corresponding to this flame motion are as high as 600K. The axial profile, as seen in figure 4.12, shows two almost symmetric maxima at the axial positions z = ±2mm. The simulations reproduce the mean temperature profile and the temperature fluctuations well. The peak values of the mean temperature predicted by both EMST and 1D-flamelet like model coincide within 4.5% with experimental data. At the tails of the fluctuation profile simulations indicate a mixing zone 1-2mm wider. The EMST-model predicts the local minimum of temperature fluctuations in the vicinity of the stagnation point particularly well.

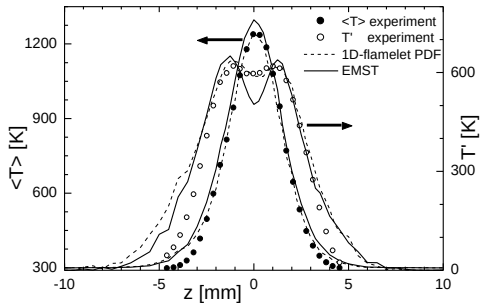

Figure 4.12
Axial profile of mean and *rms* of temperature.

Scatter plots

For a more detailed analysis of model performance, figure 4.13 shows scatter plots of H_2O- and CH_4-mass fraction. As both mixing models behave similar, only the scatter plots for the EMST-model are shown. On the lean side ($f \in [0;0.53]$), a satisfying agreement of experimental and numerical results is found. In the experiment more scatter is observed. This in parts results from experimental error that has been estimated to be 5%, based on calibration measurements in laminar opposed jet flames. At this stage already, turbulent mixing seems to be underestimated in the PDF-simulation independent of the mixing model. At the rich side, however, especially in a mixture fraction range spanning from 0.6 to 0.85, both mixing models overestimate the H_2O-concentration. These deviations clearly are outside the experimental range of confidence and can be explained by inspecting the CH_4-scatter plots. In contrast to experimental results, the turning point in the simulated scatter plots is shifted towards the rich side by approximately $\Delta f \approx 0.15$. As seen in figure 4.13, the simulation results are close to laminar flamelets for low strain ($10s^{-1} < a < 400s^{-1}$). In contrast, the experimental scatter is enclosed by flamelets with strain rates ranging from $a = 200$ to $750s^{-1}$. The experimental conditional averages (top row of figure 4.13) are fairly well represented by a laminar flamelet with $a = 400s^{-1}$ over a wide range of mixture fractions. Evidently, the turbulent flame is influenced by much higher strain than predicted by PDF-modelling. Correspondingly, at the rich side, simulated H_2O-levels exceed experimental values by far.

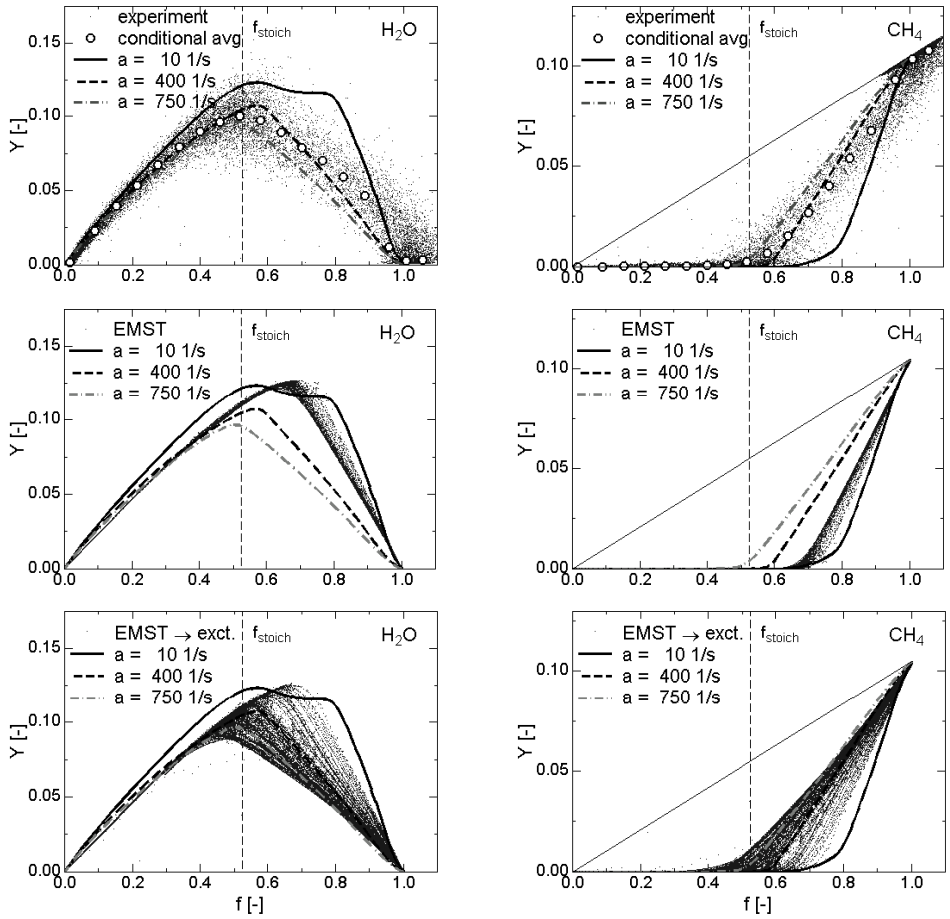

Figure 4.13
Scatter plots of H_2O- (left) and CH_4-mass fraction (right). Top: experiment, middle: EMST-mixing model, bottom: results from EMST-model close to global extinction. Using experimental scatter plots at $f = 1$, measurement accuracy can easily be illustrated. Laminar flamelet calculations of varying strain rate with full transport are included for comparison.

For the EMST-model the bottom row of figure 4.13 shows scatter plots for conditions close to global extinction. Obviously, a much wider range of conditions, especially in the rich part, is accessed in comparison to the experiment. The plot reveals that some low strain rate events might sustain a flame in simulations, while it is already extinguished at that mean bulk strain rate in the experiment. However, the majority of the samples converges against results from laminar flamelet calculations with $a = 750 s^{-1}$, the extinction limit for the laminar flame. Contrary to turbulent jet flames [24], local extinction and reignition events prior to global extinction were found neither for experiment nor for simulations. This is a strong indication that turbulence–chemistry interaction in turbulent opposed jet flames is distinctly different from jet flames.

Mixture fraction PDF-distribution

Detailed PDF-distributions of mixture fraction are compared in figure 4.14 at two locations, namely $z = -0.7\,\mathrm{mm}$ and $z = 0.0\,\mathrm{mm}$. These two locations correspond to a rich flame

(*f ~ 0.71*) and a stoichiometric flame (*f ~ 0.53*), respectively. For the rich flame, the predicted shapes by both models are similarly exhibiting a gradual decrease in the PDF from the fuel side and an almost uniform distribution once the mixture fraction drops below 0.8. The measurements reveal a similar initial decrease in the PDF from the fuel side but have more variations for mixture fractions below f = 0.9, resembling a bell shape with its peak at *f ~ 0.53*. For the stoichiometric flame, model predictions show an inversed bell shape while experimental data resemble again a bell shape around *f ~ 0.5* with two distinct peaks for pure fuel and oxidizer. These experimental data reveal the strong intermittent nature between fuel and oxidizer and the rapid mixing between them. Compared to experimental data, simulation results show a much slower mixing process with less intermittency.

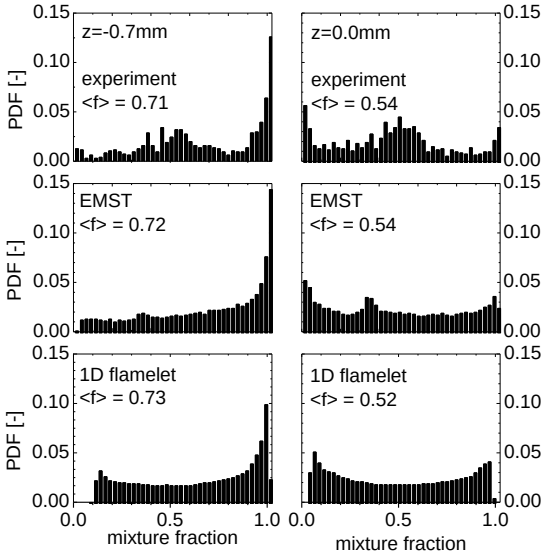

Figure 4.14
Mixture fraction PDFs at a location z = -0.7mm and at z = 0.0mm. Top: experiment, middle: EMST-mixing model, bottom: 1D-flamelet like model.

Extinction limit

Global flame extinction can be viewed as an ultimate test of intense turbulence–chemistry interaction. As mentioned above, global extinction was observed at a bulk strain rate of $a = 255s^{-1}$. Numerically, the extinction limit was evaluated by varying parametrically the bulk strain rate via axial inflow velocities in a series of different simulations. In contrast to the experimental data, extinction in the simulation occurred around $a = 560s^{-1}$, close to the extinction limit of $a = 750s^{-1}$ from laminar flame calculations. The much higher resistance to flame extinction is consistent with the high flame temperatures predicted at the rich side.

Assessment of numerical models

The above comparisons between experimental and numerical results provide a basis for the discussion of the performance of various submodels. As the 12-step chemistry has been used

previously in modelling partially-premixed jet flames with the same fuel mixture ($\Phi = 2$), showing good results in the rich parts of flame [24], the reduced chemistry mechanism is believed to be adequate. The comparison of mixture fraction PDF in 4.14 suggests that the numerical models predict a less intermittent flow with a slower mixing process compared to that implied by experimental data. The predicted mixing process is influenced by both the flow field model and the mixing model used in the PDF-approach as well as by their coupling. The observed strong intermittency between fuel and oxidizer is induced by the large flow motions around the stagnation plane. A strong intermittency is likely to associate with high turbulence fluctuations. Quantities, such as turbulent kinetic energy and axial fluctuation components, are essential to provide a critical assessment of model performance. A closer examination of figure 4.10 suggests that the noted discrepancies between experimental and numerical results near the stagnation point could be significant. Due to the uncertainties of LDV near the stagnation point, measurements of the velocity field need to be improved to yield more accurate second moment statistics to allow for a definite conclusion on the flow field prediction.

The EMST-model provided good results in modelling local extinction and reignition [24] and hence it is capable of modelling strong turbulence-chemistry interactions. Yet, both EMST and the flamelet like mixing models yield similar results in the rich parts of the flame. Both mixing models require the input of a mixing frequency that is determined only by the mean scalar dissipation in the present simulations. At the rich part of the flame, the predicted mean scalar dissipation rates are lower than the measured values by a factor of two [4]. In addition, large variations in the scalar dissipation rate were measured peaking near $f \sim 0.75$. From previous large-eddy simulations with the transient flamelet model by Pitsch [150], the variation of scalar dissipation rate was found to be the key in predicting the proper CO-levels in rich parts of flame. If variation was not properly accounted for, the predicted CO-levels were too high in comparison to data [150]. Consequently, in addition to the uncertainty in the flow field prediction, future model improvements need to include proper treatment of the scalar dissipation rate and its fluctuations.

4.4.2 Conclusions

Experimental results obtained from scalar and velocity field measurements using 1D-Raman/Rayleigh scattering and two-dimensional LDV were compared to numerical results from one-dimensional Monte Carlo PDF-simulations with a 12-step reduced chemistry and different mixing models. These comparisons revealed that the property of localness as in the EMST- and flamelet like model is essential for describing the mixing processes physically correctly whereas the IEM- and modified Curl model failed because of extinction at much too low bulk strain rates. Although extinction limits computed with these two mixing models were overestimated by a factor of more than two in terms of bulk strain rates, simulations in general revealed a very good agreement for scalar and flow field properties in the physical space. The average location and the width of the reaction zone were reproduced remarkably well, whereas deviations of the flow properties observed in the vicinity of the stagnation plane may partly be due to uncertainties in the LDV-measurements. Detailed comparisons in the mixture fraction coordinates were carried out, using scatter plots and PDF-distributions. At the lean side experimental and numerical results agreed well, while at the rich side, large discrepancies were found, indicating that the nature of both mixing and intense intermittency of the turbulent opposed jet flame are underestimated by the numerical model. These findings were supported by mixture fraction PDFs. Future model improvements are needed to properly account for the experimentally observed strong intermittency and mixing. Finally, the necessity to validate mixing models

in simple flow fields that differ from jet flames, in order to devise generally applicable models, was demonstrated.

5. Simultaneous flow and scalar field measurements

5.1 Combined LDV- and OH-PLIF-measurements in swirling premixed flames

Premixed combustion is of increasing technological relevance due to lower NOx-emissions at lean equivalence ratios. A proper design of future low-NOx-combustors depends on more reliable numerical simulations of turbulent premixed combustion processes. Although a variety of models such as the Bray-Moss-Libby (BML) model [151, 152], the thickened flame model [153], the linear-eddy model (LEM) [154, 155], or the G-equation approach [156, 157] have been applied in a RANS (Reynolds averaged Navier-Stokes)- or LES (large-eddy simulation)-context during the last two decades [158], there is still an ongoing scientific debate how to model turbulent premixed flames. To check the validity of single unclosed terms in the transport equations or to validate integral models determining entire turbulent flames, there is a need for experimentally well investigated target flames.

Whereas much progress has been attained already for non-premixed flames [24], much less comprehensive experimental data suitable for model validation of turbulent premixed and stratified target flames exist. Comprehensive studies including flow and scalar field information measured by different laser diagnostics in a highly stretched, piloted Bunsen flame are documented in [159] offering insights into turbulence–chemistry interaction and turbulence structures. A variety of other experimental studies in different lab-type flames have been conducted, for example in turbulent opposed flows [90], low swirl flames [160–162], wire-stabilised flames [163, 164] and stratified flames [165–168]. Often the emphasis was on single quantities, such as turbulent fluxes that have been measured in jet flames [169, 170], wire stabilized flames [171], and bluff-body stabilized flames [171, 71]. For more complex nozzle geometries and strong swirling flames, that are important for industrial applications, much fewer detailed experimental investigations have been performed.

In modelling premixed combustion the Favre-averaged progress variable $\tilde{c} = \overline{\rho c}/\bar{\rho}$ has been used successfully [172]. The reaction progress c is a normalized temperature given by $c = (T - T_u)/(T_b - T_u)$ with T being a temperature and the subscripts "u" and "b" denoting unburned and burnt gases, respectively. Flamelet-based models relying on the progress variable assume an infinite thin flame structure. This directly implies c to be a step function between unburned and burnt gases with a bimodal probability density function (PDF) [173]. Different planar laser diagnostic methods such as filtered Rayleigh scattering [171] or planar laser induced fluorescence (PLIF) for detection of spatial hydroxyl radical (OH) distributions [169, 170] have been used to measure mean spatial distributions of reaction progress directly.

Alongside the mean reaction term, the transport equation of $\tilde{c}$ exhibits the turbulent scalar flux $\bar{\rho}\widetilde{u''c''}$ that needs to be modelled [174]. Within the formalism of the BML-model the axial turbulent flux of $\tilde{c}$ is expressed by [172]

(43) $\bar{\rho}\widetilde{u''c''} = \bar{\rho}\tilde{c}(1-\tilde{c})(\overline{u_b} - \overline{u_u})$.

The quantities $\overline{u_b}$ and $\overline{u_u}$ denote conditional mean axial velocity components within the burnt and unburned gases, respectively. Equivalent equations apply for the two other directions. Counter-gradient diffusion, associated with thermal expansion and acceleration of fluid passing the interface dividing unburned and burnt gases exists when $\overline{u_b} > \overline{u_u}$ leading to $\bar{\rho}\widetilde{u''c''} > 0$. Gradient diffusion occurs when $\overline{u_b} < \overline{u_u}$ and the flux is assumed to be down the gradient of $\tilde{c}$.

For rather weak turbulent premixed flames counter-gradient diffusion has been observed experimentally as summarized by Veynante et al. [174]. Gradient diffusion is expected to take place when the flame is dominated by turbulent motions rather than thermal dilatation due to chemical reactions. Based on direct numerical simulations of flames exposed to isotropic turbulence, these two regimes of gradient and counter-gradient fluxes have been predicted [174]. With the turbulence intensity u', the laminar flame speed s_L, the heat release factor $\tau = (T_b - T_u)/T_u$, and the efficiency function α both regimes of turbulent transport can be distinguished by:

$$N_b \equiv \frac{\tau s_L}{2\alpha u'} \geq 1 \quad \text{counter-gradient diffusion}$$
$$N_b \equiv \frac{\tau s_L}{2\alpha u'} < 1 \quad \text{gradient diffusion.} \tag{44}$$

According to this criterion high values of the ratio u'/s_L and low heat release factors favour gradient diffusion. The efficiency function α is dependent on the length scale ratio L_t/l_F (with L_t the integral length scale and l_F the laminar flame thickness). Decreasing L_t/l_F promote an increase of N_b and thereby counter-gradient diffusion. A crossover from a counter-gradient regime to a gradient regime has been proven experimentally [170] for a piloted Bunsen-type natural-gas/air flames with various equivalence ratios and turbulence intensities. In a different study investigating wire and bluff-body stabilized CH_4/air flames [171], regimes of gradient and counter-gradient diffusion have been observed depending on local flame conditions.

The overall motivation for this chapter is to measure the turbulent flux for the premixed swirl flames presented in section 2.2. Strong swirl and high ratios of u'/s_L are used. By varying the *Re*-number between 10000 and 29900 the regime of thin reaction zones and corrugated flamelets is accessed. Turbulent flux is deduced from combined laser Doppler velocimetry (LDV, section 3) and OH-planar laser-induced fluorescence (PLIF, section 4). Hereby, OH-contours are interpreted as interfaces between burnt and unburned gases.

5.1.1 Optical setup and synchronisation of simultaneous LDV- and OH-PLIF-measurements

According to equation (43) the measurement of the turbulent flux rests upon **conditional** velocities. In the present study LDV and OH-PLIF have been therefore applied simultaneously. The transient OH-contour deduced from single-shot PLIF-images was used to determine the radial displacement Δr of the actual velocity measurement from the turbulent flame front allowing designation of conditional velocities. These simultaneous measurements were restricted to a few selected locations within the flame brush as the repetition rate of the optical method was terminated by the read-out times of the ICCD used within the PLIF-setup.

Close to a flame front LDV-seeding particles can be exposed to large temperature gradients. Thermophoretic effects might therefore influence the measured gas velocities. Thermophoretic velocities u_{TP} normal to the flame front and down the temperature gradient can be estimated by $u_{TP} \approx 0.5\nu \frac{\nabla T}{T}$ [175] with the kinematic viscosity ν. In [170] u_{TP} was deduced from strained laminar flame calculations. For stoichiometric conditions thermophoretic velocities are below $0.09 ms^{-1}$ and can be therefore neglected in comparison to convection velocities.

For OH-PLIF a tuneable KrF-Excimer laser (EMG 150 Lambda Physik) was used to excite the $P_1(8)$-line within the $A^2\Sigma \leftarrow X^2\Pi$ (3, 0)-band. By a f = 1000mm cylindrical lens a 17mm high and 0.5mm thick light sheet was formed in the measurement plane intersecting the flame at its vertical symmetry axis. Using a 105mm f/4.5 UV-lens, non-resonant OH-fluorescence within the (3, 2)-band around 295nm was imaged perpendicularly to the laser pointing onto a 1300x1300 pixel, thermoelectrically cooled, and intensified charge-coupled device (ICCD, Pi-Max, Roper Scientific). In front of the ICCD-camera a band pass filter (central wavelength 297nm, FWHM ~45nm, arrangement build out of four dichroic mirrors) was placed. Gating the intensifier with 200ns long exposure times prevented any spurious radiation from the laboratory environment and flame chemiluminescence. By limited interline transfer rates, the camera read-out times were restricted to two samples/sec determining the overall repetition rate of simultaneous LDV/PLIF-measurements.

LDV is random and intermittent in nature. For this reason validated Doppler bursts have been used as master trigger in the experiment. To avoid any feedback on the LDV-signal pro-cessing by electrical interferences from the thyratron, the excimer laser and the ICCD-camera were triggered 5µs after a validated LDV-burst. According to section 3.3 [8] integral time scales were measured to be of the order of 0.17 to 1.12ms, depending on the case and the location within the flow field. This is sufficiently larger than the 5µs time lag between the LDV- and OH-PLIF-measurement. From this point of view the LDV- and PLIF-measurements can be taken as simultaneously. Allocation of PLIF-shots and validated LDV-signals was achieved by synchronized masterclocks within the PC recording the PLIF-data and the LDV-controller.

Due to the presence of seeding particles the intense excimer laser pulses excited laser-induced incandescence (LII) in addition to the OH-fluorescence. As LII exhibits a wide spectral distribution of thermal radiation, the ICCD, although band pass filtered, detected significant amounts of LII-signals. For this reason seeding density was reduced furthermost to keep cross-talk and spectral interferences at minimum. However, data post-processing described below was still crucial to discriminate OH-PLIF- from LII-signals.

For LDV a conventional fiber-optic system was used in backscatter mode (Dantec) recording two velocity components employing a multi-line Ar^+-laser (Coherent). The measurement volume extended approximately 1mm in length and 80µm in cross direction, respectively. Doppler bursts were evaluated electronically (controller TSI IFA 750). Magnesium oxide (MgO) served as seeding material. This choice was motivated by its thermal stability and small slip. Point-wise axial and radial velocity components were measured within selected locations in the flame brush. The overall error of the mean conditional velocity components shown in the results section was ~ 3%.

Figure 5.1 shows the experimental setup for the combined OH-PLIF- and LDV-measurements. For each axial height, the LDV-measurement position was fixed at a radial position R_{LDV} corresponding to a location of high probability to find the OH-contour. The angle between pointing of the LDV-probe and the PLIF-laser sheet was 81°. So far the resulting bias for the radial

velocity component at order of 4% was not accounted for in the following treatment. Typically, up to 25000 statistically uncorrelated samples suitable for the determination of conditional velocities were recorded. This large number of data is crucial to allow for detection of small changes in mean conditional velocities. Notice, that the actual number of recorded samples was much higher as approximately 20% of the samples were rejected due to too strong interference from LII (compare figure 5.2).

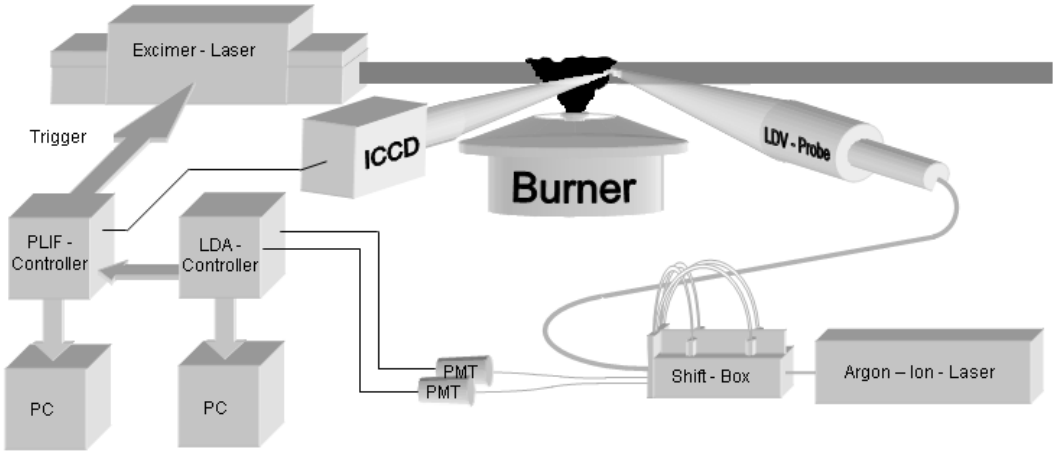

Figure 5.1
Experimental setup for combined LDV- and OH-PLIF-measurements based on conventional equipment.

5.1.2 Data post-processing

Electronic excitation of OH was based on the rather weak (3-0)-band within the A-X-electronic system. This necessitated intense UV-radiation around 248nm that led to strong LII-signals in the particle-laden flow. In many cases LII was not observed at the LDV-measurement location, as one would expect, but randomly distributed in the imaged area. Presumably measurable LII stemmed from large (clustered) seeding particles that exceeded the LDV-fringe separation (< 4µm). Particles substantially larger than the fringe separation decrease the contrast in the LDV-burst and are not validated.

Generally, a distinction between OH-PLIF- and strong LII-signals was possible because of the high LII-signal levels. This enabled the usage of an intensity-threshold to distinguish LII from OH-PLIF. After subtraction of the dark current and normalization on the laser intensity profile, the areas showing LII-signals were set to zero in the original image. The image was converted subsequently into a binary image by using a threshold 50% of the maximum observed OH-PLIF-intensity. By using a-priori-knowledge regarding the rough flame location, the OH-interface dividing hot products and unburned gases was reconstructed by finding the edge in the binary image. Remaining noise was smoothed by a 3x3 pixel median filter. Finally, a spatial resolution of 300µm was achieved. Figure 5.2 summarizes the steps from the intensity image to a contour plot. The intensity-image shows a typical occurrence of LII that was successfully removed by image post-processing.

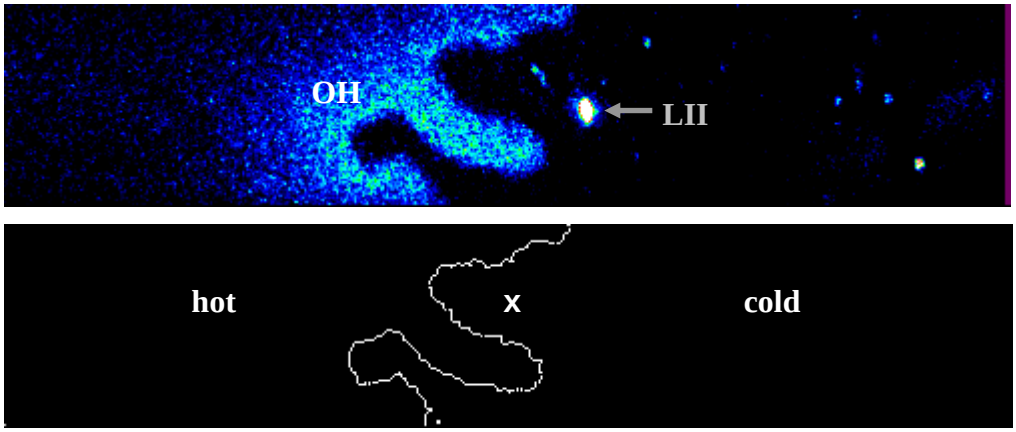

Figure 5.2
Top: Original intensity image showing OH-PLIF- and LII-signals (marked by an arrow) at much higher signal intensities. The image corresponds to 50.8x10.2mm. Bottom: Interface dividing hot and cold gases reconstructed from the OH-intensity image resulting in an OH-contour. The spatially fixed LDV-measurement location is marked by the white cross.

5.1.3 Results and discussions

Planar distributions of OH-radicals are used to locate the flame brush and the mean reaction progress. For this purpose instantaneous two-dimensional OH-contours (as presented in figure 5.2) are ensemble averaged resulting in a two-dimensional histogram. This histogram provides the Reynolds mean progress variable $\bar{c}$ [169] from which the extension of the flame brush and the spreading rate of the flow can be derived.

For the 30kW-case, the left hand side of figure 5.3 presents a radial cut through the two-dimensional histogram at an axial height of x = 30mm. Obviously, the distribution is almost symmetric (notice, further downstream slight asymmetries occur towards the unburned gases that are due to imperfections in the data post-processing removing parasitic effects from LII). Using results from a Gaussian fit (not shown), the probability to measure the OH-contour tops at r = 26.5mm. According to the thin flame assumption this histogram can be identified as the probability to find burnt or unburned gas mixtures, respectively. For radii smaller than 26.5mm hot products occur in average whereas further outside cold gases are present more often. Within this concept any finite rate chemistry effects are neglected and the temperature of hot products is given by the adiabatic flame temperature T_b of the gas mixture. It is worth mentioning, that local equivalence ratios can differ significantly from the gas mixture emana-ting from the nozzle caused by secondary air entrainment. In an ongoing effort secondary air entrainment is measured by one-dimensional Raman/Rayleigh spectroscopy but is not consi-dered any further here.

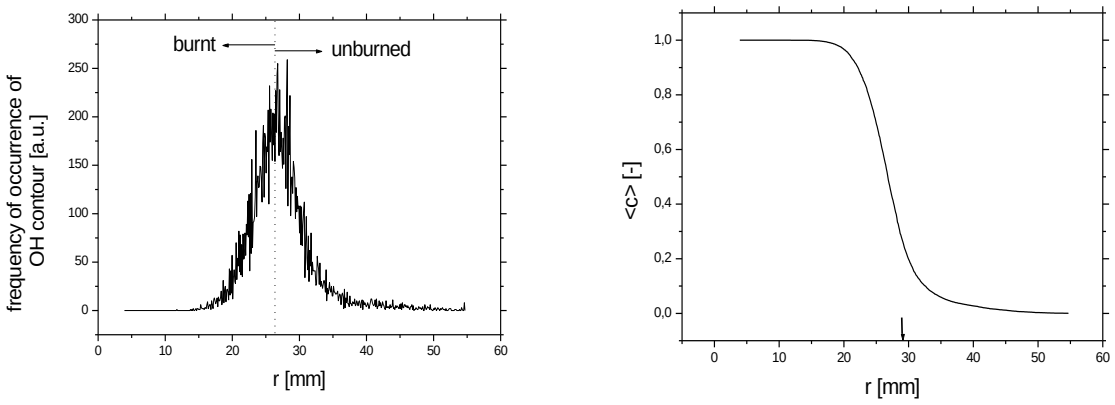

Figure 5.3
Left: One-dimensional histogram obtained by a radial cut through the ensemble averaged 2D-OH-contours at an axial height of x = 30mm. The vertical dashed line marks the average position of the cold–hot interface. For this distribution 16000 OH-PLIF-single-shots have been processed. Right: Mean reaction progress resulting from integration of the figure at the l.h.s. The arrow marks the spatially fixed position of LDV-measurements (R_{LDV}) taken at this respective height.

By integrating the mean reaction progress, $\overline{c}(r)$ can be obtained from the normalised histogram. The result is shown at the right hand side of figure 5.3 and can be interpreted as a non-linear transformation of laboratory into flame coordinates. A value of $\overline{c} = 0.5$ corresponds to the average location of the cold – hot interface (r = 26.5mm) at this axial height. The separation between $\overline{c} = 0.1$ and $\overline{c} = 0.9$ can be taken as the radial extension of the flame brush. For the 30kW-case the width is increasing from 10.5mm at x = 30mm to approximately 28mm at x = 50mm. The spreading rate of the flame can be quantified by the radial position of the $\overline{c} = 0.5$-values ($r_{\overline{c}=0.5}$). As stated above, at x = 30mm in average the flame is positioned at $r_{\overline{c}=0.5}$ = 26.5mm. Downstream the corresponding positions are $r_{\overline{c}=0.5} = 35$mm at x = 40mm and $r_{\overline{c}=0.5}$ = 42mm at x = 50mm.

As described in the previous sections, axial (u) and radial (v) velocity components were measured simultaneously with the spatial OH-distribution tagging the interface. For instantaneous realisations, the radial displacement $\pm\Delta r$ of the actual LDV-measurement location from the cold – hot interface was determined. Results of these measurements can be accor-dingly termed conditional velocities $\overline{u_u}$, $\overline{u_b}$, $\overline{v_u}$, and $\overline{v_b}$. For *PSF-30* at various axial heights conditional mean velocities are shown in figure 5.4. Data are binned in 4mm wide intervals (symbols). Additionally a floating average is presented (lines). Varying radial LDV-measurement locations for each height are specified in table 5.1. Obviously, for the axial velocity component at low axial heights $\overline{u_b} < \overline{u_u}$. Further downstream this turns around and for x = 50mm $\overline{u_b} > \overline{u_u}$. This crossover is not observed for the mean conditional radial velocity component. For all locations investigated, radial velocities for the cold gases exceed the hot gas velocities.

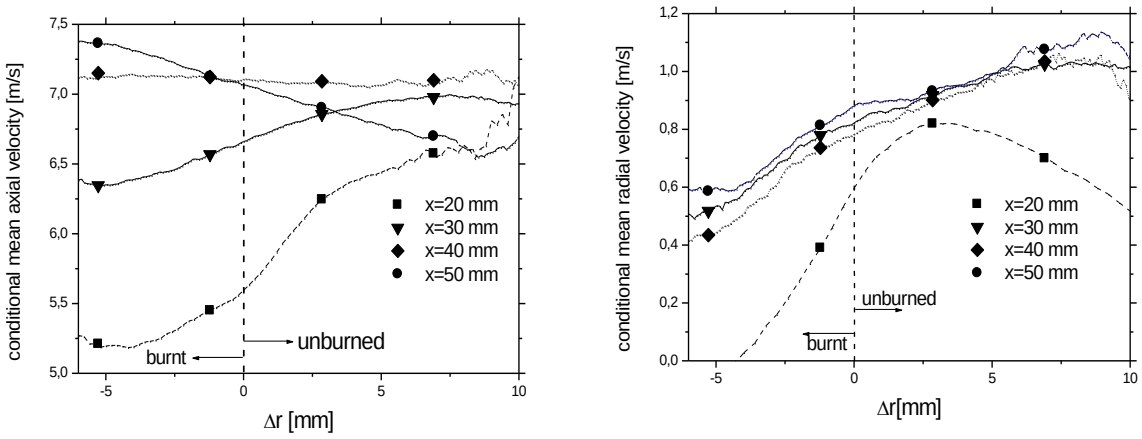

Figure 5.4
Conditional velocities measured at various axial heights for the 30kW-case. Different lines represent results from a floating average, symbols represent results from fixed 4mm wide bin intervals. Measurement locations R_{LDV} are listed in table 5.1. Left: Mean axial conditional velocity component. Right: Mean radial conditional velocity component.

Table 5.1
Favre-mean fluxes. LDV-measurement locations at different heights correspond to various values of the mean reaction progress. Counter-gradient diffusion is apparent for positive fluxes.

		20mm	**30mm**	**40mm**	**50mm**
R_{LDV}	[mm]	24	29	34	38.5
$\bar{c}$	[-]	0.34	0.22	0.57	0.66
$\widetilde{u''c''}$	[ms^{-1}]	-0.033	-0.008	0.004	0.026
$\widetilde{v''c''}$	[ms^{-1}]	-0.020	-0.004	-0.016	-0.017

For a more detailed discussion, conditional velocities in the vicinity of the cold–hot interface are considered now. For this purpose conditional velocities are ensemble averaged within $\Delta r = \pm 2.5$ mm wide stripes. For the lowest axial position at x = 20mm, stripe-conditioned velocities in the burnt region are lower than in the region of unburned gases. The axial component decreases from $\overline{u_u} = 6.0$ms^{-1} to $\overline{u_b} = 5.5$ms^{-1}. This corresponds to a 9%-change of the conditional axial velocity across the interface. The corresponding values for the radial velocity component decrease from 0.6 to 0.3ms^{-1} (50%). At this location turbulent velocity fluctuations exceed variations of the velocity induced by gas expansion effects. At x = 30mm the differences between $\overline{u_u}$ and $\overline{u_b}$ decreased already to 0.2ms^{-1} or 3% which is at the same order of magnitude as the experimental error. However, the relative changes in the conditional radial velocity did not change significantly. Further downstream, at x = 40mm, the mean conditional axial velocity component is nearly independent on Δr, whereas the radial component still exhibits higher velocities at the unburned side of the interface. For the same width of the stripes, the radial

velocity component decreases already by nearly 15%. At x = 50mm the value of $\overline{u_u}$ equals 7.0ms^{-1}, slightly below $\overline{u_b} = 7.15\text{ms}^{-1}$. The trend from $\overline{u_b} < \overline{u_u}$ at x = 20mm to $\overline{u_b} > \overline{u_u}$ at x = 50mm is in contrast to the progression observed for the radial component where $\left(\overline{v_b} - \overline{v_u}\right) < 0$ remains, independent on the axial position. The different behaviour for axial and radial velocity components at x = 50mm indicates that gas expansion effects can dominate axially whereas in radial direction turbulent fluctuations determine the direction of turbulent transport.

The experimental data can be used to determine two components of the turbulent flux presented in equation (43). For this purpose the corresponding stripe-conditioned axial and radial velocity components are used. In conjunction with Favre-averaged reaction progress

$$\tilde{c} = \frac{\overline{c}}{\overline{c} + \rho_b / \rho_u \left(1 - \overline{c}\right)} \quad [170], \tag{45}$$

Favre-mean fluxes can be calculated and are listed in table 5.1. For each axial location the fixed LDV-measurement location R_{LDV} (compare arrow at r.h.s. of figure 5.3) corresponds to a certain value of the mean reaction progress $\overline{c}$.

Whereas for the Favre-mean radial flux in all cases gradient diffusion was observed, for the axial component a cross-over from gradient diffusion at x = 20mm to counter-gradient diffusion at x = 50mm was apparent.

These experimental results can be used to check the validity of the criterion introduced in [174] and presented in equation (43). The efficiency function α was introduced to take into account the variable ability of turbulent eddies to act on the flame front and is dependent on the length scale ratio L_t/l_F. For the configuration under investigation, longitudinal and transversal length scales have been measured by two-point LDV [8]. Longitudinal length scales at the nozzle exit plane $L_{11,x=1mm}$ were between 6 and 8mm, depending on the radial position. Due to viscous forces this length scale in general increases axially. Therefore length scale ratios L_t/l_F, using the laminar flame thickness l_F from table 2.3, exceeded clearly values of 20. According to figure 15 in [174] for values $L_t/l_F > 20$ the efficiency function α is approximately unity. Within the flame brush the ratio between turbulence intensity and laminar flame speed, u'/s_L , does not vary significantly between x = 20 and 50mm ($u'/s_L \approx 5.5$). With the heat release factor τ (neglecting any effects of secondary air entrainment on adiabatic flame temperature) one finally finds that $N_b \equiv \frac{\tau s_L}{2\alpha u'} \approx 0.5$, approximately independent of the axial heights considered. This value implies higher velocities in the unburned regions ($\overline{u_u}, \overline{v_u} > \overline{u_b}, \overline{v_b}$) and thus gradient diffusion. This provision is in agreement with conditional mean radial velocity measurements, but for the axial component the trend from $\overline{u_u} < \overline{u_b}$ to $\overline{u_u} > \overline{u_b}$ is not in accordance with the DNS-based predictions. Notice, that isotropic turbulence was assumed for the DNS-calculations but the present experimental configuration shows clearly anisotropic features. However, due to the small relative changes observed for the conditional axial velocities that are at the same order of magnitude as experimental uncertainties, for swirling flames a final conclusion on the validity of the criterion proposed in [174] can not be drawn. More work and especially velocity measurements with even less experimental uncertainties are needed to fully understand the transition from gradient to counter-gradient diffusion. Additionally, an investigation of the tangential velocity component is desirable and is planned in a future experiment.

The influence of increasing *Re*-number on conditional axial velocities is shown in figure 5.5 for a selected height at *x* = 20mm. Except of the *Re*-number, that has been increased from 10000 (*PSF-30*) to 29900 (*PSF-90*), all other parameters have been kept constant. The much higher absolute turbulence levels clearly promote gradient diffusion. The relative change of the stripe-conditioned axial velocity component across the cold – hot interface increased from 9% for *PSF-30* to 28% for *PSF-90*. This strongly supports the findings from previous studies that gradient diffusion is promoted by increasing ratios of u'/s_L . Consequently, flames classified in the regime of thin reaction zones show more likely gradient diffusion than corrugated flames.

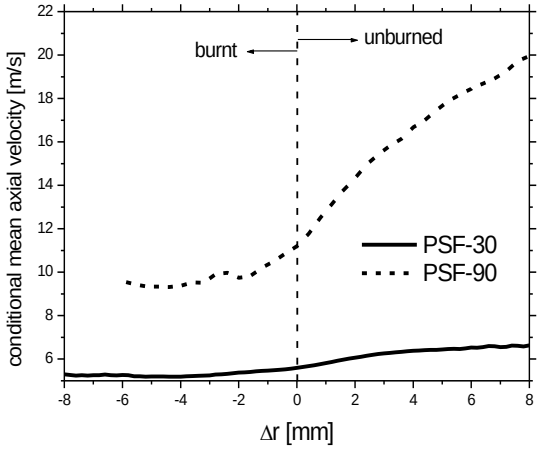

Figure 5.5
Comparison of conditional mean axial velocities for different Reynolds-numbers. The Re-numbers for PSF-30 and PSF-90 were 10000 and 29900, respectively.

5.1.4 Conclusions

Joint velocity/scalar measurements have been performed in swirling premixed natural gas/air flames with two Reynolds-numbers using combined laser Doppler velocimetry and planar laser-induced fluorescence. For various locations in the flame brush conditional mean axial and radial velocities have been measured. The focus of the discussion was on stripe-conditioned velocities in the vicinity of the cold – hot interface that was tagged by two-dimensional OH-distributions. In general and in accordance with previous investigations, high levels of turbulence promote gradient diffusion. For this reason turbulent fluxes of flames within the regime of thin reaction zones are more likely dominated by gradient diffusion. However, mean conditional axial and radial velocity components can exhibit different schemes of turbulent transport. It was shown that with increasing distances from the burner for the axial velocity component a crossover from gradient to counter-gradient diffusion takes place whereas the radial component constantly shows gradient diffusion. The cross-over from gradient to counter-gradient diffusion is shown to be in disagreement to a criterion deduced from previous DNS-calculations. It should be considered that the DNS-data were obtained for homogeneous isotropic turbulence, not matching the conditions of the present turbulent flow. However, a final conclusion on the validity of the DNS-based criterion should not de drawn from the current data because of these different flow characteristics. Furthermore, the behaviour of the conditional tangential velocity needs to be studied in future experiments as well.

The present study is part of an ongoing effort. Flow and scalar field are characterised in detail using various laser diagnostics such as Raman/Rayleigh spectroscopy, laser-induced fluorescence, laser Doppler velocimetry, and particle imaging velocimetry. This data base already serves for validating numerical simulations such as LES [176].

5.2 Combined PIV- and OH-PLIF-measurements in partially-premixed turbulent opposed jet flames

Recent improvements in combustion technology are built on an advanced understanding of physical and chemical processes underlying turbulent flames. As outlined in the introduction this knowledge is usually gained from generic configurations such as turbulent jet [177], opposed jet [117] or bluff-body stabilized [8, 178] flames. While stable non-premixed flames are well studied and are most accessible for deterministic numerical simulations [158], transient phenomena such as flame extinction, founded on the complex interaction between turbulent mixing and chemical reactions, are much less understood [24].

In non- and partially-premixed flames, the scalar dissipation rate was identified as a suitable measure to quantify finite rate chemistry effects [13]. Using 1D-Raman/Rayleigh scattering [118, 117] or combined 2D-Rayleigh/planar laser-induced fluorescence (PLIF) [179], scalar dissipation rates were measured in hydrocarbon-fueled piloted jet and opposed jet flames. As scalar dissipation rates in reaction zones are determined by local properties of the turbulence field such as strain or vorticity in the region of the reactive mixing layer, additional conditional flow field measurements relying on combined flow/scalar measurements are imperative.

Although simultaneous Raman/Rayleigh/laser Doppler velocimetry (LDV) approaches were shown to be feasible [180, 181], the data rate precludes building up a statistically reliable data base. Instead, a simultaneous application of particle imaging velocimetry (PIV) and a visualization of the reaction zone by PLIF is preferable because the presence of seed particles impacts much less on the fluorescence signals. Furthermore, the two-dimensional nature of PIV provides estimates of vorticity and dilatation. Transient locations of the reaction zones can be identified by radical distributions such as OH or CH measurable by PLIF and serve to deduce local flow field properties conditioned by the reaction zone [182, 183, 64].

Turbulent opposed jet flames are prominent configurations for studies of flame extinction [90] as summarized recently in [117]. Mean scalar dissipation rates can be easily increased by increasing the momentum of the impinging gas flows. Hence, these flames can be operated very close to extinction. However, conditional flow field properties, as demonstrated in [184] for premixed stagnation-type flames, in the vicinity of the reaction zone influencing local scalar dissipation rates were not measured for non- or partially-premixed opposed jets.

The inhomogeneous density fields associated with combustion pose a challenge for PIV-application. In the exhaust gas regions seeding particle densities are reduced approximately by $\rho_{burnt}/\rho_{unburned}$ with ρ being the density. For example, in [185] this was compensated by extremely high seeding densities that inhibited PIV-data processing in unburned regions. Consequently it is impossible to achieve velocity vectors with the same resolution in the burnt and unburned regions with standard PIV-algorithms. For the opposed jet configuration flame characteristics like the extinction limits, in addition, are very sensitive to disturbances such as radiative heat losses by seed particles. This requires low densities of seeding particles, reducing the achievable spatial resolution of PIV, particularly in the exhaust regions. To avoid a significant alteration of the extinction limits and to provide a sufficient spatial resolution, velocities in the

burnt gas regions are deduced in the present study from a particle tracking algorithm (PTV), while upstream of the flame PIV is used. A single-shot illustration of this procedure for an extinguishing flame is discussed subsequently (figure 5.6).

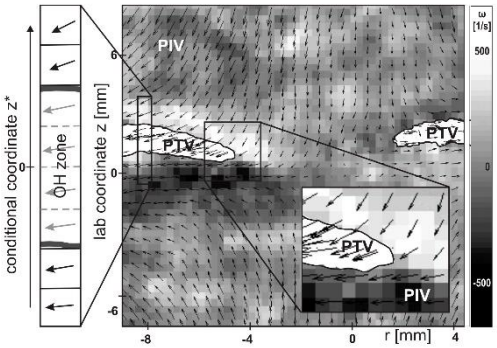

Figure 5.6
Single-shot of OH-PLIF and PIV/PTV during flame extinction showing the transient OH-distribution (white areas) and velocity vectors resulting from the PIV-algorithm outside the OH-layer and the PTV-algorithm inside the OH-layer. Outside the OH-layer the vorticity field is shown in shades of grey. The edge of the extinguishing flame including the local flow and vorticity field is inset. At the left the definition of the conditional coordinate *z** is highlighted. As the PIV-interrogation areas are fixed to the upper and lower OH-contour and of a certain size, the PTV-area is divided into 4 subregions while the origin of z* is located at the middle of the OH-zone.

To allow comparison to 1D-Raman/Rayleigh measurements and to complement the data base of [117, 140] suitable for combustion LES-validation, the identical burner shown in figure 2.1 and operational points including those from [117] are used. Since conditional scalar dissipation rates were previously measured, it is crucial to relate the PIV/PTV-measurements to the transiently intermitting reaction zone of the turbulent flame. This is accomplished by recording OH-distributions by PLIF simultaneously with PIV/PTV. With the help of flamelet models for instance the Raman/Raleigh results can be conditioned on the OH-zone as well. Conditional flow field statistics are reported for varied equivalence ratios of the fuel jet and two different Reynolds-numbers, including on and off-axis data evaluation of the large data base.

5.2.1 Optical setup

The combined PIV/PTV/OH-PLIF-setup is shown in figure 5.7. Two separate laser systems were used. The laser beams were formed into sheets and overlapped to illuminate a planar region of the flame cutting the vertical centerline of the burner. For OH-PLIF, a frequency doubled Nd:YAG-laser (Pro270, Quanta Ray) pumped a dye-laser (Sirah Precision Scan). After frequency doubling of the tunable radiation, the UV-laser beam was formed into a sheet with a height of 16mm and a thickness of ~250µm in the probe volume region. OH was excited via the $R_1(8)$-transition of the (0,1)-band in the A-X-system at 281.3nm with a temperature-insensitive population distribution. Fluorescence from the A-X (1,1)- and (0,0)-bands was detected using a UV-lens (Nikkor, f = 105mm, f/# = 4,5), a dichroic long pass filter and two *WG305*-filter (Schott) in front of an intensified CCD-camera (Roper Scientific, PiMax, 1300x1340 pixels). The field of view was 20x20mm^2 and the measured resolution 70µm. After background

subtraction and correction for laser profile variations, OH-contours were deduced using a threshold-method. Variations in the contour detection were insensitive to the findings discussed below.

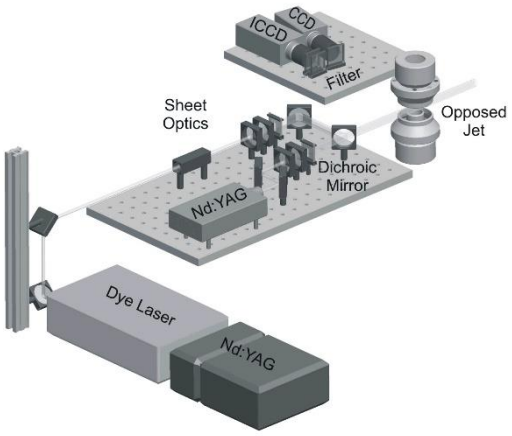

Figure 5.7
Optical layout for simultaneous PIV/PTV/OH-PLIF-measurements.

Due to the slow three-body recombination rates of OH, the use of OH-PLIF as a reaction zone marker has been questioned [186]. It has been shown additionally that OH-mole fractions show a similar but retarded dependence as heat release on increasing strain [90]. However, laminar opposed-jet flamelet calculations [140] yielded that the lower OH-boundary can be considered as an approximate reaction zone marker in the opposed jet configuration.

The beams of two frequency doubled Nd:YAG-lasers (New Wave) were overlapped to provide successive illumination for PIV/PTV. The energy in each pulse was set to 40mJ and the pulse separation was $\Delta t = 50\mu s$. In the probe volume the light sheet had a height of 24mm and a thickness of ~600µm. A frame-transfer-CCD (PCO, 1376x1040 pixels) was used with an imaged area of 20x24mm². Cameras for PIV/PTV and PLIF were aligned using a backside-illuminated mask consisting of a 2D-array of 90 holes each with a diameter of 150µm. De-warping and identification of corresponding pixels on both CCDs was accomplished based on this mask in a post-processing step.

For the combined PIV/PTV-approach dry MgO with a mean diameter of about 1µm was used as seed material. Approaching the reaction zone the particle temperature increased causing additional radiative heat losses. This disturbance impacted the flame as seeding was increased and shifted the extinction limit to lower Reynolds-numbers relative to un-seeded flames. To assure that changes in extinction limits were less than 5%, the seeding density of approximated 8g/Nm³ gas was controlled carefully. Two seeders were installed to seed both jets individually. To assure stable and reproducible seeding densities, a combination of static meshes and rotating brushes were installed at the bottom of a MgO-storage tank. The speed of the motor driving the rotating brushes determined the seeding density. Mie scattering intensities 3mm downstream of

the nozzle exits were monitored to achieve as much as possible constant and equal seeding in both jets.

5.2.2 PIV/PTV-data post-processing

The PIV-data processing is performed on a regular grid consisting of 32×32 pixels (or 16×16 pixel) with a resolution of 600µm (300µm) and fixed to the OH-front. In a first step a standard PIV-algorithm using multi-pass interrogation with window-shifting and three-point Gaussian subpixel interpolation is used [187]. Starting with interrogation areas of 64×64 pixels, the initially determined displacement is used as an estimate for successively smaller subregions of size S = 32 and 16 pixels each side. This improves the search for spatially refined correlations. Efficient noise was applied as outlined in section 3.1.3.

To relate the PIV/PTV-measurements to the transient reaction zone of the turbulent flame and to avoid a bias due to different seeding densities in cold and hot gases, simultaneous contributions from the reactant and product regions to the velocity vector resulting from a single PIV-interrogation area must be avoided. For each image, a coordinate system is introduced that is fixed to the reaction zone at the radial position of current interest as deduced from the OH-image. Starting from the upper OH-contour, flame-fixed axial coordinates z_u* are positive, and starting from the lower OH-contour, flame-fixed coordinates z_l* are defined as negative. Thus, z* denotes the flame-fixed axial coordinate and displacements are determined on a shot-by-shot basis relative to the reaction zone. The definition of the flame-fixed coordinate system is visualized by the insert left of figure 5.6. The mean of the instantaneous upper and lower OH-contours in the laboratory system are located at $z_{\text{upper OH-contour}}$ = 1.4, 1.9, 2.7 and $z_{\text{lower OH-contour}}$ = 0.2, 0.5, 1.6mm for the flames TOJ2D, TOJ2C, and TOJ1C, respectively, with z being the laboratory coordinate system. These positions are assigned by vertical lines in figures 5.8, 5.9 and 5.11 where the focus is on a region z* = ±6mm.

Seeding densities are reduced significantly in the burnt gas regions by approximately 85%. Since successful PIV-post-processing relies on the statistical average of about 10 particles per subregion [50], the PIV-algorithm outlined above would be accessible only on a grid con-sisting of at least 48×48 pixels. Higher seeding densities are, as discussed, prohibitive because of their impact on flame characteristics. Therefore particle tracking velocimetry (PTV) is used in regions with high temperatures where the seeding density is low. An initial guess for velo-city in the PTV-regions is obtained from the PIV-algorithm using a 32×32 pixels subregion after spurious vectors are removed and replaced by interpolation. Identification of single particles is done in the first PIV-image. Subsequently, subregions of 5×5 pixels are centered around the currently considered particle in the first image and the respective location in the second image deduced from the initial guess of the velocity vector. A cross-correlation is applied resulting in an improved estimation of the single velocity vector. Finally, the OH-layer at the radius of current interest is subdivided into four squared subregions and PTV-results in the corresponding subregions are statistically averaged. For the case of TOJ2D, these re-sulting subregions are S = 16±4 pixels each side (this corresponds to an average thickness of the OH-layer of 1.2±0.3mm). Obviously, PTV and PIV exhibit very similar spatial resolution. However, with a reduced PTV-subregion of 3×3 pixels, PTV-results proved to be consistent with PIV-data prior to the reaction zone as demonstrated in Fig. 5.8.

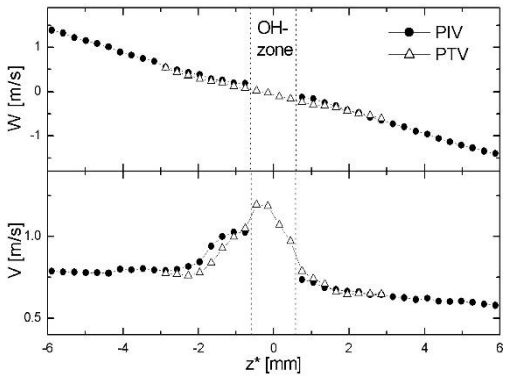

Figure 5.8
Mean axial (W) and radial (V) velocities of flame TOJ2D at r = 4mm conditioned on the transient OH-contours. The abscissae, z^*, is a spatial coordinate fixed to the transient OH-contours. The vertical lines denote the location of the upper and lower mean OH-contours and their separation is the mean thickness of the OH-layer. Axial velocities are positive when pointing in $+z^*$-direction. Radial velocities are positive when pointing away from the centerline. PTV-results are extended into the region of unburned gases for comparison to PIV.

PTV is more accurate and precise than correlation-based PIV-algorithms, comparably insensitive to out-of-plane motion and accepting of larger velocity gradients [188]. However, thermophoretic effects are inherent to any velocimetry relying on seed particles [189]. Thermophoretic velocities u_{TP} normal to the reaction zone and down the temperature gradient can be estimated by $u_{TP} \approx 0.5\nu \nabla T/T$ [175] with the kinematic viscosity ν. For stagnation point flows such as turbulent opposed jets, thermphoretic effects are considerable. According to estimations by Sung et al. [190] in a comparable opposed jet configuration u_{TP} is 0.15ms^{-1} at worst for the flame TOJ2D.

In summary, the flame-fixed coordinate system and the improved PIV-algorithm for un-reacted gases in connection with PTV in the vicinity of the reaction zone is a suitable way to deduce conditional flow field properties in flames. This holds even more in flames highly sensitive to external disturbances by seeding. The following results comprise for each flame up to 2000 PIV/PTV/PLIF-single-shots.

5.2.3 Results and discussions

In this section, conditional flow field properties are shown along the centerline (r = 0mm) and one off-centerline location at r = 4mm. All velocities, vorticity, dilatation or strain rates are shown as values conditioned on the instantaneous flame location.

Mean and fluctuations of the axial and radial velocity components as well as mean vorticity and dilatation are presented in figure 5.9 for flames TOJ1C, TOJ2C and TOJ2D listed in table 2.1 and 2.2. This figure exhibits results only from PIV-data post-processing using a 32×32 pixel resolution. The absolute value of the mean axial velocity component $|\mathrm{W}|$ decreases almost constantly approaching the respective OH-contour. As expected for higher bulk exit velocities (TOJ2D) the profiles show a steeper slope which is independent on the radial position. For the

same Re (TOJ1C and TOJ2C) but different fuel mixtures (ϕ = 3.18 and 2.0) the profiles coincide. The mean radial velocity (V) centerline profile shows constant values independent of the axial displacement from the respective OH-contour. On the air-side V is very close to V = 0ms^{-1} as expected but on the fuel side a slight deviation from zero is observed (TOJ2D: 0.2ms^{-1}; TOJ1C, TOJ2C: 0.1ms^{-1}). This indicates small imperfections of the symmetry of the flow system that are increased slightly for higher Re. Consistently higher mean radial velocities are observed for the off-axis profiles at r = 4mm. The enhanced mean radial velocities on the fuel side are due to the higher exit velocities of the methane/air mixture which are required to balance the higher density of the air in order to achieve an equal momentum for both gas streams. The fluctuation levels of axial and radial velocity components show an opposite trend when they approach the respective OH-contour. Whereas the axial fluctuations decrease, the radial fluctuations slightly increase. This behavior is more prominent on the fuel side. The turbulent kinetic energy (TKE) $k = 1/2\left(\mathrm{w}'^2 + 2\mathrm{v}'^2\right)^{1/2}$ (compare figure 5.11 for TOJ2D) exhibits an increase particularly at the lower OH-contour indicating the presence of enhanced axial strain.

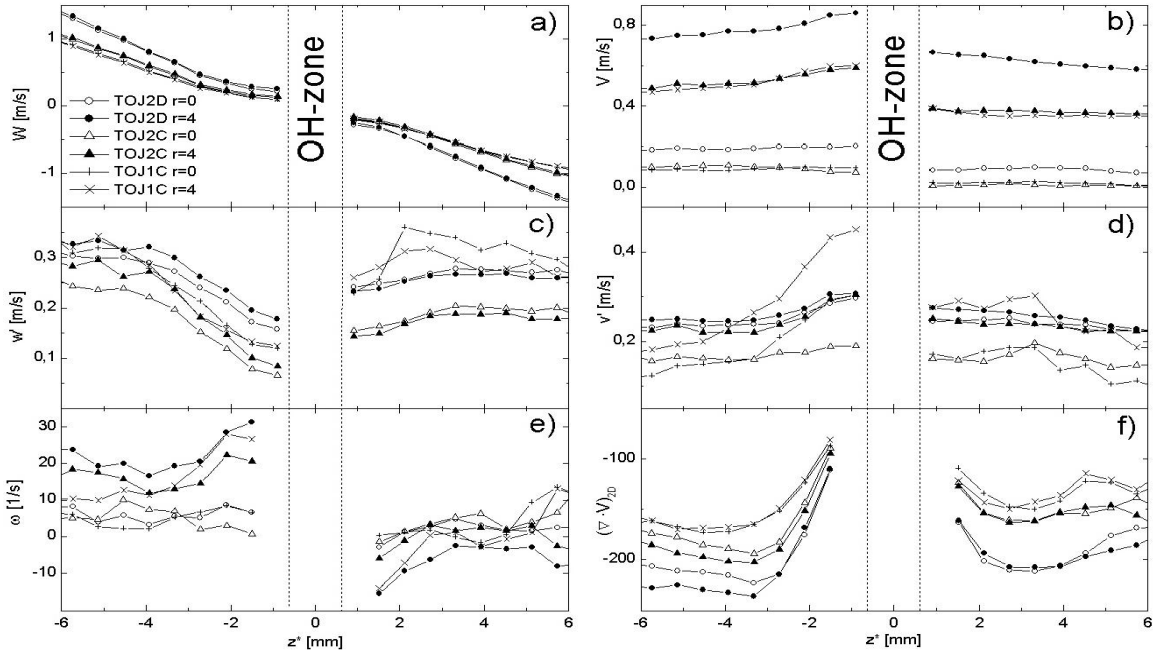

Figure 5.9
Axial profiles of conditional mean velocities (a) and (b), velocity fluctuations (c) and (d), vorticity (e) and dilatation (f). Vertical lines denote mean upper and lower OH-contours (see text). All three flames and two radial locations (r = 0 and 4mm) are included.

At off-axis locations, the modulus of the out-of-plane vorticity-component $\omega = 1/2\left|\partial \mathrm{w}/\partial r - \partial \mathrm{v}/\partial z^*\right|$ grows as the OH-contour is approached. Notice that the algebraic signs of vorticity are opposite for fuel and air flow, respectively, following the definition of z^* and the velocity directionality. The rise of $1/2\left|\partial \mathrm{w}/\partial r - \partial \mathrm{v}/\partial z^*\right|$ is already seen close to the OH-distribution on the left hand side of figure 5.6. In the ensemble-averaged data presented in figure 5.9(e) this trend is observable particularly for the off-axis profiles at r = 4mm and the fuel side

where the stoichiometric contour is located close to the OH-contour. The correlation of vorticity with the onset of the reaction zone observed here is similar to findings in [191] and might be due to inhibited momentum mixing across the reaction zone.

At the centreline, vorticity is approximately independent on the displacement from the respective OH-contours and close to zero as expected. This indicates that eddies are generated preferably close to the reaction zone particularly at off-centerline positions. This conclusion is consistent with the observation of larger radial velocity fluctuations at off-axis locations.

Visual inspection of high speed movies by operating a CMOS-camera (Photron) at 1kHz and exciting Mie scattering at 10kHz using a diode pumped intra-cavity frequency doubled Nd:YLF-laser (Coherent) at 527nm additionally confirm the formation of eddies in a zone of high strain near the reaction zone. Only a fraction of these time-sequences is shown in Fig. 5.10. Light-grey areas show flame luminosity, the 10-dot-arrays (partly blurred and appearing as lines for low velocities) are due to Mie scattering of a single seed particle illuminated 10 times per camera exposure. Consequently, particle trajectories can be tracked in time. In this sample an eddy is formed in the close vicinity of the lower contour of the luminous flame area.

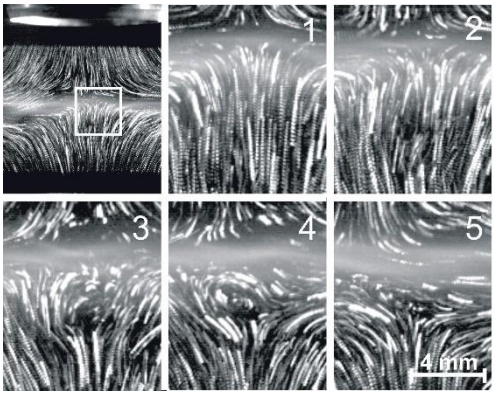

Figure 5.10
Simultaneously measured flame luminosity (grey areas) and Mie scattering from 10 laser shots during each 1kHz camera exposure. Temporal sequence (images 1-5) is from the 11.5x11.5mm^2 white box in the enlarged left top image.

The 2D-dilatation $(\nabla \cdot V)_{2D} = (\partial \mathrm{w}/\partial z^* + \partial \mathrm{v}/\partial r)$ presented in figure 5.9(f) is negative in the whole region. It features a weak minimum around $z^* = \pm 3$mm. For smaller values of z^*, the modulus $|\partial \mathrm{w}/\partial z^* + \partial \mathrm{v}/\partial r|$ is decreasing with a rather steep slope, whereas for $z^* > 3$mm this slope is much less. As $\partial \mathrm{v}/\partial r$ is always almost positive, axial strain (acting compressive) exceeds radial strain (acting excessive). Thus, $|\partial \mathrm{w}/\partial z^*| > |\partial \mathrm{v}/\partial r|$ holds. This can be explained by the fact that the time-averaged flame is aligned horizontally posing density gradients which cause again axial velocity gradients - mainly in the axial direction. However, when the respective OH-contour is approached, the difference $(|\partial \mathrm{w}/\partial z^* - \partial \mathrm{v}/\partial r|)$ diminishes since gas expansion by heat release predominantly accelerates radial velocities in the vicinity of the stagnation plane (compare figure 5.8).

Figure 5.11(a), (b) shows axial profiles of conditional vorticity, dilatation, TKE, axial and radial strain resulting from the combined PIV/PTV-evaluation for the case TOJ2D at the off-axis position r = 4mm. Here, the enhanced spatial resolution based on the 16×16 pixels subregions is used. The PTV-region is extended by $z^* \approx \pm 2$mm outside the OH-layer. This is motivated by the fact that in the vicinity of the OH-layer, the seed particle density declined significantly and PTV is believed to be more reliable in this region. The profiles from the PIV- and PTV-parts lead very smoothly into each other and supplement the data presented in figure 5.9. The vorticity profile shows a change of sign within the OH-layer, crossing zero shortly after the lower OH-contour. At the same position, the dilatation exhibits a local minimum. Peak values of all profiles presented in figure 5.11(a), (b) coincide to each other fairly well at $z^* \approx -1.4$ and $z^* \approx +0.6$mm. As stated earlier, axial and radial strain possess opposite signs. Minima in radial strain coincide with maxima in axial strain and vice versa. The off-axis axial strain profile here is in close agreement to laminar flamelet calculations. This indicates a relaminarisation of flow and scalar fields close to the heat release zones in agreement to [4, 191].

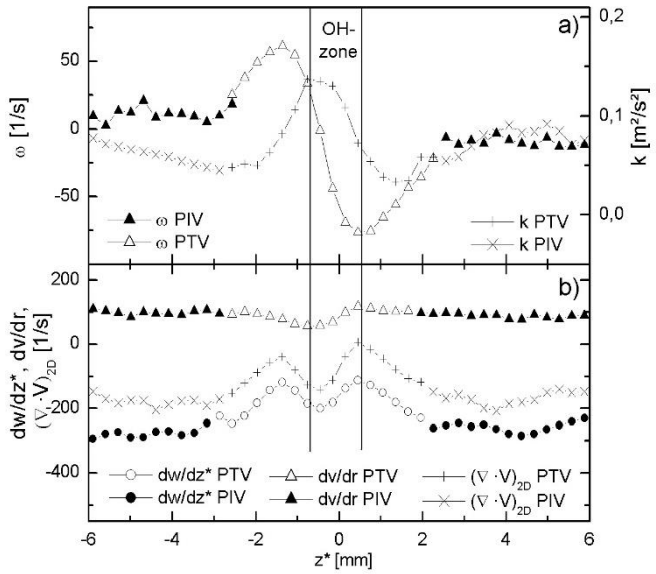

Figure 5.11
Axial profiles of conditional vorticity, TKE (a), dilatation, axial and radial strain (b) at the off-axis position r = 4mm for the case TOJ2D. Vertical lines denote the mean locations of upper and lower OH-contours.

With respect to the lower OH-contours associated with the reaction zone, the profiles are approximately symmetric. Contrary, profiles are asymmetric relative to the upper OH-contour. This might be explained by the fact that the upper OH-contour is extended at the lean side of the reaction zone by slow three-body reactions.

5.2.4 Conclusions

Flames burning very close to extinction are very sensitive to external disturbances. Particle seeding required for velocimetry can cause significant shifts of the extinction limits. Thus seeding densities must be reduced and this entails poor spatial resolution for PIV. In the present study a combined PIV/PTV-post-processing was developed and applied to turbulent opposed

jet flames. Cold gas regions were processed by an improved PIV-algorithm and hot gas regions by PTV. Overlapping PTV- and PIV-profiles showed that both methods are in agreement in overlapped regions. Despite a rather low seeding density, an in-plane resolution of 300µm was achieved.

This method was applied with simultaneous OH-PLIF-measurements to enable the evaluation of conditional flow field statistics. The results show that vorticity is generated particularly close to the reaction zone where axial strain and dilatation exhibit local minima. Thus, the emergence of flow disturbances directly in the reaction zone could be observed with the presented method. Sequences of simultaneous Mie scattering/chemiluminescence imaging at high repetition rate were additionally used to temporally track the generation of eddies in the vicinity of the reaction zone verifying qualitatively the results from quantitative conditional PIV/PTV. Measurements for different equivalence ratios and Re showed that approaching the extinguishing flame conditions only gradually changes the conditional flow field statistics.

6. High repetition-rate diagnostics

In the previous section the focus was on laser-based measurement of velocity components, gas temperatures and species concentrations. Point-wise as well as planar techniques were discussed that allow determining mean values and fluctuations. Common to all these approaches is the fact that the repetition rate was fairly low. For many combustion processes it is desirable to complement this information by additional insights. In the following, examples are highlighted, namely gas-phase diagnostics at high repetition rates ("high-speed diagnostics").

In case of low repetition rates (typically below 150 Hz) and high levels of turbulence experimental samples are statistically uncorrelated. To calculate time averaged mean quantities or *rms*-values, statistically uncorrelated sampling is a prerequisite. However, the view on specific processes occurring in turbulent flames, such as island formation in lifted jet flames, flame extinction, ignition or flash back, using first and second statistical moments of different physical and chemical quantities only is not sufficient. This can be related to the fact that the sampling rate of conventional combustion diagnostics (>5ms) is slow compared to the time scales typical for flame transients such as extinction, ignition or flash back (time scales typically below 5ms). Therefore tracking the temporal evolution of such an event and building up statistics of individual realizations of those processes urgently requires data rates in the kHz-regime. Ideally, repetition rates of the laser diagnostics are adaptable to the time scales of the transient process under investigation.

New developments in the fields of diode-pumped solid-state laser and CMOS-camera technology opened up new and exciting perspectives for turbulent flame diagnostics. Compared to previous approaches [192], much longer sequences can be monitored consisting of thousands of frames recorded during one individual process. Furthermore, due to the cyclic data storage architecture of current CMOS-cameras, the experiment can be run until the transient event occurred. Then the experimentalist releases the trigger and actually stops further data acquisition. Those frames taken before the trigger signal was released (during the transient process of interest) are stored. Thereby the "success rate" of capturing the transient event, such as turbulent flame extinction or flash back, poses no longer any limitation to the statistics.

Laser diagnostics at high sampling rates can be based on different methods. A major difficulty is that solid-state laser pulse energies at several kHz repetition rate are still limited to few milli-

Joules (unless one goes to pulse-burst laser systems [193–196]). This low energy favours the application of linear methods with high quantum yields. Techniques proved to be applicable at several kHz repetition rates are Rayleigh scattering [197, 198], Mie scattering for PIV [199] and PLIF [90]. Of course, interesting information on transients in turbulent flames can be drawn from chemiluminescence even without a laser [200].

The present section presents some more information on the instrumentation of present high speed technology for planar laser-induced fluorescence (PLIF) applications and some recent advances of diagnostics at repetition rates up to 30kHz. Examples of applications are turbulent mixing, flame extinction in a partially-premixed turbulent opposed jet burner (figure 2.1), flash-back in a premixed swirl-flame (figure 2.2(b)) and cyclic variations in a direct-injection spark-ignition (DISI) Otto engine. OH PLIF measurements are presented to show the feasibility of planar flame-radical detection at 5kHz. A recent review with the focus on multi-parameter high-speed imaging in combustion applications can be found in [201, 202].

6.1 Instrumentation for high speed PLIF applications: general considerations

Planar LIF (PLIF) is a technique that is based on resonant excitation. Tuneable lasers are therefore mandatory for electronic excitation of small molecules such OH, CH, NO, or CO. For larger molecules with broad excitation bands, such as formaldehyde [203] or commonly used fuel-tracers such as acetone or 3-pentanone [204], lasers with fixed emission wavelengths are used.

Formaldehyde or fuel-tracers can be excited electronically by radiation at 355 or 266nm emission wavelengths that are easily generated by frequency tripling or quadrupling of the fundamental of Nd:YAG lasers. To generate tuneable radiation for excitation of diatomic molecules such as OH, CH, NO, or CO, frequency-doubled or -tripled dye lasers (not yet pushed aside by all-solid-state alternatives such as optical parametric oscillators (OPO)) are most commonly used. Dye lasers and OPOs are commonly pumped by frequency-doubled or tripled Nd:YAG lasers at 532nm and 355nm, respectively. For low repetition rates and hence statistically uncorrelated information, OPOs, Nd:YAG and dye lasers were developed over many years and are commercially available.

Laser repetition rates exceeding 1 kHz are needed for acquisition of statistically correlated data. High pulse repetition rates can be achieved by either pulse bursts with high single pulse energies or continuously pulsed operation with much lower single pulse energies.

In the first approach pulse bursts that consist of between 4 and 100 single pulses are generated. Repetition rates within such bursts can be up to MHz [205] but the bursts´ repetition rate is typically ≤10Hz [194]. In [206], pulse trains of 20 single pulses were generated with pulse lengths of approximately 8ns and pulse energies of up to 400mJ/pulse at 50µs spacing (20kHz). In the next step, tuneable radiation at 226nm was generated with single pulse energies of ~0.5mJ using an OPO and sum-frequency mixing. This allowed for the tracking of NO distributions cinematographically by PLIF in a Mach 3 wind tunnel. In [207]'s earlier approach, a cluster of four double-pulsed Nd:YAG lasers was presented. Using staged frequency doubling, a pulse train of up to 8 pulses was emitted from a conjoint port. A single tuneable dye lasers was pumped with this pulse train. Pulse-to-pulse separations were 125µs (8kHz). After frequency doubling, pulse energies of 1mJ/pulse were achieved at 282nm. The beam profile quality setup was improved recently by combining radiation of four individual Nd:YAG-pumped dye lasers.

The second approach takes advantage of recent developments in all-solid-state lasers and new dye lasers specially designed for continuously pulsed high repetition rate operation. All-solid-state lasers are diode-pumped and q-switched devices in the majority of the cases. In contrast to the burst mode, laser operation is quasi-continuous. At 10 kHz repetition rate, single-pulse energies of approximately 10mJ are obtained – obviously much lower than 100ths of mJ achieved with burst mode operation. Among the all-solid-state lasers, two types are commercially available which exhibit either pulse durations above ~90ns (Quantronix, Coherent, Lee Lasers and others) or below 15ns (EdgeWave). Long-pulse lasers produce lower intensities. Therefore intra-cavity frequency conversion is required to generate VIS or UV light (such as 355nm, Quantronix Hawk-II). Shorter pulse durations allow extra-cavity frequency conversion (EdgeWave [208]). Other specifications, such as M^2-factor, can differ significantly as well.

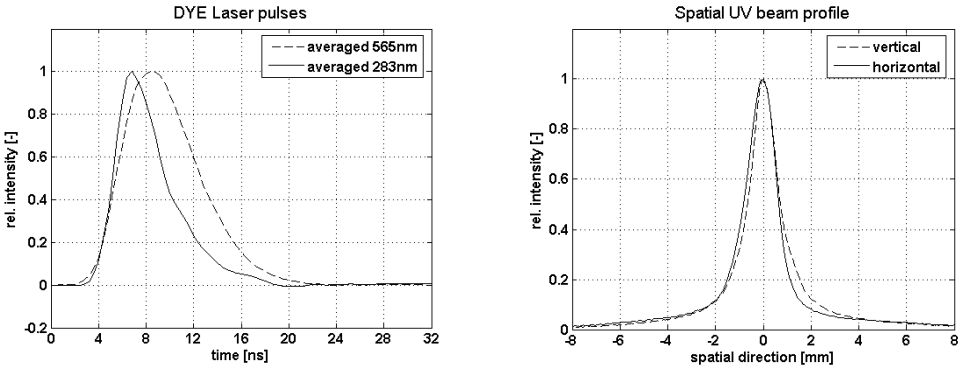

Figure 6.1
Left: Temporal profile of the fundamental and second harmonic of the dye laser system. Right: Vertical and horizontal beam profiles of the second harmonic, 2m from the doubling crystal.

UV laser pulses generated by frequency tripling or quadrupling from all-solid-state lasers can be used to excite fuel-tracers such as biacethyl [209] or combustion intermediates such as OH [210]. Frequency-doubled radiation from these all-solid-state lasers can be used to pump dye lasers to produce tuneable radiation that can be frequency-doubled into the UV-region. In contrast to the burst-mode operation the challenge here is to pump dye lasers with single-pulse energies below 10mJ but quasi-continuous power levels up to 100W. Obviously, higher pulse intensities of short-pulsed pump lasers are beneficial, especially for subsequent frequency conversion into UV. To avoid bleaching of the dye and significant triplet-state population, the flow rate of the dye solution needs to be increased. Flow rates of these devices are typically up to 12 l/min. In addition, lowest possible oscillator laser thresholds are needed. Based on the most recent laser design, at 10 kHz 2.4W were achieved around 282nm using 50W pump power (Sirah Allegro). The repetition rate of dye lasers has been extended even to 50 kHz but of the expense of single-pulse energies [211]. Typical averaged dye laser profiles in space and time are shown in Figure 6.1. Pulse-to-pulse fluctuations in the UV were reduced to below 10% rms.

Planar detection of laser-induced fluorescence needs suitable optics and a sensitive array detector. In the case of fluorescence within the UV-range, the collection lens needs to be UV-transparent and the array detector UV-sensitive. High repetition rates go along with low LIF-signal intensities. For this reason high collection efficiencies are mandatory. Figure 6.2 presents raw OH PLIF data recorded in the flame brush of an unconfined lean premixed methane air flame.

The laser system was tuned to the $Q_1(6)$ line within the $A^2\Sigma^+ \leftarrow X^2\Pi$ (1-0) band. The single-pulse energy was 22µJ. For otherwise identical conditions the UV-lens was changed from 105/f#4.5 (Nikkor) to 100/f#2.0 (B-Halle Nachfl. GmbH). This simple measure improved the signal-to-noise ratio by an order of magnitude.

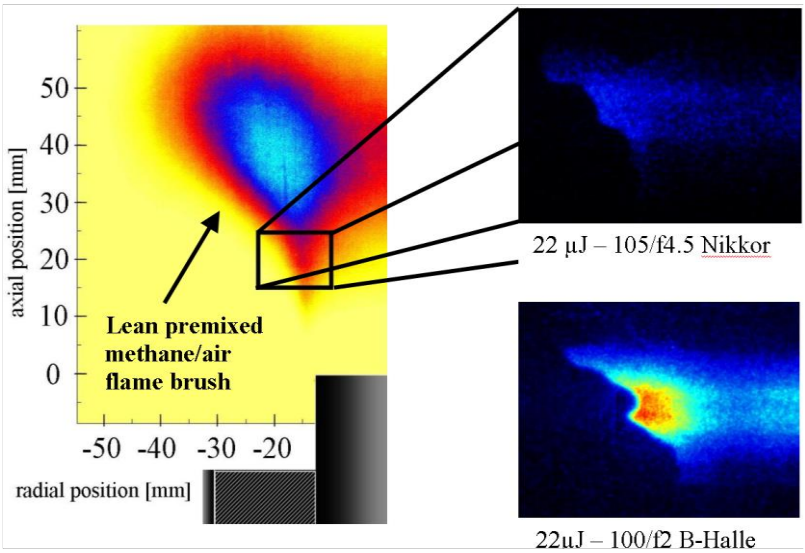

Figure 6.2
Snapshots of raw OH distributions recorded by PLIF. For otherwise identical conditions the SNR improved remarkably by increased collection efficiency of the UV-lens.

A variety of different array detectors suitable for PLIF-applications can be operated at high framing rates. An ultra fast framing camera (Hadland) was used for high speed OH PLIF, as demonstrated in [207]. It consisted of 8 independent intensified CCD cameras (CCD: charge-coupled device), each with 8bit dynamic resolution and 576 x 384 pixels. Individual events were imaged onto the respective ICCDs by a special 8-facet pyramid beam splitter. An additional intensifier was placed in front of the beam splitter at the optical entrance to the camera to increase the UV sensitivity. This camera had a maximum frame rate of 1MHz but was limited to a sequence of 8 images only.

The PSI-4 (Princeton Scientific Instruments) framing single-stage-intensified CCD camera is another type of CCD-based camera technology that takes advantage of memory buffers integrated to each pixel (*in situ* storage): it integrates up to four image sensors [212]. Each of these four image sensors is composed of an 80 x 160 pixels array. Each pixel extends by 115 x 115 µm and has its own integrated 28 element buffer memory, reducing the fill factor to about 50%. Images are transferred to the buffer with a maximum frame rate of up to ~3MHz, storing the last 28 acquisitions before a stop trigger is released.

Another CCD [213] commercialized by Shimadzu takes advantage of the *in situ* storage concept. Up to 103 successive frames can be stored with a maximum frame rate of 1MHz. This increased storage capacity has a fill factor of only 13% of the 8 x 8 µm sized pixels. The array consists of 312 x 260 pixels and the nominal dynamic resolution is 10bit. In combination with a lens-coupled IRO (intensified relay optics) this camera can be made UV sensitive.

High frame rates can also be achieved with CMOS cameras (CMOS: complementary metal-oxide semiconductors). The key difference between a CMOS array detector and a CCD is that

the charge to voltage conversion occurs at each individual pixel. In connection with a multitude of A/D –converters, the information read-out is parallel rather than serial, as in a CCD. The digitized images are transferred to an on-board memory. For a given image size and dynamic range, the on-board memory limits the number of frames that can be recorded during one run. The largest on-board memories are currently up to 16GB and record thousandths of frames during a single run. In comparison to CCDs, this feature allows temporally tracking of transients in combustion for much longer durations. This is obviously beneficial as time-intervals of interest often spread over tenths of milliseconds.

Although high frame rates exceeding 1000 kHz are possible with CMOS-cameras, the number of active pixels is reduced remarkably at these high frame rates. At lower frame rates, i.e. up to ~25 kHz, a mega pixel resolution is commercially available (for example Photron SA-Z or Phantom v2512). The dynamic range of CMOS cameras typically is 12 bit. However, in comparison to CCDs that are available at standards of scientific grade quality, CMOS cameras are less well characterized and optimized in terms of homogeneity or linearity due to them being commercialized for very different applications in industry, such as automotive crash test. These current imperfections of CMOS cameras hamper their use in quantitative scalar imaging. A calibration per pixel has to be performed to account for varying intensity offsets, sensitivities and possible non-linearities. A per pixel calibration is exemplified in [48]. A more fundamental investigation of present CMOS has been presented in [47].

Similar to CCDs, CMOS cameras are not UV sensitive. For this reason and for shorter gating times, CMOS cameras are combined with image intensifiers (lens or fibre coupled) for PLIF applications in combustion. Due to the lower LIF signal intensities at high laser repetition rates, two-stage intensifiers are commonly used. Present technology combining a MCP (multi-channel plate) and a booster allows frame rates exceeding 20 kHz without electron depletion, thus reducing the effective dynamic range.

6.2 High speed diagnostics in turbulent opposed jet flows

6.2.1 Instrumentation and setup

In a pioneering study some years ago, different types of lasers were tested. For repetition rates up to 30kHz a conventional argon-ion laser (Innova, Coherent) was used. The power was limited to 2.5W. Thereby this laser was suitable only for Mie scattering from aerosol particles that can be used to visualize mixing processes (quantitative light scattering) or for particle imaging velocimetry (PIV). For Mie scattering and PIV a dual-cavity laser was used. Pulse energies were up to 1mJ/pulse and maximal rates of double-pulses up to30 kHz (Nd:YVO_4 IS4II-DE, EdgeWave).

For planar laser-induced fluorescence (PLIF) of radicals relevant to combustion processes such as hydroxyl (OH), tuneable radiation in the ultraviolet spectral range is required. For this purpose an extra-cavity frequency-doubled diode-pumped solid-state Nd:YLF-laser (Edge Wave) was operated at 5kHz repetition rate to pump a tuneable dye laser. The average power of the pump laser peaked up to 17W (more recent lasers based on the same operation principle provide well above 100W quasi-cw power). This corresponded to single-pulse energies of 3.4mJ. The pulse length was below 10ns. The dye laser was based on a conventional system designed originally for 10Hz operation (Radiant Dyes). To adapt the dye laser to the needs of high repetition rates, at these early times of technology development several modifications of the laser were essential (nowadays high speed dye lasers are commercialized and are optimized for low pump

pulse energies). The low pump energies allowed pumping only the oscillator and the preamplifier. Consequently no main amplifier was operated. The dye cuvette was connected to a dye circulator equipped with a stronger pump than in 10Hz-applications and a larger dye reservoir. Flow rates of the dye were 12l/min. The delay-line of the beam pumping the preamplifier was shortened. A general issue was the long-term stability. To reduce thermal drifts, the rear panel of the cuvette mount was water-cooled. The output coupling mirror was shielded by masks from both sides to prevent heating of the mount by radiation other than the laser beam. The maximum average output power achieved at 283nm was 150mW. This corresponds to pulse energies of 30µJ. The spectral width was approximately 0.04cm^{-1} based on etalon measurements.

Signals from chemiluminescence (CL), Mie scattering and fluorescence, respectively, were monitored by a state-of-the art CMOS-camera (HSS5 or HSS6, LaVision). At maximal repetition rates of 30kHz the exposure time was 10µs. At this high repetition rates 256x256 pixels of the CMOS (HSS5) were active. At 10kHz the usable area of the array increased to 512x512 pixels. The A/D-conversion had a dynamic range of 10bit. If not stated otherwise the CMOS-camera was equipped with a lens-coupled two-stage image intensifier (High Speed IRO, LaVision). In case of 5kHz-PLIF the gate width of the IRO was set to 100ns. For Mie and CL-measurements the gate width was in the order of few µs.

Several flow configurations were investigated, namely the turbulent opposed jet (figure 2.1), the swirling flow (figure 2.2) and an in-cylinder flow of a DISI engine. In the turbulent opposed jet configuration, the non-reacting mixing layer was investigated by Mie scattering off aerosol particles. Aerosol was seeded hereby only to the lower fluid flow. In case of reacting conditions CL and Mie were measured simultaneously during extinction of a partially-premixed flame. In this case both flows were seeded. The fuel was composed of 17.4vol% CH_4 in air. The Reynolds-numbers were 7200 corresponding to flames at the extinction limit (compare section 2).

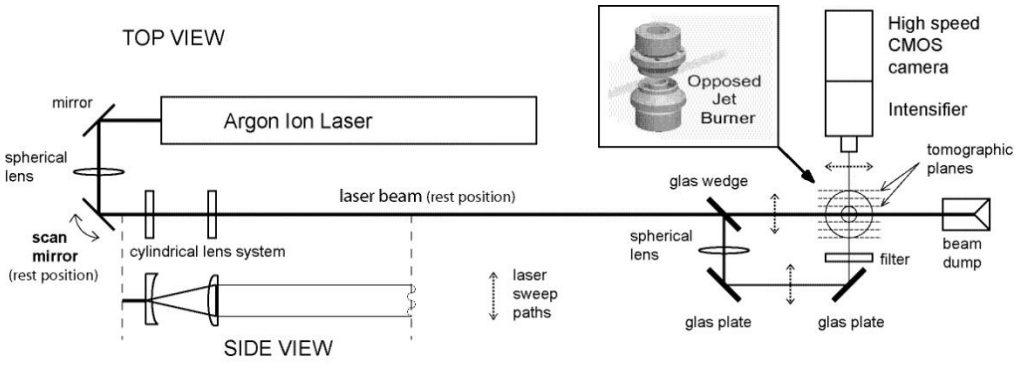

Figure 6.3
Optical setup for Mie scattering experiments in the opposed jet configuration.

Figure 6.3 shows the optical layout of the Mie experiment using the argon-ion laser. The laser beam was formed to a light sheet 20mm in height and 1mm wide. The beam was scanned across the probe volume by a galvanic mirror (GSI Lumonics). The maximum scan rate per sweep was 2kHz. Multiple 2D-planes were monitored successively over a range of 15mm. The depth of field of the camera lens was adapted to this range. The field of view in this case was 12x12mm. In case of the simultaneous CL- and Mie experiments the argon-ion laser was replaced by the pulsed solid-state laser as mentioned above.

The swirling nozzle is shown in figure 2.2(b). The swirl number S was changed by a stepper motor connected to a gear box. Minimal increments were 0.02. For $S < 0.8$ the flame was stable.

At $S \geq 0.8$ the flame passed over into a metastable state. The stabilization point left the rim of the central bluff-body and moved upstream to the shell of the bluff-body. Additionally the flame spun around the bluff-body. Passing $S = 1.0$ the flame flashed back into the nozzle. Figure 2.5 shows snap-shots of the CL for different swirl numbers taken at a repetition rate of the CMOS-camera of 7.2kHz.

With the OH-PLIF-experiments at repetition rate of several kHz new ground was broken. So far OH-PLIF-measurements were restricted to 1kHz [214]. The dye laser was tuned to the $Q_1(5)$-line in the $A^2\Sigma$-$X^2\Pi$ (1-0)-band. The laser sheet height was approximately 15mm. OH-radicals were monitored in the flame shown in figure 2.1. The scope was to measure the temporal variation of the OH-radical distribution in combination with 2-component-PIV. During this study the signals were not corrected for pulse-to-pulse fluctuations of the total energy or variations in the laser profile.

6.2.2 Results and Discussion

6.2.2.1 Mie scattering at 30kHz

In non- and partially-premixed flames reaction takes place within the mixing layer of fuel and oxidizer streams. It is therefore of special interest to visualize and understand the dynamics of turbulent mixing layers. A generic bench mark for such investigations is the turbulent opposed jet configuration.

The turbulent non-reacting mixing layer in the turbulent opposed jet configuration, shown in figure 2.1, was investigated by Mie scattering where only the lower flow was seeded by aerosols. Figure 6.4 shows an example of a sweep of the laser beam across ±7.5mm around the symmetry axis of the burner. The repetition rate of the CMOS-camera was 30kHz with an exposure time of 10µs. The clearance between the 15 measurement planes varies according to the sinusoidal motion of the scanning mirror. The Reynolds-number in this example was 7200. The duration of the complete sweep was 500µs, well below large-eddy turn-over times in the order of 16ms (compare table 2.2). Thereby the instantaneous eddy appears frozen during the sweep. From this multiple 2D-information the topology of the mixing surface between both flows can be reconstructed in quasi-3D.

As the sweeps were repeated temporally at 2kHz, one can monitor the temporal evolution of the mixing layer. For this purpose, 2D-images as in figure 6.2 were converted to binary images. Using 15 binary images from a single sweep, the quasi-instantaneous 2D-interface between upper and lower fluid flow was reconstructed by a triangulation procedure. Figure 6.5 shows the temporal evolution of the mixing layer. In this figure only every 3rd sweep is shown (1.5ms between images). This shows the feasibility for quasi-4D-diagnostics using repetition rates in the kHz-regime. More recently mechanical have been advanced in terms of the scan rate [215] or have been replaced by acousto-optical deflectors [216].

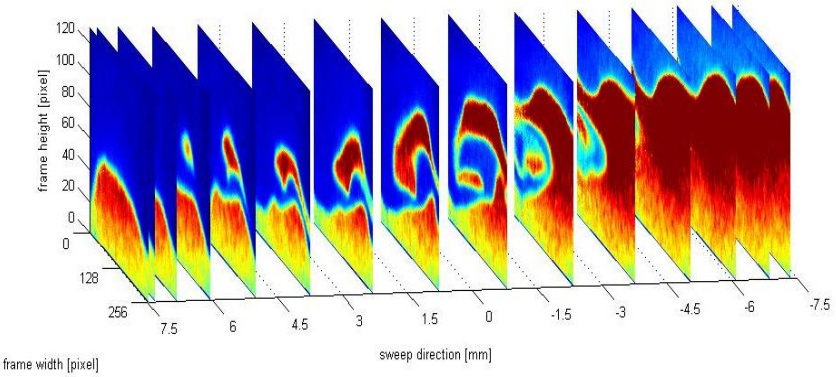

Figure 6.4
Mie scattering from aerosols shown in false colors. These 15 planes have been recorded consecutively during 500µs (30kHz).

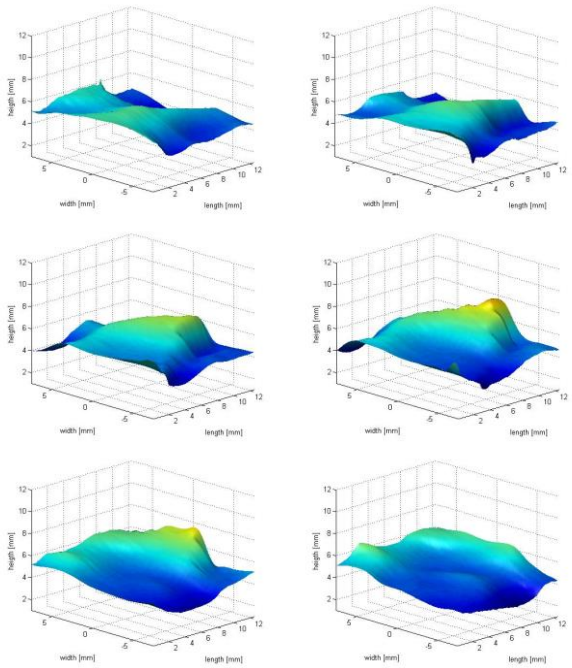

Figure 6.5
Each of the six images shows an instantaneous mixing layer reconstructed from multi-2D-Mie scattering images during one sweep as shown in figure 6.4.

6.2.2.2 Simultaneous Mie scattering and chemiluminescence

Under chemically reacting conditions Mie scattering can be combined with chemiluminescence. Whereas the particles observed by Mie scattering represent the turbulent fluid motion in a two-dimensional plane, chemiluminescence gives an estimation of the approximate flame position. In the example shown in figure 5.10 the CMOS-camera (without IRO) was operated at 1kHz while Mie scattering of 0.5µm-MgO-particles was laser-excited at 10kHz. Each exposure

shows particle trajectories of up to 10 subsequent particle positions in top of the chemiluminescence image. In the selected example the formation of an eddy is highlighted. The formation of such eddies generate vorticity when the fluid approaches the turbulent flame located in the vicinity of the mean stagnation plane (compare section 5.2.3).

6.2.2.3 High speed PIV conditioned on extinction

Replacing the chemically inert MgO-particles by oil droplets and instead of using chemiluminescence, the transient location of the flame front can be monitored in a two-dimensional plane due to droplet evaporation in areas of elevated temperature.

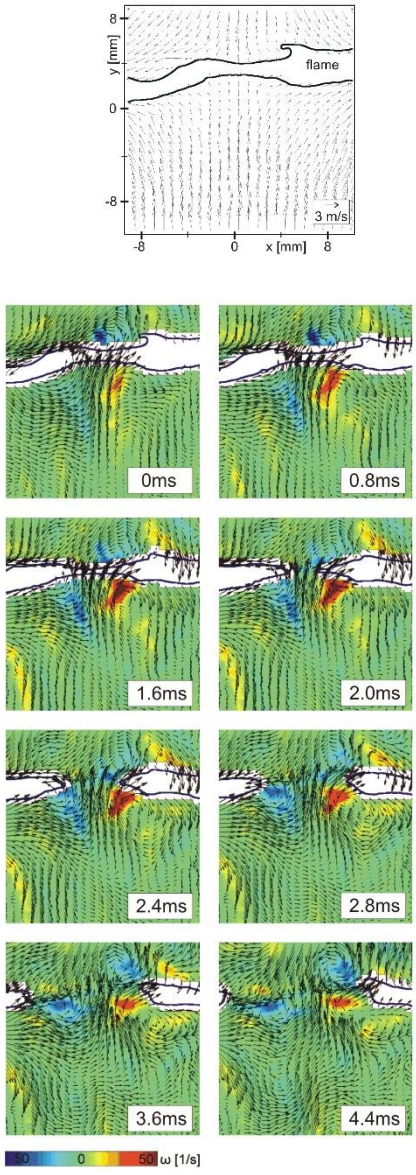

Figure 6.6
The top of the figure shows the transient flow field prior to extinction. The location of the flame is represented by the white areas. PIV-evaluation was possible only in the cold gases where the

aerosol droplets have not yet evaporated. The bottom of the figure shows the filtered velocity maps during extinction. Filtering was based on a POD-decomposition.

The Mie scattering from the cold gas can be used simultaneously for processing instantaneously two velocity components. In the following example, double pulses from the Nd:YVO_4-laser with a pulse-to-pulse separation of 50µs were generated at an overall repetition rate of 2.5kHz. The CMOS-camera was operated without IRO. The data post-processing was based on a PIV-algorithm presented in section 3.1.3. Interrogation areas of 16x16 pixels corresponded to 400x400µm^2 in the measurement plane. The top of figure 6.6 shows one individual velocity map out of a sequence consisting of up to 4500 exposures.

The aim of this experiment was to track the temporal development of eddies approaching the flame front and causing flame extinction. For this purpose a proper orthogonal decomposition (POD) of the considered data set was conducted [217]. POD provides an optimal set of basis functions for the selected ensemble of data. For each velocity map time-dependent coefficients were extracted resulting in an amplitude spectrum. This spectrum was band-pass filtered. A band-pass filter was chosen such that mean velocity and large-scale shear was subtracted. Finally, in a back-transformation a velocity map was reconstructed that carried mainly the information of the vorticity. The lower part of figure 6.4 shows a temporal sequence of filtered velocity maps. In this example modes (n,k) for n,k = 3-10 in the amplitude spectrum were used. The first frame in this sequence corresponds to the unfiltered velocity map shown in the top of this figure. Obviously, filtering in the POD-domain allows visualizing vortices.

In figure 6.6 the instantaneous flame position in the measurement plane is shown by white areas. The selected sequence shows the onset of flame extinction in a time-resolved manner. It can be observed that the flame is thinned over a period of few ms. This thinning is a consequence of a counter-rotating pair of vortices located on the fuel side. During the extinction process the location of the counter-rotating vortices is moving only marginally. In between the vortices a high local fluid flow is observed penetrating into the flame.

This experiment has been optimized by monitoring the instantaneous position of the flame front by using the OH radical distribution recorded at 5 kHz and simultaneously with the velocity taken from the 2-component-PIV measurements [218]. Figure 6.7 shows two individual measurement sequences prior to extinction, spanning from t*= -4.4 to +0.8 ms (N.B. frame-to-frame intervals in this figure are not identical). Instantaneous OH contours are represented by black lines. Imposed on the instantaneous velocity vectors are the POD-filtered out-of-plane vorticity and the absolute values of the strain, calculated from the two velocity components. Up to approximately 4 ms prior to extinction regular patterns were not observed in the vorticity or strain fields. Turbulence appeared as stochastically distributed eddies in space and time. Starting from approximately t* = -4 ms, characteristic flow field structures observed to appear and peak strain and vorticity values increased progressively.

Inspection of 14 individual data sequences revealed two classes of extinction events. For 8 cases we observe two counter-rotating vortices from the fuel side convecting towards the lower OH contour (denoted as Class I, shown in Fig. 6.7a). These eddies align below the flame. By expansion due to heat release at the flame front the vortices distorted radially. They lingered in approximately the same spatial location as their vorticity rapidly increased. The centers of rotation of each eddy stabilized approximately 2-3 mm below the lower OH contour and were radially separated from each other by 5-6 mm. The magnitude of the radial separation was likely driven by the lengthscale of the turbulence enhancement plates (interhole spacing: 5 mm). The

counter-rotating vortices transported fuel that impinged perpendicularly (in a jet-like manner) upon the flame front to produce greater compressive and extensive strains. Strain increased with vorticity until t*=-0.8 ms. By that time the OH-contour began to contract and was finally breached at t*=-0 ms. Convection pushed the flame tips in opposing radial directions. After the breach occurs, convection appears to dominate the flame's radial propagation. In rare cases (not shown here), flame breaches were observed to occur in the vicinity of the mean stagnation point and then collapse and convect outwards to allow the reestablishment of a self-sustaining turbulent flame.

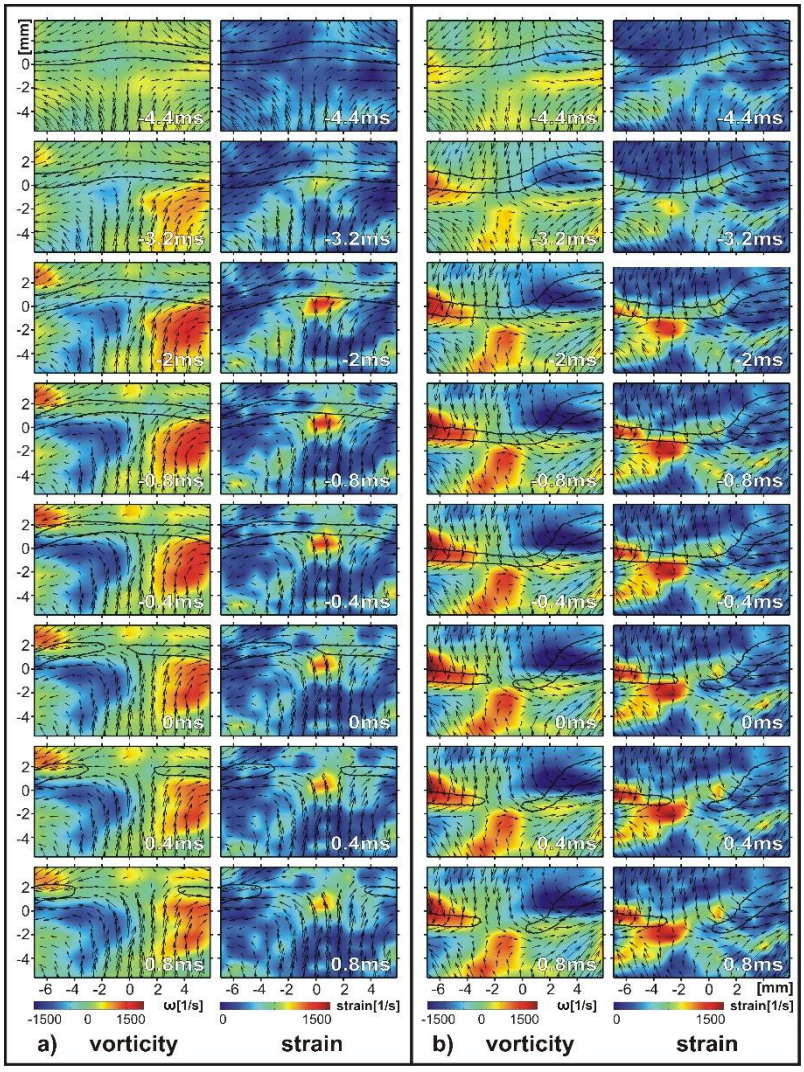

Figure 6.7
Two individual sequences of extinction. Vorticity and strain are superimposed by false colours in top of the in-plane velocity vectors. Look-up tables in all cases are identical. Instantaneous locations of the OH contours are presented by black lines.

The remaining 6 extinction events were classified as Class II events. In general they showed less regularity than Class I extinctions. Figure 6.7b shows one of six events. A counter-rotating vortex pair originating from the air side and a single vortex from the fuel side surround the

flame starting from t*=-5 to -4 ms. These vortices were smaller and more distorted than in Fig. 6.7a. During the vortex-flame interaction the flame becomes significantly distorted. In a manner reminiscent of Class I events however, a region of high strain developed just below the lower OH contour. For both Class I and II type events, peak strain values are observed to be of the same order of magnitude. In Class II events flame tips resisted the radial direction convection for a longer period. This could be caused either by different local mixture fraction distributions or by lower instantaneous radial velocity at the location of the flame tip. No experimental evidence of the former is present, however evidence of the latter was observed at the left side of the flame between t*=0 and 0.8 ms, as shown in Fig. 6.7b

These single temporal sequences show that vorticity does play a vital, but not exclusive, role in understanding extinction of turbulent opposed jet flames. A few ms prior to extinction, multiple vortices acting coherently generate strain over extended regions close by the flame. According to Lemaire et al. [219] peak strain was identified to be a significant controlling parameter. However, in Katta et al. [220], based on numerical simulations, unsteady flames were observed to resist strain twice the extinction level of laminar flames. Single sequences shown in Fig. 6.7a and b exhibit strain increased locally up to 1500 s^{-1}. To draw further conclusions, extinction progress must be averaged appropriately. This is accomplished by multidimensional conditioning in space and time, as detailed in the previous section.

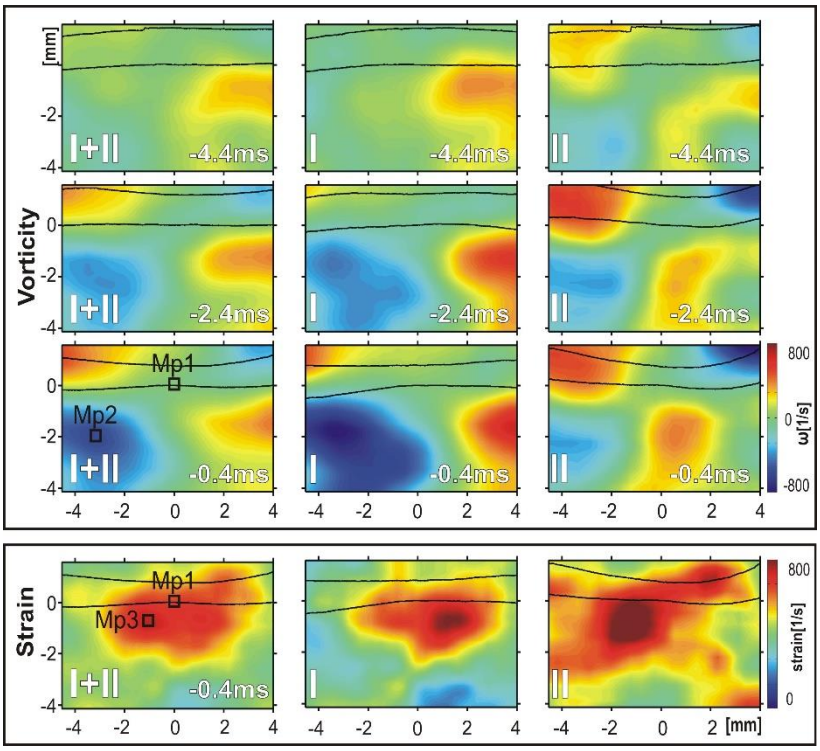

Figure 6.8
Conditional averages of vorticity and strain for all events (I+II), class I and class II events at distinct times prior to extinction.

Figure 6.8 shows the conditional average of POD-filtered out-of-plane vorticity and two-component strain for all 14 experiment runs (I+II, left), as well as for Class I (middle) and Class II

cases (right) separately. The black lines denote the mean OH contours. Vorticity fields are presented for t*=-4.4, -2.4 and -0.4 ms whereas strain is shown only for t*=-0.4 ms. Conditional averages of the temporal evolution of both vorticity and strain for Class I as well as for Class II support the conclusions drawn already from the single events. Class I showed primarily strong counter-rotating vortex pairs from the fuel side, causing a distinct region of peak strain values. Class II showed less regular vortices predominantly from the air side. The shape of individual vortices and regions of high strain differed for individual extinction sequences. Consequently, peak values in the conditional mean data were reduced by a factor of approximately two compared to individual progressions. Despite the differences in the conditionally averaged vorticity fields areas of maximum strain were observed to align in all cases (I+II) slightly below the lower OH contour.

The measured strain components can only give an approximation of the principal strain rates because the flow measurements are limited to two components of the flow field. The absolute strain given in this work includes only two components of strain while the flame experiences an additionally extensive component out of the measurement plane. Because the flame is approximately horizontal with slight inclinations caused by eddies it can be assumed to be normal to the measurement plane and thereby the out of plane component is approximately a principal strain rate [118]. The conditional average of the axial strain component acting compressive (negative) and radial component extensive (positive) are shown in figure 6.9 for all 14 runs (I+II). Two local maxima of extensive strain begin to form at t=-4.4 ms in the region of the lower OH-contour ~1-2 mm radially to the right and left of the point were extinction is going to occur (z*=0, r*=0 mm) while a maximum of compressive strain is formed in-between these peaks at the lower OH-contour just below the region where the OH layer is breached first.

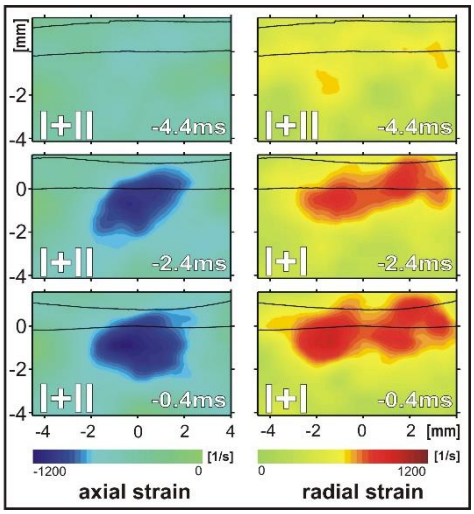

Figure 6.9
Conditional averages of axial strain (acting compressive) and radial strain (extensive) for all events (I+II) at distinct times prior to extinction.

For a more quantitative representation of the conditional averages, Fig. 6.10 shows temporal evolutions of strain and vorticity recorded at various monitor points. The spatial location of each monitor point is shown in Fig. 6.8. The temporal traces proceed only up to t*=-0.2 ms as the definition of z* is based on continuous OH contours. MP1 corresponds to the origin of the

newly introduced conditional co-ordinate system. MP2 is at the maximum of the conditionally averaged vorticity and MP3 is at maximum strain (compare Fig. 6.8, left column). Independent of classification, at MP1 and MP3 the conditional average of the strain was constantly 400s^{-1} up to 5 ms prior to extinction. These early times correspond to statistically stationary turbulence. Strain increased from a conditional average of 400 s^{-1} at t*=-4.4 ms to 700 s^{-1} (MP1) and 800 s^{-1} (MP2) at t*=-1.4 ms. The conditional average subsequently decreased slightly until the flame breached. Minimum and maximum values of conditional strain are shown by bars in Fig 6.10d. These bars do not indicate error ranges but rather the variability due to randomness of the turbulent flow field. In contrast to strain at MP1, conditional vorticity remained close to zero at all times. However, at MP2 the absolute value of conditional vorticity increased in a similar manner as the strain until it reached a plateau at t*=-1.4 ms (I+II). Differences in vorticity between Classes I and II were observed. For Class II, absolute values still increased, whereas in Class I, vorticity decreased.

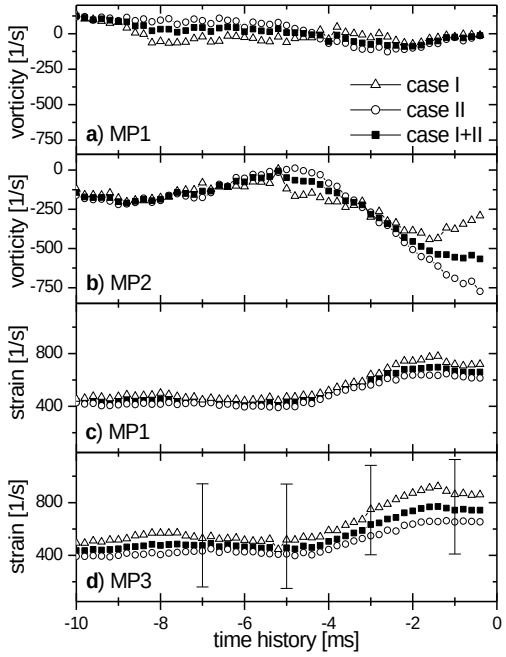

Figure 6.10
Temporal traces of conditional averaged vorticity and strain at monitor points (MP) assigned in Fig. 6.8.

MP1 is the location where the flame is first breached. Only conditionally averaged strain increased at this location. This indicates that for this type of turbulent flame, while vorticity acts to generate strain at distinct locations close to the flame, the magnitude of the vorticity is not as important as that of the strain for determining extinction. Traces of conditionally averaged strain pass a weak maximum at t*=-1.4 ms. This is a clear indication that peak strain values alone are not an appropriate measure to determine extinction for these unsteady flame conditions.

This finding is in agreement with Katta et al. [220]: Strain describes the flow structure. If strain is generated faster than diffusion time-scales, diffusion is delayed with respect to velocity imposition. Consequently non-equilibrium flow may occur, as described in Katta et al. [220]. During non-equilibrium situations, either of the two following mechanisms might be responsible for final extinction:

1) An increased flux of reactants into the reaction zone cools the flame, reduces reaction rates and promotes extinction.
2) The local Damköhler number will be decreased, also promoting extinction.

Increasing strain creates large scalar gradients. These gradients should reveal themselves by high values of scalar dissipation rate (SDR). Unfortunately, the temporal evolution of SDR conditioned to regions of high strain was not measurable in this experiment. Therefore, the hypothesis from Katta et al. [220] that even SDR is an insufficient measure of extinction in unsteady flames and for chemical non-equilibrium conditions (chemistry- rather than diffusion-limited conditions) could not be evaluated experimentally.

6.2.2.4 Conclusions on turbulent opposed jet investigations

Previous experimental studies using simultaneous PIV/OH-PLIF on a turbulent, opposed jet flame were extended from 1 Hz to 5 kHz. This enabled the acquisition of statistically dependent datasets and allowed for tracking of the evolution of vortex-flame interactions in real time. Previous studies of PDFs of scalar dissipation rate (SDR) have displayed statistical errors at the peripheries, which are exactly the regions of the PDF most closely associated with extinction (as high SDRs are believed to cause extinction). The technique employed in this study allows one to focus specifically on the small fraction of measurement time directly relevant to extinction and thus vastly increases the accuracy, resolution and physical insight of experiments relating to this important phenomenon.

For the flame studied, two classes of flow structure leading to global extinction were identified. The newly introduced technique of multidimensional conditioning used new criteria to compare individual extinction events in a meaningful, statistical manner and avoid smearing important spatiotemporal information. It was found that turbulent vortices generate strain close to the flame and that extinction occurred when the resulting increase in strain exceeded critical values for sufficient time. Although strain was a more important measure for extinction than vorticity, peak strain alone was not a sufficient measure to predict extinction.

6.3 Chemiluminescence at 10kHz to observe flash back in lean premixed flames

Lean premixed combustion offers the potential for low NOx-emissions. These flames, however, are hindered in their application as they are prone to instabilities and flash back. Therefore more knowledge is required to predict the transient behavior of such flames.

The burner presented at the right hand side of figure 2.2(b) was designed to investigate the transition from stable flames into flash back. With the central bluff-body sticking out of the nozzle exit plane by 20mm a meta-stable state of the flame can be achieved that can be stabilized between stable operation and flash back. This state is connected to a precession of the flame around the shell of the bluff-body [11]. Approaching a Reynolds-number dependent critical swirl number, the flame looms into the annular slot during precession. To enable optical observation of the flame dynamics during flash back, the outer tube of the burner was replaced by a quartz tube.

Figure 6.11 shows a sequence of chemiluminescence images during the event of a flash back. Tracking the temporal dynamics of the flame continuously is the only possibility to capture the point in time where flash back occurs. Thereby characteristics such as flame propagation speed

can be measured conditioned on the transient event and during flash back. Conventional repetition rates of several 10Hz would be much too slow to capture the onset and dynamics of such an event.

At the critical swirl number most of the times the flame extends into the slot. The arrow in the image at t = 0ms marks the instantaneous flame tip from which the flame shoots upstream subsequently. During this upstream movement the flame spins around the bluff body. Within 4ms the flame covered a distance of 14mm. This corresponds to an average axial velocity of 3.5m/s. During other events the velocity peaked up to 12m/s. The turbulent burning velocity is much less. In [11] for the present conditions it was estimated to be below 2m/s. As the kinematics of the premixed flame front can be determined by the vectorial addition of turbulent burning velocity and convection, the flash back must be caused by instantaneous negative axial gas velocities. This finding actually was confirmed by PIV-velocity measurements conditioned on the flame tip [221]. More recent PIV/OH PLIF high speed measurements provide even more details into the mechanisms of flash back [10].

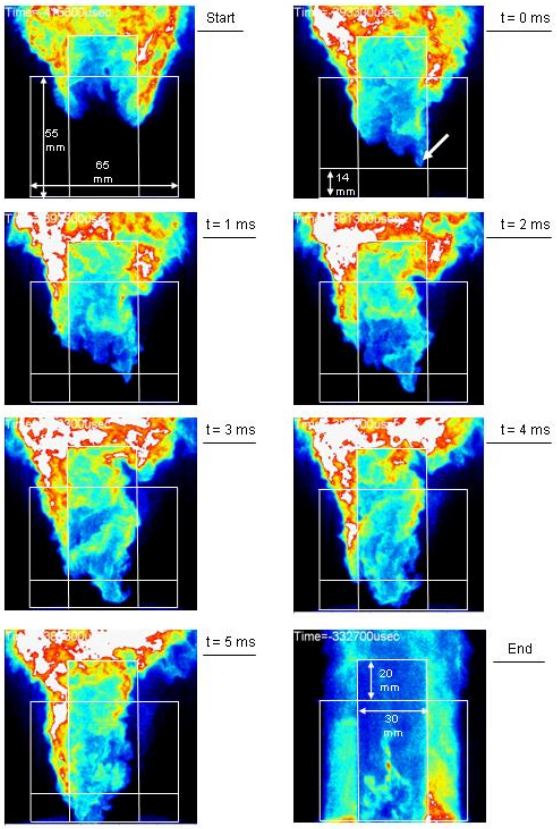

Figure 6.11
Sequence of CL-images during flash back in the annular slot of the burner presented in figure 2.2(b). Although the IRO/CMOS-data rate was 10kHz only every 10th image is shown in the sequence labeled 0 to 5ms. Finally the flame stabilizes at the swirler assembly inside the nozzle.

6.4 High speed flow field measurements in an DISI engine using PIV

A key challenge with present engine development is an improved understanding of cyclic variations [222]. During the intake and compression stroke, variations of the intake and in-cylinder flow field occur that impact fuel/air mixing and ignition. These variations result in differing

early flame kernel development or even misfire, effecting engine efficiency and emissions of pollutants such as unburned hydrocarbons. Although origins of cycle-to-cycle variations (ccv) have been investigated since more than 100 years [223], the interest has been renewed with the advent of direct-injection spark-ignition (DISI) engines introduced in 1996 [224]. Compared to homogeneous charged operation, stratified charging especially at idle and light load reveal increased levels of ccv.

A closer insight into origins of ccv is based on instantaneous recordings of in-cylinder conditions. Such experiments are performed mostly by using planar laser diagnostics due to their inherent high temporal and spatial resolution [225]. Recent laser-based studies specifically on ccv can be divided into scalar and flow field measurements. Scalar field measurements aim to monitor local equivalence ratios near the spark plug at the instant of ignition or to identify variations during the early flame kernel development [90]. In flow field studies two velocity components are measured in selected planes using 2C-PIV (2-component particle image velocimetry). Until recently, repetition rates of flow and scalar field measurements were restricted to one exposure per cycle [90]. This restriction resulted in observations of statistically uncorrelated instantaneous realizations of the flow field from which maps of the first two statistical moments perpendicular or parallel to the cylinder axis were calculated. Depending on the vortices sizes, large-scale coherent structures were separated from small-scale fluctuations, sometimes named "true turbulence" [226]. Whereas small-scale structures are believed to be isotropic, large-scale structures are associated with cyclic variability of the flow [90].

This "high-speed" technology has been already applied successfully to in-cylinder flow [78, 227, 228] and mixing field measurements [209]. [227] analyzed ccv associated with low frequency structures by subtracting the 'ensemble mean velocities' from the low pass filtered flow fields giving a measure of the spatially resolved cyclic variability. These were recorded with a resolution of 128x128 pixels. [228] extended this approach to a higher resolution using 512 x 512 pixel arrays. Different to these approaches [81] quantified cyclic variations using a proper orthogonal decomposition scheme. These authors analyzed 64 cycles from cinematographic PIV to deduce temporal evolutions of time-dependent flow patterns. In their findings an initial increase of ccv during the compression stroke was observed that decreased when the top dead center (TDC) was approached. In [229] UV-PIV at 6 kHz was applied to measure two components of the in-cylinder velocity field in a 15x15 mm^2 region near the spark plug. Ensemble-averaged kinetic energy and turbulent kinetic energy were calculated for progressively increased band-pass filters showing the transfer of energy from larger to smaller scales during the cycle.

On the basis of these previous studies the present investigation [80] aims to monitor the in-cylinder flow field by cinematographic 2C-PIV but with a significantly increased field of view reaching 43 x 44mm^2. For instance, due to improved CMOS camera technology, 73 cycles with a resolution of one degree crank angle (CA) at 1000rpm were recorded. The temporal evolution of the compression stroke was recorded spanning over 80° CA until TDC. Although this enlarged field of view comes along with a reduced signal-to-noise ratio, at early stages of the compression stroke more than 75% validated vectors were achieved. This allowed tracking of the large-scale tumble charged motion from which ccv were deduced for different engine operation conditions.

6.4.1 Experimental setup

A schematic of the optically accessible internal combustion engine together with the PIV setup is shown in figure 6.12. The engine was a one cylinder spray-guided, spark-ignition, direct-injection engine with an 82 mm bore and an 86 mm stroke with a compression ratio of 9.6:1. It uses a central mounted injector and a spark plug mounted at the side as indicated in figure 6.13, both of which were removed for these isothermal investigations. It was optically accessible through a 30 mm high quartz-glass ring forming the upper part of the cylinder (cylinder window). Additionally, two pent roof windows on both sides as well as a quartz window embedded into the flat piston crown enabled the camera to record the flow field. The cylinder head was preheated to 80°C to mimic steady-state engine conditions and was equipped with a horizontally dividable twin inlet manifold. By closing the lower half of the twin inlet manifold pipes, a tumble charged motion was induced. The tumble motion was oriented parallel to the cameras field of view.

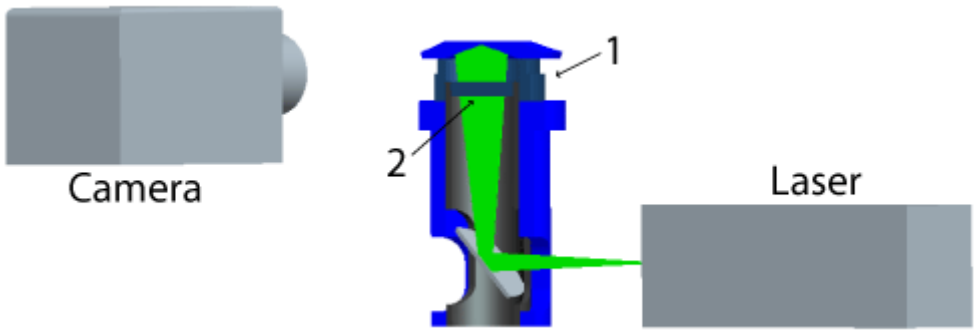

Figure 6.12
Experimental setup; 1: Quartz glass ring and pent roof windows; 2: Piston crown glass disc

The main focus of the temporally resolved velocity measurements was on the compression stroke, being relevant for cyclic variations due to impact on fuel/air mixing, ignition and combustion. The engine was motored at 500, 1000 and 2000 rpm (see table 6.1) without firing. The compression stroke was tracked temporally by 40 to 160 images depending on the engine speed spanning from 80° BTDC (before top dead center) up to TDC. As each data set consisted of approximately 5800 vector fields due to the cameras on-board storage capacity (8GB) up to 146 subsequent cycles were recorded during a single engine-run.

Table 6.1 Overview of experimental configurations and variation of parameters.

Engine speed [rpm]	No. of recorded cycles	No. of images/cycle	PIV time delay [µs]
500	36	160	60
1000	73	80	20
2000	146	40	10

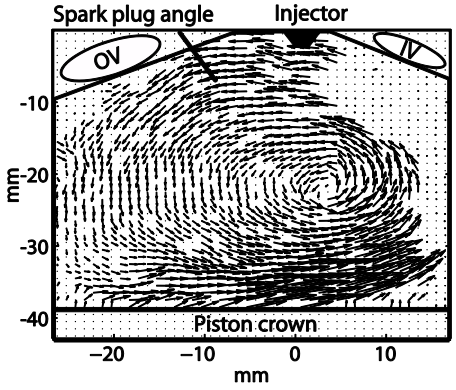

Figure 6.13
Field of view of in-cylinder flow field; OV: outlet valve, IV: inlet valve

High speed PIV was used to capture the transient behavior of the instantaneous flow field. For this purpose a frequency-doubled, dual-cavity Nd:YVO_4 slab laser (Edgewave, INNOSLAB) operated at 532 nm with a pulse energy of 0.7mJ/pulse was used. The repetition rate was set to 6 kHz with a pulse to pulse separation of 10-60 µs according to engine speed. The laser beam was formed into a light sheet and then guided through the piston window into the cylinder. The light sheet width was ~45 mm with a thickness of ~1 mm. Light scattered by oil droplets was recorded at right angles through the quartz glass ring and the pent roof window by a CMOS camera (La Vision, HSS6). The pixel-resolution of the recorded images was 62.5 µm and the field of view spanned 688x704 px, resulting in a spatial resolution of 43x44 mm^2. The seeding oil was generated by an aerosol generator (Palas) using hydraulic oil (Liquimoly). The size of the droplets was ~1 µm. Seeding was led into the intake air resulting in a homogenous droplet distribution within the cylinder.

Data processing was based on a PIV-algorithm presented in [62]. A multipass interrogation with window shifting was used with a final grid consisting of 16x16 px, resulting in a resolution of 1x1 mm. The number of valid vectors depends on operational conditions. In general, at low engine speeds and low gas densities and at early crank angle degrees during the compression stroke, the quality of the PIV data was above average and spurious vectors occurred predominantly at the edges (piston crown, cylinder head). For example, at 1000 rpm ~75% valid vectors were achieved at 60° BTDC while this number decreased monotonically to ~55% at 20° BTDC. This decline is caused by the evaporation of the droplets during the compression stroke leading to a decrease in particle size and to deposits on the windows which began to appear predominantly at the cylinder head. For this reason the vector fields were filtered carefully using a set of filters based on the signal-to-noise ratio, the correlation peak height as well as a comparison with the local neighboring vectors to remove inconsistent vectors.

6.4.2 Results and discussion

To give an overall impression of the flow field, a sequence of ensemble averaged flow fields is presented in figure 6.14. It was calculated from 73 consecutive engine cycles for a tumble charged motion at 1000 rpm. The engine speed of 1000 rpm was selected as the standard case in this work, from which variations of speed are shown for comparison. The investigated crank angle range spans from 80° BTDC until TDC corresponding to the time period when fuel is

injected and ignited. During this period local flow fluctuations may lead to poor combustion or even misfires as observed by [72]. This may happen for example when an elongation of the spark or the early flame kernel moves in opposite direction away from the ignitable mixture.

The tumble motion can be observed with a vortex diameter of about 20-30 mm. During compression the vortex is squeezed vertically and moves diagonally towards the upper right corner. The strong vortex is visible until ~30° BTDC. Beyond that the quality of the vector field is poor due to evaporating seeding and deposits on the upper part of the pent roof window. Note that in this work the isothermal flow was investigated only for a motored configuration without any injection of fuel.

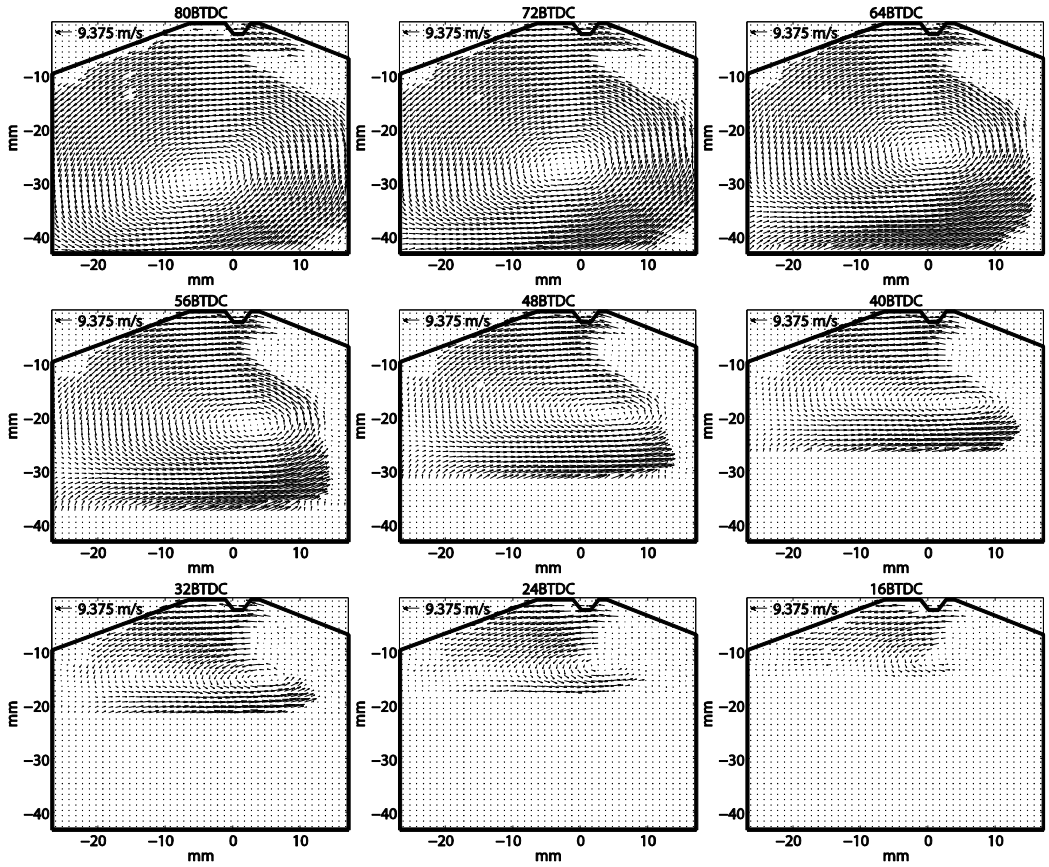

Figure 6.14
Temporal evolution of the ensemble averaged flow field at 1000 rpm, tumble charge motion

Tumble Vortex Center

To characterize the tumble motion and its progress in more detail the vortex center was detected based on the vorticity map as demonstrated in figure 6.15. The vortex center was located as the interrogation window with the highest vorticity peaks. An additional criterion similar to [81] was that the velocity field of this interrogation window had to present a minimum according to its adjacent velocity vectors. To accomplish this, a sub region of the flow was selected which included the vortex center for the investigated crank angle range. In a first step spurious vectors were removed using sets of conventional PIV filters and then interpolated using neighboring velocity vectors. Furthermore, a proper orthogonal decomposition (POD) for the selected ensemble of data was performed. This provides an optimal set of basis functions. The first 20 modes containing more than 99% of the kinetic energy were selected to reconstruct the flow

field in a reverse-transformation. Because spurious vectors contribute to high frequencies (corresponding to high modes) the removal of them effectively corrects the vorticity map. Otherwise the spurious velocity vectors would contribute on a large scale to the vorticity map and dilute its validity. As the flow contains vortices of different size and strength an additional 2D-Gaussian low pass filter was applied to separate the large tumble flow structure from the smaller underlying vortices. The $1/e^2$ width of the Gaussian filter was set to 20 mm in order to only retain the large vortex structure.

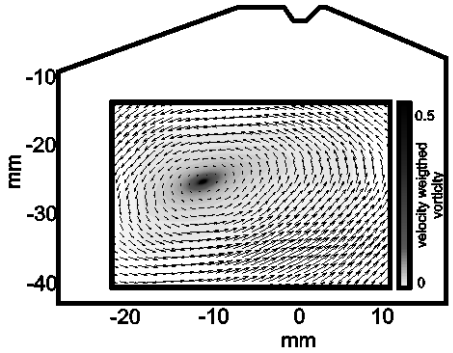

Figure 6.15
Vortex center detection (1000rpm, tumble charge motion): The indicated region of the flow was used to identify the vortex center. The zoom shows the filtered flow field in which a POD was applied to remove the spurious vectors. Additionally, it was filtered using a low pass Gaussian filter to extract the large scale structures only. The background color gives the velocity weighted vorticity field; the identified vortex center is marked by a circle

Figure 6.16a shows the averaged location of the vortex center obtained from 73 individual cycles during compression stroke from 80 to 62° BTDC. During this time period the piston moves upwards displacing the vortex center diagonally from the lower left corner towards the cylinders centerline. For the standard case at 1000 rpm the main vortex is displaced horizontally by ~8 mm from x = -7 to x = 1 mm and vertically by ~5.5 mm from y = -29 to -23.5 mm. While the horizontal displacement varies with engine speed (~6 mm for 2000 and ~7 mm for 500 rpm) the vertical displacement is constant at 5.5 mm for all cases. The paths for 1000 and 2000 rpm are very close to each other and begin to merge towards TDC. In contrast to them an enormous difference is observed at 500 rpm where apparently a different flow pattern exists. This is an engine speed where combustion would be very unstable under fired conditions.

The ccv in respect to the mean vortex center is shown as the standard deviation of the instantaneous vortex center distributions in figure 6.16b. The rms was calculated using 36 cycles per configuration. The statistical error of the rms-values are estimated by analyzing the scatter of the quantity by taking different samples (subsets of individual cycles) out of the whole available data-set of 146 cycles at 2000 rpm. The rms was calculated from 36 arbitrarily selected cycles within each sample, each sample gives one value for the rms. For an adequate number of samples the resulting PDF represents the distribution of the quantity. The width of the PDF quantifies the statistical error when calculating the quantity from a given number of individual data points. The variation of the rms value calculated from 36 individual cycles was found to be within +/- 0.2 mm. The rms of the vertical location is constant over the observed crank angle range for all engine speeds at approx. 1.5 mm. This indicates that the flow field with an induced

tumble motion is approximately constant in its vertical direction. The vertical location itself is stabilized by the upwards moving piston. The horizontal location in contrast shows a larger variability which decreases slightly between ~0.2-0.5 mm from 80° towards 62° BTDC resulting in a rms of 2.2 mm for 2000 rpm, 2.7 mm for 1000 rpm and up to 3.4 mm for 500 rpm at 62° BTDC. [81] observed in a similar analysis that the cyclic variability of the vortex center increases during the compression stroke until approximately 110° BTDC and is reduced again towards the end of the compression stroke. While their analysis ends at 78° BTDC a similar trend is recognized in this work in which the vortex center is tracked from 80° to 62° BTDC.

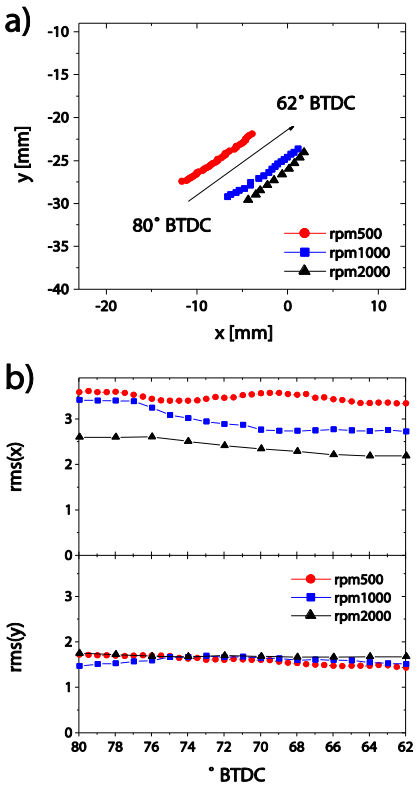

Figure 6.16
Averaged location of the vortex center for 80 to 62° BTDC (a) and the rms given in terms of the horizontal coordinate x and the vertical coordinate y (b) for 500, 1000 and 2000 rpm. The arrow in 5a indicates the general direction of the main vortex

The substantial ccv are shown in figure 6.17 by histograms of the vortex centers locations at 80° and 62° BTDC. Due to the experimental setup the maximum number of cycles for 500rpm is 36, for 1000rpm 73 and for 2000rpm 146. For the vertical axis y the ccv are a few millimeters and similar for all engine speeds. The fluctuations along the horizontal axis x in contrast are much larger. For 500 rpm the histogram shows a very broad distribution with a random structure. For higher engine speeds the distribution becomes narrower. Still some isolated outliers can be found, as for example the 51st cycle at x = -20 mm for 1000 rpm. This is approximately 14 mm off the average location ($\bar{x}$ = -7 mm at 80° BTDC) to the left towards the side of the outlet valve. Two outliers out of 73 cycles (~2.7%) were found for 1000 rpm while only a single outlier was found for 146 cycles (~0.7%) at 2000 rpm.

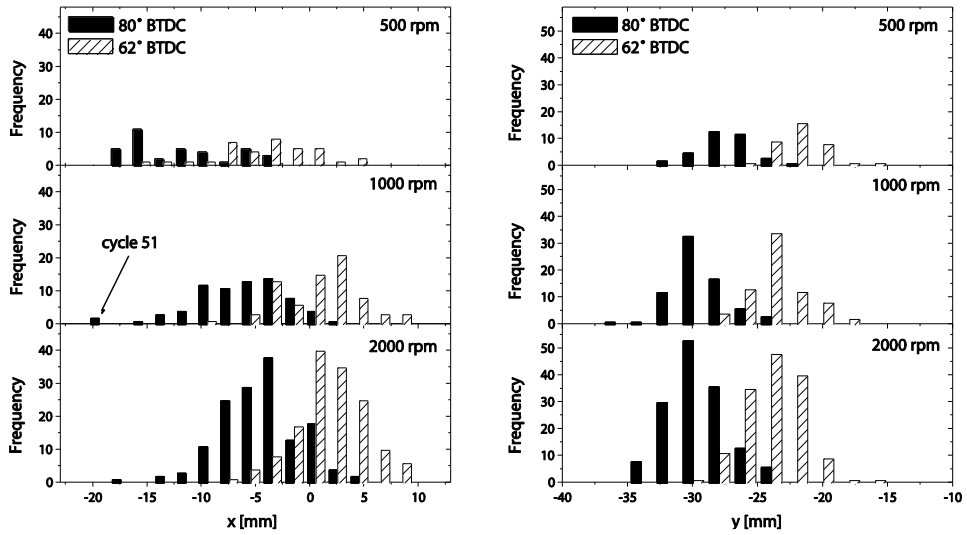

Figure 6.17
Histogram of the vortex center locations for 80 and 62° BTDC for the horizontal coordinate x (left) and the vertical coordinate y (right) for 500, 1000 and 2000 rpm

For two individual cycles at 1000 rpm the path of the vortex centers is shown in figure 6.18. The 11th cycle appears to be close to the averaged data points in respect to location of the vortex centers and the path length. A different behavior is seen for the 51st cycle which had already been identified as an outlier in the histogram in figure 6.17. At 80° BTDC the vortex center is located at x = -18 mm and moves with a faster speed towards x = 0 mm at 62° BTDC than the averaged vortex center locations. Interesting to note is the huge step between 77 and 76° BTDC where the vortex center moves from x = -15 to x = -9.5 mm. It is apparent that a different flow regime exists for the 51st cycle.

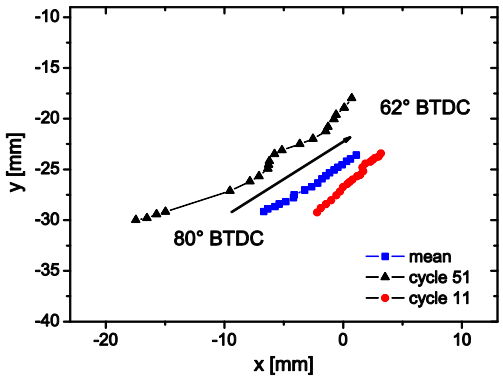

Figure 6.18
Mean path and two individual paths of the vortex centers for 80 to 62° BTDC for 1000 rpm. The arrow indicates the general direction of the main vortex.

Instantaneous Flow fields

Figure 6.19 shows the temporal development of the instantaneous flow field of the 11th and 51st cycle. The flow field is given for 80, 60, 50, 40 and 30° BTDC with the velocity magnitude shown by the underlying color map. The flow field here is represented by validated vectors only i.e. no interpolation was performed after removing the spurious vectors. This demonstrates the quality of the PIV results and shows the influence of deposits on the windows especially in the upper right corner. Additionally, the influence of the evaporating particles towards TDC can be observed by the decreasing quality of the vector field. Although the piston was masked out before the PIV post-processing one can see from 60° BTDC onwards that when the piston moves into the field of view there are some remaining vectors at the piston crown. These are a result from the pistons movement rather than from the actual flow. These vectors were not taken into account for the further analysis.

The 11th cycle represents a typical cycle with one large vortex center at 80° BTDC. Given the upwards movement of the piston the flow is accelerated in the lower right corner leading to regions of high velocity. Thereby the vortex center is distorted and vertically compressed. From 60° BTDC onwards the kinetic energy begins to dissipate. The large vortex center breaks up into smaller vortices. These are aligned horizontally in a region between $-25 < y < -15$ mm separating regions of high velocity at the piston crown and the cylinder head. At the cylinder head in the vicinity of the centerline ($x = 0$ mm and $0 > y > -12$ mm) the flow moves from the right side (inlet valves) towards the left. Thus, the flow passes the region where the injection nozzle is located towards the region of the spark plug. This is indicated in figure 6.13 (both the injection nozzle and spark plug were removed for these isothermal measurements). Further on the flow moves down towards the piston where the fuel cloud would be found under stratified conditions. This flow pattern is the standard case. In contrast, the 51st cycle shows a different behavior. Two vortices are found at 80° BTDC which are already compressed vertically due to a larger region of high velocity at the piston pointing upwards for $x > -20$ mm. Several crank angle degrees later the left vortex which was larger in size seems to have merged with the second vortex. This is the reason why there is such a great step of the vortex center location between 77 and 76° BTDC in figure 6.18. The vortex moves upwards to the cylinder head at $x = 0$ mm. Compared to the 11th cycle regions of higher velocities are found from 60° BTDC onwards pointing down towards the piston. The vortex moves along the cylinder head back to the left and is found for 30° BTDC at the location of the spark plug ($x = -15$ and $y = -10$ mm).

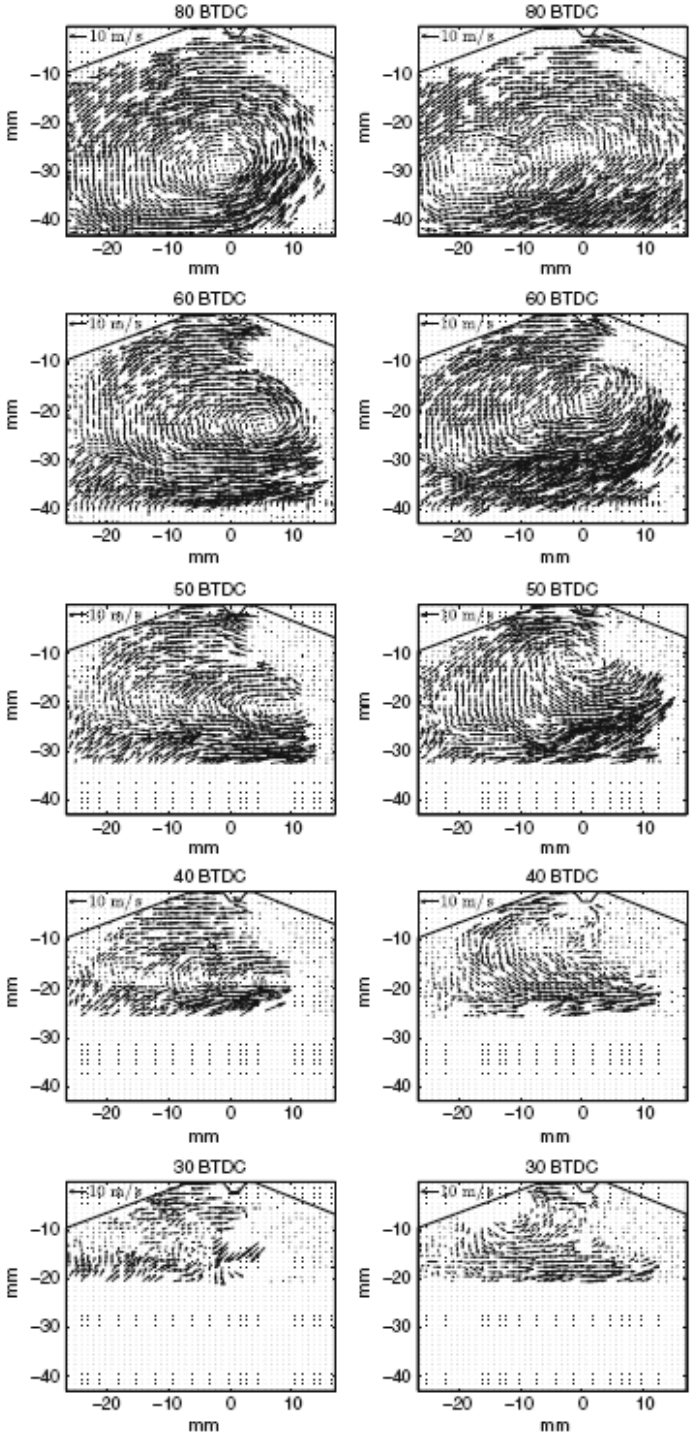

Figure 6.19
Individual flow fields of the 11th cycle (left) and the 51st cycle (right) at 80, 60, 50, 40 and 30° BTDC for 1000 rpm, tumble charge motion.

Kinetic Energy

Ignition, flame kernel growth and flame propagation are influenced by the direction of the flow [72], the flow structures size and their corresponding energy content [229]. Therefore another statistical analysis of the cyclic variability was performed in terms of the kinetic energy of the

flow field. In a first step the spatially averaged kinetic energy was calculated using all available velocity vectors. Here again only validated vectors were taken into account (no interpolation was performed). Furthermore, the kinetic energy was calculated using only the two available in-plane velocity components. Although the out of plane component is missing, it can be assumed to have a far lower influence than the in-plane components because of the tumble charge motion. The spatially averaged kinetic energy *E* and the turbulent kinetic energy *k* are calculated according to [81]

$$E = \sum_{i=1}^{n_x} \sum_{j=1}^{n_y} \frac{1}{2} \frac{u_1^{\,2}(x_i, y_j) + u_2^{\,2}(x_i, y_j)}{n_x \cdot n_y} \tag{6.1}$$

$$k = \sum_{i=1}^{n_x} \sum_{j=1}^{n_y} \frac{1}{2} \frac{u_1^{\,'2}(x_i, y_j) + u_2^{\,'2}(x_i, y_j)}{n_x \cdot n_y} \tag{6.2}$$

with n corresponding to the number of valid vectors.

Figure 6.20 shows the temporal progress of the spatially averaged kinetic energy *E* and *k* averaged over all recorded cycles for 500, 1000 and 2000 rpm, respectively. According to the scaling law of the intake flow which is proportional to the engine speed, the kinetic energy is normalized by the square of the engine speed. While 1000 rpm is the standard case the kinetic energy for 2000 rpm is divided by 4 and 500 by 0.25, respectively. Thus, the resulting energy values of *E* and *k* are in the same order of magnitude for all investigated engine speeds. Note that the level of reliance upon these values decreases after 40° BTDC as the number of valid vectors is reduced rapidly (see figure 6.19).

Viewing the standard case at 1000 rpm with a tumble charge motion *E* first increases until the piston moves into the field of view (at 65° BTDC). This is due to the regions of high velocities found in the vicinity of the piston crown (see figure 6.19). These velocities are forced into the field of view. Over the next 20° CA *E* decreases by approximately 25%. This corresponds to the time where the large vortex center breaks up into smaller vortices. Further on the dissipation of energy slows down for 10° CA before it decreases again rapidly (at ~ 35° BTDC). This decay changes significantly with engine speed. The peak of E moves to earlier CA with increasing engine speed (from 61° BTDC for 500 up to 66° BTDC at 2000 rpm). While dissipation outbalances the production of kinetic energy at 500 rpm, the production balances dissipation for several crank angles at 2000 rpm resulting in a plateau at 52 to 44° BTDC. After this plateau the gradient in decline is larger than compared to the 500 and 1000 rpm case. Interestingly the minimum of *E* is reached earlier for 2000rpm (at 20°BTDC) than for both other cases (at 10° BTDC).

The turbulent kinetic energy (see figure 6.20b) declines earlier with increasing engine speed similar to *E* (see figure 6.20a). At an engine speed of 1000 rpm a peak is found at 30° BTDC (25° at 500 and 38° at 2000 rpm). This corresponds to the CA where the decay of kinetic energy is maximal (largest negative gradient). In respect to engine speed, the turbulent kinetic energy *k* reaches its minimum at the same CA as the corresponding minimum of kinetic energy *E*.

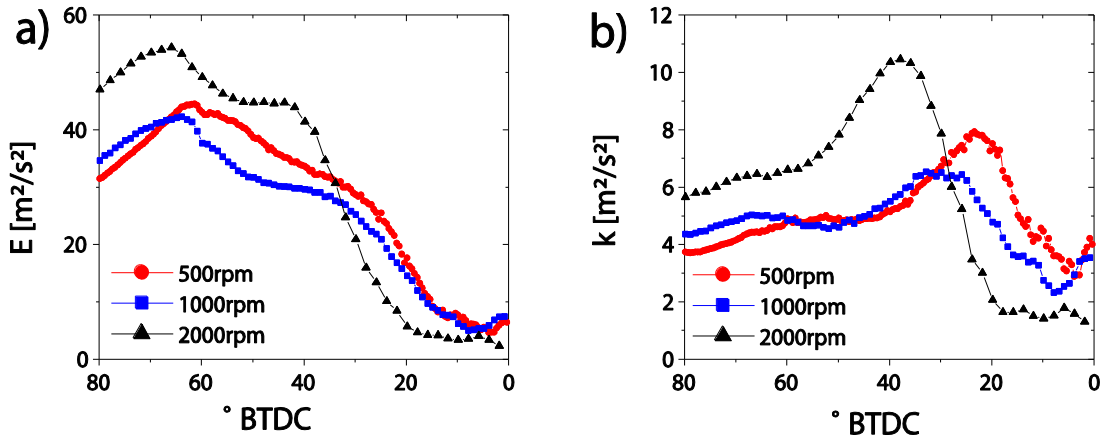

Figure 6.20
Ensemble average of the spatial averaged kinetic energy *E* (a) and turbulent kinetic energy for 500, 1000 and 2000 rpm. Values are normalized by the square of the engine speed in regard to the standard case of 1000rpm.

The individual traces of kinetic energy for the 11th and 51st cycle are shown in figure 6.21. They are consistent with the flow field as shown in figure 6.19 in regard of their peak velocities. The larger regions of high velocity located in the vicinity of the piston crown lead to a higher and broader peak for the 51st cycle. Interestingly, the decline of *E* is faster than for the 11th cycle and thus leads to similar values of *E* after 35° BTDC. The turbulent kinetic energy is a more sensitive value to identify cycles with a change in its flow structure. While the values of *k* for the 11th cycle are close to the mean of *k* (representing all cycles), the 51st cycle presents values of *k* which are up to 3 times larger than the mean. This great difference is caused by a varying energy distribution within the flow field (see figure 6.19). To demonstrate the ccv, scatter plots are shown for every 5th CA (see figure 6.21).

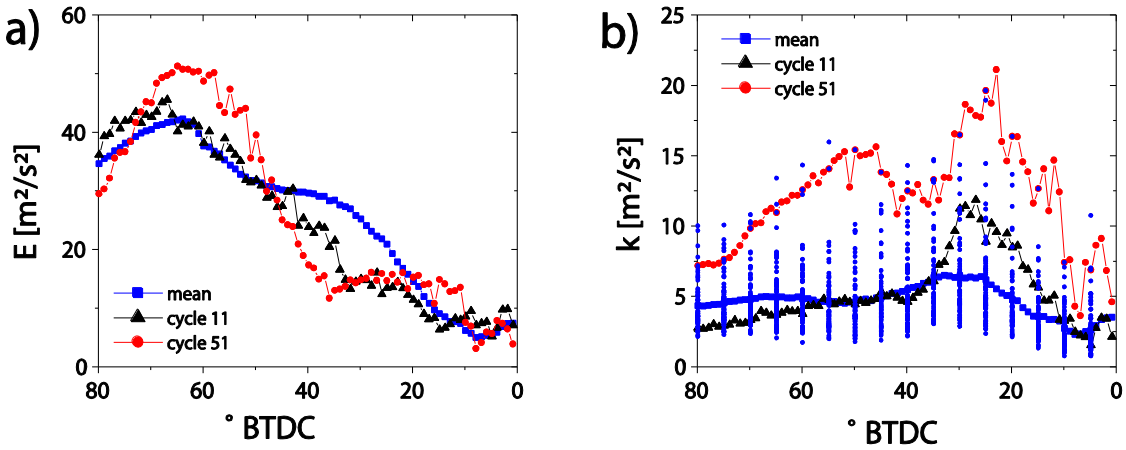

Figure 6.21
Kinetic energy (left) and turbulent kinetic energy (right): mean (black), 11th cycle (blue) and 51st cycle (red) for 1000rpm, tumble charged motion.

6.4.3 Conclusions high speed engine flow field measurements

High speed PIV has been applied to an optically accessible direct-injection spray-guided internal combustion engine to investigate the temporal evolution of the isothermal flow field and its

cyclic variability. Based on recent improvements in all-solid-state diode-pumped laser- and CMOS camera-technology a large field of view (43 x 44 mm^2) was achieved at 6 kHz resulting in a temporal resolution of 1° CA at 1000 rpm. The isothermal flow field was recorded during the latter half of the compression stroke (80 to 0° BTDC) for a tumble charged motion at 500, 1000 and 2000 rpm.

The flow structure was investigated by individual flow fields and an automated analysis of ensemble averaged flow fields. The temporal evolution of the large scale vortex induced by the tumble motion revealed a substantial variability in the horizontal direction while the vertical location was mainly determined by the upwards moving piston resulting in far lower variability. This was supported by an analysis of kinetic energy and turbulent kinetic energy based on the two measured velocity components. A few cycles revealed great variations compared to the ensemble average in terms of the vortex center location as well as its temporal evolution and kinetic energy. Their individual flow fields revealed a different flow structure resulting in a change of the flows velocity and directionality in the area of the spray injector and the spark plug. A more advanced investigation and correlation of these flow structures with flame kernel development would be of great interest.

6.5 Flame kernel growth in DISI engine observed by OH PLIF at 6kHz

Information on transient flame propagation inside the cylinder of an internal combustion engine is a substantial part for an improved understanding guiding the development of higher efficiencies and reduced pollutant emissions. This study [230] presents the feasibility to temporally resolve the evolution of spark-ignited flame kernels using a single laser/camera system. In contrast to previous approaches based on multiple intensified CCD and clustered lamp-pumped Nd:YAG laser technology [231], the methodology presented here relies on continuous pulse sequences and intensified CMOS-cameras. This enables a more detailed view upon cycle-to-cycle variations (ccv) because a large number of sequential combustion cycles is recorded. The appearance of ccv is an unwanted disturbance in engines, especially in current spray guided direct injection spark ignition (DISI) engine configurations. To characterize ccv, an adequate temporal resolution is required to comprehend the flame structures and their variability in time and space. Therefore the flame kernel evolution of sequential cycles is an important cornerstone of understanding the origins of ccv during combustion.

The method of choice to mark the flame front is planar laser-induced fluorescence (PLIF). The excitation of diatomic molecules such as OH is a standard procedure within laser combustion diagnostics and is widely accepted for representing the instantaneous flame front position [93]. High-speed imaging of atmospheric turbulent flames using the steep gradient of OH radicals as an indicator of the flame front has been demonstrated in [232–234]. Depending on the time-scales to be resolved, such as the integral time-scale of a turbulent flow, the repetition rate must be chosen accordingly. Integral time-scales in turbulent flames are typically in the ms-range [8]. Therefore repetition rates must be in the kHz-range. Time-scales of interest studying flame dynamics and ccv in IC-engines are 1 degree CA and therefore scale with the engine speed. At 1000 rpm, the temporal resolution of 1 degree CA per image corresponds to 6 kHz. Thus, the techniques developed for studying transients in turbulent flames are transferred and adopted to in-cylinder processes of a DISI engine.

Temporal flame kernel development and flame propagation throughout the cylinder is of common interest [235, 231, 236]. Whereas recording OH chemiluminescence within an IC engines

at standard 10 Hz repetition rates is well established, measuring the transient flame front propagation during individual cycles is still a challenge. The benefit of the present approach using OH-PLIF at 6 kHz is temporally resolved imaging of the flame kernel development at a large field of view. From this transient data flame contours and their propagation speeds can be extracted for individual cycles. Parameters such as engine speed, charge motion and timing influence the propagation speed and burning time. Especially exhaust gas recirculation (EGR) does strongly impact the engine characteristics. Most notably, EGR at partial load operation is used to reduce NOx exhaust emissions and increase engine efficiency by mixing intake air with exhaust gas to a ratio of up to 30%. As a result of this mixing process flame speeds are retarded and burning times increase. Using high speed flame kernel imaging, this influence can be studied in detail as presented here.

6.5.1 Experimental setup

OH radicals were excited at the $Q_1(6)$ line within the $A^2\Sigma^+ \leftarrow X^2\Pi$ (1-0) band using a frequency doubled dye laser (Sirah Allegro). The dye laser was pumped by a frequency-doubled Nd:YAG laser at 532 nm (EdgeWave). The pump laser was operated at a repetition rate of 6 kHz. Average pulse energies and pulse lengths were 5.3 mJ/pulse and10 ns, respectively. To lower the peak intensities at the dye laser optics the beam of the pump laser was expanded by a telescope with an expansion factor of 1.4. Resonator and amplifier were operated with Rhodamine 6G dissolved in ethanol. Dye laser radiation at 566 nm was frequency doubled using a BBO crystal. First and second harmonics were separated by four Pellin-Broca prisms. At 283 nm average pulse energies of up to 360 µJ/pulse were achieved at a repetition rate of 6 kHz (2.15 W quasi-cw).

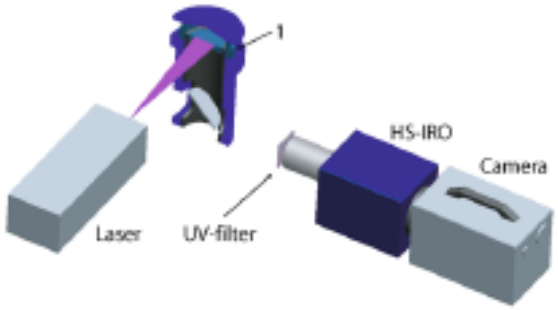

Figure 6.22
Experimental setup for 6 kHz OH PLIF measurements tracking early flame kernel developments in an operating DISI engine.

A laser light sheet was formed using a combination of three lenses. The light sheet entered the cylinder through a quartz glass ring and was aligned horizontally just above the top dead center (TDC) position of the piston. At the measuring plane the light sheet was 54mm wide and approximately 200 µm thick. Due to reflective losses at the lenses and the quartz cylinder ring pulse energies decreased to 290 µJ/pulse inside the cylinder. Vertical and horizontal alignment of the laser profile were checked regularly during the experiments.

Fluorescence around 308 nm was collected using a UV lens (Bernhard Halle Nachfl. GmbH, f = 100 mm, f# = 2). A band pass filter with 80% transmission at 308 nm (mso Jena) was used to reduce spuriously scattered light and resonance fluorescence. PLIF-signals were recorded by a

lens-coupled dual-stage intensified CMOS camera (LaVision HSS6). The intensifier consisted of a multi-channel plate followed by a booster (LaVision). It was operated at 65% gain and a gate width of 100 ns. At 6 kHz 992 x 1024 px of the CMOS chip were active resulting in a field of view of 53 x 54. Temporally resolved OH-PLIF was observed through the piston window and using a 90°-mirror located within the extended piston as shown in figure 6.22. The camera on-board memory was limited to 8 GB resulting in 5400 images per sequence. Due to this storage capacity during a single engine run lasting approximately 21 s 180 sequential cycles were recorded enabling statistical analysis. Camera and intensifier were synchronized with the engine timing through the engine timing unit.

The engine design is thoroughly described in [80] and only the most important operating parameters for the present study are listed in table 6.2. A standard multi-hole injector with a piezoelectric actuator was applied. The fuel used was similar to standard gasoline, but with a low percentage of aromats. This was necessary to avoid superposition from LIF signals of other species. Selected randomly from a sequence comprehending thousands of frames, a sample image of the OH-PLIF signal intensity is shown in figure 6.23. Because of high temperatures during the fired mode the engine was skip fired with a ratio of 1:3. Furthermore, the spark duration time was adjusted so that a safe operation of the intensifier was possible. It was set between 0.75 and 0.85 ms, corresponding to the EGR rate (the more EGR, the longer the spark duration). Amplifying the ignition spark would have caused irreversible damage to the intensifier. In early tests, the ignition of the engine was thoroughly inspected for such a short duration. In a parametric study external EGR rates were varied from 0 to 20%. The composition of exhaust gases was mimicked by N_2 and CO_2 in a mixing ratio of 9:1.

Note that various other parameters such as injection timing, ignition timing, charge motion, and injection nozzle geometry were varied but this parametric variation and the corresponding statistical analysis is not within the scope of the present chapter.

Table 6.2
Parameters for engine operation.

Parameter	Setting/value
Engine speed [rpm]	1000
Compression ratio	8.24
Charge motion	neutral
Fuel/air ratio [–]	1
Rail pressure [MPa]	10
Injection end [° BTDC]	290
Start of ignition [° BTDC]	45
Manifold inlet pressure [mbar]	600
Camera start trigger [° BTDC]	39
Skip fire ratio	1:3

A post-processing procedure was applied to the raw images to extract the local flame front. In a first step a cuevette was used to examine the decline in signal intensity along the laser light sheet. This resulted in a horizontal linear decline of the signal with a ratio of 4:1. Secondly, a non-linear diffusion filter was applied for denoising, similar to [237]. In a final step, to clearly differentiate between burnt and unburned regions each image was evaluated with a histogram

of the pixel intensities to deduce an appropriate threshold. The binarized images were then used for all analyses.

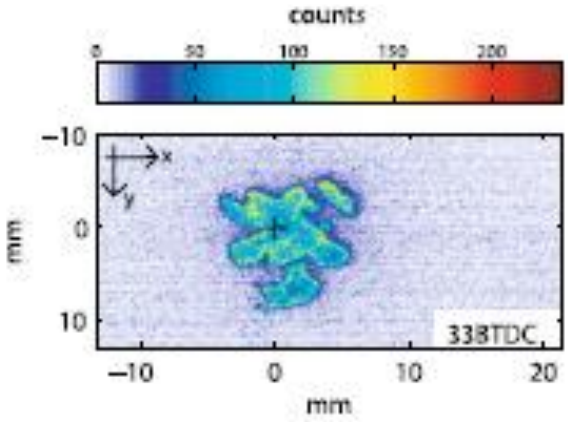

Figure 6.23
Sample image of OH sampled at 6 kHz repetition rate. Amplifier noise is clearly apparent.

6.5.2 Results and discussion

Figure 6.24 shows the temporal evolution of individual flame kernels represented by instantaneous OH radical distributions. Images shown are after post-processing as outlined above. They are separated by 1 or 2°CA and only sectors of the full view are presented. EGR is varied from 0 - 20% as noted in the figure captions.

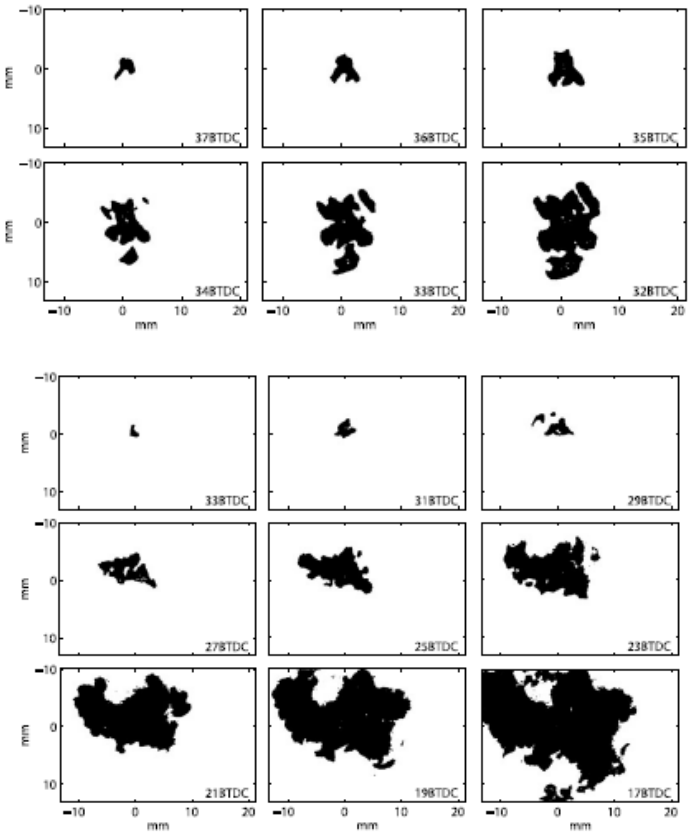

Figure 6.24
Flame kernel evolution of individual engine cycles at 0% (top) and 20% EGR (bottom)

Obviously, the location of the first entry of the flame front into the laser light sheet plane is near the spark plug. The size of the flame kernel expands continuously until the edge of the field of view is reached. The PLIF-signal intensity is sufficiently good to extract the flame front and its propagation in the measurement plane during individual engine cycles. A preliminary statistical analysis of the flame area propagation is shown in figure 6.25. The error bars represent the standard deviation (1σ-range) of the dataset and the central measurement points represent the average flame area growth. The dataset consists of 50 individual cycles which were consecutively recorded. Due to cyclic variations of local turbulence properties and residual gas composition the flame area scatters significantly. To illustrate the variability of the process two extreme cases with growth rates above and below the 1σ-range are included to figure 6.25. Notice that temporally tracking flame growth of individual cycles as demonstrated here is only possible by high speed technology based on infinite pulse sequences at kHz repetition rates.

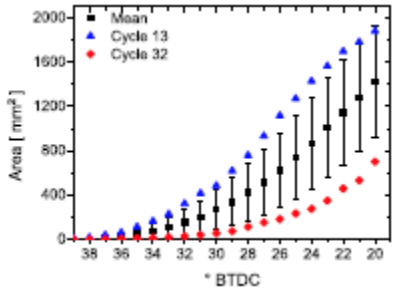

Figure 6.25
Analysis of the flame area propagation at 1000 rpm without EGR.

For different EGR rates the temporal development of the initial spark-ignited flame kernel differs significantly. With increasing EGR the flame growth speed is reduced. For 0% EGR the flame kernel growths into the measurement plane approximately at 35°CA BTDC. Increasing the EGR rate to 10% the arrival at the measurement plane is delayed by only 1 - 2°CA (not shown) but at an EGR rate of 20% first OH PLIF signals appear earliest at 32°CA BTDC. Similarly, the flame kernel growth rate is decreasing significantly with increasing EGR-rate. Differences in the flame area growth rate are most pronounced when switching from 0% to 10% EGR. For 20% EGR especially during the initial phase up to 25°CA BTDC, the flame kernel grows only marginally whereas without EGR the kernel increases constantly and much more rapidly. These differences are shown in figure 6.26. Mean and coefficient of variation are computed from 50 cycles at each EGR level.

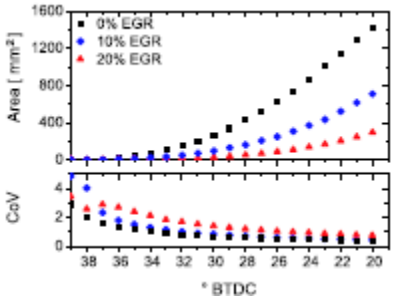

Figure 6.26
Statistical analysis of data at 1000 rpm with different EGR rates.

Imaging a three-dimensional process using a two-dimensional approach of course does not allow for final evidence. However, decreasing growth rates with increasing EGR illustrated in figure 6.26 are expected because laminar flame speeds decrease with increasing mole fraction of inert gases and decreasing flame temperatures. Lower laminar flame speeds in turn reduce turbulent flame speeds that are actually observed here in a two-dimensional projection.

6.5.3 Conclusion and Perspectives of high speed OH PLIF in DISI engine

This study shows the feasibility of engine in-cylinder OH radical imaging at multiple kHz repetition rates using planar laser-induced fluorescence. The data is sufficiently good to extract transient flame front propagation resolving individual engine cycles. The large CMOS camera on-board memory used for detection in combination with continuous UV laser pulse sequences allowed for recording of hundreds of subsequent cycles. Although not the focus of the present paper, in future this large data set enables more detailed statistical analysis of in-cylinder flame dynamics and the investigation of cyclic variations at different operational conditions. Using exhaust gas recirculation as a prominent route to reduce NOx-emissions, the method clearly allows quantifying the impact of gas composition on flame dynamics. Further investigations are necessary to thoroughly understand the influences of the flow field onto the flame kernel propagation. This may be achieved using a combinative application of particle image velocimetry and OH-PLIF.

6.6 Towards volumetric scalar imaging

Two-dimensional laser measurement techniques such as particle image velocimetry (PIV) and planar laser-induced fluorescence (PLIF) have been widely used in combustion diagnostics [238]. However, these methods suffer from deficient out-of-plane information which limits the understanding of complex three-dimensional transient events. Particularly, in turbulent flames and ignition events out-of-plane motion plays an important role [239]. Therefore, spatially and temporally resolved measurements are essential for a deeper understanding of flame-flow interactions.

In recent years, many efforts have been made towards obtaining spatially resolved experimental data in combustion studies. Multiple laser sheets, including crossed- and parallel-plane measurements of OH-PLIF combined with normal [240] or stereoscopic PIV [241, 242] have been used to produce quasi four-dimensional (4D) information during experiments with turbulent flames. Volumetric imaging employing volumetric laser illumination and multiple cameras for the detection has been applied for tomographic measurements of the velocity field [243–246] and flame chemiluminescence [247].

By sweeping a laser sheet fast enough across the measurement volume, quasi three-dimensional (3D) measurements can be achieved. These techniques can be divided in two groups: oscillating mirrors (e.g., galvanometric scanners and stepper motors) [248, 249] and polygonal mirrors [215, 250]. Although they are proved to be effective for tracking transient events in combustion and fluid dynamics applications, their maximal scan frequency is restricted by the inertia related to the moving mechanical parts [215]. The high inertia is an additional safety issue which needs to be considered.

An alternative to mirror-based mechanical deflection is the optical solid state deflection by means of an acousto-optic deflector (AOD) [251]. With an AOD, a light beam can be deflected

by inducing a high-frequency acoustic wave through a crystal to change its refractive index periodically [216].

Another option is tomographic laser-induced fluorescence (Tomo-LIF) which has been developed for the 3D imaging and temporally tracking of flame structures (i.e. high-temperature reaction regions) [252, 253]. The Tomo-LIF approach combines volumetric laser illumination with a multi-camera detection system for the volumetric reconstruction of scalar distributions.

In the following example, time-resolved Tomo-LIF of OH was used to study the spatial and temporal evolution of auto-ignition kernels formed during the continuous injection of methane jets into a NOx-vitiated, high-turbulence, hot air co-flow generated by a microwave heater. The 3D size, structure, location, and orientation of auto-ignition (AI) kernels and their temporal evolution were determined from the time-resolved tomographic reconstructed fluorescence signals and analyzed for different flow conditions as an initial effort to better understand the transient 3D phenomena involved in AI of turbulent mixing flows.

Experimental setup, operation conditions and data post-processing

Figure 6.27 shows a schematic cross section of the burner head of the 75 kW microwave plasma heater (MWPH) test rig, including the geometrical boundaries at the exit of the nozzles. For the current configuration, the fuel lance and the co-flow nozzles had inner diameters of 6 and 82 mm, respectively. The outer diameters of the jet and co-flow nozzles were 7 and 84 mm, respectively. The fuel lance had a total length of 550 mm. The co- flow can be heated up to 1400 K (± 2 K), with a top-hat radial temperature distribution within the region of interest for AI studies. Bulk co-flow exit velocities can reach up to 40 ms^{-1}. Up- and downstream of the contoured nozzle, two turbulence enhancing perforated plates, with a hole diameter of 8 mm and a blockage ratio of 35%, were employed to control the integral length scale and to generate a turbulence intensity in the co-flow of ~13% (at 1273 K) at locations where AI events initiate. A detailed description of the test rig and the characterization of the most important inflow boundary conditions have been reported previously [254]. Pure CH_4 was used for the fuel jet while the co-flow was mainly composed of air. However, as a side effect of the MWPH, high concentrations of nitrogen oxides (NO and NO_2) are produced. Mole fractions of NO ranging from 4000 to 10,000 ppm and of NO_2 from 100 to 1300 ppm are generated depending on the temperature and bulk exit velocity of the co-flow [254]. The addition of NO/NO_2 can significantly reduce ignition delay times of hydrocarbon fuels at low initial temperatures.

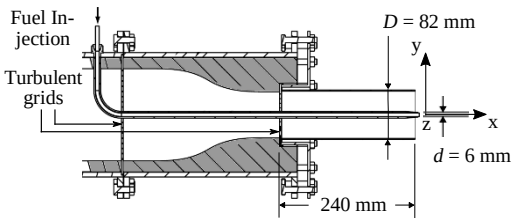

Figure 6.27
Schematic cross section of the burner head of the microwave plasma heater (MWPH) test rig with geometrical boundaries.

Table 6.3 summarizes the operating conditions employed for the time-resolved Tomo OH-LIF measurements. The Reynolds numbers of the co-flow, $Re_{co-flow}$, and fuel, Re_{jet}, were calculated based on the bulk exit velocities, $U_{co-flow}$ and U_{jet}, the hydraulic diameter of the

nozzles and the kinematic viscosity of the gases at the given temperatures, $T_{co-flow}$ and T_{jet}. For all conditions, $T_{co-flow}$ was kept constant at 1323 K with a $Re_{co-flow}$ = 10,000 and $U_{co-flow}$ = 25 ms^{-1}. The NO and NO_2 concentrations in the air co-flow were 9000 ±180 and 1200 ±24 ppm, respectively. All measurements in the present study were spatially referred to the coordinate system (x,y,z) located at the tip of the fuel lance shown in Fig. 6.27. In the present configuration, the continuous injection of fuel results in the continuous formation of kernels and a lifted flame is stabilized. As a reference, the lift-off-height (LOH) was measured for each condition by chemiluminescence (CL) imaging and the values are included in Table 6.3. OH* CL was collected at 10 Hz using a CCD camera (Imager E-lite, LaVision) with an image intensifier (LaVision, intensified relay optics, IRO), a UV lens (CERCO, f = 100 mm, f/8) and a band pass filter (BP300- 325, Laser Components). The LOH was determined from the CL images as detailed in Ref. [254].

Table 6.3
Operating conditions for the time-resolved Tomo OH-LIF measurements along with the lift-off-height (LOH). For all conditions: $T_{co-flow}$ = 1323 K, $Re_{co-flow}$ = 10,000 and $U_{co-flow}$ = 25 ms^{-1}.

Re_{jet} [−]	T_{jet} [K]	U_{jet} [ms^{-1}]	LOH [mm]
5000	720	69	76 (x/d = 12.7)
10,000	594	99	85 (x/d = 14.2)
15,000	536	123	94 (x/d = 15.7)

The experimental setup for the time-resolved Tomo OH-LIF is schematically illustrated in Fig. 6.28. The $Q_1(6)$ line of (0,1) vibrational band of the A-X transition of OH was excited using a burst dye laser system at 283.01 nm. The $Q_1(6)$ line provides a strong fluorescence signal and it has a weak temperature dependence on the range of the present measurements. The burst consisted of four UV laser pulses from two identical double-pulsed dye lasers, temporally separated by 100 µs (corresponding to 10 kHz) and with a repetition rate of 10 Hz. Each dye laser (Sirah Lasertechnik GmbH, DoubleDye) was operated with Rhodamine 6G and pumped with a 10 Hz frequency-doubled Nd:YAG laser (Spectra Physics, PIV400) in double-pulse mode (Δt= 100 µs). Volumetric illumination was achieved by expanding the laser beams with two UV-coated cylindrical telescopes (f_1 = -25 mm, f_2 = +20 mm, f_3 = -50 mm and f_4 = +200 mm). After the telescopes, the collimated laser slab was cut by an adjustable sharp-edge aperture to form a volumetric illumination with a cross section of 20 × 27 mm^2 (xz-plane) at the measurement volume, so that the entire region where AI kernels were formed was excited. For each burst, the mean pulse energy was ~4.5 mJ for pulses 1 and 2, and ~3 mJ for pulses 3 and 4 at the location of the measurement volume.

The emitted fluorescence signal of OH was simultaneously collected by four high-speed CMOS cameras (3× Phantom v711, 1× HSS6), each coupled with an image intensifier (LaVision, intensified relay optics, IRO), a 100 mm UV lens (CERCO 100, f/8) and a high-transmission band-pass filter (LaVision, OH filter, 320 nm ± 20 nm >80% transmission). An image doubler, consisting of two high-reflection UV mirrors and one prism, was coupled in front of each UV lens to image two separated views onto each camera (i.e. eight independent views). The cameras

and image doublers were mounted at the same horizontal level (parallel to the *xz*-plane) to collect the signal from eight independent perspectives with a large viewing angle [255].

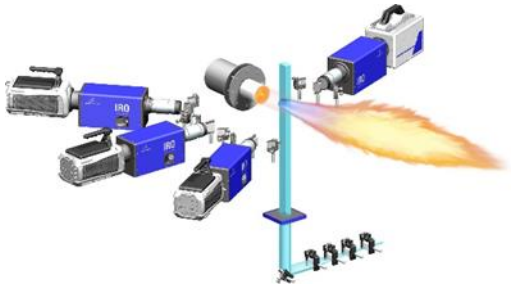

Figure 6.28
Experimental setup of volumetric laser illumination, 8-views detection system and burner head for the time-resolved Tomo-LIF measurements.

The axial position of the measurement volume was defined by the LOH of each operating condition (see Table 6.3). Spatial matching of the eight independent views was carried out by imaging a 3D calibration target (LaVision, Target 058-5). The temporal synchronization of cameras, IROs and pump lasers was achieved by means of a Programmable Timing Unit (LaVision, PTU X), IRO controllers (LaVision) and two pulse generators (Quantum Composers 9520). The intensifiers were gated at 200 ns to suppress the interference from chemiluminescence while the gain was adjusted to roughly match the signal intensities of the 2D views. Because the detection system could operate continuously at 10 kHz and the laser system produced bursts of four pulses at 10 kHz every 10 Hz, the triggering was set up to simultaneously record 1000 sequences of 5 images per camera (1 image per laser pulse + 1 background image) using the software DaVis (LaVision, Version 8.4).

Sequences of 3D distributions of OH fluorescence signal were reconstructed within an effective volume of 30 × 30 × 30 mm^3, to guarantee capturing the entire region where AI kernels are formed. Each sequence consisted of four single shots, corresponding to the 4 pulses of the burst.

Prior to tomographic reconstruction, the processing of the 2D images from the four cameras included: (1) background subtraction, (2) averaged laser pulse intensity correction, (3) 2 × 2 binning and (4) image thresholding. To account for energy differences among the lasers, the average intensity of all pixels of all eight views was calculated over 1000 sequences. Using the ratio between the averaged intensities, the signal level of the 2D raw images was equalized to the laser pulse with lowest averaged intensity. The 2D binned images had a size of 192 × 384 pixels with a pixel size of 190 µm/pixel. The signal-to-noise ratio (SNR) of 80 was estimated from the mean signal and the standard deviation of the residual noise distribution [255]. A spatial resolution of ~0.8 mm was determined by imaging a Siemens-star with 36 segments and calculating the optical modulation transfer function. A 3–5% threshold was introduced to set the background to zero, thus reducing reconstruction artifacts and further decreasing the computational costs.

The tomographic reconstruction was performed using the simultaneous multiplicative algebraic reconstruction technique (SMART) [244], implemented in the DaVis software (LaVision, Version 8.4). For each reconstruction, 100 iterations were used for a volume with 3.7 million voxels of 1903 μm^3. The number of iterations was determined, using test cases, by controlling the voxel intensity change between iterations until it was ≤0.1%. Between individual iterations, a

3 × 3 × 3 voxel average filter with a weighting factor of 0.5 for the surrounding voxels was applied for smoothing. The effect of the reconstruction algorithm on the spatial resolution of reconstructed signals was previously evaluated for different structure sizes, by comparison of signal intensity gradients from tomographic and planar imaging [255]. The smoothing effect of the tomographic reconstruction was imitated by filtering the planar images using Gaussian filters with different windows sizes. Structures up to 2 mm can be reconstructed with a spatial resolution as good as the one of the 2D raw images. In the present study, the typical size of the detected AI kernels was ~4 mm, thus the added smoothing effect of the reconstruction corresponds to a 3 × 3 Gaussian filter. A spatial resolution of 1.3 mm for the Tomo OH-LIF was estimated based on the spatial resolution of the 2D raw images (0.8 mm) and the size of ± σ of the filter. For the purpose of studying the onset of AI and the subsequent events, it is interesting to analyze isolated kernels (i.e. isolated high-temperature reaction regions) rather than the base of the lifted flame. In this sense, an algorithm to detect auto-ignition kernels as closed surfaces was developed using MATLAB R2016a (The MathWorks, Inc.). The algorithm was based on the 3D gradient of the reconstructed OH fluorescence signal intensity. Unlike 1D and 2D flame detection algorithms [256], defining a closed surface as a 3D auto-ignition kernel based only on the local maximum gradient is not straightforward. To address this, the boundary of each kernel was defined as an iso-surface of an OH signal level (I_{surf}) corresponding to the maximum signal intensity gradient. I_{surf} was calculated for each kernel to reduce the effect of shot-to-shot laser energy fluctuations and spatial non-uniformity of the laser slab. First the 3D signal intensity gradient was calculated using fourth-order central differencing. Then, a histogram of the signal intensities was calculated for regions where the magnitude of the gradient was above a threshold value. This threshold was defined as the 80th percentile (P80) of the signal gradient. I_{surf} was finally determined by the peak of the intensity histogram.

To illustrate the algorithm, Fig. 6.29 shows a cross section of a 3D reconstructed signal intensity along with iso-lines of magnitude of the intensity gradient in percentile (contour lines in Fig. 6.29a) and their resulting iso-lines of I_{surf} (markers in Fig. 6.29b). If the detection is based only on the local maximum of the signal gradient, as in the conventional algorithms, the shape of resultant surface will be highly sensitive to the threshold value (Fig. 6.29a). On the other hand, the resultant surface based on I_{surf} (Fig. 6.29b) exhibits low variations with different threshold values between the 60th (P60) and the 90th percentile (P90) of the intensity gradient. Thresholding with low values results in a surface not corresponding to the maximum gradient region. Too high threshold values lead to higher uncertainties because only small regions exhibit such high gradient, hence I_{surf} is not representative of the entire kernel. Therefore in this study, the threshold value of the 80th percentile (P80) was selected for processing the whole data set.

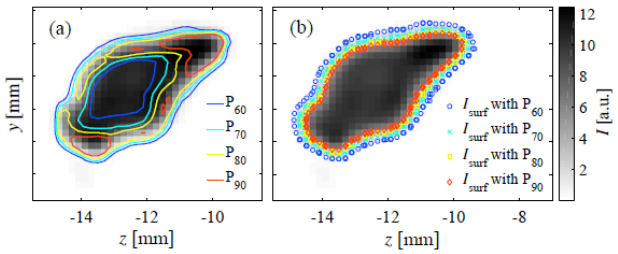

Figure 6.29
Example of a cross section from a 3D reconstructed signal intensity along with (a) iso-lines of magnitude of the intensity gradient in percentile (contour lines) and (b) their corresponding iso-lines of I_{surf} (markers) delimiting the resultant boundary of the kernel.

Results and discussion of auto-igniting flame kernels

Figure 6.30 shows an example sequence of AI kernels detected during four consecutive shots recorded at Re_{jet} =15,000. The spatial location of the kernels is referred to the coordinate system (*x*,*y*,*z*) located at the tip of the fuel lance. As a reference, the central axis of the jet is represented by a dashed line. Because it is possible to detect multiple kernels in a single shot of the laser burst, each kernel was marked with the label $K_{i,j}$, to indicate the *i*-th kernel detected in the *j*-th shot. The tracking of each kernel was performed by analyzing the position of its centroid in the four consecutive shots available from each recorded sequence. The centroid position of each kernel detected in one shot was compared to those of all kernels detected in the next shot. The pair of kernels whose displacement (d_i with $i = x, y, z$) in the main flow direction, in one time step of 100 µs, was larger than in the radial direction, $d_x > d_r = (d_y^2 + d_z^2)^{1/2}$, was listed as a potential kernel detected in the two consecutive shots. If the condition was fulfilled for more than one kernel, the one with the smallest d_r was selected. Because the local velocity field was unknown, the data was conditioned based on the mean, $\overline{d_i}$, and standard deviation, σ_{di} , of d_i of all listed kernel pairs. Kernel pairs with $|d_i - \overline{d_i}| > 2\sigma_{di}$ were excluded from further analysis.

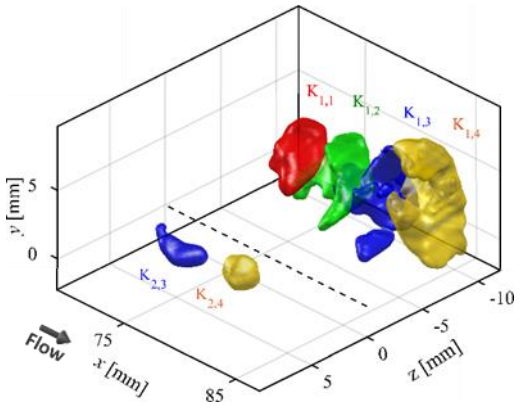

Figure 6.30
Detected kernels and their spatial and temporal evolution in an example sequence at Re_{jet} =15,000. For reference, the central axis is indicated by the dashed line. The label $K_{i,j}$ indicates *i*-th kernel detected in the *j*-th shot.

For the sequence of Fig. 6.30, the kernel K_1 was detected and tracked during the four consecutive shots ($K_{1,1}$ to $K_{1,4}$) while the kernel K_2 was first detected only in the third shot. The spatial and temporal evolution of the 3D structure of the kernels can be clearly observed. K_1 was growing in size while K_2 seems to be shrinking during the available shots. K_1 and K_2 appeared to be independent events, based on their radial location from the central axis. The elongated portion of the K_1 growing towards the central axis ($K_{1,2}$ and $K_{1,3}$) could be an indication that either the kernel was experiencing local extinction or a secondary AI event was triggered. The experimental observation of such phenomena has been reported in literature using CL [257]. However, a clear distinction of such localized 3D events using either planar or line-of-sight imaging methods is challenging. $K_{1,4}$ reached the boundary of the measurement volume probably to merge into the lifted flame base. Kernels touching the boundary of the measurement volume, whose structures could not be completely resolved, were not included in the statistical analysis of the present study.

For the characterization of the detected AI kernels, each kernel structure was fitted to an ellipsoid, using linear least squares. The orientation of the kernel was determined by the three principal axes of the ellipsoid. The size of the kernel was defined by the Feret diameters l_1, l_2 and l_3 along the major, intermediate and minor axes, respectively. Figure 6.31 presents the probability density functions (PDF s) of l_1, l_2 and l_3 of the AI kernels detected in the Re_{jet} = 5000 case. The PDF s were computed using only the first appearance of each tracked kernel (around 1000 statistically and spatially independent AI events). For the current system, a typical size of ~4 mm was defined from the PDF of l_1. Similar distributions were obtained for the operating conditions with higher Re_{jet}. An analysis of the orientation and growth of the kernels with respect to the mean flow field will be presented below.

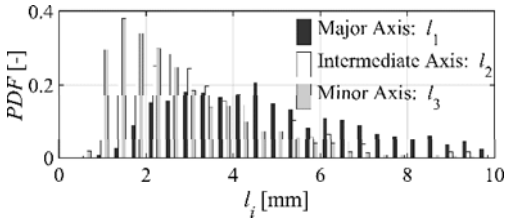

Figure 6.31
PDFs of the Feret diameters along the major, intermediate and minor axes of AI kernels at Re_{jet} = 5000.

To provide an insight of the spatial location of AI zones, the 3D distribution of the PDF of the volume occupied by all independent AI kernels, detected at the condition with Re_{jet} = 5000, is presented in Fig. 6.32 (left) along with corresponding 2D distributions of the PDF on transverse planes at different axial locations in Fig. 6.23 (rigght). For the computation, 3300 independent kernels were used. A high-probability, fairly axisymmetric region with a torus-like shape was obtained, indicating that the random occurrence of AI was radially well distributed in space at a defined axial location. The long tail distribution of the PDF in the flow direction (*x*-axis) implies a high fluctuation of the auto-ignition delay time.

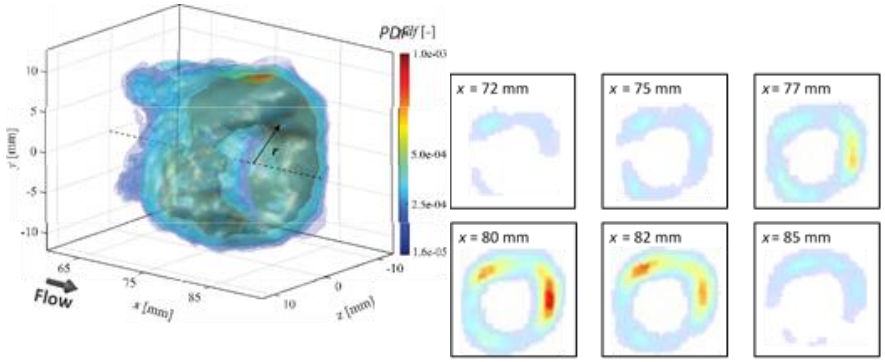

Figure 6.32
(Left) 3D distribution of the PDF of the volume occupied by AI kernels and (right) corresponding 2D distributions of the PDF on transverse planes at different axial locations. For the computation, 3300 independent kernels were used. The central axis and the radial direction are also indicated. Re_{jet} = 5000.

A detailed evaluation of the auto-ignition location was done by statistically analyzing the upstream edge position of the kernels in the radial and axial directions. Figure 6.33a presents the

PDFs of the upstream edge position of independent AI kernels along the radial direction for different Re_{jet}. The probabilities are approximately symmetrically distributed and shifted towards outer radial locations with the increase of Re_{jet}. This could be related to the difference in the development of the mixing layer for different U_{jet} at constant $U_{co-flow}$.

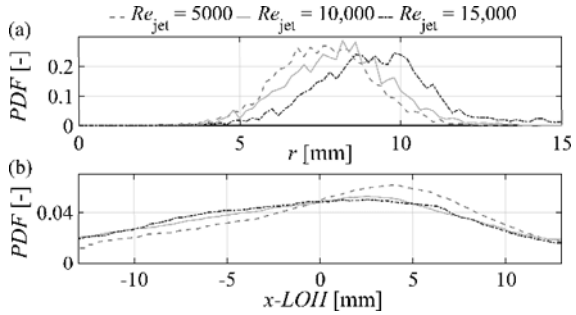

Figure 6.33
PDF s of the upstream edge position of the AI kernels along the (a) radial and (b) axial directions for different Re_{jet}. The axial position is given relative to the LOH of each operating condition.

In Fig. 6.33b, the PDF s of the axial position are plotted relative to the LOH of each operating condition (see Table 6.3). In this case, all distributions show a peak downstream relative to the LOH. To explain this counterintuitive result, a comparison of the two methods is necessary. Conventionally, the LOH is measured by means of chemiluminescence imaging. The LOH is determined by the statistics of the shortest axial distance of the CL signal (edge), measured from the fuel injection nozzle [254]. This implies the assumption that the measured distance corresponds to the first AI event (i.e. auto-ignition delay time). However, by examining again the third shot of Fig. 6.30, it is observed that if a CL image was taken from a plane perpendicular to the *z*-axis, integrated signal from the kernels $K_{1,3}$ and $K_{2,3}$ would be collected by the camera. Without any information of the depth, only the kernel $K_{2,3}$ would be considered for the conventional statistical analysis of the LOH, even though both kernels appear to be independent events. Despite of the statistical discrepancy between the conventional LOH and the axial location of the kernels in the present 3D measurements, it is possible that some of the kernels considered here as independent AI events were interacting with each other, via secondary auto-ignition, propagation or convection. Moreover, CL imaging might have a lower detection limit than Tomo OH-LIF, therefore being able to resolve smaller kernels. Additionally, because of the limited size of the measurement volume, the Tomo-LIF technique is not able to capture the whole range of fluctuations of the location of AI events. A comprehensive study of the LOH, including 3D effects, could be achieved by means of tomographic CL [261].

In strong shear flow fields such as the one of the present experimental configuration, there are strong differences in the flow along the axial, radial and tangential directions. Therefore, it is interesting to analyze the orientation and growth of kernels with respect to the mean flow field. This analysis was performed in this study for the operating condition with Re_{jet} = 5000.

As can be deduced from Fig. 6.31, kernels tend to show an elongated shape. To statistically analyze the orientation of the kernels, a local coordinate was defined for each kernel based on the three principal axes of the fitted ellipsoid. To illustrate the evaluation, Fig. 6.34a shows a 3D sketch of an actual detected kernel along with the nozzle of the burner head (not at scale) as spatial reference. The direction of the major axis of the kernel is indicated by the vector l_1, and it was compared to the direction of the main flow (unit vector $\boldsymbol{e_x}$) by evaluating the angles k_{1x}

and k_{1r}. k_{1x} is the angle between l_1 and $\boldsymbol{e_x}$, while k_{1r} is the angle between l_1 and $\boldsymbol{e_r}$ (unit vector in the radial direction). Figure 6.34b shows PDF s of the magnitude of the direction cosines, |cos k_{1x}| and |cos k_{1r}|. Both PDFs exhibit a tendency towards zero with a higher probability of the |cos k_{1r}| ≈ 0. This means that the major axis of the AI kernels tends to be simultaneously perpendicular to $\boldsymbol{e_x}$ and $\boldsymbol{e_r}$, and that the kernels are preferentially oriented along the tangential direction with respect to the mean flow. The number of views and their angular orientation have an influence on the quality and accuracy of the tomographic reconstructions along the line-of-sight direction [255]. However, the preferential orientation of the kernels is not aligned with the line-of-sight of the views and therefore these findings are not biased by the limitations of the current setup.

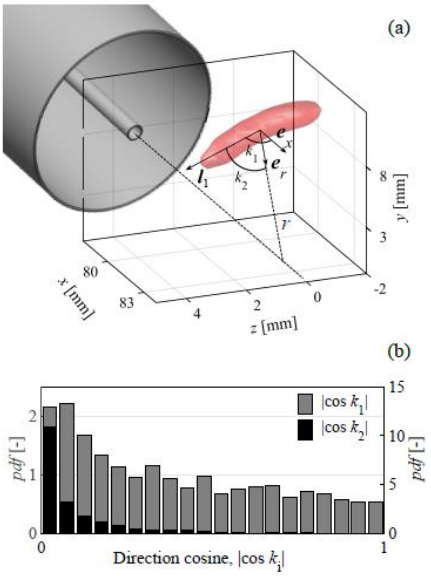

Figure 6.34
(a) 3D sketch of an actual detected kernel along with the nozzle of the burner head (not at scale) as spatial reference. The direction of the major axis of the kernel is indicated by the vector l_1. $\boldsymbol{e_x}$ and $\boldsymbol{e_r}$ represent unit vectors along the axial and radial directions, respectively. (b) PDF s of the magnitude of the direction cosines |cos k_{1x}| (left axis) and |cos k_{1r}| (right axis).

The growth of the ignition kernels was evaluated by the change of the Feret diameter along the major, intermediate and minor axes during one time step of 100 µs and the resulting PDF s are plotted in Fig. 6.35. The size along the major axis exhibit a larger growth than those of the intermediate and minor axes. This result, combined with the finding of the orientation analysis, suggests that the AI kernels are not only oriented tangentially to the flow but temporally evolve towards this same direction as the auto-ignition event progresses. This preferential direction of the growth could be aligned with a mean iso-surface of any scalar field (e.g. mixture fraction or temperature) [263, 256]. However, extended measurements to resolve such scalar fields are desirable to clarify these phenomena.

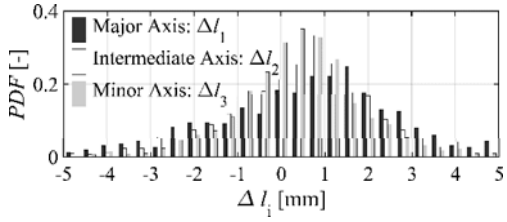

Figure 6.35
PDFs of the change of the Feret diameter along the major, intermediate and minor axes of AI kernels in a time step of 100 µs.

6.7 Conclusions high speed diagnostics

This chapter demonstrates the application of different optical diagnostic methods at repetition rates in the kHz-regime. For the selected examples the temporal resolution was short enough to resolve flow and flame dynamics at least of the larger scales. It was demonstrated that by rapid scanning of a measurement plane quasi-4D-information can be gained. Furthermore transient events such as flash back, ignition or extinction can be temporally tracked over thousands of frames. For auto-ignition it was demonstrated how tomographic imaging can be transferred to scalar fields, using multiple directions of observation.

Parts of the image sequences can be selected to extract information on flow or scalar properties of the flow at the instant of extinction, flash back or ignition. This selection can be regarded as "conditioning on a transient event". These high-speed diagnostics complement the view on turbulent flames that have been investigated mainly by statistically independent sampling. For close-to realistic systems, it is shown that these diagnostics can be applied to in-cylinder engine measurements; more recent papers in this context are [22, 23]. Due to the high repetition rates, temporal developments during individual cycles can be studied providing insides into cyclic variations. The large on-board memory additionally allows tracking many subsequent cycles during one engine run. This in addition reduces engine-run times.

In summary, high speed diagnostics is a constantly emerging field with new insights into combustion phenomena to be expected.

7. Quantities to be measured for LES-validation

The focus of this chapter is on validation of combustion-LES. In this context it is not directly evident how a measurand compares to its LES-calculated counterpart. Although it is common practice to assign a certain measurand to a physical or chemical quantity such as velocity component, temperature or species concentration, this measurand might be altered by different disturbing processes, spatial filtering or other reasons. Thus, the measurand containing the physical-chemical information is distorted.

This issue was addressed already in previous studies [258, 259, 118, 260]. Some aspects of these previous papers are recapitulated and some few are added. However, for a systematic analysis of LES-validation practice different aspects need to be considered.

The role of transients

A validation builds on statistical quantities extracted both from numerical simulation and experiment. This demand was clearly displayed in [259]. However, probability density functions (PDF) and statistical moments will be insufficient when processes are considered that occur seldom and individually. An example for such an event is flame extinction displayed in figure 6.6. If extinction would be caused by instantaneous large values of vorticity located in the close neighbourhood of the flame front, the PDF of vorticity measured by conventional low-repetition-rate-PIV would not represent values during extinction. Therefore it is crucial to measure vorticity – to stay within this example – during the course of the extinction process. In the data post-processing the quantity of interest can then be conditioned on the one hand on a suitable flame-coordinate (for example flame front or isoline of stoichiometric contour, compare [62]) and on the other hand on the instant when the extinction process starts (in figure 6.6 this would be some time between 1.6 and 2ms in the sequence). If several of such individual processes were evaluated, repeating mechanisms leading to extinction could be identified. In numerical experiments in a similar manner these kind of transients could be investigated. A thoroughful validation including the transient behaviour needs still a comparison in the statistical sense. However, even if just single events are compared due to computational cost or other restrictions, a qualitative comparison still would be valuable to evaluate the numerical simulation.

Favre-averages

Combustion-LES computes Favre-averaged filtered quantities. Measurands in experiments deliver in most cases filtered quantities that are not density-weighted. Exceptions are diagnostics that include the determination of density such as Rayleigh or Raman scattering from which the Favre-averaged value can be calculated. Common practice is that Favre-averaged quantities from numerical combustion are compared to unweighted measurands. This approach should be questioned and passable procedures need to be discussed to evaluate the impact on validation. When scalars are measured but excluding density, in a first step, the assumption of infinite fast chemistry and some a-priori-knowledge about the flame (i.e. location of rich or lean regions) could serve to estimate local densities from the measured scalar. For example in the lean branch of non-premixed methane/air combustion temperature is fairly well correlated to other scalars.

In the course of velocity measurements seeding densities directly monitored in PIV or arrival times recorded during LDV might be used for the estimation of local densities. For a temporally constant supply of chemically inert seeding at the nozzle exit and neglecting thermophoretic effects (particle velocity u_{TP} induced by temperature gradient, $u_{TP} \approx 0.5\nu \nabla T/T$ [175], ν is the kinematic viscosity), the local seeding density scales inversely with the gas density. Negligence of thermophoretic effects might be not justified close to flame fronts where temperature gradients are steep. However, at least in the post flame gases, the effect of Favre-averaging could be roughly estimated taking advantage of information already available. In case of simultaneous velocity-scalar measurements, the local density could be estimated by a one-dimensional state relationship as outlined above.

Filtering

LES provides filtered quantities whereas the filter-operation commonly is connected to the computational grid (implicit filtering). Experiments provide filtered quantities as well. Experimental filters are caused by extended probe volumes. Experimental and numerical filters are in general different and the question rises whether common validation practice compares apples and oranges.

From the experimental point of view, the probe volume shape should be characterised as precisely as possible. For example, in imaging experiments a pixel-resolution might not be sufficient. Blurring by optical elements for example can worsen the pixel-resolution considerably [262]. A better estimate of the real spatial resolution than just reporting the pixel-resolution might be obtained by measuring line-spread functions [264].

The measured probe volume size needs to be compared to scales that are necessary to resolve the structures within the fluid flow. Different strategies were discussed in the literature. Often Kolmogorov or Batchelor scales are estimated and compared to the achieved experimental resolution. However, in [118] the usefulness of this approach is questioned. In the same reference, it is outlined how different investigators have varied the effective probe size in turbulent flame measurements. For scalar means and variances this is reported to be a passable way: Means are influenced only marginally when the probe volume size is augmented, variances decrease linearly. This allows extrapolation back to full resolution.

In [260] it is proposed that for the condition of a filter size Δ much smaller than typical length scale $L_{\langle\,\rangle}$ of the turbulent combustion process ($\Delta << L_{\langle\,\rangle}$), averaged filtered and averaged unfiltered quantities can be directly compared ($\langle\overline{Q}\rangle \approx \langle Q\rangle$ with bar denoting "filtered" and brackets "averaged"). Typical length scales reported in [260] are mixing layers or flame brushs. In contrast, the variance of the considered quantity consists of a resolved part and a subfilter scale variance. These investigators doubt that neglecting the subfilter scalar variance is justified. However, this finding compares well with the "recipe" based on variation of effective probe sizes and reconstruction of "full resolution" by extrapolation summarized in [118].

If filter sizes and typical length scales are of the same order of magnitude or if filter sizes are even larger than typical length scales the situation is very different. An example is the determination of scalar dissipation rate especially at high *Re*. Downsizing of probe volumes is hindered either by constraints such as gas break down in case of laser radiation focused at a too small volume or simply by increase of noise that decreases signal-to-noise too much or causes positive bias (compare summary in [118]). Whereas for moderate *Re* the scales required to resolve scalar dissipation rates were successfully quantified [265], for very intense turbulence and high *Re* occurring in practical combustors so far no universally accepted procedure exists to the authors knowledge, to quantify scales resolving scalar dissipation. Spatial filtering of scalar dissipation rate measurements at high *Re* is therefore unavoidable without exactly knowing the ratio $\Delta / L_{\langle\,\rangle}$.

To summarize this aspect, experimental and LES-results can be directly compared in case of mean scalars (such as means of mixture fraction, temperature, velocity components, etc.). For variances a subfilter contribution exists both in experiment and simulation. Following [260] for velocities this subfilter part can be neglected but for scalar variances it has to be accounted for. Variation of probe sizes and extrapolation back is feasible for experiments to estimate the un-

filtered value. For LES, [260] proposes to model the subgrid variance. Comparison of experimental and numerical results should then occur using the corrected scalar variances. For quantities calculated from gradients such as scalar dissipation rate, it is at present not evident, how experimental and LES-calculated data compare especially at high *Re*. An "emergency measure" is here to assimilate LES-filter and experimental probe volume shape furthermost.

Noise

Measurands are disturbed by noise. Noise can be due to shot noise, thermal detector noise, readout noise etc. and is to a certain limit unavoidable. It was discussed above that noise can cause a positive bias (velocity variance [8], "apparent" dissipation, see [118] and references therein). The noise should be quantified in an experiment used for validation. A common way is to quantify the signal-to-noise ratio. This is possible by measuring the considered quantity in a calibration standard. This implies that the conditions of flow and scalar fields during these calibration measurements are laminar, stationary and well-known. Successful standards are heated gas flows, laminar flames, and wind-tunnels. From these calibration measurements a PDF is extracted. If it is Gaussian the variance is a reasonable measure to be used as "error bar".

Systematic errors such as bias due to noise are much more difficult to quantify. As exemplified in [4], computations based on LES help to study systematic errors.

Extinction and beam steering

Laser and signal beam paths transit different zones of a turbulent flame. During this transit, extinction (scattering and absorption, radiation trapping) and beam steering occurs. The effect of these processes on local laser intensity, laser pointing, local signal intensity and signal pointing depends on the specific flame. The impact will be higher for larger flame dimensions, higher pressures and presence of a dispersed phase such as in spray combustion. For validation experiments the impact on "effective" spatial resolution (flame-induced blurring) and bias in case of intensity-based scalar measurements must be known (trapping of signal radiation). Although blurring by beam steering can be estimated experimentally, it is proposed here to move the plane where experimental and numerical results are mutually compared from inside the flame to the detection plane. This implies that extinction and beam steering are included to the combustion-LES [266].

Here, just beam steering is discussed in some more detail. Beam steering is known as the effect of density and mixture fraction gradients on the propagation direction of radiation. In photodeflection spectroscopy [267] this effect can be used for combustion diagnostics. However, in other optical diagnostics this effect causes additional blurring (termed here flame-induced blurring).

The well-known formulation of beam steering in geometrical optics is based on the *"minimum principal"* postulated by Pierre de Fermat (1658). This principal prescribes the optimization of the optical path which is defined as

$$L = \int n\left(\vec{r}\right) ds \quad , \tag{46}$$

where $n\left(\vec{r}\right)$ represents the index of refraction varying as a function of position and s the length of the beam path. With the attainments of the calculus of variations, which is about

finding paths such that some integral along the path is extremized, one can straightforwardly derive the nonlinear partial differential equations (47) describing the beam propagation in space

$$(47) \quad \frac{\partial n}{\partial x_i} = \frac{d}{ds}\left(n \frac{dx_i}{ds} \right).$$

Using the initial direction of the beam (dx_i / ds), which depends on the chosen laser/signal pointing of a particular experimental setup, the ray propagation can be described up to a specified detector position. The fact that the speed of light propagation is much faster than typical combustion flow field velocities, makes this approach favourable since the local thermo-kinetic states can be assumed temporally constant as the beam propagates from laser to detector.

The only unknown variable remain to be defined is the index of refraction ($n\left(\vec{r}\right)$). The deflection of a beam arises mainly from the refractive index gradients which in turn arise from a combination of density and composition changes. The well-accepted Lorenz-Lorentz equation

$$(48) \quad n = \left(\frac{RT/P + 2\langle R_L \rangle}{RT/P - \langle R_L \rangle} \right)^{1/2},$$

where *R*, *T* and *P* denote the gas constant, temperature and pressure respectively, is proper for this purpose. The average molar refractivity $\langle R_L \rangle$ used in equation (48) can be calculated for a gas mixture containing *S* species that contribute significantly to refraction as

$$(49) \quad \langle R_L \rangle = \sum_{i=1}^{S} R_{L_i} X_i \ ,$$

where X_i is the mole fraction of the species. The molar refractivity R_L is tabulated for many combustion relevant species in [268]. Alternative relations for the calculation of index of refraction, like the Gladstone-Dale equation, are also examined in literature [269].

The experimental quantification of the species concentrations and temperature along the probable beam path (laser excitation and signal) on a single-shot base is impossible in practice. For this reason the effect of flame-induced beam steering can be considered only in a statistical sense. Combustion-LES is able to deliver the required spatially and temporally resolved information for the evaluation of the index of refraction with an adequate computer cost which makes post-processing of LES-data convenient for this purpose. Using local species concentrations and temperatures the volumetric distribution of the index of refraction can be reconstructed.

The time resolved information enables also the use of Monte-Carlo method to construct a PDF (probability density function) to estimate the beam deviation statistics on the detector (flame-induced blurring). This PDF can be used for the correction of the experimental data measured by laser diagnostic methods. Another information that may be gained is the path length of the traced beam. The path of the traced beam is, as expected, a curved path which differs in length and course from a straight one. Combining this information with the absorption coefficients of the species along the path, the Lambert-Beer law can be applied to calculate the absorption of the beam from its start location up to a desired destination or a detector. Thereby radiation trapping can be in principle accounted for.

Acknowledgements

Financial support of Deutsche Forschungsgemeinschaft and TU Darmstadt is kindly acknowledged.

References

1. M. Hage, A. Dreizler, J. Janicka, ASME-GT **2007-27108** (2007).
2. J. Köser, L.G. Becker, A.-K. Goßmann, B. Böhm, A. Dreizler, Proceedings of the Combustion Institute **36**, 2103 (2017).
3. L.G. Becker, H. Kosaka, B. Böhm, S. Doost, R. Knappstein, M. Habermehl, R. Kneer, J. Janicka, A. Dreizler, Fuel **201**, 124 (2017).
4. D. Geyer, A. Kempf, A. Dreizler, J. Janicka, P Combust Inst P Combust Inst **30**, 681 (2005).
5. H. Tennekes, J.L. Lumley, *A first course in turbulence* (The MIT Press, Cambridge, Massachusetts 1972).
6. S. Weitemeyer, N. Reinke, J. Peinke, M. Hölling, Fluid Dynamics Research **45**, 61407 (2013).
7. M. Petit, B. Coriton, A. Gomez, A. Kemp, Proc. Comb. Inst. **33**, 1391 (2011).
8. C. Schneider, A. Dreizler, J. Janicka, Flow Turbulence and Combustion **74**, 103 (2005).
9. M.A. Gregor, F. Seffrin, F. Fuest, D. Geyer, A. Dreizler, Proc. Comb. Inst. **32**, 1739 (2009).
10. C. Heeger, R. Gordon, M.J. Tummers, T. Sattelmayer, A. Dreizler, Exp. Fluids **49**, 853 (2010).
11. A. Nauert, P. Petersson, M. Linne, A. Dreizler, Exp. in Fluids **43**, 89 (2007).
12. R. Borghi, *On the structure and morphology of turbulent premixed flames* (Pergamon Press, London 1984).
13. N. Peters, *Turbulent combustion* (Cambridge University Press, Cambridge 2000).
14. J. Hermann, M. Greifenstein, B. Boehm, A. Dreizler, Flow, Turbulence and Combustion **69**, 178 (2019).
15. M. Greifenstein, J. Hermann, B. Boehm, A. Dreizler, Experiments in Fluids **60**, 169 (2019).
16. B. Janus, A. Dreizler, J. Janicka, Proc. Combust. Inst., **31**, 3091 (2007).
17. M. Chrigui, A. Sadiki, J. Janicka, M. Hage, A. Dreizler, Atomization and Sprays **19**, 929 (2009).
18. E. Baum, B. Peterson, B. Böhm, A. Dreizler, Proc. Comb. Inst. **34**, 2903 (2013).
19. E. Baum, B. Peterson, B. Böhm, A. Dreizler, Flow Turbulence and Combustion **92**, 269 (2014).
20. B. Peterson, E. Baum, B. Böhm, A. Dreizler, Proc. Comb. Inst. **35**, 3829 (2015).
21. B. Peterson, E. Baum, B. Böhm, V. Sick, A. Dreizler, Proc. Comb. Inst. **35**, 2925 (2015).
22. A. Renaud, C.-P. Ding, S. Jakirlic, A. Dreizler, B. Böhm, International Journal of Heat and Fluid Flow **71**, 366 (2018).
23. C.-P. Ding, B. Peterson, M. Schmidt, A. Dreizler, B. Böhm, Proceedings of the Combustion Institute **37**, 4973 (2019).
24. R.S. Barlow, *International Workshop on Measurement and Computation of Turbulent Non-premixed Flames (TNF)* (Sandia National Laboratories).
25. *Sandia National Laboratories Engine Combustion Network* (http://www.sandia.gov/ecn/).
26. J.N. Forkey, N.D. Finkelstein, W.R. Lempert, R.B. Miles, AIAA Journal **34**, 442 (1996).

27. C. Schulz (2007).
28. A. Schneider, J. Mantzaras, R. Bombach, S. Schenker, N. Tylli, P. Jansohn, Proc. Comb. Inst. **31**, 1973 (2007).
29. C. Jainski, L. Lu, V. Sick, A. Dreizler, Intl. J. Heat and Mass Transfer **74**, 101 (2014).
30. R.P. Lucht, D. Dunn-Rankin, T. Walter, T. Dreier, S.C. Bopp, SAE Technical Paper Series **910722** (1991).
31. M. Mann, C. Jainski, M. Euler, B. Böhm, A. Dreizler, Comb. Flame **161**, 2371 (2014).
32. A. Dreizler, B. Böhm, Proc. Comb. Inst. **35**, 37 (2015).
33. [Der Titel "#0" kann nicht dargestellt werden – Die Vorlage "Literaturverzeichnis - Zeitschriftenaufsatz - (Standardvorlage)" beinhaltet nur Felder, welche bei diesem Titel leer sind.]
34. H. Kosaka, F. Zentgraf, A. Scholtissek, L. Bischoff, T. Häber, R. Suntz, B. Albert, C. Hasse, A. Dreizler, International Journal of Heat and Fluid Flow **70**, 181 (2018).
35. J. Brübach, C. Pflitsch, A. Dreizler, B. Atakan, Prog. Energy Combust. Sci. **39**, 37 (2013).
36. S.W. Allison, Rev. Sci. Instrum **68**, 2615 (1997).
37. N. Fuhrmann, J. Brübach, A. Dreizler, Proc. Comb. Inst. **34**, 3611 (2013).
38. M. Aldén, A. Omrane, M. Richter, G. Särner, Prog. Energy Combust. Sci. **37**, 422 (2011).
39. N. Fuhrmann, J. Brübach, A. Dreizler, Rev. Sci. Instrum. **84**, 114902 (2013).
40. J. Brübach, A. Dreizler, J. Janicka, Meas. Sci. Tech. **18**, 764 (2007).
41. E.H. van Veen, D. Roekaerts, Appl. Optics **44**, 6995 (2005).
42. J. Brübach, M. Hage, J. Janicka, A. Dreizler, P Combust Inst P Combust Inst **32**, 855 (2009).
43. A. Omrane, F. Ossler, M. Aldén, Proc. Combust. Inst., 29, 2653 (2002). **29**, 2653 (2002).
44. A. Khalid, K. Kontis, Meas. sci. Technol. **20**, 25305 (2009).
45. N. Fuhrmann, M. Schild, D. Bensing, S.A. Kaiser, C. Schulz, J. Brübach, A. Dreizler, Appl. Phys. B **106**, 945 (2012).
46. N. Fuhrmann, M. Schneider, D.C. P, J. Brübach, A. Dreizler, Meas. Sci. Tech. **24**, 95203 (2013).
47. V. Weber, J. Brübach, R. Gordon, A. Dreizler, Appl. Phys. B **103**, 421 (2011).
48. T. Kissel, J. Brübach, E. Baum, A. Dreizler, Appl. Phys. B **96**, 731 (2009).
49. H.-E. Albrecht, M. Borys, N. Damaschke, C. Tropea, *Laser Doppler and phase Doppler measurement techniques* (Springer verlag 2003).
50. M. Raffel, C. Willert, J. Kompenhans, *Particle imaging velocimetry. a practical guide* (Springer verlag, Berlin 1998).
51. F. Scarano, Meas. Sci. Tech. **24**, 12001 (2013).
52. C. Willert, M. Jarius, Exp. Fluids **33**, 931 (2002).
53. D.P. Hart, Exp. in Fluids **29**, 13 (2000).
54. H.G. Maas, A. Gruen, D. Papantoniou, Exp. Fluids **15**, 133 (1993).
55. C.H. Brücker, Meas. Sci. Tech. **8**, 1480 (1997).
56. J. Bode, J. Schorr, C. Krüger, A. Dreizler, B. Böhm, Proceedings of the Combustion Institute **36**, 3477 (2017).
57. R. Konrath, W. Schröder, W. Limberg, Exp. Fluids **33**, 781 (2002).
58. J. Kitzhofer, T. Nonn, C. Brücker, Exp. Fluids **51**, 1471 (2011).
59. G.E. Elsinga, F. Scarano, B. Wieneke, B.W. van Oudheusden, Exp. Fluids **41**, 933 (2006).
60. R.A. Humble, F. Scarano, B.W. van Oudheusden, Exp. Fluids **43**, 173 (2007).

61. R. Hain, C.J. Kähler, D. Michaelis, Exp. Fluids **45**, 715 (2008).
62. B. Böhm, D. Geyer, A. Dreizler, K.K. Venkatesan, N.M. Laurendeau, M.W. Renfro, Proc. Combust. Inst., **31**, 709 (2007).
63. K.A. Watson, K.M. Lyons, J.M. Donbar, C.D. Carter, Combustion and Flame **117**, 257 (1999).
64. A. Nauert, A. Dreizler, Z. Phys. Chem. **219**, 635 (2005).
65. W. Hösel, W. Rodi, Rev. Sci. Instrum, 910 (1977).
66. J.C. Rotta, *Turbulente Strömungen* (Teubner Verlag, Stuttgart 1972).
67. S.B. Pope, *Turbulent Flows* (Cambridge University Press, Cambridge 2000).
68. A.K. Gupta, D.G. Lilley, N. Syred, *Swril flows* (Tunbridge Wells: Abacus Press, Cambridge 1984).
69. M.P. Escudier, J.J. Keller, AIAA Journal, 111 (1985).
70. M. Freitag, M. Klein, M. Gregor, D. Geyer, C. Schneider, A. Dreizler, J. Janicka, Int. Journal of Heat and Fluid Flow **27**, 636 (2006).
71. P. Ferrao, M.V. Heitor, Exp. in Fluids **24**, 399 (1998).
72. T.D. Fansler, M.C. Drake, B. Böhm, High-Speed Mie-scattering diagnostics for spray-guided gasoline engine development, in: (2008).
73. B. Peterson, D.L. Reuss, V. Sick, Proc. Comb. Inst. **33**, 3089 (2011).
74. J.C. Oefelein, R.W. Schefer, R.S. Barlow, AIAA J. **44**, 418 (2011).
75. D.L. Reuss, R.J. Adrian, C.C. Landreth, D.T. French, T.D. Fansler, Instantaneous planar measurements of velocity and large-scale vorticity and strain rate in an engine using particle-image velocimetry, in: (1989).
76. D.L. Reuss, Cyclic variability of large-scale turbulent structures in directed and undirected IC engine flows, in: (AIAA 2000).
77. C. Funk, V. Sick, D.L. Reuss, W.J.A. Dahm, Turbulence properties of high and low swirl in-cylinder flows, in: (2002).
78. C. Fajardo, V. Sick, Proc. Comb. Inst. **31**, 3023 (2007).
79. M. Voisine, L. Thomas, J. Boreé, P. Rey, Exp. Fluids **50**, 1393 (2011).
80. S.H.R. Müller, B. Böhm, M. Gleißner, R. Grzesik, S. Arndt, A. Dreizler, Exp. Fluids **48**, 281 (2010).
81. P. Druault, P. Guibert, F. Alizon, Exp. in Fluids **39**, 1009 (2005).
82. B. Peterson, V. Sick, Appl. Phys. B **97**, 887 (2009).
83. P.O. Calendini, T. Duverger, A. Lecerf, M. Trinite, In-Cylinder Velocity Measurements with Stereoscopic Particle Image Velocimetry in a SI engine, in: (AIAA 2000).
84. [Der Titel "#0" kann nicht dargestellt werden – Die Vorlage "Literaturverzeichnis - Zeitschriftenaufsatz - (Standardvorlage)" beinhaltet nur Felder, welche bei diesem Titel leer sind.]
85. J. Dannemann, K. Pielhop, M. Klaas, W. Schröder, Exp. Fluids **50**, 961 (2011).
86. B. Wieneke, Exp. Fluids **45**, 549 (2008).
87. G.T. Herman, A. Lent, Comput. Biol. Med. **6**, 273 (1976).
88. J. Westerweel, Exp. Fluids **16**, 236 (1994).
89. J. Zhang, B. Tao, J. Katz, Exp. Fluids **23**, 373 (1997).
90. O. Keck.
91. A. Eckbreth, *Laser Diagnostics for Combustion Temperature and Species* (Taylor & Francis 1998).
92. K. Kohse-Höinghaus, Prog. Energy Combust Sci. **20**, 203 (1994).
93. J.W. Daily, Prog. Energy Combust Sci. **23**, 133 (1997).

94. C. Schulz, A. Dreizler, V. Ebert, J. Wolfrum, *Handbook of Experimental Fluid Mechanics. Combustion Diagnostics* (Springer, Berlin 2007).
95. E.W. Rothe, Y. Gu, A. Chryssostomou, P. Andresen, Appl. Phys. B **66**, 251 (1998).
96. J. Luque, D.R. Crosley, *LIFBASE. Database and spectral simulation for diatomic molecules* (SRI International 1999).
97. W.G. Bessler, C. Schulz, V. Sick, J.W. Daily, A versatile modeling tool for nitric oxide LIF spectra (www.lifsim.com), in: (2003).
98. R. Kienle, M.P. Lee, K. Kohse-Höinghaus, Appl. Phys. B **63**, 403 (1996).
99. W.G. Bessler, M. Hofmann, F. Zimmermann, G. Suck, J. Jakobs, S. Nicklitzsch, L. T, J. Wolfrum, C. Schulz, Proc. Combust. Inst., **30**, 2667 (2005).
100. J.M. Seitzman, R.K. Hanson, Appl. Phys. B **57**, 385 (1993).
101. A. Roller, A. Arnold, M. Decker, V. Sick, J. Wolfrum, W. Hentschel, K.P. Schindler, SAE Paper, 952461 (1995).
102. M.P. Lee, B.K. McMillin, R.K. Hanson, Appl. Optics **32**, 5379 (1993).
103. M. Tamura, P.A. Berg, J.E. Harrington, J. Luque, J.B. Jeffries, G.P. Smith, D.R. Crosley, Combustion and Flame **114**, 502 (1998).
104. M. Tamura, J. Luque, J.E. Harrington, P.A. Berg, G.P. Smith, J.B. Jeffries, D.R. Crosley, Appl. Phys. B **66**, 503 (1998).
105. M. Tsujishita, A. Hirano, M. Yokoo, T. Sakuraya, Y. Takeshita, JSME International Journal Series B **42**, 119 (1999).
106. W.G. Bessler, F. Hildenbrand, C. Schulz, Appl. Optics **40**, 748 (2001).
107. J.B. Bell, M.S. Day, J.F. Grcar, W.G. Bessler, C. Schulz, P. Glarborg, A.D. Jensen, Proc. Combust. Inst., **29**, 2195 (2002).
108. R. Cattolica, Appl.Optics **20**, 1156 (1981).
109. W.G. Bessler, C. Schulz, Appl. Phys. B **78**, 519 (2004).
110. D.A. Long, *The Raman effect. A unified treatment of the theory of Raman scattering by molecules* (Wiley 2002).
111. D. Geyer, *1D Raman/Rayleigh experiments in a turbulent opposed-jet* (Darmstadt).
112. J. Zetterberg, Z.S. Li, M. Afzelius, M. Aldén, Two-dimensional temperature measurements in flames using filtered Rayleigh scattering at 254 nm, in: (2003).
113. R.W. Dibble, R.E. Hollenbach, P Combust Inst P Combust Inst **18**, 1489 (1981).
114. T. Landenfeld, A. Kremer, E.P. Hassel, J. Janicka, T. Schäfer, J. Kazenwadel, C. Schulz, J. Wolfrum, Proc. Combust. Inst., **27**, 1023 (1998).
115. C. Schulz, V. Sick, J. Wolfrum, V. Drewes, M. Zahn, R. Maly, Proc. Combust. Inst., **26**, 2597 (1996).
116. J. Warnatz, U. Maas, R.W. Dibble, *Combustion* (Springer verlag, Berlin 1999).
117. D. Geyer, A. Kempf, A. Dreizler, J. Janicka, Combustion and Flame **143**, 524 (2005).
118. R.S. Barlow, Proc. Combust. Inst., **31**, 49 (2007).
119. H.W. Schrötter, *Linear Raman Spectroscopy. A state of the art report* (Nato Advanced Study Institute Series, Series C, Mathematical and Physical Sciences, Dordrecht NL 1982).
120. D. Geyer, *1D-Raman/Rayleigh experiments in turbulent-opposed jet flows*. Ph.D. (Darmstadt).
121. R.S. Barlow, C.D. Carter, R.W. Pitz, Multiscalar diagnostics in turbulent flames, in: K. Kohse-Höinghaus, J.B. Jeffries (eds), *Applied Combustion Diagnostics* (Taylor & Francis, New York 2002).
122. D. Geyer, A. Dreizler, J. Janicka, A.D. Permana, J.-Y. Chen, P Combust Inst P Combust Inst **30**, 711 (2005).

123. D. Geyer, A. Dreizler, Evaluation of Raman scattering experiments in turbulent hydrocarbon-air flames, in: (2004).
124. W. Meier, S. Prucker, M.H. Cao, W. Stricker, Combustion Science and Technology **118**, 293 (1996).
125. A. Brockhinke, P. Andresen, K. Kohse-Höinghaus, Appl. Phys. B **61**, 533 (1995).
126. W. Meier, O. Keck, Measurement Science and Technology **13**, 741 (2002).
127. G. Herzberg, *Molecular Spectra and Molecular Structure. Volume II Infrared and Raman Spectra of Polyatomic Molecules* (Krieger Publishing Company, Malabar, Florida 1989).
128. M.M. Tacke, D. Geyer, E.P. Hassel, J. Janicka, Proceedings of the Combustion Institute **27**, 1157 (1998).
129. R.S. Barlow, P.C. Miles, P Combust Inst P Combust Inst **28**, 269 (2000).
130. G. Magnotti, D. Geyer, R.S. Barlow, Proc. Comb. Inst. **35**, 3765 (2015).
131. R.J. Hall, Opt. Commun. **52**, 360 (1985).
132. M. Pealat, M. Lefebvre, J.-P. Taran, P.L. Kelley, Phys. Rev. **38**, 1948 (1988).
133. S. Kröll, M. Aldén, T. Berglind, R.J. Hall, Appl. Optics **26**, 1068 (1987).
134. P.R. Regnier, J.-P. Taran, Appl. Phys. Lett. **23**, 240 (1973).
135. A.C. Eckbreth, Combustion and Flame **39**, 133 (1980).
136. W.A. England, J.M. Milne, S.N. Jenny, D.A. Greenalgh, Appl. Spectroscopy **38**, 867 (1984).
137. M. Schenk, T. Seeger, A. Leipertz, Appl. Optics **44**, 6526 (2005).
138. F.A. Maury, P.A. Libby, Combustion and Flame **102**, 341 (1995).
139. J. Eckstein, J.Y. Chen, C.P. Chou, J. Janicka, P Combust Inst P Combust Inst **28**, 141 (2000).
140. S.K. Omar, D. Geyer, A. Dreizler, J. Janicka, Progress in Computational Fluid Dynamics **4**, 241 (2004).
141. B. Böhm, O. Stein, A. Kempf, A. Dreizler, Flow Turbulence and Combustion **85**, 73 (2010).
142. B.E. Launder, G.J. Reece, W. Rodi, Journal of Fluid Mechanics **68**, 537 (1975).
143. C.P. Chou, J.-Y. Chen, J. Janicka, E. Mastorakos, International Journal of Heat and Mass Transfer **47**, 1023 (2004).
144. A. Permana, *Turbulent combustion in opposed jet flows*. Ph.D. thesis (London).
145. C.J. Sung, C.K. Law, J.-Y. Chen, P Combust Inst P Combust Inst **27**, 295 (1998).
146. S.B. Pope, Combustion Theory and Modelling **1**, 41 (1997).
147. S. Subramaniam, S.B. Pope, Combustion and Flame **115**, 487 (1998).
148. R.W. Bilger, P Combust Inst P Combust Inst **22**, 475 (1988).
149. E. Korusoy, J.H. Whitelaw, Exp. in Fluids **33**, 75 (2002).
150. H. Pitsch, P Combust Inst P Combust Inst **29**, 1971 (2002).
151. K.N.C. Bray, P.A. Libby, J.B. Moss, Combust. Sci. and Techn. **41**, 143 (1984).
152. P.A. Libby, Progress in Energy and Combustion Science **11**, 83 (1985).
153. T.D. Butler, P.J. O´Rourke, Proc. Combust. Inst., **16**, 1503 (1977).
154. A.R. Kerstein, Journal of Fluid Mechanics **231**, 361 (1991).
155. S. Menon, Int. Journal of Engine Research **1**, 209 (2000).
156. G. Markstein, *Nonsteady flame propagation* (Pergamon Press, Oxford 1964).
157. F.A. Williams, *Combustion theory* (Addison-Wesley, Massachusetts 1985).
158. J. Janicka, A. Sadiki, P Combust Inst P Combust Inst **30**, 537 (2005).
159. Y.C. Chen, N. Peters, G.A. Schneemann, N. Wruck, U. Renz, M.S. Mansour, Combustion and Flame **107**, 223 (1996).

160. B. Bédat, R.K. Cheng, Combustion and Flame **100**, 485 (1995).
161. T. Plessing, C. Kortschik, N. Peters, M.S. Mansour, R.K. Cheng, Proc. Combust. Inst., **28**, 359 (2000).
162. C. Kortschik, T. Plessing, N. Peters, Combustion and Flame **136**, 43 (2004).
163. A. Soika, F. Dinkelacker, A. Leipertz, Proc. Combust. Inst., **27**, 785 (1998).
164. S. Sattler, D.A. Knaus, F.C. Gouldin, Proc. Combust. Inst., **29**, 1785 (2002).
165. F. Seffrin, F. Fuest, D. Geyer, A. Dreizler, Comb. Flame **157**, 384 (2010).
166. G. Kuenne, F. Seffrin, F. Fuest, T. Stahler, A. Ketelheun, D. Geyer, J. Janicka, A. Dreizler, Combustion and Flame **159**, 2669 (2012).
167. M.S. Sweeney, S. Hochgreb, M.J. Dunn, R.S. Barlow, Combustion and Flame **159**, 2896 (2012).
168. M.S. Sweeney, S. Hochgreb, M.J. Dunn, R.S. Barlow, Combustion and Flame **159**, 2912 (2012).
169. P.A.M. Kalt, J.H. Frank, R.W. Bilger, P Combust Inst P Combust Inst **27**, 751 (1998).
170. J.H. Frank, P.A.M. Kalt, R.W. Bilger, Combustion and Flame **116**, 220 (1999).
171. D. Most, F. Dinkelacker, A. Leipertz, P Combust Inst P Combust Inst **29**, 2669 (2002).
172. K.N.C. Bray, *Turbulent flows with premixed reactants* (Springer verlag, Berlin 1980).
173. K.N.C. Bray, J.B. Moss, Acta Astonautica **4**, 291 (1977).
174. D. Veynante, A. Trouvé, K.N.C. Bray, T. Mantel, J. Fluid Mech. **332**, 263 (1997).
175. A. Gomez, D.E. Rosner, Combust. Sci. and Techn. **89**, 335 (1993).
176. B. Wegner, A. Maltsev, C. Schneider, A. Sadiki, A. Dreizler, J. Janicka, heat and Fluid Flow **25**, 528 (2004).
177. R.S. Barlow, A.N. Karpetis, P Combust Inst P Combust Inst **30**, 673 (2005).
178. B.B. Dally, A.R. Masri, R.S. Barlow, G.J. Fiechtner, Combustion and Flame **114**, 119 (1998).
179. J.H. Frank, S.A. Kaiser, M.B. Long, P Combust Inst P Combust Inst **29**, 2687 (2002).
180. R.W. Dibble, V. Hartmann, R.W. Schefer, W. Kollmann, Experiments in Fluids **5**, 103 (1987).
181. L.P. Goss, D.D. Trump, W.M. Roquemore, Exp. in Fluids **6**, 189 (1988).
182. J.M. Donbar, J.F. Driscoll, C.D. Carter, Combustion and Flame **122**, 1 (2000).
183. D. Han, M.G. Mungal, Proc. Combust. Inst., **29**, 1889 (2002).
184. P.A.M. Kalt, Y.-C. Chen, R.W. Bilger, Combustion and Flame **129**, 401 (2002).
185. N. Paone, Velocity measurements in turbulent premixed flames. development of a PIV measurement system and comparison with LDV, in: (1994).
186. R.S. Barlow, R.W. Dibble, J. Chen, R.P. Lucht, Combustion and Flame **82**, 235 (1990).
187. M. Stanislas, K. Okamoto, Kähler, C.J., Westerweel, J., Exp. in Fluids **39**, 170 (2005).
188. E.A. Cowen, S.G. Monismith, Exp. in Fluids **22**, 199 (1997).
189. L. Muniz, R.E. Martinez, M.G. Mungal, Application of PIV to turbulent reacting flows, in: (1996).
190. C.J. Sung, C.K. Law, R.L. Axelbaum, Combust. Sci. and Techn. **99**, 119 (1994).
191. J.E. Rehm, N.T. Clemens, Proc. Combust. Inst., **27**, 1113 (1998).
192. C.F. Kaminski, M.B. Long, Multi-dimensional diagnostics in space and time, in: K. Kohse-Höinghaus, J.B. Jeffries (eds), *Diagnostic Challenges for Gas Turbine Combustor Model Validation* (Taylor & Francis, New York 2002).
193. N.B. Jiang, M.C. Webster, W.R. Lempert, Appl. Opt. **48**, B23-B31 (2009).
194. M.J. Papageorge, T.A. McManus, F. Fuest, J.A. Sutton, Appl. Phys. B **115**, 197 (2014).
195. M.J. Papageorge, C. Arndt, F. Fuest, W. Meier, J.A. Sutton, Exp. Fluids **55**, 1763 (2014).

196. S. Roy, J.D. Miller, M. Slipchenko, P.S. Hsu, J.G. Mance, T.R. Meyer, J.R. Gord, Opt. Lett. **39**, 6462 (2014).
197. G.H. Wang, N.T. Clemens, P.L. Varghese, Appl. Optics **44**, 6741 (2005).
198. B. Bork, B. Böhm, C. Heeger, S.R. Chakravarthy, A. Dreizler, Appl. Phys. B **101**, 487 (2010).
199. A. Upatnieks, J.F. Driscoll, S.l. Ceccio, P Combust Inst P Combust Inst **29**, 1897 (2002).
200. S.F. Ahmed, R. Balachandran, E. Mastorakos, P Combust Inst P Combust Inst **31**, 1507 (2007).
201. B. Böhm, C. Heeger, R. Gordon, A. Dreizler, Flow Turbulence and Combustion **86**, 313 (2011).
202. (Taylor&Francis, New York 2002).
203. B. Bäuerle, J. Warnatz, F. Behrendt, P Combust Inst P Combust Inst **26**, 2619 (1996).
204. C. Schulz, V. Sick, Prog. Energy Combust Sci., 75 (2005).
205. P. Wu, W.R. Lempert, R.B. Miles, AIAA J. **38**, 672 (2000).
206. N. Jiang, M.C. Webster, W.R. Lempert, Appl. Opt. **48**, B23-B31 (2009).
207. C.F. Kaminski, J. Hult, M. Aldén, Appl. Phys. B **68**, 757 (1999).
208. D. Li, Z. Ma, P. Loosen, Du K, Opt. Lett. **32**, 1272 (2007).
209. C.M. Fajardo, V. Sick, Appl. Phys. B **85**, 25 (2006).
210. W. Paa, D. Müller, H. Stafast, W. Triebel, Appl. Phys. B **86**, 1 (2007).
211. S. Hammack, C. Carter, C. Wuensche, T. Lee, Appl. Opt. **53**, 5246 (2014).
212. W.R. Lempert, P. Wu, B. Zhang, R.B. Miles, J.L. Lowrance, V. Mastracola, W.F. Kosonocky, Pulse-burst laser system for high speed flow diagnostics, in: (1996).
213. T.G. Etoh, D. Poggemann, G. Kreider, H. Mutoh, A.J.P. Theuwissen, IEEE Transactions on Electron Devices **50**, 144 (2003).
214. A. Winkler, J. Wäsle, T. Sattelmayer, Fachtagung "Lasermethoden in der Strömungs-messtechnik" **12**, 18 (2004).
215. J. Weinkauff, M. Greifenstein, A. Dreizler, B. Böhm, Meas. Sci. Technol. **26**, 105201 (2015).
216. T. Li, J. Pareja, L. Becker, W. Heddrich, A. Dreizler, B. Böhm, Applied Physics B **123**, 1243 (2017).
217. R.J. Adrian, K.T. Christensen, Z.-C. Liu, Exp. in Fluids **29**, 275 (2000).
218. B. Böhm, C. Heeger, I. Boxx, W. Meier, A. Dreizler, P Combust Inst P Combust Inst **32**, 1647 (2009).
219. A. Lemaire, T.R. Meyer, K. Zähringer, J.R. Gord, J.C. Rolon, Exp. in Fluids, 36 (2004).
220. V.R. Katta, T.R. Meyer, J.R. Gord, W.M. Roquemore, Comb. Flame, 639 (2003).
221. C. Heeger, R.L. Gordon, M.J. Tummers, A. Dreizler, High repetition rate simultaneous laser diagnostics pplied to understanding in-nozzle mechanisms controlling flashback in lean premixed swirl flows, in: (2009).
222. C. Arcoumanis, J.H. Whitelaw, Proc. Inst. Mech. Eng. **201**, 57 (1987).
223. Clark **Patent No. 347,469**, *The Gas Engine*.
224. T. Kume, Y. Iwamoto, K. Lida, M. Murakami, K. Akishino, H. Ando, Combustion Control technologies for direct injection SI engine, in: (1996).
225. K. Kohse-Höinghaus, J. B. Jeffries (eds), *Applied Combustion Diagnostics* (Taylor&Francis, New York 2002).
226. R. Rouland, M. Trinté, F. Dionnet, A. Floch, A. Ahmed, Particle image velocimetry measurements in a high tumble engine for in-cylinder flow structure analysis, in: (1997).
227. D.P. Towers, C.E. Towers, Mea. Sci. Tech. **15**, 1917 (2004).

228. S. Jarvis, T. Justham, A. Clarke, C.P. Garner, K. Hargrave, N.A. Halliwell, J. of Physics: Conf. Series **45**, 38 (2006).
229. V. Sick, Development and application of high-speed imaging diagnostics for spray-guided spark-ignition direct-injection engines, in: (2008).
230. S.H.R. Müller, B. Böhm, M. Gleißner, S. Arndt, A. Dreizler, Appl. Phys. B **100**, 447 (2010).
231. J. Hult, M. Richter, J. Nygren, M. Aldén, A. Hultqvis, M. Christensen, B. Joansson, Appl. Optics **41**, 5002 (2002).
232. I. Boxx, M. Stöhr, C. Carter, W. Meier, Appl. Phys. B **95**, 23 (2009).
233. C. Kittler, A. Dreizler, Applied Physics B **89**, 163 (2007).
234. M. Konle, F. Kiesewetter, T. Sattelmayer, Exp. Fluids **44**, 529 (2008).
235. H. Becker, A. Arnold, R. Suntz, P. Monkhouse, J. Wolfrum, R. Maly, W. Pfister, Appl. Phys. B **50**, 473 (1990).
236. T.D. Fansler, M.C. Drake, B. Böhm, [Nachname nicht vorhanden], High speed diagnostics based on Mie scattering in the development of spray guided spark-ignition engines, in: (2008).
237. H. Malm, G. Sparr, J. Hult, C.F. Kaminski, Journal of the Optical Society of America A **17**, 2148 (2000).
238. C. Tropea, A.L. Yarin, *Springer handbook of experimental fluid mechanics* (Springer Science & Business Media 2007).
239. I. Boxx, C. Heeger, R. Gordon, B. Böhm, M. Aigner, A. Dreizler, W. Meier, 3. (2009, Proc. Combust. Inst. **32**, 905 (2009).
240. A.M. Steinberg, I. Boxx, C.M. Arndt, J.H. Frank, W. Meier, Proceedings of the Combustion Institute **33**, 1663 (2011).
241. B. Peterson, E. Baum, B. Böhm, A. Dreizler, Proc. Comb. Inst. **35**, 3829 (2015).
242. P.J. Trunk, I. Boxx, C. Heeger, W. Meier, B. Böhm, A. Dreizler, Proceedings of the Combustion Institute **34**, 3565 (2013).
243. J. Weinkauff, D. Michaelis, A. Dreizler, B. Böhm, Exp Fluids **54**, 2903 (2013).
244. C. Atkinson, J. Soria, Exp Fluids **47**, 553 (2009).
245. M. Petit, B. Coriton, A. Gomez, A. Kemp, Proc. Comb. Inst. **33**, 1391 (2011).
246. B. Coriton, J.H. Frank, Proceedings of the Combustion Institute **35**, 1243 (2015).
247. J. Weinkauff, J. Köser, D. Michaelis, B. Peterson, A. Dreizler, B. Böhm, 17th International Symposium on Applications of Laser Techniques to Fluid Mechanics Lisbon, Portugal, 07-10 July, 2014.
248. R. Wellander, M. Richter, M. Aldén, Exp Fluids **55**, 579 (2014).
249. L. Bischoff, M. Stephan, C.S. Birkel, C.F. Litterscheid, A. Dreizler, B. Albert, Scientific reports **8**, 602 (2018).
250. C.H. Brücker, Meas. Sci. Tech. **8**, 1480 (1997).
251. G.R.B.E. Römer, P. Bechtold, Physics Procedia **56**, 29 (2014).
252. B.R. Halls, P.S. Hsu, N. Jiang, E.S. Legge, J.J. Felver, M.N. Slipchenko, S. Roy, T.R. Meyer, J.R. Gord, Optica **4**, 897 (2017).
253. J. Pareja, A. Johchi, T. Li, A. Dreizler, B. Böhm, Proceedings of the Combustion Institute **37**, 1321 (2019).
254. F. Eitel, J. Pareja, D. Geyer, A. Johchi, F. Michel, W. Elsäßer, A. Dreizler, Exp Fluids **56**, 37 (2015).
255. T. Li, J. Pareja, F. Fuest, M. Schütte, Y. Zhou, A. Dreizler, B. Böhm, Meas. Sci. Technol. **29**, 15206 (2018).

256. F. Eitel, J. Pareja, A. Johchi, B. Böhm, D. Geyer, A. Dreizler, Combustion and Flame **177**, 193 (2017).
257. Markides, Journal of Engineering for Gas Turbines and Power, 011502-1 (2008).
258. E.P. Hassel, S. Linow, Measurement Science and Technology **11**, R37-R57 (2000).
259. S.B. Pope, New Journal of Physics **6**, 35 (2004).
260. D. Veynante, R. Knikker, Journal of Turbulence **6**, 1 (2006).
261. N.A. Worth, J.R. Dawson, Meas. Sci. Technol. **24**, 24013 (2013).
262. N.T. Clemens, Flow Imaging, in: J.P. Hornak (ed), *Encyclopedia of imaging science and technology* (J. Wiley, New York 2002).
263. S.G. Kerkemeier, C.N. Markides, C.E. Frouzakis, K. Boulouchos, Journal of Fluid Mechanics **720**, 424 (2013).
264. G.H. Wang, N.T. Clemens, Exp. in Fluids **37**, 194 (2004).
265. G.H. Wang, R.S. Barlow, N.T. Clemens, Proc. Combust. Inst., **31**, 1525 (2007).
266. C.K. Ertem, J. Janicka, A. Dreizler, Appl. Phys. B **107**, 603 (2012).
267. A. Rose, R. Gupta, Proc. Combust. Inst., **20**, 1339 (1984).
268. W.C. Gardiner, JR., Y. Hidaka, T. Tanzawa, Combustion and Flame **40**, 213 (1981).
269. J.R. Patington, *An advanced Treatise on physical chemistry, Vol. 4* (Green, London 1953).